IN THE UNITED STATES PATENT AND TRADEMARK OFFICE

In re Patent Application of

Applicants: Bednorz et al.

Serial No.: 08/479,810

Filed: June 7, 1995

Date: May 15, 2008

Docket: YO987-074BZ

Group Art Unit: 1751

Examiner: M. Kopec

For: NEW SUPERCONDUCTIVE COMPOUNDS HAVING HIGH TRANSITION TEMPERATURE, METHODS FOR THEIR USE AND PREPARATION

Commissioner for Patents
United States Patent and Trademark Office
P.O. Box 1450
Alexandria, VA 22313-1450

APPEAL BRIEF
PART IX

CFR 37 § 41.37(c) (1) *(ix)*

SECTION 1

VOLUME 4

Part 3

BRIEF ATTACHMENTS F TO O

Respectfully submitted,

/Daniel P Morris/
Dr. Daniel P. Morris, Esq.
Reg. No. 32,053
(914) 945-3217

IBM CORPORATION
Intellectual Property Law Dept.
P.O. Box 218
Yorktown Heights, New York 10598

BRIEF ATTACHMENT F

IN THE UNITED STATES PATENT AND TRADEMARK OFFICE

In re Patent Application of
Applicants: Bednorz et al.
Serial No.: 08/479,810
Filed: June 7, 1995

Date: March 1, 2005
Docket: YO987-074BZ
Group Art Unit: 1751
Examiner: M. Kopec

For: NEW SUPERCONDUCTIVE COMPOUNDS HAVING HIGH TRANSITION TEMPERATURE, METHODS FOR THEIR USE AND PREPARATION

Commissioner for Patents
P.O. Box 1450
Alexandria, VA 22313-1450

FIRST SUPPLEMENTAL AMENDMENT

Sir:

In response to the Office Action dated July 28, 2004, please consider the following:

ATTACHMENT F

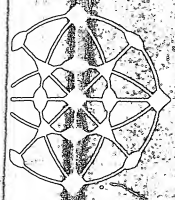

Journal of Solid State Chemistry

ACADEMIC PRESS
New York and London
A Subsidiary of Harcourt Brace Jovanovich, Publishers

JOURNAL OF SOLID STATE CHEMISTRY 39, 120–127 (1981)

Oxygen Defect K_2NiF_4-Type Oxides: The Compounds $La_{2-x}Sr_xCuO_{4-x/2+\delta}$

NINH NGUYEN, JACQUES CHOISNET,[1] MARYVONNE HERVIEU, AND BERNARD RAVEAU

Laboratoire de Cristallographie et Chimie du Solide, L.A. 251, ISMRA, Université de Caen, 14032 Caen Cedex, France

Received December 29, 1980; in final form February 18, 1981

Oxygen defect K_2NiF_4-type oxides $La_{2-x}Sr_xCuO_{4-x/2+\delta}$ have been synthesized for a wide composition range: $0 \leq x \leq 1.34$. From the X-ray and electron diffraction study three domains have been characterized: orthorhombic compounds with La_2CuO_4 structure for $0 \leq x < 0.10$, tetragonal oxides similar to $LaSrCuO_4$ for $0.10 \leq x < 1$ and several superstructures derived from the tetragonal cell ($a \simeq n.a_{LaSrCuO_4}$ with $n = 3, 4, 4.5, 5, 6$) for $1 \leq x \leq 1.34$. The compounds corresponding to $0 < x < 1$ differ from the other oxides in that they are characterized by the presence of copper with two oxidation states: +2 and +3. A model structure for $La_{0.8}Sr_{1.2}Cu\square O_{3.4}$, in which copper has only the +2 oxidation state, and for which the actual cell is tetragonal—$a = 18.80$, Å and $c = 12.94$ Å—has been established. The particular structural evolution of these compounds is discussed in terms of a competition between the capability of Cu(II) to be oxidized to Cu(III) and the ordering of oxygen vacancies.

Introduction

A lot of oxides, with the A_2MO_4 formula, characterized by the intergrowth of perovskite- and sodium chloride-type layers are known at the present time. Contrary to the perovskite oxides, no oxygen defect has been observed for this structural series to our knowledge. Copper, due to its ability to take different coordinations smaller than six, is a potential candidate which could form such anion defect compounds. However the only isostructural copper compounds which have been synthesized, La_2CuO_4 (*1*, *2*) and $SrLaCuO_4$ (*3*) are stoichiometric. Nevertheless, the recent results concerning the oxides $La_{2-x}A_{1+x}O_{6-x/2}$ (A = Ca, Sr) (*4*), whose structure is strongly related to that of $Sr_3Ti_2O_7$ (*5*) suggest the possibility of oxygen defect for A_2CuO_4 compounds. Thus, the present work deals with the oxides $La_{2-x}Sr_xCuO_{4-x/2+\delta}$, for which the replacement of lanthanum by strontium leads to the formation of oxygen vacancies, involving order phenomena.

Experimental

For the synthesis of the compounds of the system La_2CuO_4–Sr_2CuO_3, $SrCO_3$, CuO and La_2O_3 were mixed according to the following ratios: $(2-x)/2La_2O_3/x\,SrCO_3/1\,CuO$. All these reactions were made in a platinum crucible in air. The synthesis of the compounds with high purity strongly depends on the temperature for a fixed pressure. The mixtures were thus first heated for 5 hr at 900°C, and then at tem-

peratures ranging
12 hr.

The oxidation s
oxygen defect, wa
the compounds by
reactions were foll
try using a Setara

The crystallogr
lished by two com
ray diffractometry
with a Philips goni
fraction using an
scope.

Results

Study of the Syste The Compounds L

According to the
scribed, K_2NiF_4-t
sponding to the
$La_{2-x}Sr_xCu^{II}O_{4-x/2}$
large composition r
microthermogravin
ides under hydro
that a part of Cu(I

Range	x	
I	0	0
	0.08	0.0
II	0.25	0.0
	0.33_3	0.1
	0.50	0.1
	0.66_6	0.0
	0.88_8	0.0
III	1.00[a]	0.0
	1.28[a]	0.0
	1.34[a]	0.0
	1.20	0.0

[a] The "a" parameters
composition are given in

[1] Author to whom reprint requests should be addressed.

0022-4596/81/100120-08$02.00/0

peratures ranging from 1000 to 1200°C for 12 hr.

The oxidation state of copper, i.e., the oxygen defect, was determined by reducing the compounds by hydrogen: the reduction reactions were followed by thermogravimetry using a Setaram microbalance.

The crystallographic data were established by two complementary methods: X-ray diffractometry using Cu$K\alpha$ radiation with a Philips goniometer and electron diffraction using an EM 200 Philips microscope.

Results

Study of the System La_2CuO_4–Sr_2CuO_3: The Compounds $La_{2-x}Sr_xCuO_{4-x/2+\delta}$

According to the methods previously described, K_2NiF_4-type compounds corresponding to the nominal composition $La_{2-x}Sr_xCu^{II}O_{4-x/2}$ were synthesized in a large composition range: $0 \leq x \leq 1.34$. The microthermogravimetric study of these oxides under hydrogen showed, however, that a part of Cu(II) had been oxidized to Cu(III), leading to the formula $La_{2-x}Sr_xCuO_{4-x/2+\delta}$ with $0 \leq \delta < 0.12$. For $x > 1.34$ a mixture of the K_2NiF_4-type phase and Sr_2CuO_3 (*6*) was observed.

The crystallographic data of different compositions are summarized in Table I. The study of the X-ray patterns showed a continuous evolution of the structure and allowed to characterize three composition ranges which were studied by electron diffraction.

(*I*) $0 \leq x < 0.10$. The X-ray patterns very similar to that of La_2CuO_4 (*1*) were indexed in an orthorhombic cell with:

$$a_I = 2a_p \sin \beta/2 \simeq a_{La_2CuO_4},$$

$$b_I = 2a_p \cos \beta/2 \simeq b_{La_2CuO_4},$$

$$c_I \simeq c_{La_2CuO_4},$$

where a_p is the parameter of the perovskite cubic cell, and β defines the monoclinic distortion of the cell.

From the conditions limiting possible reflections—$hkl: h + k, l + h, k + l = 2n$—three space groups are possible: *Fmmm*, *Fmm*2, and *F*222.

TABLE I

CRYSTALLOGRAPHIC DATA OF $La_{2-x}Sr_xCuO_{4-x/2+\delta}$ COMPOUNDS

Range	x	δ	Composition	a (Å)	b (Å)	c (Å)	Heating temperature (°C)
I	0	0	La_2CuO_4	5.366(2)	5.402(2)	13.149(4)	1100
	0.08	0.030(1)	$La_{1.92}Sr_{0.08}CuO_{3.99}$	5.351(1)	5.368(2)	13.200(5)	1000
II	0.25	0.060(4)	$La_{1.75}Sr_{0.25}CuO_{3.955}$	3.775(2)		13.247(5)	1000
	0.33[a]	0.119(4)	$La_{1.67}Sr_{0.33}CuO_{3.95}$	3.776(1)		13.250(2)	1100
	0.50	0.100(4)	$La_{1.50}Sr_{0.50}CuO_{3.85}$	3.773(1)		13.204(3)	1160
	0.66[a]	0.092(4)	$La_{1.35}Sr_{0.66}CuO_{3.75a}$	3.775(1)		13.150(4)	1170
	0.88[a]	0.088(4)	$La_{1.12}Sr_{0.88}CuO_{3.64a}$	3.773(1)		13.073(5)	1170
III	1.00[a]	0.0	$LaSrCuO_{3.50}$	3.767(1)		13.002(3)	1200
	1.28[a]	0.0	$La_{0.72}Sr_{1.28}CuO_{3.36}$	3.761(2)		12.922(9)	1200
	1.34[a]	0.0	$La_{0.66}Sr_{1.34}CuO_{3.33}$	3.759(3)		12.907(9)	1200
	1.20	0.0	$La_{0.80}Sr_{1.20}CuO_{3.40}$	18.803(7)		12.941(7)	1200

[a] The "*a*" parameters of these compounds (range III) are those of the tetragonal subcell; *n* values for every composition are given in Table II.

(*II*) $0.10 \leq x < 1$. The symmetry is tetragonal like that of $LaSrCuO_4$ (*3*); the cell parameters are related to the latter and to I in the following manner:

$$a_{II} \simeq a_I/2^{1/2} \simeq a_p \simeq a_{LaSrCuO_4},$$

$$c_{II} \sim c_I \sim c_{LaSrCuO_4}.$$

The reflection conditions are those of $LaSrCuO_4$—*hkl*: $h + k + l = 2n$—involving the space groups: *I4/mmm*, *I4/m*, *I*422 and *I*42*m*.

(*III*) $1 \leq x \leq 1.34$. The X-ray diffractograms are characterized by the existence of a system of strong peaks, which was already observed for the compounds (II), involving at least the existence of a tetragonal subcell of the same type. However, for all these patterns, weak peaks were always observed which could not be indexed in this cell. An electron diffraction study was thus undertaken: about 50 crystals were examined for each value of x given in Table II. Several types of crystals were isolated:

—Small number of crystals, about 10%, were characterized by a tetragonal cell similar to that of $LaSrCuO_4$:

$$a_{III} \sim a_{II} \sim a_p \sim a_{LaSrCuO_4},$$

$$c_{III} \simeq c_{II} \simeq c_I \sim c_{LaSrCuO_4}.$$

—Most of the crystals, i.e., about 90%, presented, in addition to the fundamental reflections previously described, superstructure reflections with a variable intensity. The electron diffraction patterns allowed us to find the following relations for the actual tetragonal cell for a composition x:

$$a^*_{III} = na_{III} \sim na_{II},$$

$$c^*_{III} = c_{III} \# c_{II} \simeq c_I.$$

For a same composition x, several sorts of superstructures were generally observed, characterized either by integral n values (n = 4, 5, or 6) or nonintegral values of n (n ranging from 4.5 to 5.6), as shown for several compositions in Table II. Figure 1 shows, as an example, the electron diffraction patterns of the (001) planes for $La_{2/3}Sr_{4/3}CuO_{3.33}$. From Table II it can be seen that a pure term, characterized by a superstructure with an integral value of n (n = 5), is only obtained for $x = 1.20$. It has thus been attempted to elaborate a structural model for this phase.

TABLE II

n VALUES OBSERVED BY ELECTRON DIFFRACTION FOR COMPOUNDS OF RANGE III

Composition	x	n
$LaSrCuO_{3.5}$	1.00	I; 4.5
$La_{0.88}Sr_{1.12}CuO_{3.44}$	1.12	I; 4.5; 5
$La_{0.80}Sr_{1.20}CuO_{3.40}$	1.20	5
$La_{0.75}Sr_{1.25}CuO_{3.36}$	1.28	I; 4.6; 5; 5.3; 5.4
$La_{0.66}Sr_{1.34}CuO_{3.33}$	1.34	I; 4; 5; 5.6; 6

A Structural Model for $La_{0.8}Sr_{1.2}CuO_{3.4}$

The actual cell of this compound is tetragonal: $a = 18.80_4$ Å and $c = 12.94$ Å (Z = 50). The conditions limiting possible reflections are the same as those of the subcell ($a = 3.760$, $c = 12.94$ Å; $Z = 2$), leading to the space groups *I4/mmm*, *I4/m*, *I*422, and *I*42*m*. The intensity calculations were first made in the K_2NiF_4 type cell, with the most symmetric space group *I4/mmm*. For these calculations, reflections corresponding only to the subcell were used. Copper atoms were placed on 2(*a*), lanthanum and strontium atoms were statistically distributed on 4*e*, and oxygen atoms and anionic vacancies were statistically distributed over two sorts of sites 4*e* (O_I) and 4*c* (O_{II}). After refinement of the atomic parameters the discrepancy factor could not be lowered below $R = 0.104$. The possibility of an order of the oxygen atoms and vacancies over the O_I and O_{II} sites was thus considered. The occupancy factors of both sites

FIG. 1. Electron dif
(d) 6.

were refined successi
neously and the best
(Table IV) was obtain

TABL

$La_{0.80}Sr_{1.20}O_{3.40}$: ATOM PO

	Sites	x	y
La, Sr	4(*e*)	0	0
Cu	2(*a*)	0	0
O_I	4(*e*)	0	0
O_{II}	4(*c*)	0	0,5

[a] $a = 3.760$ Å; $c = 12.94$

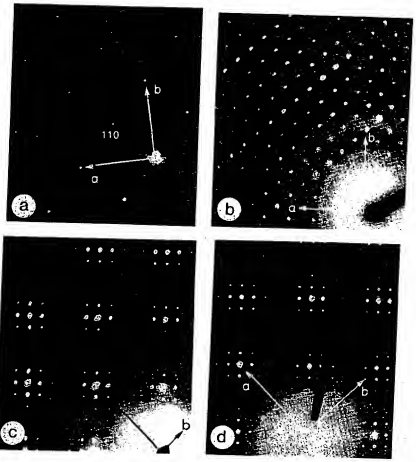

FIG. 1. Electron diffraction patterns of the (001) planes for $La_{n+1}Sr_{4/3}CuO_{3n+2}$: (a) $n = 1$, (b) 4, (c) 5.6, (d) 6.

were refined successively and then simultaneously and the best value of $R = 0.081$ (Table IV) was obtained for a total occupation of the O_I sites, while vacancies and oxygen atoms were distributed over the O_{II} sites. The location of the vacancies preferentially on the O_{II} sites, at the same level as the copper atoms, can be considered as significant, on account of the relatively weak scattering factor of oxygen. This is confirmed by the high R value ($R = 0.153$) obtained for a total occupation of the O_{II} sites, vacancies and oxygen atoms being distributed on the O_I sites. The first results which are summarized in Table III show the atoms are located in positions very close to those usually observed in K_2NiF_4 type structures. The main difference with

TABLE III

$La_{0.80}Sr_{1.20}O_{3.40}$: ATOM POSITIONS IN THE SUBCELL[a]

	Sites	x	y	z	B (Å²)
La, Sr	4(e)	0	0	0.357 ± 0.001	0.88
Cu	2(a)	0	0	0	0.85
O_I	4(e)	0	0	0.168 ± 0.002	1.68
O_{II}	4(c)	0	0.5	0	4.25

[a] $a = 3.760$ Å; $c = 12.94$ Å.

TABLE IV

$La_{0.8}Sr_{1.2}CuO_{3.4}$: OBSERVED AND CALCULATED INTENSITIES FOR ATOMIC POSITIONS OF TABLE III[a]

h k l	I_{obs}	I_{calc}
0 0 2	4.0	4.0
1 0 1	13.0	15.1
0 0 4	17.0	16.9
1 0 3	164.0	156.1
1 1 0	114.0	115.1
1 1 2	0.1	1.7
0 0 6	29.0	23.6
1 0 5	27.0	23.5
1 1 4	35.0	34.6
2 0 0	44.0	49.8
2 0 2	0.1	0.4
1 1 6	26.0	25.2
2 1 1	3.9	3.8
1 0 7	12.0	11.1
2 0 4	10.3	8.2
0 0 8	6.6	5.3
2 1 3	48.0	48.1
2 0 6	15.8	18.1
2 1 5	8.1	9.4
1 1 8	9.0	7.5
1 0 9	0.1	1.7
2 2 0	9.0	12.4
2 2 2	0.1	0.1
0 0 10	0.1	0.8
3 0 1	0.1	0.7
2 1 7	6.0	7.0
2 2 4	3.3	3.0
2 0 8	7.6	6.9
3 0 3	7.0	8.8

[a] Subcell, space group $I4/mmm$; R = 0.081.

the ideal structure concerns the existence of vacancies located in the same plane as the copper atoms (Fig. 2). Moreover, the high B value for oxygen of O_1 sites (4.2 Å^2) suggests that in this plane oxygen and vacancies were ordered.

Calculations in the actual cell in space group $I4/mm$, were undertaken with 136 possible reflections, including superstructure reflections. Using the position and distributions determined from the subcell, the R factor increased to 0.104, showing, of course, a weak contribution of the superstructure reflections to the R value. The

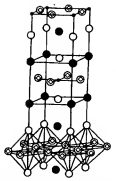

FIG. 2. Ideal drawing of the tetragonal K_2NiF_4-type structure showing the localization of oxygen vacancies for $La_{0.8}Sr_{1.2}CuO_{3.4}$.

atomic parameters were then refined and the R value was lowered to 0.07 for the final atomic parameters given in Table V. From this table it can be seen that copper atoms are not significantly displaced from their ideal positions, while the bigger cations La, Sr, and the oxygen atoms are only slightly displaced from their ideal positions, but enough to produce the superstructure reflections. These small displacements are certainly induced by an order of the oxygen vacancies, whose contribution to intensities is too small to be detected here. Thus, on account of the numerous possibilities of order between vacancies, and oxygen atoms, and of the weak scattering power of these atoms, we did not try any hypothesis of distribution. Nevertheless, the very likely ordering of vacancies in the "copper plane," should also involve an ordering of lanthanum and strontium over the different sites. Refining the occupancy factors of La and Sr, led to an R value of 0.064 which is not very significant due to the weak contribution of La and Sr to the superstructure reflexions; a preferential occupation of the different sites is, however, likely: A_1, A_4, and A_5 would only be occupied by strontium, while lanthanum would occupy 90% of A_6 sites, the remaining strontium and lanthanum atoms being located statistically over the A_2 and A_3 sites.

T

$La_{0.8}Sr_{1.2}SuO_{3.4}$: A1
ACI

Sites	x
$A_1(4e)$	0
$A_2(16n)$	0.194
$A_3(16n)$	0.403
$A_4(16m)$	0.200
$A_5(16m)$	0.410
$A_6(32O)$	0.389
$A_7(2a)$	0
$A_8(8i)$	0.200
$A_9(8i)$	0.400
$A_{10}(8h)$	0.200
$A_{11}(8h)$	0.405
$A_{12}(16l)$	0.403
$A_{13}(4e)$	0
$A_{14}(16n)$	0.216
$A_{15}(16n)$	0.382
$A_{16}(16m)$	0.182
$A_{17}(16m)$	0.400
$A_{18}(32O)$	0.400
$A_{19}(8i)$	0.100
$A_{20}(8i)$	0.300
$A_{21}(4c)$	0
$A_{22}(16l)$	0.214
$A_{23}(16l)$	0.430
$A_{24}(16l)$	0.300
$A_{25}(16l)$	0.390
$A_{26}(8j)$	0.200
$A_{27}(8j)$	0.400

[a] a = 18.804 Å; c = $I4/mmm$).

Discussion

The stabilization, Cu(III) by only heati worthy of note. Bu characteristic of this existence of a Cu(III) $< x < 1$) which lies regions (x = 0 and x strongly related one t be explained by two c are competitive: the stoichiometric K_2NiF La_2CuO_4 and $LaSrCu$ form a related defect

TABLE V

$La_{0.8}Sr_{1.2}SuO_{3.8}$: ATOMIC PARAMETERS OF THE ACTUAL CELL[a]

Sites	x	y	z	B (Å²)
$A_1(4e)$	0	0	0.347	0.35
$A_2(16n)$	0.194	0	0.359	1.00
$A_3(16n)$	0.403	0	0.356	0.39
$A_4(16m)$	0.200	0.200	0.357	0.32
$A_5(16m)$	0.410	0.410	0.358	1.00
$A_6(32O)$	0.389	0.192	0.357	0.86
$A_7(2a)$	0	0	0	0.80
$A_8(8i)$	0.200	0	0	0.51
$A_9(8i)$	0.400	0	0	0.43
$A_{10}(8k)$	0.200	0.200	0	0.31
$A_{11}(8k)$	0.405	0.405	0	1.00
$A_{12}(16l)$	0.403	0.205	0	0.37
$A_{13}(4e)$	0	0	0.168	1.00
$A_{14}(16n)$	0.216	0	0.168	1.00
$A_{15}(16n)$	0.382	0	0.168	1.00
$A_{16}(16m)$	0.182	0.182	0.172	1.00
$A_{17}(16m)$	0.400	0.400	0.168	1.00
$A_{18}(32O)$	0.400	0.202	0.163	1.00
$A_{19}(8i)$	0.100	0	0	1.00
$A_{20}(8i)$	0.300	0	0	1.00
$A_{21}(4c)$	0	0.500	0	1.00
$A_{22}(16l)$	0.214	0.100	0	1.00
$A_{23}(16l)$	0.430	0.100	0	1.00
$A_{24}(16l)$	0.300	0.200	0	1.00
$A_{25}(16l)$	0.390	0.310	0	1.00
$A_{26}(8j)$	0.200	0.500	0	1.00
$A_{27}(8j)$	0.400	0.500	0	1.00

[a] a = 18.804 Å; c = 12.941 Å (space group I_4/mmm).

Discussion

The stabilization, in this system, of Cu(III) by only heating the oxides in air is worthy of note. But the most important characteristic of this system concerns the existence of a Cu(III) composition range ($0 < x < 1$) which lies between two Cu(II) regions ($x = 0$ and $x \geq 1$), for structures strongly related one to the other. This can be explained by two opposite effects which are competitive: the trend to preserve a stoichiometric K_2NiF_4 structure as for La_2CuO_4 and $LaSrCuO_4$ and the trend to form a related defect structure but with an ordering of the oxygen vacancies. Thus, rather close to the stoichiometric compound La_2CuO_4 ($x < 1$), the trend to stoichiometry is favored and the vacancies formed from the nominal compositions involving only Cu(II) are partly balanced by the oxidation of Cu(II) to Cu III. For $x \geq 1$, i.e., rather far from stoichiometry, the La_2CuO_4 or "$LaSrCuO_4$" stoichiometric compounds cannot be stabilized any more and orderings of the oxygen vacancies appear leading to different microphases as observed from the electron diffraction study, favoring Cu(II) with smaller coordinations (*2*, *5*).

Structure is not, of course, the only factor governing the relative stability of Cu(II) and Cu(III) in these oxides. Kinetics play an important part for determining the ratio Cu(III)/Cu(II) in the richer Cu(III) oxides. For $0 < x < 1$, we have indeed noticed that the pure compounds could only be synthesized by heating at least 12 hr at the formation temperature (Table I) in order to ensure a good crystallization. Annealing the same samples at the same temperature, during longer periods (24 hr) allows us to prepare pure phases with the same structure, but with greater amount of Cu(III). The oxygen pressure will also influence the Cu(III)/Cu(II) ratios. Heating, for example, some Cu(III) samples at low temperature under vacuum, involves a decrease of Cu(III) amount without destroying the structure. In the same way, a reaction under oxygen allows us to increase the Cu(III) amount.

The influence of the Cu(III) amount can also be detected by considering the structural evolution, especially the c parameter, of these compounds as a function of composition (Fig. 3). This evolution is rather complex and quite different from that usually observed for single solid solutions. The substitution of strontium for lanthanum, should not affect this evolution, due to the similar sizes of these cations. It seems interesting to take the Cu(II) compounds as

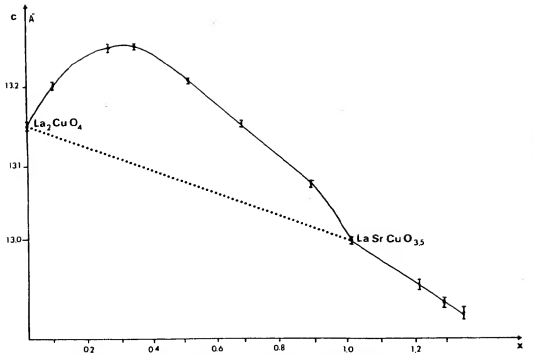

FIG. 3. Evolution of the "c" parameter as a function of x.

a reference (dotted lines). Although we have only our compositions for comparison it can be seen that from $La_2Cu^{II}O_4$ to $La_{0.7}Sr_{1.3}Cu^{II}O_{3.35}$, a continuous decrease of a and c parameters could be foreseen for all Cu(II) compounds, as x increases, in agreement with the increase of oxygen vacancies. This evolution is not linear, probably due to ordering of the vacancies observed for different compositions. What is worthy of note is the large deviation from this law observed for the only compounds containing Cu(III) (continuous line): the c parameter is greater than that obtained from the "reference line" corresponding to the presence of Cu(II) only, while the a parameter is smaller. Moreover, the largest deviations are observed for $x = 0.33$ which corresponds to the maximum value of δ ($\delta = 0.119$), i.e., for the greatest amount of Cu(III). It can thus be observed that the c/a ratio increases with the Cu(III)/Cu(II) ratio in agreement with the observations previously made by Goodenough *et al.* (*3*). Attempts to modify the a and c parameters for $x = 0.16$ and 0.5, were successful: heating these compounds under vacuum at 500°C led to a decrease of c and a slight increase of a, while a decrease of the Cu(III)/Cu(II) ratio was confirmed.

Conclusion

The stabilization of a great number of oxygen vacancies in the K_2NiF_4-type structure has been shown. It is easily explained by the ability of copper to show square and square-pyramidal coordinations. During the synthesis in air, two phenomena are competitive: the substitution of Cu^{3+} for Cu^{2+}, and ordering of oxygen and vacancies involving the existence of microphases.

The influence of the o
formation of these str
tigated. The relations
properties and the str
will be studied.

References

1. J. M. LONGO AND P. M
Chem. **6**, 526 (1973).

The influence of the oxygen pressure on the formation of these structures will be investigated. The relations between the electrical properties and the structure of these oxides will be studied.

References

1. J. M. Longo and P. M. Raccah, *J. Solid State Chem.* **6**, 526 (1973).
2. B. Grande, H. K. Müller-Buschbaum, and M. Schweizer, *Z. Anorg. Allg. Chem.* **428**, 120 (1977).
3. J. B. Goodenough, G. Demazeau, M. Pouchard, and P. Hagenmuller, *J. Solid State Chem.* **8**, 325 (1973).
4. N. Nguyen, L. Er-Rakho, C. Michel, J. Choisnet, and B. Raveau. *Mater. Res. Bull.* **15**, 891 (1980).
5. S. N. Ruddlesden and P. Popper, *Acta Crystallogr.* **11**, 54 (1958).
6. C. H. R. L. Teske and H. K. Müller-Buschbaum, *Z. Anorg. Allg. Chem.* **371**, 325 (1969).

BRIEF ATTACHMENT G

IN THE UNITED STATES PATENT AND TRADEMARK OFFICE

In re Patent Application of
Applicants: Bednorz et al.
Serial No.: 08/479,810
Filed: June 7, 1995

Date: March 1, 2005
Docket: YO987-074BZ
Group Art Unit: 1751
Examiner: M. Kopec

For: NEW SUPERCONDUCTIVE COMPOUNDS HAVING HIGH TRANSITION TEMPERATURE, METHODS FOR THEIR USE AND PREPARATION

Commissioner for Patents
P.O. Box 1450
Alexandria, VA 22313-1450

FIRST SUPPLEMENTAL AMENDMENT

Sir:

In response to the Office Action dated July 28, 2004, please consider the following:

ATTACHMENT G

Mat. Res. Bull., Vol. 20, pp. 667-671, 1985. Printed in the USA.
0025-5408/85 $3.00 + .00

THE OXYGEN DEFECT PEROVSKITE $BaLa_4Cu_5O_{13.4}$, A METALLIC CONDUCTOR

C. Michel, L. Er-Rakho and B. Raveau
Laboratoire de Cristallographie, Chimie et Physique des Solides, U.A. 251
ISMRa-Université de Caen, 14032 Caen Cedex, France

(Received March 14, 1985; Refereed)

ABSTRACT

A new oxygen defect perovskite $BaLa_4Cu_5O_{13.4}$, characterized by a mixed valence of copper has been isolated ; the parameters of the tetragonal cell are closely related to that of the cubic perovskite: $a = 8.644(4)$ Å $= a_p\sqrt{5}$ and $c = 3.867(3)$ Å $= a_p$. The X-ray diffraction study shows that the atoms are displaced from their ideal positions in the cubic cell, owing to the presence of ordered oxygen vacancies. The study of conductivity, magnetic susceptibility and thermoelectric power versus temperature shows that this oxide is a very good metallic conductor.

INTRODUCTION

Oxygen defect perovskites, have been more extensively studied these last years owing to their potential applications in catalysis, electrocatalysis or as gauges (1-3). In this respect mixed valence copper oxides offer a wide field for investigation : several perovskites (4) or perovskite-related structures have been isolated (5-6). These materials in which copper takes several coordinations simultaneously and a valence state intermediate between II and III can intercalate large amounts of oxygen according to the oxygen pressure and the temperature. Their electron transport properties ranging from semi-conductive to metallic (7) are closely correlated to the amount of intercalated oxygen.

The present paper deals with a new oxygen defect perovskite $BaLa_4Cu_5O_{13.4}$, which is like $La_3Ba_3Cu_6O_{14.5}$ (6) a mixed valence copper oxide but whose behavior is quite different.

EXPERIMENTAL

Synthesis

Samples were prepared in platinum crucible and in air from appropriate mixtures of dried oxides La_2O_3, CuO and carbonate $BaCO_3$. The mixtures were first heated a few hours at 900°C, ground and heated at 1000°C during several hours. They were then ground again, and mixed with an organic binder, compressed into bars and then slowly heated up to 1000°C. After 24 hours or more at 1000°C, the bars were finally quenched to room temperature. The use of a binder was necessary to avoid that the compressed bars break before

heating. In these conditions the compactness of bars was of about 80 %.

Chemical analysis

In order to determine the oxidation state of the transition metal ions, chemical analysis were carried out by iodometric titration using KI and by reduction in a flow of 25 % hydrogen in argon up to about 1000°C using a SETARAM microbalance for weight loss measurements.

Structural analysis

The cell parameters were determined from X-ray powder diffractograms registered with a Philips goniometer using Cu K_α radiation. The space group was determined by electron diffraction using a JEOL 120CX electron microscope.

Magnetic and electrical measurements

The magnetic susceptibility was measured on powders by the Faraday method in the range 80-300K using a Cahn RG microbalance.

The conductivity was measured by the four points method on sintered bars. It was calculated by measuring the intensity/voltage ratio between the points in each current circulation direction in order to minimise the dissymetry effect between the contacts. The Seebeck coefficient was measured on the same sintered bars bold between two Pt heads.

Measurements were carried out up to 600K under an helium pressure of 200 mbars for T < 290K and in air for T > 290K in order to avoid possible departure of oxygen.

RESULTS AND DISCUSSION

The scanning of the system La_2O_3-BaO-CuO for the compositions corresponding to the molar ratio (La + Ba)/Cu = 1 allowed us to isolate a perovskite for La/Ba = 4. The X-ray diffraction pattern of this compounds presents besides the intense lines which can be indexed in a cubic perovskite cell, extra lines which are rather weak. This feature is confirmed by the electron diffraction study, which shows superstructure reflections, leading to a tetragonal cell whose parameters are related to the cubic perovskite subcell (a_p) as follows :

$$a = a_p\sqrt{5} \qquad c = a_p$$

all the lines of the X-ray diffraction patterns can be then indexed with accuracy in the tetragonal system with a = 8.644(4) Å and c = 3.867(3) Å. No reflection conditions are observed. The analysis of the oxygen content leads to the formulation $BaLa_4Cu_5O_{13.4}$ involving the presence simultaneously of Cu(II) and Cu(III) in spite of the presence of numerous oxygen vacancies (10.7 %). The measure of the density by pycnometry in benzene at 25°C (d_{exp} = 7.05) confirms this composition for one mole per cell (d_{calc} = 7.03). Thus it appears that the oxide $BaLa_4Cu^{II}_{2.2}Cu^{III}_{2.8}O_{13.4}$ 1.6 exhibits a great similarity with the oxygen defect perovskite $Ba_2La_3Cu^{II}_{5-2\delta}Cu^{III}_{1+2\delta}O_{14+\delta}$ previously described. However, this compound is very different from $Ba_2La_3Cu_5O_{14+\delta}$ from the point of view of the oxygen intercalation : no intercalation or deintercalation of oxygen has been observed by annealing this phase at low temperatures (400°C to 500°C) and under different oxygen pressures up to 1 bar contrary to $Ba_2La_3Cu_5O_{14+\delta}$. In the same way, no oxygen loss has been observed by TGA measurements for temperatures up to 650, 750 and 850°C and under oxygen pressures of 0.02, 0.2 and 1 bar respectively.

Taking into account the fact that the fundamental lines are indexed in a cubic perovskite cell and are strong with respect to the superstructure lines it was interesting to determine whether the metallic atoms were displaced from their ideal positions in the perovskite, or if the superstructure lines

were only due to the ordering of oxygen vacancies. However, owing to the small amount of oxygen vacancies it was not likely to determine the distribution of the oxygen atoms by X-ray powder diffraction. Thus the structural study was undertaken for the composition $La_4BaCu_5O_{13}$ just to determine the positions of the atoms with respect to the cubic perovskite subcell. Eight space groups were possible, they were reduced to three P4, P$\bar{4}$ and P4/m taking into account the analogy with the perovskite structure. Calculations were carried out in the most symmetrical space group P4/m. For a ranging from 0 to 48°, 37 peaks i.e. 84 hkl were registered. The disparity between phkl and F hkl led us to introduce 139 hkl in the calculations. In the same angle range 13 diffraction peaks (14 hkl) were indexed in the cubic perovskite cell with a = 3.867 Å, and used in a calculation with the atoms in the ideal positions of the cubic perovskite cell, involving only a refinement of the thermal factors B ; this first refinement led to a discrepancy factor $R = \Sigma|I_{obs} - I_{calc}|/\Sigma I_{obs}$ of 0.066 with B(La, Ba) = 1.2 Å^2, B(Cu) = 2.6Å^2, B(O) = 3.9 Å^2. The high B values let us think that the atoms were displaced from their ideal positions. A calculation carried out with all the intensities in the P4/m space group and the same ideal positions and overall B = 1 Å^2 (Table 1a), led to R = 0.35 in agreement with this point of view. Starting from these ideal positions, and assuming a statistical distribution of the oxygen vacancies in the oxides $BaLa_4Cu_5O_{13.4}$, the R factor was lowered to 0.083, by refinement of the atomic parameters, the B factor being fixed at 1 Å^2. From the final atomic parameters (Table 1,b) it can be seen that several atoms are displaced from their ideal positions in the cubic perovskite.

TABLE 1

Atomic Parameters of $BaLa_4Cu_5O_{13.4}$ (a) ideal positions (b) after refinement in the space group P4/m

Atom	Site	(a) X	(a) Y	(a) Z	(b) X	(b) Y	(b) Z
Ba, La	1(d)	0.5	0.5	0.5	0.5	0.5	0.5
Ba, La	4(k)	0.1	0.3	0.5	0.124(1)	0.277(1)	0.5
Cu	1(a)	0.0	0.0	0.0	0.0	0.0	0.0
Cu	4(j)	0.4	0.2	0.0	0.415(3)	0.168(2)	0.0
O	1(b)	0.0	0.0	0.5	0.0	0.0	0.5
O	2(e)	0.0	0.5	0.0	0.0	0.5	0.0
O	4(j)	0.3	0.4	0.0	0.261(7)	0.384(8)	0.0
O	4(j)	0.2	0.1	0.0	0.229(8)	0.063(6)	0.0
O	4(k)	0.4	0.2	0.5	0.428(10)	0.155(6)	0.5

Further refinements, concerning the ordered distribution of oxygen in this structure, which is most probable, were not carried out due to the rather low content of oxygen vacancies, and the too small number of reflections.

This oxide is a very good conductor : its conductivity is about $1.6\ 10^3\ (\Omega\ cm)^{-1}$ at room temperature. Figure 1 which represents the resistivity ρ versus temperature, shows that this oxide exhibits a metallic conductivity from 200 to 600K. The γ value deduced from the equation $\rho = \rho_0(1+\gamma t)$ ($\gamma = 4.1\ 10^{-3}\ C^{-1}$) is very close to that of free electrons ($\gamma = 3.7\ 10^{-3}\ C^{-1}$).

The molar magnetic susceptibility is very weak and nearly independent of temperature. This suggests a Pauli paramagnetism which is characteris-

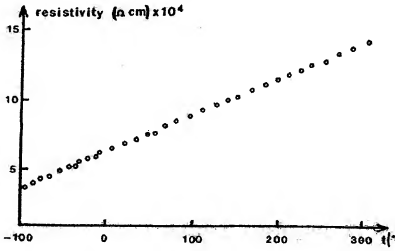

FIG. 1

Resistivity plotted as a function of temperature

tic of delocalized carriers. The Pauli susceptibility (8) calculated with $m^*/m = 1$ and for one carrier per Cu(III) ($\chi_M = 5.3\ 10^{-5}$ e.m.u) is however one order of magnitude lower than the experimental value : $\chi_M = 6\ 10^{-4}$ e.m.u. The increasing of the Pauli susceptibility up to the experimental value needs $m^*/m = 10$. This suggests a strongly correlated carriers gaz (degenerated spin polaron gaz) which was introduced by Mott (9) to explain the magnetic susceptibility of $LaCuO_3$ and $LaNiO_3$ which are metals (10). At room temperature, the Seebeck coefficient is also very weak and positive ($\alpha = 9\ \mu VK^{-1}$) and increases slightly with temperature ($\alpha_{500K} = 18\ \mu VK^{-1}$) (Fig. 2). This

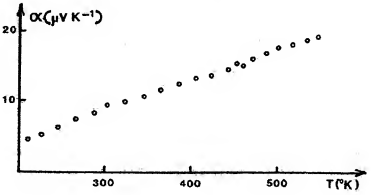

FIG. 2

Evolution of the thermoelectric power as un function of absolute temperature.

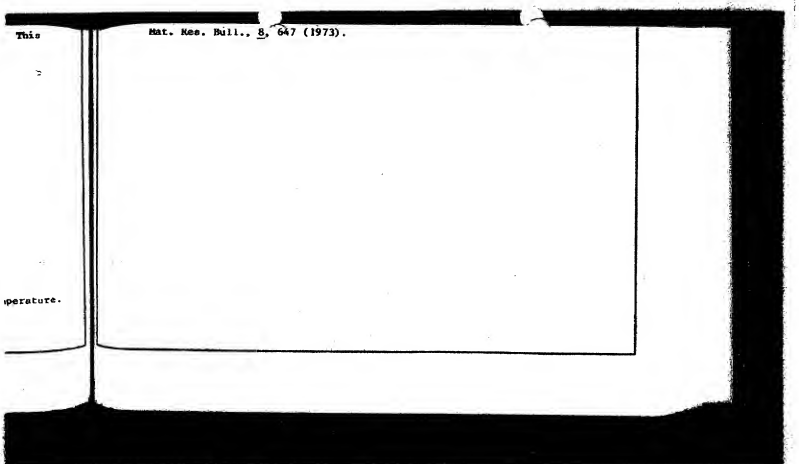
This
Mat. Res. Bull., 8, 647 (1973).
perature.

BRIEF ATTACHMENT H

IN THE UNITED STATES PATENT AND TRADEMARK OFFICE

In re Patent Application of
Applicants: Bednorz et al.
Serial No.: 08/479,810
Filed: June 7, 1995
For: NEW SUPERCONDUCTIVE COMPOUNDS HAVING HIGH TRANSITION TEMPERATURE, METHODS FOR THEIR USE AND PREPARATION

Date: March 1, 2005
Docket: YO987-074BZ
Group Art Unit: 1751
Examiner: M. Kopec

Commissioner for Patents
P.O. Box 1450
Alexandria, VA 22313-1450

FIRST SUPPLEMENTAL AMENDMENT

Sir:

In response to the Office Action dated July 28, 2004, please consider the following:

ATTACHMENT H

REVUE DE CHIMIE MINÉRALE

Avec la collaboration de :

AHEL, I. (Paris)
ARENO M. (Zürich)
AUBRY J. (Nancy)
BARTLETT N. (Berkeley)
BERARD J. (Paris)
BERNARD I. (Beaucouze)
BERTAUT E. F. (Grenoble)
BESSON J. (Grenoble)
BEVAN D. J. M. (Bedford, Australie)
BONNIER E. (Grenoble)
BRONGER W. (Aachen)
BRUCE-WAGNER J. Jr. (Tempe)
CHANG T. L. (Beijing, Pékin)
CHE M.
COHEN-ADAD R. (Lyon)
COTTON F. A. (Texas A & M University)
COUSSINS J. C. (Clermont-Ferrand)
DESCHANVRES A. (Caen)
DUNCAN J. F. (Wellington, New Zealand)
FRUNDLICH W. (Paris)
FUKKI K. (Tokyo)
GALLAIS F. (Toulouse)
GAMBLE F. R. (Exxon, Linden)
GIGUÈRE P. A. (Québec)
GILLESPIE R. J. (Hamilton, Ontario)
GONZALES-GARCIA F. (Sevilla)
GOODENOUGH J. B. (Oxford)
GRØNVOLD B. (Oslo)
GUTMANN V. (Wien)
HABER J. (Kraków)
HAGENMÜLLER P. (Bordeaux)
HANNAY N. B. (Bell Labs, Murray Hill)
HARALDSEN H. (Oslo-Blindern)
HÉROLD A. (Nancy)
HEUBEL J. (Lille)
HOLTZBERG F. (I. B. M., New York)
HOPPE R. (Giessen)
HUGEL R. (Reims)
HUGGINS R. A. (Stanford)
HURET J. (Commissariat à l'Energie Atomique)
IANDELLI A. (Genova)
JELLINEK F. (Groningue)
JORGENSEN C. K. (Genève)
KLEMM W. (Münster in Westfalen)
KOLDITZ L. (Berlin)
LANG J. (Rennes)
LEFEBVRE J. (Paris)
MAGNELI A. (Stockholm)
MAURIN M. (Varsovie)
OSKAM A. (Amsterdam)
PALCZEWSKA W. (Warszawa)
POUCHARD M. (Bordeaux)
RABINAU A. (Stuttgart)
RAO C. N. R. (Bangalore)
REID A. F. (C. S. I. R. O., Port Melbourne)
ROLLET A. P. (Paris)
ROUXEL J. (Nantes)
SAITO N. (Osaka University)
SERRATOSA J. M. (Madrid)
SHULTZ M. (Lemingrad)
SIMON A. (Stuttgart)
SLEIGHT A. W. (Du Pont de Nemours Wilmington)
SPITSYNE V. (Moskva)
TAI L. F. (Nankin)
TAKI S. (Kofu)
TARTE P. (Liège)
VLČEK A. (Prahra)
WIEKER W. (Berlin)
WYART J. (Paris)

Sous la direction de A. CHRÉTIEN

Secrétaire Général : P. SILBER
Université Pierre-et-Marie-Curie — Chimie Minérale — Tour 44,
4, Place Jussieu, 75230 PARIS — CEDEX 05

Relations with Foreign Countries: P. HAGENMULLER
Directeur du Laboratoire de Chimie du solide du C. N. R. S.,
351, cours de la Libération, 33405 TALENCE Cedex

ABONNEMENTS — SUBSCRIPTIONS

C. D. R. — Centrale des Revues
11, rue Gossin, 92543 Montrouge Cedex, France. Tél. 656-52-66

6 numéros par an — 6 issues a year — 6 Hefte pro Jahr

Parution : 10 mars, 10 mai, 10 juillet, 10 septembre, 10 novembre, 10 janvier

Tarif d'abonnement annuel — France . . . . . 700 F

Annual Subscription (including postage) — Autres pays / Other countries . . . 1 000 FF

Jahresbezugspreis (einschliesslich Porto)

Envoi d'un spécimen sur simple demande. Specimen copy graciously sent on request

Table des matières

CHIMIE DOUCE — SOFT CHEMISTRY

RAVEAU
all. Soc. Chim., 1973, 1237.
7, 623.
RAVEAU, *J. Solid State Chem.*, 1980, 33, 321.
JOIN and B. RAVEAU, *J. Solid State Chem.*,
State Chem., 1980, 33, 161.
BAO, *J. Solid State Chem.*, 1982, 41, 37.
RAVEAU, *Acta Cryst.* (to be published).
and B. RAVEAU, *Mat. Res. Bull.*, 1975, 10,

(Received November 30, 1983).

Revue de Chimie minérale,
t. 21, 1984, p. 407

Oxygen intercalation in mixed valence copper oxides related to the perovskites

by

Claude MICHEL and Bernard RAVEAU

Équipe Oxydes du Laboratoire de Cristallographie,
Chimie et Physique des Solides, L. A. 251, ISMRa,
Université, 14032 Caen Cédex, France.

ABSTRACT. — Intercalation of oxygen in ternary copper oxides has been studied for three series of compounds: $Ba_2La_2Cu_2O_{5+\delta}$, $La_{2-x}A_{1+x}Cu_2O_{5-x/2+\delta}$ and $La_{2-x}A_xCuO_{3-x/2+\delta}$ (A = Ca, Sr, Ba). These mixed valence copper oxides, characterized by the presence of Cu(II) and Cu(III) simultaneously are oxygen defect compounds whose structure is closely related to that of the perovskite, and to those of the two members of the intergrowths SrO-perovskite: $Sr_2Ti_2O_4$ and K_2NiF_4 respectively. The localization of the oxygen vacancies in (0 0 1) planes of these structures makes that two of these families: $Ba_2Ca_2Cu_2O_{5+\delta}$ and $La_{2-x}A_{1+x}Cu_2O_{5-x/2+\delta}$ can be considered in their most reduced state as oxides with low dimensionality. The influence of oxygen intercalation on the structure is described. The electrical properties of these phases are described and discussed: they are strongly influenced by the intercalation process. A progressive transition from a *p* type semiconductive to a *p* type semi-metallic or metallic state is indeed observed which depends on the oxygen pressure and on the nature of the oxides.

RÉSUMÉ. — L'intercalation d'oxygène dans les oxydes ternaires de cuivre a été étudiée pour trois séries de composés : $Ba_2La_2Cu_2O_{5+\delta}$, $La_{2-x}A_{1+x}Cu_2O_{5-x/2+\delta}$ et $La_{2-x}A_xCuO_{3-x/2+\delta}$ (A = Ca, Sr, Ba). Ces oxydes de cuivre à valence mixte, caractérisés par la présence simultanée de Cu(II) et Cu(III), sont des composés déficitaires en oxygène dont la structure est étroitement liée respectivement à celle de la pérovskite et à celles des deux membres de la série d'intercroissances pérovskite-SrO : $Sr_2Ti_2O_4$ et K_2NiF_4. La localisation des lacunes anioniques dans les plans (0 0 1) de ces structures fait que deux de ces familles : $Ba_2La_2Cu_2O_{5+\delta}$ et $La_{2-x}A_{1+x}Cu_2O_{5-x/2+\delta}$ peuvent être considérées, dans leur état le plus réduit, comme des oxydes de basse dimensionalité. L'influence de l'intercalation d'oxygène dans la structure est décrite. Les propriétés électriques de ces phases sont décrites et discutées : elles sont fortement influencées par le processus d'intercalation. Une transition progressive d'un état semi-conducteur de type *p* à un état semi-métallique ou métallique de même type, qui dépend de la pression d'oxygène et de la nature des oxydes, est en effet observée.

REVUE DE CHIMIE MINÉRALE, 0035-1032/84/04/407/19/$ 3.90/© Gauthier-Villars

INTRODUCTION

Intercalation of oxygen in an oxide, by a simple reversible exchange with O_2 in air or in a gaseous atmosphere can be used for different applications such as electrocatalysis, or gauges for materials with electrical properties sensitive to the oxygen content. Thus it appears that such oxides must exhibit rather large oxygen defects in their « reduced » form, and must be able to absorb oxygen from atmosphere tending towards a stoichiometric phase in their « oxidized » state. This phenomenon supposes a reversible change of the oxidation state and of the coordination number of the metallic atoms which participate to the framework of the oxide. In this respect, copper oxides are very good candidates, owing to the ability of copper to take several coordinations—octahedral, square pyramidal, square planar—and several oxidations states: + 1, + 2, + 3. Cu(II) and Cu(III) must be especially considered owing to their possibility to take the same octahedral coordination in similar structures as shown from previous works on $La_2Cu^{II}O_4$ [1-2] and $LaSrCu^{III}O_4$ [3], which are isostructural with K_2NiF_4. Ternary oxides $ACuO_3$ containing Cu(III) are more difficult to prepare than those with Cu(II), since oxygen pressures ranging from 1 bar [4-7] to several kbars [3-8] are most of the time necessary to synthesize these compounds. However, the presence of A elements like barium favours the formation of Cu(III) in normal pressure conditions [9-10]. The present paper deals with the soft intercalation of oxygen, *i. e.* at low pressure ($p \leqslant 1$ atm) and at low temperature ($T \sim 400$-$500°$ C) in three series of ternary copper oxides related to the perovskite [11-13] and belonging to the systems La_2O_3-AO-CuO with A = Ca, Sr, Ba. The influence of oxygen intercalation on the electron transport properties of these phases are discussed.

STRUCTURAL CONSIDERATIONS

Three families with an oxygen defect structure have been isolated in the systems La_2O_3-AO-CuO:

— The oxygen defect perovskites $La_2Ba_2Cu_6O_{14+\delta}$.

— The oxygen defect intergrowths $Sr_3Ti_2O_7$ type,

$$La_{2-x}A_{1+x}Cu_2O_{6-x/2+\delta},\ A = Ca,\ Sr.$$

— The oxygen defect intergrowth K_2NiF_4 type, $La_{2-x}A_xCuO_{4-x/2+\delta}$.

The most reduced form which has been isolated for the defect perovskites $La_2Ba_2Cu_6O_{14+\delta}$ corresponds to the formulation $La_2Ba_2Cu_6O_{14}$. Its

structure (fig. 1) can be described as an ordered oxygen defect perovskite. All the metallic sites corresponding to the stoichiometric perovskite are occupied by copper ions and lanthanum and barium ions respectively, whereas only 7/9 of the anionic sites are occupied in an ordered manner.

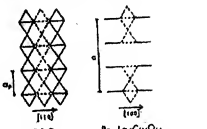

Fig. 1. — Schematic structure of a stoichiometric ABO_3 perovskite and the defect oxygen perovskite $Ba_2La_2Cu_6O_{11}$.

Considering the tetragonal cell of this compound ($a \simeq a_p\sqrt{2} \simeq 5.525$ Å, $c \simeq 3a_p \simeq 11.721$ Å), it can indeed be seen that the basal planes of the octahedra, parallel to (0 0 1) are preserved, that one apex out of two is missing at the levels $z = 1/6$ and $5/6$, whereas all the apices of these octahedra are missing at $z = 1/2$. It results that this reduced form can be considered as a true layer structure: double defect perovskite layers $\lfloor Ba_{1+x}La_{2-2x}Cu_3O_7 \rfloor_2$ built up from corner-sharing, octahedra CuO_6 square pyramids CuO_5 and square groups CuO_4 are observed whose cohesion is ensured by lanthanum ions located at $z = 1/2$. It is remarkable that such an oxide is characterized by a high Cu(III) content in spite of the high oxygen defect content. Site potential calculations confirm that the Cu^{3+} ions are located preferentially on the octahedral sites. It must also be noted that this limit compound has not really been synthesized. By heating in air at 1 000° C for 24 h the mixture of La_2O_3, CuO and $BaCO_3$ and quenching the samples at room-temperature a slight excess of oxygen is indeed observed corresponding to the formulation $La_2Ba_2Cu_6O_{14.10}$. The most reduced phase $La_2Ba_2Cu_6O_{14.05}$ is then synthesized by annealing the sample $La_2Ba_2Cu_6O_{14.10}$ at 400° C under low oxygen pressure ($\sim 5.10^{-3}$ bar) during several hours.

The deviation from stoichiometry in the oxides $La_{2-x}A_{1+x}Cu_2O_{6-x/2+\delta}$ is more complex owing to the possibility of substitution of calcium or strontium for lanthanum, in a small homogeneity range ($0 \leqslant x \leqslant 0.14$ for

strontium and $x = 0.10$ for calcium). The most reduced oxide which has been isolated in this family corresponds to the formulation $La_2SrCu_2O_5$. Its tetragonal cell ($a = 3.865$ Å, $c = 19.887$ Å), corresponds to a structure closely related to that of $Sr_4Ti_3O_7$ (fig. 2 *a*). Cu^{2+} ions are indeed located on the Ti^{4+} sites, La^{3+} and Sr^{2+} ions are located on the Sr^{2+} sites, whereas six anionic sites out of seven are occupied by oxygen in an ordered manner; thus, this oxide can be considered as an intergrowth of double oxygen perovskite layers and SrO type layers. The perovskite layers exhibit some similarity with those observed for $La_3Ba_3Cu_6O_{14}$: the basal planes of the octahedra parallel to (0 0 1) are also preserved whereas at $z = 0$ and $z = 1/2$ all the apices of the oxygen octahedra are missing. However, the resulting configuration of the framework is different from $La_3Ba_3Cu_6O_{14}$: Cu(II) exhibits here only one coordination which is square pyramidal. Nevertheless this oxide, like $La_3Ba_3Cu_6O_{14}$, must be considered as a structure with low dimensionality. It can indeed be described as built up from slabs $|LaSrCu_2O_5|_\infty$ parallel to (0 0 1) whose cohesion is ensured by Sr^{2+} and La^{3+} ions located at $z = 0$ and $z = 1/2$. The $|LaSrCu_2O_5|_\infty$ slabs are themselves an intergrowth of SrO-type layers and corner-sharing square pyramid layers. Such slabs are in fact derived from the K_2NiF_4 structure: the latter corresponds indeed to the superposition of two $|K_1Ni_2F_5|_\infty$ slabs which would share the face of their square pyramids, forming NiF_6 octahedra (fig. 2 *b*). Like $La_3Ba_3Cu_6O_{14+\delta}$, $La_2SrCu_2O_5$ is

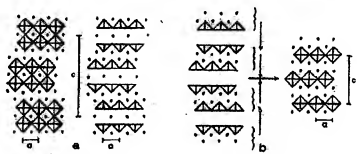

Fig. 2.

a) Schematic structure of $Sr_4Ti_3O_7$ and $La_2SrCu_2O_5$ (projection on to (1 0 0) plane), showing the oxygen vacancies.

b) Schematic representation of K_2NiF_4 slabs sharing the square faces of the NiF_6 pyramids to give the K_2NiF_4 structure.

characterized by a great stability in spite of its oxygen defect structure: it is indeed synthesized by heating the stoichiometric mixture of CuO, La_2O_3 and $SrCO_3$ at 1 050-1 100° for 24 h in air and by quenching them at room temperature in order to avoid their oxidation at lower temperature. Contrary to $La_3Ba_3Cu_6O_{14}$, copper is in its lower oxidation state, Cu(II) in this oxide.

The oxides $La_{2-x}A_xCuO_{4-x/2+\delta}$ exhibit an oxygen defect K_2NiF_4 type structure involving different coordinations of copper: octahedral, square pyramidal and eventually square planar (fig. 3). Their oxygen content

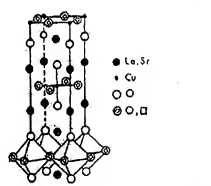

Fig. 3. — Perspective view of the structure of the oxides $La_{2-x}Sr_xCuO_{4-x/2+\delta}$ with oxygen vacancies located in the basal plane of the octahedra.

depends on the nature of the A ions (A = Ca, Sr, Ba) and on the substitution rate x which can lead to wide homogeneity ranges: $0 \leqslant x \leqslant 0.20$ for A = Ca and Ba and $0 \leqslant x \leqslant 4/3$ for A = Sr. The most reduced phase which exhibits the highest deviation from stoichiometry has been synthesized in the case of strontium for $x = 4/3$: $La_{2/3}Sr_{4/3}CuO_{3.33}$. Contrary to the two other series, the oxygen vacancies are located in the basal plane of the octahedra which are parallel to the (0 0 1) plane of the tetragonal cell ($a = 3.759$ Å, $c = 12.907$ Å). It must also be emphasized that this type of localization of the oxygen vacancies is always observed whatever the nature of the A ions, and whatever the rate of substitution x may be. However, symmetry changes and order-disorder phenomena in this plane may appear according to the nature of A and x value (table I). So, the calcium and barium oxides are characterized by a monoclinic distortion of the tetragonal K_2NiF_4 structure, whatever the x value may be $0 \leqslant x \leqslant 0.20$; the same

is true for the strontium compounds with $0 \leqslant x \leqslant 0.10$. Thus, the oxides corresponding to these homogeneity ranges exhibit an orthorhombic cell related to that of K_2NiF_4 in the following way: $a \simeq b \simeq aK_2NiF_4\sqrt{2}$ and $c \simeq cK_2NiF_4$.

TABLE I

The oxides $La_{1-x}A_xCuO_{4-y/2+\delta}$: crystallographic data and analytical results (quenched materials).

A	x	δ	Cell parameters (Å) a	b	c	Heating temperature °C
Ba	0		3.866	3.402	13.149	1,100
	0.05	0.01	3.861	3.380	13.201	1,100
	0.1	0.02	3.859	3.364	13.245	1,100
	0.2	0.05	3.856		13.320	1,100
Ca	0.05	0.01	3.851	3.387	13.150	1,100
	0.1	0.02	3.856	3.385	13.174	1,100
	0.2	0.05	3.857	3.360	13.210	1,100
Sr	0.05	0.03	3.851	3.368	13.200	1,000
	0.16	0.04	3.774		13.231	1,000
	0.25	0.07	3.775		13.247	1,000
	0.33	0.11	3.774		13.254	1,100
	0.50	0.10	3.776		13.210	1,160
	0.66	0.075	3.775		13.160	1,170
	0.88	0.05	3.769		13.070	1,170
	1.0	0.005	3.767 (*)		13.002	1,200
	1.20	0.0	5 x 3.76		12.946	1,200
	1.33	0.0	3.759 (*)		12.907	1,200

(*) These a parameters are those of the tetragonal subcell.

On the other hand, the strontium compounds exhibit a tetragonal symmetry similar to that of K_2NiF_4 or $LaSrCuO_4$ [3] for $0.10 < x < 1$ ($a \simeq aK_2NiF_4$; $c \simeq cK_2NiF_4$), whereas for $1 \leqslant x \leqslant 4/3$, superstructures appear on the electron diffraction patterns which involve tetragonal cells with $a \simeq b \simeq naK_2NiF_4$, n ranging from 1 to 6 according to the composition; c remaining unchanged ($c \simeq cK_2NiF_4$). These oxides are very stable in spite of the high deviation from stoichiometry; for instance $La_{2/3}Sr_{4/3}CuO_{3.33}$ is prepared by heating a mixture of the compounds La_2O_3, CuO and $SrCO_3$ at 1 200° C and quenching the phase at room temperature. It appears here that the most reduced phase exhibits also only Cu(III) like $La_{2/3}SrCl_2O_4$ belonging to the second series. The oxides $La_{2-x}A_xCuO_{4-x/2+\delta}$ appear very closely related to the second series formulated $La_{2-A_{4\delta}}Cu_3O_{6-x/2+\delta}$ in that they can be considered as being respectively the members $n = 1$ and 2 of a series of oxygen defect intergrowths between perovskite and

SrO structures, corresponding to the general formulation $A_{n+1}B_nO_{3n+1}$. However the behaviour of $La_{2-x}A_xCuO_{4-x/2+\delta}$ is very different from the two other series in that it cannot be considered in its most reduced form as an oxide with low dimensionality.

OXYGEN INTERCALATION AND DESINTERCALATION: INFLUENCE ON THE STRUCTURE

Oxygen can be intercalated in these three series of oxides by simple annealing of the materials at low temperature, *i. e.* 400° C-500° C, under different oxygen pressures.

The oxygen defect perovskite $La_2Ba_2Cu_5O_{14.10}$ synthetized in air can absorb rather important oxygen amounts by annealing the samples at 400° C under oxygen pressures ranging from 10^{-2} to 1 bar as shown from table II. In the same way, oxygen can be desintercalated from the structure of $La_2Ba_2Cu_5O_{14.10}$ or from more oxidized compounds by simply annealing the samples always at 400° C under lower oxygen pressure, 5.10^{-3} bar (table II). Thus it appears that the intercalated oxides $La_2Ba_2Cu_5O_{14+\delta}$

TABLE II

Evolution of δ as a function of the oxygen pressure after annealing the oxide $La_2Ba_2Cu_5O_{14.10}$ at 400° C.

PO_2 (bar)	5.10^{-3}	10^{-2}	2.10^{-2}	5.10^{-2}	0.1	0.2	1
δ	0.05	0.19	0.25	0.31	0.33	0.37	0.43

exhibit a rather wide homogeneity range $0.05 \leqslant \delta \leqslant 0.43$. The intercalation of oxygen in this structure does not influence the cell parameters, since the most oxidized compound, $La_2Ba_2Cu_5O_{14.43}$, is characterized by parameters very similar to those of $La_2Ba_2Cu_5O_{14.10}$: $a = 5.529$ Å and $c = 11.729$ Å, whereas no parameter change with respect to the air synthesized oxide is observed when δ tends towards zero. It is of course not possible to localize the additional oxygen in the structure by X ray diffraction; however site potential calculations [14], assuming that Cu^{2+} is octahedrally coordinated, show that this additional oxygen should be located between two square pyramids CuO_5, *i. e.* at $z = 1/2$, between the layers described above, forming corner-sharing ribbons of CuO_6 octahedra running along $\vec{c}$. The electron transport properties of these compounds, which will be discussed further, are in agreement with this hypothesis. The fact that

the c parameter does not vary, in spite of the intercalation of rather great amounts of oxygen is easily explained by the high oxygen defect content in the structure: the slabs $|\,Ba_{1.5}La_{0.5}Cu_2O_7\,|_\infty$ exhibit, themselves, oxygen defects, which may favour slight displacements of the copper and oxygen atoms along c during oxygen intercalation, between the slabs, without changing the c parameter.

The oxygen intercalation in the second series, $La_{2-x}A_{1+x}Cu_2O_{6-x/2+\delta}$, depends on the nature of the A ions, calcium or strontium, on the rate of substitution x, and on the oxygen pressure as shown from table III. It can

TABLE III

Crystallographic data and analytical results for the oxides $La_{2-x}A_{1+x}Cu_2O_{6-x/2+\delta}$.

Quenched oxides (in air)			Annealed oxides (in O_2)		
Composition	δ	Cell parameters	Composition	δ	Cell parameters
$La_2SrCu_2O_6$	0	$a=3.865$ Å $c=19.887$ Å	$La_2SrCu_2O_{6.2}$	0.20	$a=3.865$ Å $c=20.065$ Å
$La_{1.98}Sr_{1.02}Cu_2O_{6.02}$	0.02	$a=3.863$ Å $c=19.963$ Å			b
$La_{1.88}Sr_{1.12}Cu_2O_{6.07}$	0.04	$a=3.959$ Å $c=19.956$ Å	$La_{1.88}Sr_{1.12}Cu_2O_{6.32}$	0.29	$a=3.868$ Å $c=20.051$ Å
$La_{1.7}Ca_{1.3}Cu_2O_{6.07}$	0.02	$a=3.825$ Å $c=19.404$ Å	$La_{1.7}Ca_{1.3}Cu_2O_{6.31}$	0.06	$a=3.825$ Å $c=19.404$ Å

indeed be seen for the strontium oxides synthesized in air, like $La_2SrCu_2O_6$, that δ increases with the strontium content tending towards the formulation $La_{2-x}A_{1+x}Cu_2O_6$. It results that the Cu^{3+} content increases with the divalent A ion content, in order to compensate the oxygen vacancies due to the substitution of Sr^{2+} or Ca^{2+} for La^{3+}. The annealing of the latter oxides at 400° C under an oxygen pressure of one bar shows the ability of these phases to intercalate oxygen, δ ranging from 0 to 0.29 for $La_{2-x}Sr_{1+x}Cu_2O_{6-x/2+\delta}$ whereas $0.02 \leqslant \delta \leqslant 0.08$ for $La_{1.7}Ca_{1.3}Cu_2O_{6.35+\delta}$. One can see that the rate of intercalation is higher for the strontium oxides than for the calcium compound. Moreover it seems that in the strontium oxides the maximum rate of intercalation increases with the strontium content. Contrary to the oxides $La_2Ba_2Cu_2O_{4+\delta}$, the compounds $La_{2-x}Sr_{1+x}Cu_2O_{6-x/2+\delta}$ exhibit a variation of the interlayer distances: the c parameter of the tetragonal cell increases with the oxygen content δ, for a same x value. This influence of

intercalation on the c parameter, can be explained by the fact that the $|\,La_{1-x}Sr_xCu_2O_6\,|_\infty$ slabs, which are stoichiometric and formed of SrO-type layers are more rigid than the $|\,Ba_{1.5}La_{0.5}Cu_2O_7\,|_\infty$ slabs, and are only displaced by the introduction of oxygen between them. However the behaviour of the oxides $La_{1.7}Ca_{1.3}Cu_2O_{6-x/2+\delta}$ where c parameter is independent of δ is not explained; nevertheless in this latter case δ remains rather weak ($\delta \leqslant 0.08$). The oxygen desintercalation of these oxides is similar to that observed for the first family: for instance heating the most oxidized compound $La_2SrCu_2O_{6.20}$ at 400° C under low oxygen pressures ($\sim 10^{-3}$ bar) leads progressively to the reduced phase $La_2SrCu_2O_6$.

The behaviour of the oxides $La_{2-x}A_xCuO_{4-x/2+\delta}$ is much more complex owing to the wide homogeneity ranges observed for these oxides especially in the case of strontium. For instance, the δ values observed for the strontium oxides synthesized in air (table I) do not increase progressively with x contrary to $La_{2-x}Sr_{1+x}Cu_2O_{6-x/2+\delta}$, but increase up to $x \simeq 1/3$ and then decrease again up to $x \simeq 1$. These δ values are difficult to compare owing to the fact that the different compositions were not synthesized at the same temperature in order to obtain pure oxides. It is sure that equilibrium is rarely reached for this series. So, for $0 \leqslant x \leqslant 1$ the δ values given in table I correspond to heating times of 12 h and annealing these samples in the same conditions, but for longer times (24 h to 48 h) allowed us to prepare pure phases with the same structure but characterized by greater δ values. Thus it appears that kinetics plays an important part for oxygen intercalation in this phase at a given temperature and a given oxygen pressure. Like for the two other series, oxygen can be intercalated or desintercalated by annealing the samples synthesized in air, at 400° C under an oxygen pressure of one bar or under vacuum (10^{-3} bar) respectively. The curves $\delta = f(x)$ are given in figure 4 for the strontium compounds where they are compared with the line $\delta = x/2$ which represents the maximum rate of intercalation available in this structure. It can be seen that oxygen can easily be desintercalated, tending towards the most oxygen defect structure; it appears that intercalation tends to be maximum for low x values ($0 \leqslant x \leqslant 0.25$), whereas it is only partial for higher x values ($0.33 \leqslant x \leqslant 1.20$), 11 % to 33 % of the available anionic sites being only occupied in this latter composition range. From these results it seems that intercalation is governed by two opposite effects which are competitive: the trend to preserve a stoichiometric K_2NiF_4 structure as for $La_2Cu^{II}O_4$ and $LaSrCu^{II}O_4$ and the trend to form a related defect structure but with an ordering of the oxygen vacancies. Thus, rather close to the stoichiometric compound La_2CuO_4 the trend to stoichiometry is favoured by partial oxi-

dation of Cu(II) to Cu(III), whereas rather far from La_2CuO_4, for example for $x = 1$, the stoichiometric oxide $LaSrCuO_4$ [3] cannot be stabilized any more under normal oxygen pressure, and oxygen vacancies are favoured; the resulting great amount of anionic vacancies are ordered, leading to different microphases as observed by electron diffraction. The « a » parameter which characterizes the corresponding K_2NiF_4 type tetragonal cell is generally not influenced by the intercalation-deintercalation process except for high x values which exhibit superstructures. For such oxygen defect oxides, an order-disorder phenomenon of the oxygen vacancies appears in the (0 0 l) plane which contributes to the variation of the « c » parameter of the K_2NiF_4 subcell. It is for instance the case of the strontium oxide corresponding to $x = 1.20$. The sample quenched in air ($\delta = 0$) exhibits a superstructure in the (0 0 l) plane with a « c » subcell parameter of 3.76 Å (table I). The annealing at 400° C in oxygen of this phase involves an important decrease of the rate of the oxygen vacancies ($\delta = 0.33$). It results that the order desappears, leading to a true tetragonal cell with « c » greater than that of the quenched specimen ($c = 3.791$ Å), c being smaller ($c = 12.900$ Å). The evolution of the c parameter versus composition for quenched and annealed compounds is complex (fig. 5). It results from the influence of several factors: copper (III) and oxygen vacancies contents, size of Sr^{2+} which is slightly larger than La^{3+}. For every x value, c increases with the rate of intercalation, *i. e.* with the Cu^{3+}/Cu^{2+} ratio, except for high x values which exhibit order-disorder phenomena. This behavior is in agreement with the observation previously made by Goodenough *et al.* [3].

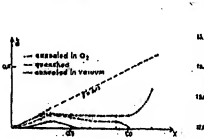

Fig. 4.

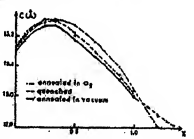

Fig. 5.

Fig. 4. — The oxides $La_{1-x}Sr_xCuO_{4-(\delta/2)}$: evolution of δ as a function of x for oxides resulting from different thermal treatments.

Fig. 5. — The oxides $La_{2-x}SrCuO_{4-(\delta/2)}$: evolution of the c parameter as a function of x for oxides resulting from different thermal treatments.

The evolution of « c » can be interpreted by two opposite effects: increasing due to substitution of Sr^{2+} for La^{3+} and decreasing due to oxygen vacancies. For small x values ($x < 0.25$) the number of oxygen vacancies remains low and tends towards zero so that c increases owing to the replacement of La^{3+} by Sr^{2+}. For $x > 0.25$ the number of oxygen vacancies becomes very large and its effects prevails on that of substitution Sr^{2+}/La^{3+}, involving a decrease of « c ».

INFLUENCE OF THE INTERCALATION PROCESS ON THE ELECTRICAL PROPERTIES OF THE MIXED VALENCE COPPER OXIDES

Most of the oxides described above are characterized by the presence simultaneously of Cu(II) and Cu(III), and are thus mixed-valence oxides. The electron transport properties of these phases, which are p type semiconductors or p type semi-metals or metals are strongly influenced by the rate of intercalation.

The evolution of conductivity versus reciprocal temperature for different

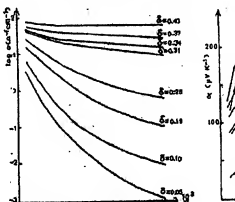

Fig. 6.

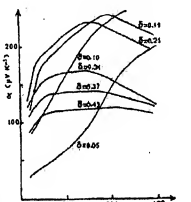

Fig. 7.

Fig. 6. — The oxides $Ba_xLa_yCu_zO_{3+\delta}$: variation of the conductivity (logarithmic scale) as a function of reciprocal temperature for different δ values.

Fig. 7. — The oxides $Ba_xLa_yCu_zO_{3+\delta}$: variation of the thermoelectric power as a function of T for different δ values.

δ values of the oxides $La_2Ba_3Cu_6O_{14+\delta}$ (fig. 6) shows that the conductivity increases drastically with the intercalation of oxygen, contrary to the structure which remains unchanged. In the same way the thermoelectric power of these phases (fig. 7) is very sensitive to the intercalation rate. These properties are interpreted by a conduction band model whose configuration is mainly determined by the splitting of the $3d$ Cu orbitals by the crystal field [15] (fig. 8 *a*). Every composition can indeed be considered as a mixing of the two limits: the reduced form $Ba_2La_2Cu_6O_{14}$ characterized by ribbons of one octahedron and two tetragonal pyramids running along $\vec{c}$, and the oxidized form $Ba_2La_2Cu_6O_{15}$ which exhibits infinite octahedral ribbons along $\vec{c}$. The $\sigma^*_{x^2-y^2}$ bands result from Cu – O – Cu interactions and strong electron-electron interactions split the dz^2_1 and dz^2_2 levels by a few eV like the $\sigma^*_{x^2-y^2}$ and $\sigma^{*2}_{x^2-y^2}$ bands. It results that the band structure of $La_2Ba_3Cu_6O_{14}$ (fig. 8 *b*) is that of an insulator but this limit has not been synthesized; on the other hand, the only level configuration which can lead to a semi-metallic or metallic conduction for the limit $Ba_2La_2Cu_6O_{15}$ corresponds to a dz^2_2 empty level located just above or accross the filled

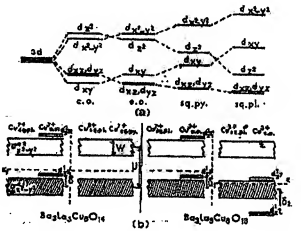

Fig. 8.

a) Crystal field splitting for d element in different environments; c. o.: compressed octahedron, e. o.: elongated octahedron, sq. py.: square pyramid, sq. pl. square plan.

b) Schematic band diagram for $Ba_2La_2Cu_6O_{14}$ and $Ba_2La_2Cu_6O_{15}$. U denotes the intra-atomic coulomb energy, δ_1, δ_2 and δ_3 the splitting due to the axial distortion of the octahedra and W the estimated band width.

$\sigma^*_{x^2-y^2}$ band (fig. 8 *b*). Thus, it appears that intercalation of oxygen which corresponds to a local change of copper coordination, will involve an increase of the density of the dz^2_2 levels above the filled $\sigma^*_{x^2-y^2}$ band, *i. e.* an increase of the number of holes in the conduction band. The approximately linear evolution of log σ vs δ at 293 K is in agreement with this model. This progressive transition from a semi-conductive to a semi-metallic state can be explained by the Mott model [16] of quasi localized holes trapped at the top of the filled $3\,d_{x^2-y^2}$ band.

The oxides $La_{2-x}A_{1+x}Cu_2O_{5-x/2+\delta}$ exhibit a similar behaviour [17]. From the evolution of the curves $\log \sigma = f(1/T)$, between 80 K and 300 K (fig. 9) it can be seen that a continuous transition from a semi-conductive to a semi-metallic state is observed as the oxygen intercalation rate increases from $\delta = 0$ ($La_{1.85}Sr_{1.15}Cu_2O_6$) to $\delta \approx 0.29$ ($La_{1.85}Sr_{1.15}Cu_2O_{6.32}$). The conductivity depends also on the nature of the A ion which influences drastically the c parameter: this calcium oxide $La_{1.90}Ca_{1.10}Cu_2O_{6.97}$ is indeed much more conductor than the corresponding strontium oxide $La_{1.90}Sr_{1.10}Cu_2O_{6.97}$. The Seebeck coefficient curves $\alpha = f(T)$ (fig. 10) confirm this influence of intercalation: α increases continuously with T for

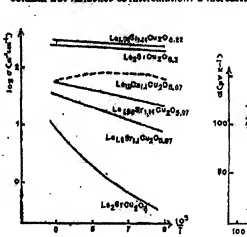

Fig. 9.

Fig. 10.

Fig. 9. — The oxides $La_{2-x}A_{1+x}Cu_2O_{6-x/2+\delta}$: evolution of the conductivity (logarithmic scale) vs T^{-1} for different compositions.

Fig. 10. — The oxides $La_{2-x}A_{1+x}CuO_{4-x/2+\delta}$: evolution of the thermoelectric power vs T for different compositions.

the small intercalation rates ($\delta = 0$ to 0.04) *i. e.* for small Cu^{3+} contents, whereas it becomes weak and nearly independent of the temperature, for high intercalation rates ($\sigma = 0.20$ to 0.29), *i. e.* for high hole concentration. These properties very similar to those obtained for $La_2Ba_2Cu_4O_{8+\delta}$ can be explained by the same Mott model of holes trapped at the top of the $\sigma^*_{x^2-y^2}$ band. However the rather high conductivity of $La_2SrCu_2O_6$ in spite of the very weak Cu^{3+} content—$\delta \simeq 0$—let us think that the intra-atomic energy U is in this case of the same order of magnitude as the band width W_σ (fig. 11). In the same manner the relatively high and metallic conductivity of the calcium oxide $La_{1.90}Ca_{0.10}Cu_2O_{4.03}$ compared to the corresponding strontium oxide shows that the band width W_σ must be larger than U in the calcium compound so that the overlapping of the two $\sigma^*_{x^2-y^2}$ bands gives rise to a higher mobility.

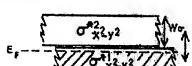

Fig. 11. — The oxides $La_{2-x}A_{x+\delta}Cu_2O_{4-x/2+\delta}$: schematic band diagram as deduced from electron transport properties.

The highest conductivities are observed for the oxides $La_{2-x}Sr_xCuO_{4-x/2+\delta}$ [18]. For a given substitution rate x, the conductivity increases with the rate of intercalation δ as shown from figure 12 for temperature ranging from 80 K to 300 K. However the evolution of $\log \sigma$ vs $1/T$ as well as $\alpha = f(T)$ is more complex than the two other series: δ is not the only factor governing the electron transport properties of the phases. Three domains must in fact be distinguished: $0 \leqslant x \leqslant 0.16$, $0.16 < x \leqslant 0.50$ and $0.50 < x \leqslant 1.20$ for the oxides quenched in air and annealed in oxygen. The compounds of the first domain ($0 \leqslant x \leqslant 0.16$) are characterized by a semi-metallic behaviour and their properties can be interpreted by the model developped by Goodenough for La_2CuO_4 [19] involving the presence of holes in the filled band $\sigma^{*1}_{x^2-y^2}$. The weak variation of conductivity which does not correspond to the metallic model $\rho = \rho_0(1 + \gamma t)$ (fig. 12 *a*), as well as the thermoelectric power values (fig. 13) greater than those of a metal are in agreement with this model. The fact that the holes may be trapped on localized levels at the top of the $\sigma^{*1}_{x^2-y^2}$ band according to the Mott Model is also confirmed by the fact that α increases with temperature (fig. 13). The

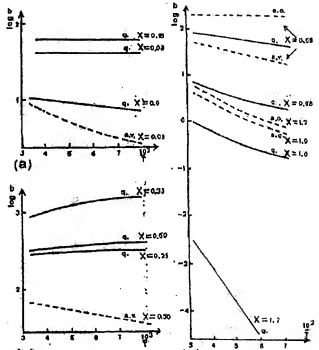

Fig. 12. — The oxides $La_{2-x}Sr_xCuO_{4-x/2+\delta}$: variation of the conductivity vs T^{-1} (*q.*: quenched in air, *a. c.*: annealed in O_2, *a. v.*: annealed in vacuum).

a) $0 \leqslant x \leqslant 0.16$; *b*) $0.16 < x \leqslant 0.50$; *c*) $0.5 < x \leqslant 1.20$.

oxides belonging to the second domain ($0.16 < x \leqslant 0.50$), exhibit a metallic conductivity (fig. 12 *b*) which increases with the intercalation rate: ρ increases linearly with temperature and the thermoelectric power values are weak and nearly temperature independent (fig. 13). The highest x compositions ($0.50 < x \leqslant 1.20$), exhibit for the less oxidized compounds synthetized in air ($\delta < 0.07$) a semi-conductive behaviour: σ decreases drastically with δ (fig. 12 *c*), and correlatively α increases as δ decreases (fig. 13). These latter oxides and especially the compositions corresponding to $x = 0.88$, 1 and 1.2 exhibit a variation of the conductivity according to the Mott relation $\sigma = A_1 \exp[-(Q/k_0T)^{1/4}]$ which characterizes a variable range hopp-

ing of holes located in the $\sigma^{*}_{x^2-y^2}$ band close to the Fermi level. It must be noted that the electrical properties of the oxides $La_{2-x}Sr_xCuO_{4-x/2+\delta}$ do not depend on the δ value only. So, for instance, the oxides corresponding to $0.33 \leqslant x \leqslant 1.0$ which have been annealed under an oxygen pressure of 1 bar exhibit the same δ value ($\delta \simeq 0.11$), but are characterized by a decrease

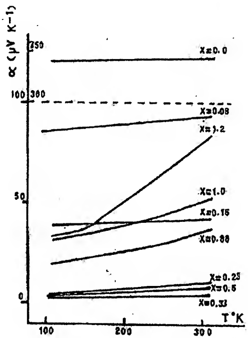

Fig. 13. — The oxides $La_{2-x}Sr_xCuO_{4-x/2+\delta}$: thermoelectric power vs T for quenched oxides with different x values.

of σ as x increases as shown figure 14. This shows the influence of the rate of anionic vacancies ($x/2$-δ) on the carrier mobility. Moreover the distribution of the oxygen defects *i. e.*; the order-disorder phenomena, may influence the electron transport properties of these compounds.

The great sensitivity of these compounds to oxygen makes that their electrical conductivity can vary drastically, under a given oxygen pressure owing to the intercalation or desintercalation of oxygen. For this reason

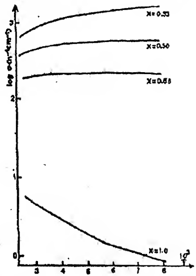

Fig. 14. — The oxides $La_{2-x}Sr_xCuO_{4-x/2+\delta}$: evolution of the conductivity as a function of reciprocal temperature for oxides annealed under an oxygen pressure of 1 bar ($\delta = 0.11$, $0.33 \leqslant x \leqslant 1.0$).

we have only discussed above the electrical properties of these phases at relatively low temperatures (T < 300 K), where all the compounds of the three families are not sensitive to intercalation or desintercalation. Such anomalies of the conductivity have indeed been observed for the oxides $La_{2-x}Sr_xCuO_{4-x/2+\delta}$ corresponding to $0 \leqslant x \leqslant 0.16$ and synthesized in air ($0 \leqslant \delta \leqslant 0.04$). One indeed observes (fig. 15), beyond 300 K under an oxygen pressure of 0.2 bar that σ decreases first drastically in the temperature range 300 K-420 K and then increases again in the temperature range 420 K-650 K. The thermogravimetric curves of these phases, characterized successively by a weight loss and weight gain, show clearly that this behaviour results from desintercalation and intercalation of oxygen successively. Similar properties are observed for the oxides $La_{2-x}Sr_{1+x}Cu_2O_{6-x/2+\delta}$ synthesized in air for $x = 0.1$ and 0.14 (fig. 15) and for which the thermogravimetric measurements confirm the oxygen desintercalation-intercalation process. The reversibility of the intercalation process in these phases is illustrated by the evolution of the conductivity of $La_{1.9}Ca_{1.1}Cu_2O_{5.97}$ versus reciprocal

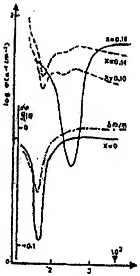

Fig. 15.

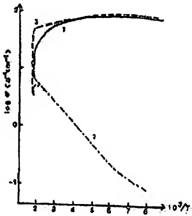

Fig. 16.

Fig. 15. — Variation of conductivity vs T^{-1} ($T > 300K$) in air for some oxides in the $La_{2-x}Sr_xCuO_{4-x/2+\delta}$ series (solid line) and in the $La_{2-x}Sr_{1+x}Cu_2O_{6-x/2+\delta}$ series (dotted line). A TG curve for $x = 0$ (first series), with the same temperature scale is given as example to illustrate the close relation between variation of conductivity and oxygen amount.

Fig. 16. — Variation of conductivity vs T^{-1} for the oxides $La_{1.9}Ca_{1.1}Cu_2O_{5.91}$ under different atmospheres:

1) —— first heating under inert atmosphere,
2) —·— first cooling and second heating under inert atmosphere,
3) – – air introduction and second cooling (in air).

temperature under argon and air (fig. 16). The behaviour of this phase is indeed very different in argon and in air. The conductivity decreases under argon as soon as the temperature is greater than 300 K owing to the departure of oxygen and at about 570 K σ decreases drastically. At this stage of the experiment, heating is stopped and the sample is cooled progressively down to 77 K. In this latter temperature range a semi-conductive behaviour is observed owing to the lower oxygen rate of intercalation. Heating again up to 500 K under argon leads to the same curve. However

beyond 500 K, σ decreases again; this phenomenon is due to the fact that the thermodynamical equilibrium is not yet reached when we stop heating at 570 K. At 570 K argon is replaced by air, and heating is stopped. It can be seen that the conductivity increases immediately owing to the oxygen intercalation. The behaviour observed from 570 K to 77 K is then similar to that observed for the starting material.

REFERENCES

[1] J. M. Longo, P. M. Raccah, *J. Solid State Chem.*, 1973, 6, p. 526.
[2] S. Grande, H. Muller-Buschbaum, M. Schweitzer, *Z. Anorg. Allg. Chem.*, 1977, 428, p. 120.
[3] J. B. Goodenough, G. Demazeau, M. Pouchard, P. Hagenmuller, *J. Solid State Chem.*, 1973, 8, p. 325.
[4] W. Klemm, G. Wehrmeyer, H. Bade, *Elektrochem. Ber. Bunsenges Phys. Chem.*, 1959, 63, p. 56.
[5] K. Hestermann, R. Hoppe, *Z. Anorg. Allg. Chem.*, 1969, 367, p. 249.
[6] K. Hestermann, R. Hoppe, *Z. Anorg. Allg. Chem.*, 1969, 367, p. 261.
[7] K. Hestermann, R. Hoppe, *Z. Anorg. Allg. Chem.*, 1969, 367, p. 270.
[8] G. Demazeau, C. Parent, M. Pouchard, P. Hagenmuller, *Mat. Res. Bull.*, 1972, 7, p. 913.
[9] M. Arjomand, D. Machin, *J. Chem. Soc. Dalton Trans.*, 1975, p. 1061.
[10] H. N. Migeon, F. Jeannot, M. Zanne, J. Aubry, *Rev. Chim. Minér.*, 1976, 13, p. 440.
[11] N. Nguyen, L. Er-Rakho, C. Michel, J. Choisnet, B. Raveau, *Mat. Res. Bull.*, 1980, 15, p. 891.
[12] L. Er-Rakho, C. Michel, J. Provost, B. Raveau, *J. Solid State Chem.*, 1981, 37, p. 151.
[13] N. Nguyen, J. Choisnet, M. Hervieu, B. Raveau, *J. Solid State Chem.*, 1981, 39, p. 120.
[14] J. Provost, F. Studer, C. Michel, B. Raveau, *Synthetic Metals*, 1981, 4, p. 147.
[15] J. Provost, F. Studer, C. Michel, B. Raveau, *Synthetic Metals*, 1981, 4, 157.
[16] N. F. Mott, *Metal-Insulator Transitions*, Taylor and Francis, London, 1974.
[17] N. Nguyen, C. Michel, F. Studer, B. Raveau, *Mat. Chem.*, 1982, 7, p. 413.
[18] N. Nguyen, F. Studer, B. Raveau, *J. Phys. Chem. Solids*, 1983, 44, p. 389.
[19] J. B. Goodenough, *Mat. Res. Bull.*, 1973, 8, p. 423.

(Received December 12, 1983)

BRIEF ATTACHMENT I

IN THE UNITED STATES PATENT AND TRADEMARK OFFICE

In re Patent Application of
Applicants: Bednorz et al.
Serial No.: 08/479,810
Filed: June 7, 1995

Date: March 1, 2005
Docket: YO987-074BZ
Group Art Unit: 1751
Examiner: M. Kopec

For: NEW SUPERCONDUCTIVE COMPOUNDS HAVING HIGH TRANSITION TEMPERATURE, METHODS FOR THEIR USE AND PREPARATION

Commissioner for Patents
P.O. Box 1450
Alexandria, VA 22313-1450

FIRST SUPPLEMENTAL AMENDMENT

Sir:

In response to the Office Action dated July 28, 2004, please consider the following:

ATTACHMENT I

Thermal Analysis

Vol. 2 Inorganic Chemistry/Metallurgy
Earth Sciences
Organic Chemistry/Polymers
Biological Sciences/Medicine/Pharmacy

Editor
W. Hemminger
Institut für Werkstoffkunde
Universität Braunschweig
Federal Republic of Germany

1980
Birkhäuser Verlag
Basel · Boston · Stuttgart

Proceedings of the Sixth International Conference on Thermal Analysis

Bayreuth, Federal Republic of Germany
July 6–12, 1980

Vol. 1 Theory
Instrumentation
Applied Sciences
Industrial Applications

Vol. 2 Inorganic Chemistry/Metallurgy
Earth Sciences
Organic Chemistry/Polymers
Biological Sciences/Medicine/Pharmacy

T

Vol. 2 Inor
Eart
Orga
Biol

Edit
W. I
Insti
Uni
Fed

B

Fore

Although the use o
sions began in the r
of the effects of hea
20th century. In t
broadly applicable
For a demonstratio
volume. From acad
quality control of ir
tools for the scienti
field of endeavour.
others employ them
and chemical proce
Growth in the valu
ing number of nati
common ground a
application of thes
a similar but broad
ing an opportunity
common interests
of experts continue
ture, standards an
together ICTA and
to work, to find st
analysis. The end i

Onta
Miss

CIP-Kurztitelaufnahme der Deutschen Bibliothek

Thermal analysis. – Basel, Boston, Stuttgart: Birkhäuser.
Bd. 1971 mit d. Erscheinungsorten: Basel, Stuttgart. – Bd. 1977 im Verl. Heyden, London, Bellmawr (NJ), Rheine.
ISBN 3-7643-1202-5
1980.
Vol. 2. Inorganic chemistry, metallurgy, earth sciences, organic chemistry, polymers, biological sciences, medicine, pharmacy: proceedings of the 6. Internat. Conference on Thermal Analysis, Bayreuth, Fed. Republic of Germany, July 6–12, 1980/ed. W. Hemminger. – 1980.
ISBN 3-7643-1086-3
NE: Hemminger, Wolfgang (Hrsg.); ICTA (06, 1980, Bayreuth)

ISBN 3-7643-1086-3
Printed in Switzerland

THERMAL BEHAVIOUR OF COMPOSITIONS IN THE SYSTEMS x $BaTiO_3$ + (1-x) $Ba(Ln_{0.5}B_{0.5})O_3$

V.S. Chincholkar* and A.R. Vyawahare
Department of Chemistry, Institute of Science, Nagpur

ABSTRACT

The effect of temperature on the dielectric constant (ε), tan δ (loss tangent) and the ferroelectric properties of compositions in the systems x $BaTiO_3$ + (1-x) $Ba(Ln_{0.5}B_{0.5})O_3$ ($0 \leq x \leq 1$, Ln^{3+} = a rare earth cation and y^{3+}, B^{5+} = Ta,Nb,V) reveal that in the Ta^{5+} system at x = 0.8, the ε_{max} (ε at T_c) and T_c (the Curie-point) exhibit an increasing trend with decreasing ionic radii of the Ln^{3+} ions, whereas in the analogous Nb^{5+} system, an almost linear behaviour has been observed. In the V^{5+} system, the pure phases (x = 0) exhibit increasing trend of ε_{max} and T_c values with decreasing rare earth cation size. Phases with x = 0.8, exhibit a break at Nd^{3+} in ε_{max} values, in contrast to an increasing trend in T_c values with decreasing rare earth cation size. Similar behaviour is observed for the polarization data. The increasing trend in the T_c values in the direction Ta^{5+}-Nb^{5+}-V^{5+} at x = 0.8 is perhaps reminiscent of the nephelauxetic effect.

The T_c values for these first order transitions have been confirmed by recording DTA curves against inert α-Al_2O_3, the enthalpy change, however, being appreciably low in the present series.

INTRODUCTION

Recently emphasis has been placed on laser research and a concentrated effort has brought new and improved materials which can be used as hosts for transition. An important part of this effort has been directed towards finding potential laser materials having fluorescent energy states with long life times. In order to determine if symmetry conditions in

THERMAL ANALYSIS . ICTA 80 . BIRKHAEUSER VERLAG,BASEL,BOSTON,STUTTGART

crystals also affect the life time of rare earth ion fluorescence, a series of ordered perovskite compounds having the general formula $A(B'_{0.5}B''_{0.5})O_3$ were studied [1]-[7]. However, temperature effects and doping characteristics were not studied. The present work concerns with the formation and the thermal characteristics of compositions in the systems $x\ BaTiO_3 + (1-x)\ Ba(Ln_{0.5}B_{0.5})O_3$ where $0 \leq x \leq 1$, Ln^{3+} = a rare earth cation and Y, $B^{5+} = Nb^{5+}$, Ta^{5+} and V^{5+}.

EXPERIMENTAL PROCEDURE

The compositions were prepared by the solid state reaction of the parent compounds (carbonates, oxides) at high temperature as described elsewhere [8],[9]. Room temperature X-ray structure was determined using Debye-Scherrer camera (14 cm diameter) and nickel-filtered Cu-K_α radiation. Temperature effects on the dielectric constant (capacitance) and loss tangent (tan δ) were measured using a 716-C GR capacitance bridge together with type 1340-B type audiobeat frequency generator and 1231-B type u null detector and amplifier with 1231 P_S type variable filter in a sample holder designed in this laboratory [10].

Modified [11] Sawyer-Tower type circuit was used to record hysteresis loops as a function of temperature in the above sample holder and a MOM Derivatograph was used to record DTA curves against α-Al_2O_3 as reference.

RESULTS AND DISCUSSION

Tables 1-3 show the room temperature ε values as also the ε_{max} and the Curie-point (T_c) values evaluated from the capacitance measurements for compositions in the various systems. The temperature study e was restricted to x = 0.8 compositions in the Ta^{5+}, Nb^{5+} systems and over the entire composition range in the V^{5+} system which exhibited the transition in the whole range of compositions. Table 4 shows these parameters at x = 0 for compositions in the V^{5+} system. In all the sy-

stems, an increasin
with decreasing rar
scent of the lantha

ε_{max}, P_s and T_c val

Composition
$Ba(La_{0.1}Ta_{0.1}Ti_{0.8}$
$Ba(Nd_{0.1}Ta_{0.1}Ti_{0.8}$
$Ba(Sm_{0.1}Ta_{0.1}Ti_{0.8}$
$Ba(Gd_{0.1}Ta_{0.1}Ti_{0.8}$
$Ba(Dy_{0.1}Ta_{0.1}Ti_{0.8}$
$Ba(Y_{0.1}Ta_{0.1}Ti_{0.8})$

ε_{max}, P_s and T_c va

$Ba(La_{0.1}Nb_{0.1}Ti_{0.}$
$Ba(Nd_{0.1}Nb_{0.1}Ti_{0.}$
$Ba(Sm_{0.1}Nb_{0.1}Ti_{0.}$
$Ba(Gd_{0.1}Nb_{0.1}Ti_{0.}$
$Ba(Dy_{0.1}Nb_{0.1}Ti_{0.}$
$Ba(Y_{0.1}Nb_{0.1}Ti_{0.8}$

ε_{max}, P_s and T_c v

$Ba(La_{0.1}V_{0.1}Ti_{0.8}$
$Ba(Nd_{0.1}V_{0.1}Ti_{0.8}$
$Ba(Sm_{0.1}V_{0.1}Ti_{0.8}$
$Ba(Gd_{0.1}V_{0.1}Ti_{0.8}$
$Ba(Dy_{0.1}V_{0.1}Ti_{0.8}$
$Ba(Y_{0.1}V_{0.1}Ti_{0.8})$

stems, an increasing trend in ε_{max} as also T_c is observed with decreasing rare earth cation size, and is perhaps reminiscent of the lanthanide contraction.

Table 1

ε_{max}, P_s and T_c values for compositions in the Ta^{5+} system

Composition	$\varepsilon_{25°C}$	P_s [$\mu c/cm^2$]	ε_{max}	T_c [°C]
$Ba(La_{0.1}Ta_{0.1}Ti_{0.8})O_3$	200	4.5	780	85
$Ba(Nd_{0.1}Ta_{0.1}Ti_{0.8})O_3$	250	6.0	850	90
$Ba(Sm_{0.1}Ta_{0.1}Ti_{0.8})O_3$	342	8.1	1050	92
$Ba(Gd_{0.1}Ta_{0.1}Ti_{0.8})O_3$	480	8.5	1120	96
$Ba(Dy_{0.1}Ta_{0.1}Ti_{0.8})O_3$	530	8.9	1400	100
$Ba(Y_{0.1}Ta_{0.1}Ti_{0.8})O_3$	580	9.6	1830	110

Table 2

ε_{max}, P_s and T_c values for compositions in the systems Nb^{5+}

$Ba(La_{0.1}Nb_{0.1}Ti_{0.8})O_3$	232	5.3	580	90
$Ba(Nd_{0.1}Nb_{0.1}Ti_{0.8})O_3$	260	6.2	900	100
$Ba(Sm_{0.1}Nb_{0.1}Ti_{0.8})O_3$	290	8.4	1100	107
$Ba(Gd_{0.1}Nb_{0.1}Ti_{0.8})O_3$	380	9.2	1220	110
$Ba(Dy_{0.1}Nb_{0.1}Ti_{0.8})O_3$	415	9.8	1350	115
$Ba(Y_{0.1}Nb_{0.1}Ti_{0.8})O_3$	530	10.2	1600	118

Table 3

ε_{max}, P_s and T_c values for compositions in the V^{5+} system

$Ba(La_{0.1}V_{0.1}Ti_{0.8})O_3$	170	4.5	1100	93
$Ba(Nd_{0.1}V_{0.1}Ti_{0.8})O_3$	225	3.5	840	124
$Ba(Sm_{0.1}V_{0.1}Ti_{0.8})O_3$	280	7.5	1130	130
$Ba(Gd_{0.1}V_{0.1}Ti_{0.8})O_3$	350	8.2	1290	135
$Ba(Dy_{0.1}V_{0.1}Ti_{0.8})O_3$	480	8.2	1600	135
$Ba(Y_{0.1}V_{0.1}Ti_{0.8})O_3$	530	12.2	2200	125

Table 4

ε_{max}, P_s and T_c values for compositions in the V^{5+} system at x = 0

$Ba(La_{0.5}V_{0.5})O_3$	60	--	--	--
$Ba(Nd_{0.5}V_{0.5})O_3$	20	7.8	260	154
$Ba(Sm_{0.5}V_{0.5})O_3$	30	10.7	500	168
$Ba(Gd_{0.5}V_{0.5})O_3$	35	11.3	850	175
$Ba(Dy_{0.5}V_{0.5})O_3$	25	12.5	1020	200
$Ba(Y_{0.5}V_{0.5})O_3$	40	17.9	1250	220

Covalency of the B-O bond is reported [12] to increase with decreasing rare earth cation size and may be responsible for the above occurrence. The behaviour, however, is linear in case of Nb^{5+} and non-linear in the case of Ta^{5+}, V^{5+}.

Table 5 shows the T_f and ΔH values as evaluated from the DTA curves, for some representative samples.

Table 5

Composition	T_f (°C)	ΔH [cal $mole^{-1}$]
$Ba(La_{0.1}Ta_{0.1}Ti_{0.8})O_3$	80	25
$Ba(La_{0.1}Nb_{0.1}Ti_{0.8})O_3$	90	45
$Ba(La_{0.1}V_{0.1}Ti_{0.8})O_3$	95	65

A glance at the ΔH values reveal dilution of the ΔH value of the 120°C transition of $BaTiO_3$ (46 cal/mole) [13] by the addition of Ta^{5+} phases, no change with addition of Nb^{5+} phases and a substantial increase with incorporation of V^{5+} phases.

Another significant result of the present study is the observation of increasing T_c (T_f) values with decreasing B^{5+} radii, keeping the Ln^{3+} ion fixed, in the sequence Ta^{5+}-Nb^{5+}-V^{5+}.

Considering the energy level diagram of an octahedrally surrounded metal ion with configuration $(np)^6$, we expect Ta^{5+} to

be more ionic
this the elec
will be less
justified by
these ions T
Jørgensen has
that the elec
Nb^{5+}-V^{5+} and
transition me
cal bond becor
Our results a

Fifth ionizati

Ion
V^{5+}
Nb^{5+}
Ta^{5+}

[1] F. Galasso
Report UAE
[2] F. Galasso
61 (1959)
[3] F. Galasso
63 (1961)
[4] F. Galasso
[5] F. Galasso
[6] F. Galasso
[7] F. Galasso
[8] V.S. Chine

be more ionically bonded than Nb^{5+} and V^{5+}. As a result of this the electron density in the t_{2g}-orbital of the Ta^{5+} ion will be less than that in the case of Nb^{5+}, V^{5+}. This is also justified by considering the fifth ionization potential of these ions T (Table 6) which also increases in this sequence. Jørgensen has concluded from the electron transfer spectra that the electron affinity increases in the sequence Ta^{5+}-Nb^{5+}-V^{5+} and from the reduced Racah parameters of several transition metal ions (nephelauxetic effect) that the chemical bond becomes more covalent in the sequence 5d-4d-3d group. Our results are consistent with the observations of Jørgensen.

Table 6

Fifth ionization potential and electron configuration of B^{5+} metal ions

Ion	Electron configuration	I_5 (eV)
V^{5+}	$3s^2 3p^6$	65
Nb^{5+}	$4s^2 4p^6$	52
Ta^{5+}	$5s^2 5p^6$	45

REFERENCES

[1] F. Galasso, United Aircraft Corporation Laboratory, Report UAR-B10, Jan 1963

[2] F. Galasso, L. Katz, and R. Ward, J.Amer.Chem.Soc. 81 (1959) 820

[3] F. Galasso, J.R. Barrante, and L. Katz, J.Amer.Chem.Soc. 83 (1961) 2830

[4] F. Galasso, and W.J. Darby, J.Phys.Chem. 66 (1962) 131

[5] F. Galasso, and J. Pyle, J.Phys.Chem. 67 (1963) 533

[6] F. Galasso, and J. Pyle, J.Phys.Chem. 67 (1963) 1561

[7] F. Galasso, and J. Pyle, Inorg.Chem. 2 (1963) 482

[8] V.S. Chincholkar, J.Inorg.Nucl.Chem. 34 (1972) 2973

[9] K. Gade, and V.S. Chincholkar, J.Chem.Soc. (Dalton) 12 (1979) 1959

[10] V.S. Chincholkar, Z.Angew.Chem. 26 (1970) 288

[11] V.S. Chincholkar, Ph.D.Thesis. Pune University, 1967

[12] R.S.Roth, J.Research NBS 58 (1957) 75

[13] J. Volger, Philips Res.Rep. 7 (1952) 21

[14] C.K.Jørgensen, "Absorption spectra and chemical bonding in complexes" Pergamon Press, 1962, pp. 147, 306 and 310-12

* Present address: Forensic Science Laboratory, Bombay-8

STUDIES

A.

Bhabha

The formation of
by Solid State re

$La_2(C_2O_4)_3$, La (
The reaction occu
depending upon th
kinetics of forma
and MoO_3 is evalu
controlled mechar
activation energy
$mole^{-1}$.
A reversible phas
observed at 823 K
x-ray diffractior

The solid state r
$La_2(C_2O_4)_3$, La (
to gain better u
general and the
formation of tri
particular.
Several $Ln_2(MoO_4$
been extensively
electrical, magn
kinetics and mec
reported scantil
reactivity of th
re-examine this
detail.

THERMAL ANALYSIS . ICT

BRIEF ATTACHMENT J

IN THE UNITED STATES PATENT AND TRADEMARK OFFICE

In re Patent Application of
Applicants: Bednorz et al.
Serial No.: 08/479,810
Filed: June 7, 1995

Date: March 1, 2005
Docket: YO987-074BZ
Group Art Unit: 1751
Examiner: M. Kopec

For: NEW SUPERCONDUCTIVE COMPOUNDS HAVING HIGH TRANSITION TEMPERATURE, METHODS FOR THEIR USE AND PREPARATION

Commissioner for Patents
P.O. Box 1450
Alexandria, VA 22313-1450

FIRST SUPPLEMENTAL AMENDMENT

Sir:

In response to the Office Action dated July 28, 2004, please consider the following:

ATTACHMENT J

Model family of high-temperature superconductors: $Tl_mCa_{n-1}Ba_2Cu_nO_{2(n+1)+m}$ ($m=1,2$; $n=1,2,3$)

S. S. P. Parkin, V. Y. Lee, A. I. Nazzal, R. Savoy, T. C. Huang, G. Gorman, and R. Beyers
IBM Research Division, Almaden Research Center, 650 Harry Road, San Jose, California 95120-6099
(Received 31 May 1988)

We describe the structures and superconducting properties of six compounds in the Tl-Ca-Ba-Cu-O system of the general form, $Tl_mCa_{n-1}Ba_2Cu_nO_{2(n+1)+m}$, where $m=1$ or 2 and $n=1$, 2, or 3. One of the compounds displays the highest known superconducting transition temperature, $T_c \simeq 125$ K. The structures of these compounds consist of copper perovskitelike blocks containing 1, 2, or 3 CuO_2 planes separated by one or two Tl-O layers and thus form a model family of structures in which both the size and separation of the copper oxide blocks can be independently varied. The superconducting transition temperature increases with the number of CuO_2 planes in the perovskitelike block for both the Tl-O monolayer and bilayer compounds. For each pair of compounds ($m=1,2$) with the same number of CuO_2 planes (same n), the transition temperatures are similar but are consistently 15–20 K lower in the materials with single Tl-O layers. Variations in the transition temperatures in the double and triple CuO_2-layer compounds are observed to correlate with increased densities of intergrowths of related structures.

Recently[1-7] several new high-temperature superconductors have been synthesized in the Tl-Ca-Ba-Cu-O system, including $Tl_2Ca_2Ba_2Cu_3O_{10\pm x}$, which displays the highest superconducting transition temperature yet found, $T_c \simeq 125$ K.[3] In this article we present data on the structures and superconducting properties of six compounds of the form $Tl_mCa_{n-1}Ba_2Cu_nO_{2(n+1)+m}$, where $m=1$ or 2 and $n=1$, 2, or 3. The structures consist of copper perovskitelike blocks containing 1, 2, or 3 CuO_2 planes separated by one or two Tl-O layers. These compounds thus form a model family of structures in which both the size and separation of the copper blocks can be independently varied. We present data that establish that the superconducting transition temperature increases with the number of CuO_2 planes in the perovskitelike block for both the Tl-O monolayer and bilayer compounds. For each pair of compounds ($m=1$, 2) with the same number of CuO_2 planes (same n), the transition temperature is 15–20 K lower in the material with single Tl-O layers. Variations in the transition temperatures in the double and triple CuO_2 layer compounds are observed to correlate with increased densities of intergrowths of related structures.

The samples were prepared by thoroughly mixing suitable amounts of Tl_2O_3, CaO, BaO_2, and CuO, and forming a pellet of this mixture under pressure. The pellet was then wrapped in gold foil, sealed in a quartz tube containing slightly less than 1 atm of oxygen, and baked for approximately 3 h at $\simeq 880$ °C. A wide range of starting compositions was studied. In most cases the resulting pellet was comprised of several phases. However, for certain ranges of starting compositions, the pellets contained only one superconducting phase of the form $Tl_mCa_{n-1}Ba_2Cu_nO_{2(n+1)+m}$ together with minor amounts ($< \simeq 20\%$) of insulating oxides such as those of Cu, Ca-Cu, Ba-Cu, and Tl-Ba. The relative amounts of each phase depended on the annealing time and temperature and the rate of cooling from this temperature. In particular, for slow cooling rates ($\simeq 100$ °C/h) the composition of the major $Tl_mCa_{n-1}Ba_2Cu_nO_{2(n+1)+m}$ phase more closely matched that of the starting composition. The composition and microstructure of the pellets were determined from complementary powder x-ray diffraction, electron microprobe, electron diffraction, and high-resolution transmission electron microscopy (TEM) studies. The superconducting properties of each pellet were examined by resistivity and dc Meissner susceptibility studies. The latter was measured with a SHE SQUID magnetometer. Cooling in a field of 100 Oe, the magnitude of the Meissner susceptibility at 5.5 K ranged from 10% to 35% of the susceptibility of a perfect diamagnet of the same volume, neglecting small demagnetizing corrections. The magnitude of the diamagnetic shielding signal is very dependent on the distribution of the normal and superconducting phases within the multiphase pellets and in most cases did not give useful information. The susceptibility data revealed that for some pellets the presence of a minority superconducting phase resulted in the resistance of the pellet dropping to zero at substantially higher temperatures than the T_c of the majority superconducting phase. This type of behavior emphasizes the importance of determining the transition temperature from a flux exclusion measurement in this complex quinary system. These results are summarized in Table I.

We have previously described the preparation and properties of the three members of the $Tl_mCa_{n-1}Ba_2Cu_nO_{2(n+1)+m}$ family, namely $Tl_2Ca_2Ba_2Cu_3O_{10}$ (2:2:2:3),[3] $Tl_2Ca_1Ba_2Cu_2O_8$ (2:1:2:2),[3] and $Tl_1Ca_2Ba_2Cu_3O_8$ (1:2:2:3),[4] which display superconducting transition temperatures of 125, 108, and 110 K, respectively. By systematically varying the starting composition of the pellets, the related compounds, $Tl_2Ca_0Ba_2Cu_1O_x$ (2:0:2:1), $Tl_1Ca_0Ba_2Cu_1O_x$ (1:0:2:1), and $Tl_1Ca_1Ba_2Cu_2O_x$ (1:1:2:2) were synthesized. The unit cells for each phase

PHYSICAL REVIEW B VOLUME 38, NUMBER 10 1 OCTOBER 1988

Model family of high-temperature superconductors: $Tl_mCa_{n-1}Ba_2Cu_nO_{2(n+1)+m}$ ($m=1,2$; $n=1,2,3$)

S. S. P. Parkin, V. Y. Lee, A. I. Nazzal, R. Savoy, T. C. Huang, G. Gorman, and R. Beyers
IBM Research Division, Almaden Research Center, 650 Harry Road, San Jose, California 95120-6099
(Received 31 May 1988)

We describe the structures and superconducting properties of six compounds in the Tl-Ca-Ba-Cu-O system of the general form, $Tl_mCa_{n-1}Ba_2Cu_nO_{2(n+1)+m}$, where $m=1$ or 2 and $n=1$, 2, or 3. One of the compounds displays the highest known superconducting transition temperature, $T_c \simeq 125$ K. The structures of these compounds consist of copper perovskitelike blocks containing 1, 2, or 3 CuO_2 planes separated by one or two Tl-O layers and thus form a model family of structures in which both the size and separation of the copper oxide blocks can be independently varied. The superconducting transition temperature increases with the number of CuO_2 planes in the perovskitelike block for both the Tl-O monolayer and bilayer compounds. For each pair of compounds ($m=1,2$) with the same number of CuO_2 planes (same n), the transition temperatures are similar but are consistently 15–20 K lower in the materials with single Tl-O layers. Variations in the transition temperatures in the double and triple CuO_2-layer compounds are observed to correlate with increased densities of intergrowths of related structures.

Recently[1-7] several new high-temperature superconductors have been synthesized in the Tl-Ca-Ba-Cu-O system, including $Tl_2Ca_2Ba_2Cu_3O_{10\pm x}$, which displays the highest superconducting transition temperature yet found, $T_c=125$ K.[3] In this article we present data on the structures and superconducting properties of six compounds of the form $Tl_mCa_{n-1}Ba_2Cu_nO_{2(n+1)+m}$, where $m=1$ or 2 and $n=1$, 2, or 3. The structures consist of copper perovskitelike blocks containing 1, 2, or 3 CuO_2 planes separated by one or two Tl-O layers. These compounds thus form a model family of structures in which both the size and separation of the copper blocks can be independently varied. We present data that establish that the superconducting transition temperature increases with the number of CuO_2 planes in the perovskitelike block for both the Tl-O monolayer and bilayer compounds. For each pair of compounds ($m=1$, 2) with the same number of CuO_2 planes (same n), the transition temperature is 15–20 K lower in the material with single Tl-O layers. Variations in the transition temperatures in the double and triple CuO_2 layer compounds are observed to correlate with increased densities of intergrowths of related structures.

The samples were prepared by thoroughly mixing suitable amounts of Tl_2O_3, CaO, BaO_2, and CuO, and forming a pellet of this mixture under pressure. The pellet was then wrapped in gold foil, sealed in a quartz tube containing slightly less than 1 atm of oxygen, and baked for approximately 3 h at $\simeq 880$ °C. A wide range of starting compositions was studied. In most cases the resulting pellet was comprised of several phases. However, for certain ranges of starting compositions, the pellets contained only one superconducting phase of the form $Tl_mCa_{n-1}Ba_2Cu_nO_{2(n+1)+m}$ together with minor amounts ($< \simeq 20\%$) of insulating oxides such as those of Cu, Ca-Cu, Ba-Cu, and Tl-Ba. The relative amounts of each phase depended on the annealing time and temperature and the rate of cooling from this temperature. In particular, for slow cooling rates ($\simeq 100$ °C/h) the composition of the major $Tl_mCa_{n-1}Ba_2Cu_nO_{2(n+1)+m}$ phase more closely matched that of the starting composition. The composition and microstructure of the pellets were determined from complementary powder x-ray diffraction, electron microprobe, electron diffraction, and high-resolution transmission electron microscopy (TEM) studies. The superconducting properties of each pellet were examined by resistivity and dc Meissner susceptibility studies. The latter was measured with a SHE SQUID magnetometer. Cooling in a field of 100 Oe, the magnitude of the Meissner susceptibility at 5.5 K ranged from 10% to 35% of the susceptibility of a perfect diamagnet of the same volume, neglecting small demagnetizing corrections. The magnitude of the diamagnetic shielding signal is very dependent on the distribution of the normal and superconducting phases within the multiphase pellets and in most cases did not give useful information. The susceptibility data revealed that for some pellets the presence of a minority superconducting phase resulted in the resistance of the pellet dropping to zero at substantially higher temperatures than the T_c of the majority superconducting phase. This type of behavior emphasizes the importance of determining the transition temperature from a flux exclusion measurement in this complex quinary system. These results are summarized in Table I.

We have previously described the preparation and properties of the three members of the $Tl_mCa_{n-1}Ba_2Cu_nO_{2(n+1)+m}$ family, namely $Tl_2Ca_2Ba_2Cu_3O_{10}$ (2:2:2:3),[3] $Tl_2Ca_1Ba_2Cu_2O_8$ (2:1:2:2),[3] and $Tl_1Ca_2Ba_2Cu_3O_9$ (1:2:2:3),[4] which display superconducting transition temperatures of 125, 108, and 110 K, respectively. By systematically varying the starting composition of the pellets, the related compounds, $Tl_2Ca_0Ba_2Cu_1O_x$ (2:0:2:1), $Tl_1Ca_0Ba_2Cu_1O_x$ (1:0:2:1), and $Tl_1Ca_1Ba_2Cu_2O_x$ (1:1:2:2) were synthesized. The unit cells for each phase

TABLE I. Summary of properties of $Tl_mCa_{n-1}Ba_2Cu_nO_x$

Conc. ratio	Tl	Relative composition Ca	Ba	Cu	O	Symmetry	Lattice parameters a (Å)	c (Å)	Superlattice wave vector (k)	T_c (K)
						$Tl_1Ca_{n-1}Ba_2Cu_nO_x$				
1:0:2:1	1.2	0.0	2	0.7	4.8	*P4/mmm*	3.869(2)	9.694(9)	a	b
1:1:2:2	1.1	0.9	2	2.1	7.1	*P4/mmm*	3.8505(7)	12.728(2)	⟨0.29,0,0.5⟩	65–85
1:2:2:3	1.1	0.8	2	3.0	9.7	*P4/mmm*	3.8429(6)	15.871(3)	⟨0.29,0,0.5⟩	100–110
						$Tl_2Ca_{n-1}Ba_2Cu_nO_x$				
2:0:2:1	1.9	0.0	2	1.1	6.4	*F/mmm*[c]	$a=5.445(2)$ $b=5.492(1)$	23.172(6)	⟨0.08,0.24,1⟩[c]	b
2:0:2:1[d]	1.8	0	2	1.1	6.4	*F/mmm*[c]	$a=5.4634(3)$ $b\sim a$	23.161(1)	⟨0.08,0.24,1⟩[c]	20
2:0:2:1	1.8	0.02	2	1.1	6.3	*I4/mmm*	3.8587(4)	23.152(2)	⟨0.16,0.08,1⟩[c]	15–20
2:1:2:2	1.7	0.9	2	2.3	8.1	*I4/mmm*	3.857(1)	29.39(1)	⟨0.17,0,1⟩	95–108
2:2:2:3	1.6	1.8	2	3.1	10.1	*I4/mmm*	3.822(4)	36.26(3)	⟨0.17,0,1⟩	118–125

[a]No superlattice spots observed.
[b]Nonmetallic or weakly metallic samples with no superconducting transition observed in resistivity and magnetic susceptibility studies for temperatures down to 4.2 K.
[c]The symmetry of the structure is *orthorhombic* if the observed superlattice is ignored. Taking the superlattice into account lowers the symmetry to *monoclinic*.
[d]Sample prepared from a Cu-rich starting composition, $Tl_2Ba_2Cu_3$.
[e]The superstructure is identical to that for the orthorhombic 2:0:2:1 polymorph.

were determined from powder x-ray diffraction patterns extending from $2\theta=3°$ to 70° and verified by electron diffraction studies. These studies showed that all of the $Tl_mCa_{n-1}Ba_2Cu_nO_{2(n+1)+m}$ compounds have tetragonal cells at room temperature. The $Tl_1Ca_{n-1}Ba_2Cu_nO_{2n+3}$ compounds contain Tl-O monolayers, resulting in primative tetragonal cells, whereas the $Tl_2Ca_{n-1}Ba_2Cu_nO_{2n+4}$ compounds contain Tl-O bilayers, resulting in body-centered tetragonal cells. The lattice parameters and symmetries of the various structures are included in Table I. As discussed later, the 2:0:2:1 compound also has an orthorhombic polymorph. As shown in Fig. 1, each oxide has a single peak in the low-angle portion ($3° \leq 2\theta \leq 10°$) of its x-ray diffraction pattern which results from the large c/a ratio in each structure. These peaks, (001) for $m=1$ and (002) for $m=2$, serve as fingerprints with which each of the compounds within the

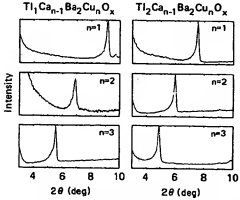

FIG. 1. Low-angle section of the powder x-ray diffraction patterns for the six phases $Tl_mCa_{n-1}Ba_2Cu_nO_{2(n+1)+m}$ ($m=1$, 2; $n=1$, 2, 3).

$Tl_mCa_{n-1}Ba_2Cu_nO_{2(n+1)+m}$ family can be uniquely identified. The peak systematically shifts to lower angles as n increases within both the $Tl_1Ca_{n-1}Ba_2Cu_nO_{2n+3}$ and $Tl_2Ca_{n-1}Ba_2Cu_nO_{2n+4}$ families, consistent with an expansion of the unit cell along the c axis by the addition of extra CuO_2 and Ca planes. The peaks are in all cases at lower angles in the $Tl_2Ca_{n-1}Ba_2Cu_nO_{2n+4}$ compounds compared to the corresponding $Tl_1Ca_{n-1}Ba_2Cu_nO_{2n+3}$ compound, consistent with the increased number of Tl-O layers in the $Tl_2Ca_{n-1}Ba_2Cu_nO_{2n+4}$ compounds. The peaks are asymmetrically broadened to low angles because of geometrical aberrations in the focusing condition resulting from the flat specimens used.[8] The arrangement of the cations in the various compounds is shown in Fig. 2. The positions of the oxygen atoms are inferred by comparison with related structures in the $La_{2-x}Sr_xCuO_4$, $YBa_2Cu_3O_x$, and $Bi_2Sr_2Ca_1Cu_2O_x$ families.[9-11] The six structures are comprised of Cu perovskitelike blocks containing one, two, or three CuO_2 planes sandwiched between Tl-O monolayers (1:0:2:1, 1:1:2:2, and 1:2:2:3 compounds) or bilayers (2:0:2:1, 2:1:2:2, 2:2:2:3 compounds). The Ba cations are located in planes adjacent to the Tl-O unit and the Ca cations form planes within the interior of the Cu perovskitelike unit.

Since the preparation, structure, and properties of the double and triple CuO_2 layer oxides appear to be much less complex than those of the single CuO_2 layer oxides for both the monolayer and bilayer Tl-O compounds, we will discuss these groups of compounds separately. As described earlier, for each of the $n=2$ and $n=3$ compounds a single tetragonal structure was found. An important structural feature of these compounds observed by TEM, scanning electron microscopy (SEM), and electron microprobe studies are intergrowths of structures related to the primary phase by the addition or removal of CuO_2 or Tl-O layers. For some samples SEM images showed contrast striations $\simeq 5$–10 μm in width within individual

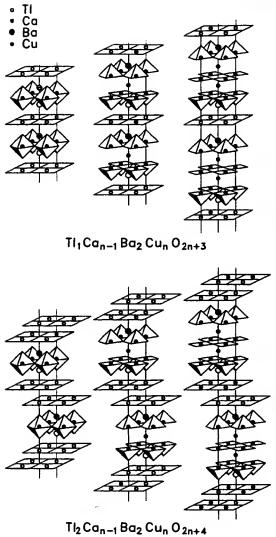

FIG. 2. Nominal structures of the six $Tl_mCa_{n-1}Ba_2Cu_nO_{2(n+1)+m}$ phases for $n=1$, 2 and $m=1$, 2, 3.

grains which result from intergrowths of regions with different proportions of heavy atoms. TEM studies revealed the existence of intergrowths on much finer length scales, as demonstrated in Fig. 3 for a sample prepared from a starting composition of $Tl_{0.85}Ca_1Ba_2Cu_2$. Figure 3(a) shows a selected area diffraction pattern along b^* which indicates that this grain contains both 1:1:2:2 and 1:2:2:3 phases. Indeed Meissner data on this sample [included in Fig 4(d)] indicate two superconducting transitions with $T_c \simeq 65$ and $\simeq 105$ K, consistent with the presence of extended regions of two distinct phases. Coincidently, the c lattice parameters of the 1:1:2:2 and 1:2:2:3 phases are almost exactly in the ration of 4/5 so that every fifth 1:2:2:3 $h0l$ spot coincides with every fourth 1:1:2:2 $h0l$ spot in Figure 3(a). High-resolution TEM micrographs in Figs. 3(b) and 3(c) show intergrowths of the

FIG. 3. (a) [010] selected area diffraction (SAD) pattern and (b) corresponding image of crystallites containing regions of 1:2:2:3 and 1:1:2:2. The arrows in (b) denote unit-cell thick intergrowths of 1:1:2:2 in 1:2:2:3. (c) High-resolution transmission electron micrograph of one unit-cell thick 1:1:2:2 intergrowth in 1:2:2:3.

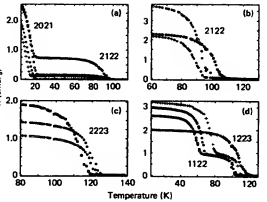

FIG. 4. Meissner susceptibility vs temperature for an applied field of 100 Oe for materials with starting cation composition, (a) $Tl_2Ba_2Cu_2$ (●), $Tl_2Ca_{0.05}Ba_2Cu_{1.05}$ (○, +), and $Tl_2Ca_{0.15}Ba_2Cu_{1.15}$ (▼); (b) $Tl_1Ca_2Ba_2Cu_3$ (●), $Tl_2Ca_1Ba_2Cu_2$ (○), and $Tl_{1.25}Ca_1Ba_2Cu_2$ (■); (c) $Tl_1Ca_2Ba_2Cu_3$ (■), $Tl_1Ca_{2.5}Ba_1Cu_3$ (○), and $Tl_1Ca_2Ba_1Cu_3$ (●); (d) $Tl_{0.85}Ca_1Ba_2Cu_2$ (○), $Tl_1Ca_1Ba_2Cu_2$ (●, +), and $Tl_{0.85}Ca_2Ba_2Cu_3$ (▼). The phases present in the pellet giving rise to the diamagnetic susceptibility are (a) 2:0:2:1 and 2:1:2:2, (b) 2:1:2:2, (c) 2:2:2:3, and (d) 1:1:2:2 and 1:2:2:3.

1:1:2:2 and 1:2:2:3 phases on length scales extending from $\simeq 1\mu m$ down to one unit cell. The intergrowths are randomly distributed along the stacking axis. Isolated intergrowths comprising four CuO_2 planes were found in some samples (see Fig. 5) but no evidence was found for extended intergrowths comprising greater than three CuO_2 layers in these or other samples especially prepared from Cu- and Ca-rich starting compositions. A second type of intergrowth was observed in samples of the 1:2:2:3 phase in which an extra Tl-O plane was occasionally inserted between the Cu perovskitelike units, creating local regions of the 2:2:2:3 phase. Microprobe data show that the Tl content is systematically high in the compounds containing single Tl-O layers and systematically low in those compounds with Tl-O bilayers (see Table I) thus suggesting that intergrowths of Tl-O monolayers in the Tl-O bilayers materials and Tl-O bilayers in the Tl-O monolayer compounds are a general feature of these materials.

FIG. 5. High-resolution TEM image of an isolated four-CuO_2-layer intergrowth. The markers denote the positions of the Cu columns.

Meissner data (see Fig. 4) established that T_c can take a range of values for all of the double and triple CuO_2 layer compounds—$T_c \simeq 95$–108 K for 2:1:2:2, $T_c \simeq 118$–125 K for 2:2:2:3, $T_c \simeq 65$–85 K for 1:1:2:2, and $T_c \simeq 100$–110 K for 1:2:2:3. For a given compound, x-ray diffraction and microprobe studies did not detect any obvious difference between the samples with different transition temperatures. TEM studies, however, showed a clear correlation between the density of intergrowths and T_c. For the 2:1:2:2, 2:2:2:3, and 1:2:2:3 phases the material with no intergrowths displayed the highest transition temperature, whereas for the 1:1:2:2 compound the sample with the lowest density of intergrowths had the lowest T_c. As the density of intergrowths increased we observed that T_c systematically decreases or increases, respectively. It is possible that the structural or electronic modifications caused by the intergrowths are directly responsible for the decreased transition temperatures. Alternatively the presence of the intergrowths may simply reflect a means whereby the system accommodates, to some extent, off-stoichiometry in the cation sites which in turn may influence T_c. It is difficult to determine whether it is the local change in structure or composition which is responsible for the decrease in T_c since these are concurrent changes.

A second important structural feature found in all of the double and triple CuO_2 layer compounds is the presence of weak superlattice reflections in the selected area electron diffraction patterns. These reflections are considerably weaker than those previously found in the $Bi_2Sr_2Ca_1Cu_2O_x$ compound[12–16] and indicate different structural modulations than those in the $Bi_2Sr_2Ca_1Cu_2O_x$ compound. The patterns can be described by a set of symmetry-related wave vectors, **k**. Each wave vector describes a pair of reflections symmetrically disposed a reciprocal distance $|\mathbf{k}|$ along **k** on either side of each Bragg peak, which would be consistent with a sinusoidal modulation of the charge density along this direction.[17] The possibility that each **k** corresponds to a different crystal variant with lowered symmetry is unresolved. The Tl-O monolayer and bilayer families each display a distinctive pattern of superlattice reflections, shown schematically in Figs. 6(a) and 6(b). One example of electron diffraction patterns showing the superlattice reflections is given in Fig. 7 for the 1:1:2:2 phase.

The structure and properties of the single CuO_2 layer compounds are more sensitive to the preparation conditions than those of the double and triple CuO_2 layer compounds. When prepared from a $Tl_2Ba_2Cu_1$ starting composition, the 2:0:2:1 compound has a face-centered orthorhombic cell and is not superconducting. The material is heavily twinned with twin planes of {110} type in the orthorhombic cell. This cell is related to the tetragonal cell by a rotation of $\simeq 45°$ about the c axis with a and b increased in size by a factor of $\simeq\sqrt{2}$. However when the 2:0:2:1 compound is prepared from a Cu-rich starting composition, $Tl_2Ba_2Cu_2$, the compound is superconduct-

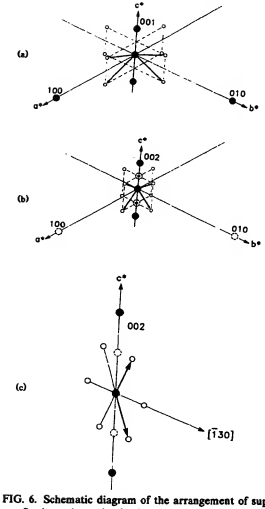

FIG. 6. Schematic diagram of the arrangement of superlattice reflections about the fundamental reflections for (a) the 1:1:2:2 and 1:2:2:3 phases, (b) the 2:1:2:2 and 2:2:2:3 phases, (c) the 2:0:2:1 phase. The fundamental reflections are shown as solid circles, and those which are systematically absent are shown as dashed circles. The superstructure is shown by open circles and the corresponding wave vectors by bold arrows.

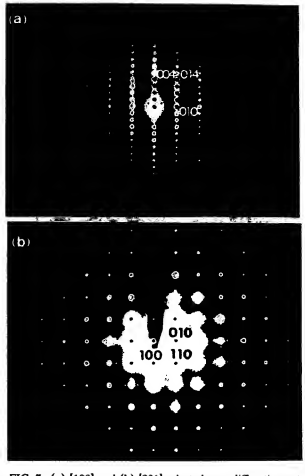

FIG. 7. (a) [100] and (b) [001] selected area diffraction patterns from crystallites of 1:1:2:2 showing superlattice reflections.

ing at $\simeq$20 K. While x-ray data indicate the structure is pseudotetragonal, transmission electron micrographs reveal a tweed pattern which is consistent with local orthorhombic distortion. A tetragonal polymorph with no evidence from TEM studies of either an average or local orthorhombic distortion can be formed by preparing the compound from a pellet containing a small amount of Ca (Tl:Ca:Ba:Cu = 2:y:2:1 + y, with $y \simeq 0.05$–0.15). This polymorph is also superconducting with a T_c which is independent of the amount of Ca in the starting composition but weakly dependent on the annealing time—$T_c \simeq 15$ and 20 K for anneal times at 880 °C of 3 and 9 h, respectively. As suggested by the Meissner data in Fig. 4(a) these pellets contain, in addition to the tetragonal 2:0:2:1 phase, a substantial amount of the 2:1:2:2 phase which increases as the proportion of Ca in the starting composition is increased. There is a sufficient amount of this phase that the resistance of these pellets actually drops to zero at $T_c \simeq 100$ K. The Meissner data in Fig. 4(a) show that for $y \simeq 0.05$ the ratio of 2:1:2:2 to 2:0:2:1 is about 8% and for $y \simeq 0.15$ the ratio is increased to $\simeq$30%. Electron microprobe analysis shows that only a small amount of Ca ($\simeq$0.2 at.%) is incorporated into the 2:0:2:1 grains and consequently the role of the Ca doping in changing the structure and properties of the 2:0:2:1 material is unclear. Moreover there are reports that the 2:0:2:1 phase can be prepared without Ca with a transition temperature as high as $\simeq$85 K.[5] Both polymorphs of the 2:0:2:1 structures display a similar superlattice with an approximate wave vector, $\mathbf{k} = [\bar{0}.08, 0.24, 1]$ in the orthorhombic setting. Taking the superlattice into account lowers the symmetry of both the orthorhombic and tetragonal structures to monoclinic with the c axis being unique. As shown in Fig. 8 this superstructure is different from those found in the double and triple CuO_2 layer compounds.

The other member of the $Tl_mCa_{n-1}Ba_2Cu_nO_{2(n+1)+m}$ family which contains single CuO_2 layers, the 1:0:2:1 phase, has a primitive tetragonal cell and is not superconducting for the wide range of preparative conditions considered in this study, including growth from Cu-rich or Ca-doped starting compositions. No superstructures have been observed in these crystals so far.

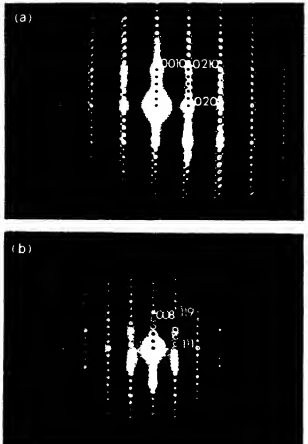

FIG. 8. (a) [100], (b) [110], and (c) [001] selected area diffraction patterns from a crystallite of 2:0:2:1.

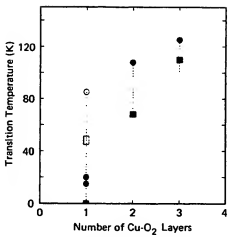

FIG. 9. Dependence of T_c on the number of CuO_2 planes within the Cu perovskitelike unit for the $Tl_1Ca_{n-1}Ba_2Cu_nO_{2n+3}$ (■) and $Tl_2Ca_{n-1}Ba_2Cu_nO_{2n+4}$ (●, this work; ○, Ref. 5) series of compounds. The dashed vertical lines correspond to the variations in T_c found for each phase. □ corresponds to data for $(Tl, Bi)_1(Ca,Sr)_2Cu_1O_x$ (Ref. 21).

As shown in Table I there is no obvious correlation of superlattice structure with the superconducting properties of the $Tl_mCa_{n-1}Ba_2Cu_nO_{2(n+1)+m}$ compounds. Note that in the closely related compound, $Bi_2Sr_1Ca_2Cu_2O_x$, it has recently been proposed that the observed incommensurate superlattice corresponds to a distortion of both the Bi-O and CuO_2 planes resulting from ordered vacancies on the Sr sites.[16] The vacancies are postulated to determine the carrier density on the CuO_2 planes and so influence the T_c in a manner similar to that first noted by Schafer, Penney, and Olsen for the $La_{2-x}Sr_xCuO_{4-y}$ compounds.[18] The number of different superlattice structures found in the Tl-Ca-Ba-Cu-O system provides a more extensive basis with which to test such hypotheses. Indeed it may be significant that, as shown in Table I, there are important variations in stoichiometry away from the ideal stoichiometries expected for the various $Tl_mCa_{n-1}Ba_2Cu_nO_{2(n+1)+m}$ phases. In particular, the [Tl]/[Ba] ratio is higher for the $n=1$ compounds compared to those for $n=2$ and $n=3$. Band-structure calculations of both the $Tl_mCa_{n-1}Ba_2Cu_nO_{2(n+1)+m}$ compounds and $Bi_2Sr_1Ca_2Cu_2O_x$ indicate that the stoichiometry of the Tl-O and Bi-O layers would have a profound impact on the carrier density in these materials.[19,20] The extent of off-stoichiometry on the cation or the oxygen sites in the Tl-Ca-Ba-Cu-O phases requires further study. Note also that one group has recently prepared a complex material of the form $(Tl,Bi)_1(Ca,Sr)_2Cu_1O_x$ with the 1:0:2:1 structure which appears to superconduct at temperatures of up to 50 K (Ref. 21). The variation of properties of the single CuO_2 layers compounds provides a fertile area for further study and highlights the difficulties in preparing these multicomponent oxides in a controlled manner.

In conclusion, these studies have shown that the superconducting transition temperature increases with the number of CuO_2 planes in the perovskitelike unit for both the $Tl_1Ca_{n-1}Ba_2Cu_nO_{2n+3}$ and $Tl_2Ca_{n-1}Ba_2Cu_nO_{2n+4}$ structures (Fig. 9). A similar dependency is found in both series of compounds with an increased spread of T_c as the number of CuO_2 planes is reduced. The range of T_c in the double and triple CuO_2 layer compounds correlates with the density of intergrowth defects. No such defects have ben observed so far in the single CuO_2 layer compounds,

even when doped with Ca. One might speculate that in this case the variation in transition temperature may result from variations in cation or oxygen site occupancy. The increase in T_c as n increases may be accounted for by various theories, including several based on the BCS theory[19] and others invoking more exotic mechanisms such as the resonating-valence-bond model.[22] The variety of structures and properties in the Tl-Ca-Ba-Cu-O system provides a model family of compounds with which various theories of high-temperature superconductivity can be evaluated.

We are indebted to S. J. La Placa, F. Herman, and J. B. Torrance for many useful discussions. We thank C. C. Torardi, R. B. Flippen, and R. M. Hazen for discussions regarding the 2:0:2:1 compound. We are grateful to Professor Sinclair at Stanford for the use of his electron microscope.

[1]Z. Z. Sheng and A. M. Hermann, Nature (London) **332**, 138 (1988); **332**, 55 (1988).

[2]R. M. Hazen, L. W. Finger, R. J. Angel, C. T. Prewitt, N. L. Ross, C. G. Hadidiacos, P. J. Heaney, D. R. Veblen, Z. Z. Sheng, A. El Ali, and A. M. Hermann, Phys. Rev. Lett. **60**, 1657 (1988).

[3]S. S. P. Parkin, V. Y. Lee, E. M. Engler, A. I. Nazzal, T. C. Huang, G. Gorman, R. Savoy, and R. Beyers, Phys. Rev. Lett. **60**, 2539 (1988).

[4]S. S. P. Parkin, V. Y. Lee, A. I. Nazzal, R. Savoy, R. Beyers, and S. J. La Placa, Phys. Rev. Lett. **61**, 750 (1988).

[5]C. C. Torardi, M. A. Subramanian, J. C. Calabrese, J. Gopalakrishnan, K. J. Morrissey, T. R. Askew, R. B. Flippen, U. Chowdry, and A. W. Sleight, Science **240**, 631 (1988).

[6]M. A. Subramanian, J. C. Calabrese, C. C. Torardi, J. Gopalakrishnan, T. R. Askew, R. B. Flippen, K. J. Morrissey, U. Chowdry, and A. W. Sleight, Nature (London) **332**, 420 (1988).

[7]S. Kondoh, Y. Ando, M. Onoda, and M. Sato, Solid State Commun. **65**, 1329 (1988).

[8]W. Parrish, *X-ray and Electron Methods of Analysis* (Plenum, New York, 1968).

[9]J. M. Tarascon, Y. Le Page, P. Barboux, B. G. Bagley, L. H. Greene, W. R. McKinnon, G. W. Hull, M. Giroud, and D. M. Hwang, Phys. Rev. B **37**, 9382 (1988).

[10]S. A. Sunshine, T. Siegrist, L. F. Schneemeyer, D. W. Murphy, R. J. Cava, B. Batlogg, R. B. van Dover, R. M. Fleming, S. H. Glarum, S. Nakahara, R. Farrow, J. J. Krajewski, S. M. Zahurak, J. V. Waszczak, J. H. Marshall, P. Marsh, L. W. Rupp, and W. F. Peck, Phys. Rev. B **38**, 893 (1988).

[11]J. B. Torrance, Y. Tokura, S. J. LaPlaca, T. C. Huang, R. J. Savoy, and A. I. Nazzal, Solid State Commun. **66**, 703 (1988).

[12]T. M. Shaw, S. A. Shivanshankar, S. J. LaPlaca, J. J. Cuomo, T. R. McGuire, R. A. Roy, K. H. Kelleher, and D. S. Yee, Phys. Rev. B **37**, 9856 (1988).

[13]D. R. Veblen, P. J. Heaney, R. J. Angel, L. W. Finger, R. M. Hazen, C. T. Prewitt, N. L. Ross, C. W. Chu, P. H. Hor, and R. L. Meng, Nature (London) **332**, 334 (1988).

[14]E. A. Hewat, M. Dupuy, P. Bordet, J. J. Capponi, C. Chaillout, J. L. Hodeau, and M. Marezio, Nature (London) **333**, 53 (1988).

[15]H. W. Zandbergen, Y. K. Huang, M. J. V. Menken, J. N. Li, K. Kadowaki, A. A. Menovsky, G. van Tendeloo, and S. Amelinckx, Nature (London) **332**, 620 (1988).

[16]P. L. Gai and P. Day (unpublished).

[17]P. M. De Wolff, Acta Crystallogr. Sec. A **30**, 777 (1974).

[18]M. W. Shafer, T. Penney, and B. L. Olsen, Phys. Rev. B **36**, 4047 (1987).

[19]M. S. Hybertson and L. F. Mattheiss, Phys. Rev. Lett. **60**, 1661 (1988).

[20]F. Herman, R. V. Kasowski, and W. Y. Hsu, Phys. Rev. B **38**, 204 (1988); F. Herman, R. V. Kasowski, S. J. La Placa, and S. S. P. Parkin (unpublished).

[21]P. Haldar, A. Roig-Janicki, S. Sridhar, and B. C. Giessen (unpublished).

[22]J. M. Wheatley, T. C. Hsu, and P. W. Anderson, Nature (London) **333**, 121 (1988).

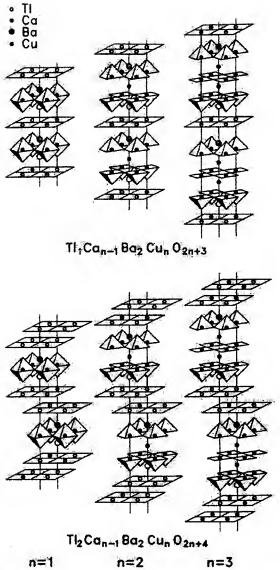

FIG. 2. Nominal structures of the six $Tl_mCa_{n-1}Ba_2Cu_nO_{2(n+1)+m}$ phases for $n=1, 2$ and $m=1, 2, 3$.

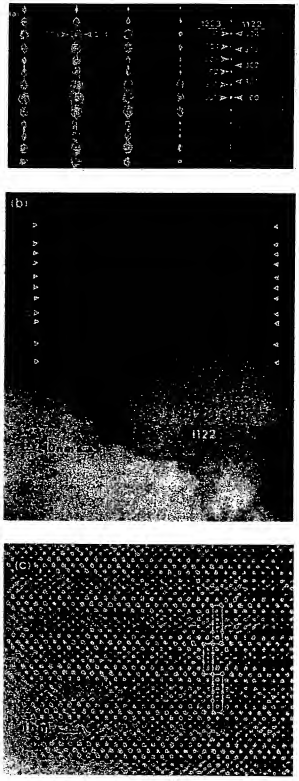

FIG. 3. (a) [010] selected area diffraction (SAD) pattern and (b) corresponding image of crystallites containing regions of 1:2:2:3 and 1:1:2:2. The arrows in (b) denote unit-cell thick intergrowths of 1:1:2:2 in 1:2:2:3. (c) High-resolution transmission electron micrograph of one unit-cell thick 1:1:2:2 intergrowth in 1:2:2:3.

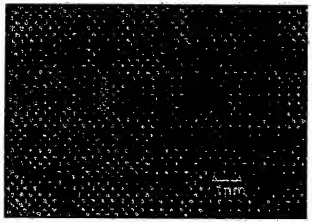

FIG. 5. High-resolution TEM image of an isolated four-CuO_2-layer intergrowth. The markers denote the positions of the Cu columns.

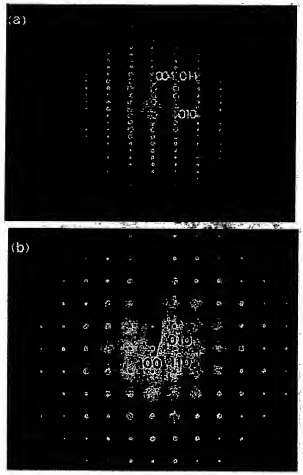

FIG. 7. (a) [100] and (b) [001] selected area diffraction patterns from crystallites of 1:1:2:2 showing superlattice reflections.

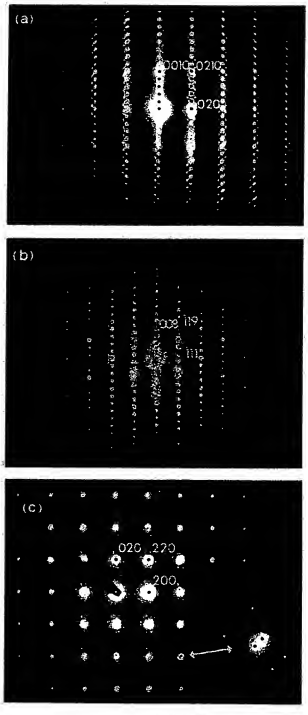

FIG. 8. (a) [100], (b) [110], and (c) [001] selected area diffraction patterns from a crystallite of 2:0:2:1.

BRIEF ATTACHMENT K

IN THE UNITED STATES PATENT AND TRADEMARK OFFICE

In re Patent Application of
Applicants: Bednorz et al.
Serial No.: 08/479,810
Filed: June 7, 1995

Date: March 1, 2005
Docket: YO987-074BZ
Group Art Unit: 1751
Examiner: M. Kopec

For: NEW SUPERCONDUCTIVE COMPOUNDS HAVING HIGH TRANSITION TEMPERATURE, METHODS FOR THEIR USE AND PREPARATION

Commissioner for Patents
P.O. Box 1450
Alexandria, VA 22313-1450

FIRST SUPPLEMENTAL AMENDMENT

Sir:

In response to the Office Action dated July 28, 2004, please consider the following:

ATTACHMENT K

JAPANESE JOURNAL OF APPLIED PHYSICS
VOL. 27, NO. 2, FEBRUARY, 1988, pp. L209–L210

A New High-T_c Oxide Superconductor without a Rare Earth Element

Hiroshi MAEDA, Yoshiaki TANAKA, Masao FUKUTOMI and Toshihisa ASANO

National Research Institute for Metals, Tsukuba Laboratories, Ibaraki 305

(Received January 22, 1988; accepted for publication January 23, 1988)

We have discovered a new high-T_c oxide superconductor of the Bi–Sr–Ca–Cu–O system without any rare earth element. The oxide $BiSrCaCu_2O_x$ has T_c of about 105 K, higher than that of $YBa_2Cu_3O_7$ by more than 10 K. In this oxide, the coexistence of Sr and Ca is necessary to obtain high T_c.

KEYWORDS: oxide superconductor, Bi–Sr–Ca–Cu–O system, rare earth, high T_c, new stable superconductor

Soon after the discovery of high-T_c superconductors of the layered perovskites $(LaBa)_2CuO_4$[1] and $(LaSr)_2CuO_4$[2] with T_c of about 40 K, $YBa_2Cu_3O_7$[3] with T_c of 94 K was synthesized. The discovery of these materials stimulated many researchers to investigate new oxide superconductors of still higher T_c and extensive studies have been carried out to search for these oxides. Up to now, however, no new stable superconductors with T_c higher than that of $YBa_2Cu_3O_7$ have been reported. The values of T_c have not improved by the substitution of other rare earth elements for yttrium.

In order to find high-T_c superconductors, we believe that it is important to investigate other classes of oxides which do not include rare earth elements. This led us to study the superconducting oxide system including the Vb-element group such as Bi and Sb of trivalent elements, and we discovered a new high-T_c superconducting material $BiSrCaCu_2O_x$. This oxide has T_c of about 105 K, being higher than that of $YBa_2Cu_3O_7$ by more than 10 K.

The value of T_c in the Bi–Sr–Cu–O oxide system which does not include Ca is very low being about 8 K.[4,5] In order to obtain high T_c, the coexistance of Sr and Ca in the Bi oxide system is found to be absolutely necessary.

The Bi–Sr–Ca–Cu–O oxide samples were prepared from powder reagents of Bi_2O_3, $SrCO_3$, $CaCO_3$ and CuO. The appropriate amounts of powders were mixed, calcined at 800–870°C for 5 h, thoroughly reground and then cold-pressed into disk-shape pellets (20 mm in diameter and 2 mm in thickness) at a pressure of 2 ton/cm^2. Most of the pellets were sintered at about 870°C in air or in an oxygen atmosphere and then furnace-cooled to room temperature.

The electrical resistivity was measured by the standard four-probe method for a bar-shaped specimen of about $1\times2\times20$ mm^3 cut out from the pellets. Magnetization measurements were carried out with a vibrating sample magnetometer. The temperature was measured by Au7%Fe-Chromel thermocouples. Figure 1 shows the resistivity vs temperatue curves of $BiSrCaCu_2O_x$ oxides thus prepared. Specimen (a) was sintered at a relatively low temperature of 800°C for 8 h while specimen (b) was sintered at a higher temperature of 882°C for 20 min followed by annealing at 872°C for 9 h. In the case of the lower sintering temperatue, the onset temperature (T_c^{on}) of the superconducting transition is about 83 K and the zero resistance state (T_c^{off}) is reached at 75 K (low-T_c phase). On the other hand, in the case of a higher sintering temperature, a high-T_c phase appears, the onset temperature of which is about 120 K and T_c extraporated to zero resistance is as high as 105 K. The value of T_c^{off} is higher than that of $YBa_2Cu_3O_7$ by more than 10 K. Since a little amount of the low-T_c phase still remained in the sample, a complete zero resistance state is achieved at 75 K which corresponds to that of the low-T_c phase. We have not succeeded in synthesizing the oxides with a single phase of the high-T_c material at this moment. From our preliminary experiments, we know that sintering at high temperatures for a short duration of time is effective enough to increase the relative amount of the high-T_c phase. This may indicate that the high-T_c phase is stable at elevated temperatures.

Figure 2 shows the magnetization vs temperature curve for the specimen (b) in Fig. 1 which was sintered at the higher temperatures. A Meissner effect showing a perfect diamagnetic state is observed exactly in the same temperature range as in curve (a) shown in Fig. 1. We conclude, therefore, that the present high-T_c phase is indeed superconducting.

The high-T_c phase appears near the composition ratios of Bi:Sr:Ca=1:1:1. As the composition deviates from

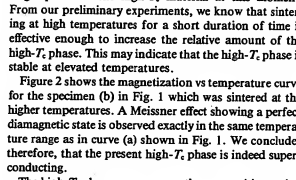

Fig. 1. Temperature dependence of resistivities in $Bi_1Sr_1Ca_1Cu_2O_x$ oxides (a) sintered in air at 800°C for 8 h, then cooled in a furnace and (b) sintered at 882°C for 20 min followed by annealing at 872°C for 9 h.

JAPANESE JOURNAL OF APPLIED PHYSICS
VOL. 27, NO. 2, FEBRUARY, 1988, pp. L209–L210

A New High-T_c Oxide Superconductor without a Rare Earth Element

Hiroshi MAEDA, Yoshiaki TANAKA, Masao FUKUTOMI and Toshihisa ASANO

National Research Institute for Metals, Tsukuba Laboratories, Ibaraki 305

(Received January 22, 1988; accepted for publication January 23, 1988)

We have discovered a new high-T_c oxide superconductor of the Bi–Sr–Ca–Cu–O system without any rare earth element. The oxide $BiSrCaCu_2O_x$ has T_c of about 105 K, higher than that of $YBa_2Cu_3O_7$ by more than 10 K. In this oxide, the coexistence of Sr and Ca is necessary to obtain high T_c.

KEYWORDS: oxide superconductor, Bi–Sr–Ca–Cu–O system, rare earth, high T_c, new stable superconductor

Soon after the discovery of high-T_c superconductors of the layered perovskites $(LaBa)_2CuO_4$[1] and $(LaSr)_2CuO_4$[2] with T_c of about 40 K, $YBa_2Cu_3O_7$[3] with T_c of 94 K was synthesized. The discovery of these materials stimulated many researchers to investigate new oxide superconductors of still higher T_c and extensive studies have been carried out to search for these oxides. Up to now, however, no new stable superconductors with T_c higher than that of $YBa_2Cu_3O_7$ have been reported. The values of T_c have not improved by the substitution of other rare earth elements for yttrium.

In order to find high-T_c superconductors, we believe that it is important to investigate other classes of oxides which do not include rare earth elements. This led us to study the superconducting oxide system including the Vb-element group such as Bi and Sb of trivalent elements, and we discovered a new high-T_c superconducting material $BiSrCaCu_2O_x$. This oxide has T_c of about 105 K, being higher than that of $YBa_2Cu_3O_7$ by more than 10 K.

The value of T_c in the Bi–Sr–Cu–O oxide system which does not include Ca is very low being about 8 K.[4,5] In order to obtain high T_c, the coexistance of Sr and Ca in the Bi oxide system is found to be absolutely necessary.

The Bi–Sr–Ca–Cu–O oxide samples were prepared from powder reagents of Bi_2O_3, $SrCO_3$, $CaCO_3$ and CuO. The appropriate amounts of powders were mixed, calcined at 800–870°C for 5 h, thoroughly reground and then cold-pressed into disk-shape pellets (20 mm in diameter and 2 mm in thickness) at a pressure of 2 ton/cm^2. Most of the pellets were sintered at about 870°C in air or in an oxygen atmosphere and then furnace-cooled to room temperature.

The electrical resistivity was measured by the standard four-probe method for a bar-shaped specimen of about $1 \times 2 \times 20$ mm^3 cut out from the pellets. Magnetization measurements were carried out with a vibrating sample magnetometer. The temperature was measured by Au7%Fe-Chromel thermocouples. Figure 1 shows the resistivity vs temperatue curves of $BiSrCaCu_2O_x$ oxides thus prepared. Specimen (a) was sintered at a relatively low temperature of 800°C for 8 h while specimen (b) was sintered at a higher temperature of 882°C for 20 min followed by annealing at 872°C for 9 h. In the case of the lower sintering temperatue, the onset temperature (T_c^{on}) of the superconducting transition is about 83 K and the zero resistance state (T_c^{eff}) is reached at 75 K (low-T_c phase). On the other hand, in the case of a higher sintering temperature, a high-T_c phase appears, the onset temperature of which is about 120 K and T_c extraporated to zero resistance is as high as 105 K. The value of T_c^{eff} is higher than that of $YBa_2Cu_3O_7$ by more than 10 K. Since a little amount of the low-T_c phase still remained in the sample, a complete zero resistance state is achieved at 75 K which corresponds to that of the low-T_c phase. We have not succeeded in synthesizing the oxides with a single phase of the high-T_c material at this moment. From our preliminary experiments, we know that sintering at high temperatures for a short duration of time is effective enough to increase the relative amount of the high-T_c phase. This may indicate that the high-T_c phase is stable at elevated temperatures.

Figure 2 shows the magnetization vs temperature curve for the specimen (b) in Fig. 1 which was sintered at the higher temperatures. A Meissner effect showing a perfect diamagnetic state is observed exactly in the same temperature range as in curve (a) shown in Fig. 1. We conclude, therefore, that the present high-T_c phase is indeed superconducting.

The high-T_c phase appears near the composition ratios of Bi:Sr:Ca=1:1:1. As the composition deviates from

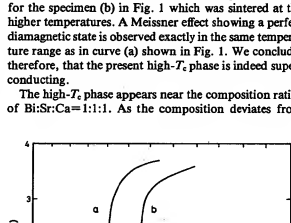

Fig. 1. Temperature dependence of resistivities in $Bi_1Sr_1Ca_1Cu_2O_x$ oxides (a) sintered in air at 800°C for 8 h, then cooled in a furnace and (b) sintered at 882°C for 20 min followed by annealing at 872°C for 9 h.

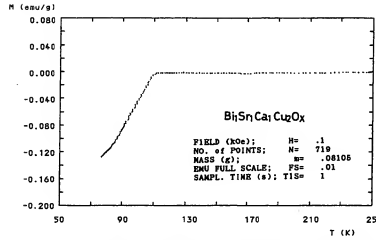

Fig. 2. Magnetization of $Bi_1Sr_1Ca_1Cu_2O_x$ for the sample (b) in Fig. 1 in a field of 100 Oe.

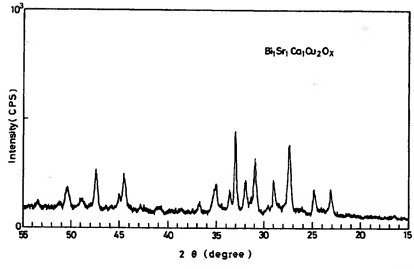

Fig. 3. X-ray (Cu kα) diffraction pattern of the $Bi_1Sr_1Ca_1Cu_2O_x$ oxide superconductor for the sample (b) in Fig. 1.

this ratio, a low-T_c phase tends to appear irrespective of the sintering conditions. In $BiSrCaCu_yO_z$ oxides, the oxide of $y=1$ is not superconducting. According to the results of the X-ray diffraction analyses, the starting material corresponding to the composition of $Bi_1Sr_1Ca_1Cu_2O_x$ seems to form a single phase. While in the nominal composition of oxides with $y>2$, unreacted CuO remained in the sample. A typical X-ray diffraction pattern for the oxide of $y=2$ (sample (b) in Fig. 1) is shown in Fig. 3. Although the structure of this oxide is not identified yet, it appears to be different from those of $(LaSr)_2CuO_4$ and $YBa_2Cu_3O_7$.

This material having high T_c above 105 K may have potential application in various industrial fields in the near future. It should be noted that these oxides are extremely stable in water and moisture and that no change in the superconducting properties has been observed even after the thermal cyclings between 4 K and room temperature or above.

Furthermore, the oxide has two phases with different T_c and their structures seem to be different from those of high-T_c oxide superconductors discovered up to now. We believe that this new oxide will contribute greatly to elucidating the high-T_c superconducting mechanism.

Acknowledgements

We would like to thank Dr. M. Uehara for the measurements of magnetization and Dr. K. Ogawa for his useful discussions.

References

1) J. G. Bednorz and K. A. Müller: Z. Phys. B64 (1986) 189.
2) S. Uchida, H. Takagi, K. Kitazawa and S. Tanaka: Jpn. J. Appl. Phys. 26 (1987) L1.
3) M. K. Wu, J. R. Ashburn, C. J. Torng, P. H. Hor, R. L. Meng, L. Gao, Z. J. Haang, Y. Q. Wang and C. W. Chu: Phys. Rev. Lett. 58 (1987) 908.
4) J. Akimitsu, A. Yamazaki, H. Sawa and H. Fujiki: Jpn. J. Appl. Phys. 26 (1987) L2080.
5) C. Michel, M. Hervieu, M. M. Borel, A. Grandin, F. Deslandes, J. Provost and B. Raveau: Z. Phys. B68 (1987) 421.

BRIEF ATTACHMENT L

IN THE UNITED STATES PATENT AND TRADEMARK OFFICE

In re Patent Application of
Applicants: Bednorz et al.
Serial No.: 08/479,810
Filed: June 7, 1995

Date: March 1, 2005
Docket: YO987-074BZ
Group Art Unit: 1751
Examiner: M. Kopec

For: NEW SUPERCONDUCTIVE COMPOUNDS HAVING HIGH TRANSITION TEMPERATURE, METHODS FOR THEIR USE AND PREPARATION

Commissioner for Patents
P.O. Box 1450
Alexandria, VA 22313-1450

FIRST SUPPLEMENTAL AMENDMENT

Sir:

In response to the Office Action dated July 28, 2004, please consider the following:

ATTACHMENT L

The resulting map (Fig. 1e) shows that the absorption feature has a mean W of 0.2 nm and stretches from roughly north to south across the entire emission line region, corresponding to a length of >30 kpc (the map presents only the area with good signal-to-noise ratio). Its spatial width is rather uncertain, because it is unresolved in the east-west direction (<1.5"). It cannot be narrower than 0.5" because otherwise even a 100% obscuration would be washed out by our beam into a relative depression of <25% (0.25 nm). So we assume a projected size of 10×10 kpc^2 for the absorber, with a deconvoluted equivalent width of about 0.5 nm.

Such an absorber can either consist of one or more clouds located well in front of 4C41.17 (if the blueshift of the absorption is cosmological, the absorber sits at a comoving distance of 5 Mpc). On the other hand, the velocity in the EELR itself is large enough to cover this blueshift, otherwise we would be unable to detect the feature. Thus, a dense, partially ionized cloud at the edge of 4C41.17 could equally explain the absorption. In this latter case more detailed observations are necessary for a physical interpretation. We therefore would like to pursue the former possibility of a physically separated absorber. Such clouds—commonly known as Lyman-forest clouds—and their properties have been extensively studied in the absorption line spectra of high redshift quasars.

For comparison we make use of a spectrum[14] of the quasar Q0000-263 ($z=4.11$), the Lyman-forest of which covers the λ range of our observation. We smoothed the original spectrum (resolution, 0.1 nm) to our instrumental resolution of 1.0 nm. The comparison between smoothed and original spectrum reveals that any absorption feature as deep as that observed in 4C41.17 typically consists of two or more narrower absorption lines. We have to realize therefore, that our 'absorption cloud' is likely to be a superposition of several individual Lyman-forest clouds. Nevertheless, we believe that the outline of the absorber in the W map (Fig. 1e) is most likely to be determined by one single cloud which made the feature strong enough to become detectable, and we assign half of the measured equivalent width (0.25 nm) to this cloud. Assuming a Doppler parameter $b=35$ km s^{-1} and $N_{\rm H_I}/N_{\rm H_{tot}}=10^{-4}$ as typical for Lyman clouds of that depth (refs 1, 3), we find a column density $N_{\rm H_I}\sim10^{15}$ cm^{-2}. A cigar-shaped cloud of 40 kpc length and 10 kpc diameter would contain a total hydrogen mass of $\sim3\times10^7\,M_\odot$.

What is the probability of detecting such an absorption feature in front of 4C41.17? Both the smoothed spectrum of Q0000-263 (ref. 14) and the standard $dN(W,z)/dz$ relation[14] yield ~25 features with $W>0.4$ nm on each line of sight and within one z unit at the observed wavelength. Considering the 'useful' wavelength range of ~1.2 nm (the blue half of the width of the emission line) in our search for line features, and the area of the EELR inspected of ~20 arcsec^2, the probability of detecting a cloud of a typical size of a few arcsec^2 is close to 1.

In conclusion, we believe that we have succeeded in obtaining the first direct observation of a Lyman absorption cloud. Either this cloud belongs directly to the mass concentration around 4C41.17 or it is a physically separated foreground object. In the latter case it would represent the population of Lyman-forest clouds known from the absorption spectra of quasars. In either case, our observations indicate that the relevant absorbers have projected sizes of some 100 kpc^2 and an elongated shape, like a cigar or a sheet seen almost edge-on in the case of 4C41.17. □

Received 23 September 1992; accepted 19 January 1993.

1. Chaffee, F. H., Foltz, C. B., Bechtold, J. & Weymann, R. J. *Astrophys. J.* **301**, 116–123 (1986).
2. Cantwell, B. F., Webb, J. K., Baldwin, J. A. & Atwood, B. *Astrophys. J.* **313**, 709–722 (1987).
3. Rauch, M. *et al. Astrophys. J.* **390**, 387–404 (1992).
4. Foltz, C. B., Weymann, R. J., Röser, H. J. & Chaffee, F. H. *Astrophys. J.* **281**, L1–L4 (1984).
5. Smette, A. *et al. Astrophys. J.* **389**, 39–52 (1992).
6. Tytler, D. *Astrophys. J.* **321**, 69–79 (1987).
7. Petitjean, M., Mücket, J. P. W., Kates, L. J. & Mar, D. P. *Mon. Not. R. astr. Soc.* **248**, 545–564 (1990).
8. Beauchi, S. in *Dark Matter in the Universe* (eds Sato, H. & Kotama, H.) 50–62 (Springer, Berlin, 1990).
9. Spinrad, H. in *Epoch of Galaxy Formation* (eds Frenk, C. S. *et al.*) 39–56 (Kluwer, Dordrecht, 1988).
10. Lilly, S. *Astrophys. J.* **333**, 161–167 (1988).
11. Chambers, K. C., Miley, G. K. & van Breugel, W. *Astrophys. J.* **363**, 21–39 (1990).
12. Meisenheimer, K. & Hippelein, H. *Astr. Astrophys.* **264**, 455–471 (1992).
13. Röser, S. & Bastian, U. *PPM Star Catalogue* (Spektrum Akad., Heidelberg, 1991).
14. Webb, J. K. *et al. ESO Messenger* **51**, 15–18 (1988).
15. Murdoch, H. S., Hunstead, R. W., Pettini, M. & Blades, J. C. *Astrophys. J.* **309**, 19–32 (1986).

ACKNOWLEDGEMENTS. We thank R. Carswell for the spectrum of Q0000-236 and H. Röser for discussions.

Superconductivity at 94 K in $HgBa_2CuO_{4+\delta}$

S. N. Putilin*†, E. V. Antipov*, O. Chmaissem† & M. Marezio†‡

* Chemical Department, Moscow State University, 119899 Moscow, Russia
† Laboratoire de Cristallographie CNRS-LUF, BP 166, 38042 Grenoble Cedex 09, France
‡ AT&T Bell Laboratories, Murray Hill, New Jersey 07974, USA

FOLLOWING the discovery[1] of high-transition-temperature (high-T_c) superconductivity in doped La_2CuO_4, several families of related compounds have been discovered which have layers of CuO_2 as the essential requirement for superconductivity: the highest transition temperatures so far have been found for thallium-bearing compounds[2]. Recently the mercury-bearing compound $HgBa_2RCu_2O_{6+\delta}$ (Hg-1212) was synthesized[3] (where R is a rare-earth element), with a structure similar to the thallium-bearing superconductor $TlBa_2CaCu_2O_7$ (Tl-1212), which has one TlO layer and two CuO_2 layers per unit cell, and a T_c of 85 K (ref. 2). But in spite of its resemblance to Tl-1212, Hg-1212 was found not to be superconducting. Here we report the synthesis of the related compound $HgBa_2CuO_{4+\delta}$ (Hg-1201), with only one CuO_2 layer per unit cell, and show that it is superconducting below 94 K. Its structure is similar to that of Tl-1201 (which has a T_c of <10 K)[4], but its transition temperature is considerably higher. The availability of a material with high T_c but only a single metal oxide (HgO) layer may be important for technological applications, as it seems that a smaller spacing between CuO_2 planes leads to better superconducting properties in a magnetic field[5].

The samples were prepared by solid state reaction between stoichiometric mixtures of $Ba_2CuO_{3+\delta}$ and yellow HgO (98% purity, Aldrich). The precursor $Ba_2CuO_{3+\delta}$ was obtained by the same type of reaction between BaO_2 (95% purity, Aldrich) and CuO (NormaPur, Prolabo) at 930 °C in oxygen, according to the procedure described by De Leeuw *et al.*[6]. The powders were ground in an agate mortar and placed in silica tubes. All these operations were carried out in a dry box. After evacuation, the tubes were sealed, placed in steel containers, as described in ref. 3, and heated for 5 h to reach ~800 °C. The samples were then cooled in the furnace, reaching room temperature after ~10 h.

The formation of the new phase $HgBa_2CuO_{4+\delta}$ was revealed by X-ray powder analysis, performed with a Guinier-Hägg focusing camera and Fe Kα radiation (1.93730 Å). Finely powdered silicon ($a=5.4308$ Å at 25 °C) was used as an internal standard. The intensities of the reflections were evaluated by means of an automatic film scanner and indexed on a tetragonal cell with lattice parameters $a=3.8797$ (5) Å, $c=9.509$ (2) Å and assignment $Z=1$. No systematic absences were observed, leading to the number of molecules per unit cell of the space group $P4/mmm$. The c parameter corresponded to the value calculated from the formula $c=9.5+3.2(n-1)$, similar to that deduced for the $TlBa_2R_{n-1}Cu_nO_{2n+3}$ homologous series. We took this as a strong indication that the powder pattern corresponded to that of the first member of the $HgBa_2R_{n-1}Cu_nO_{2n+2+\delta}$ series.

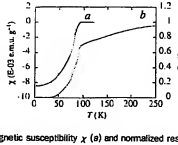

FIG. 1 AC magnetic susceptibility χ (*a*) and normalized resistivity (*b*) as a function of temperature for $HgBa_2CuO_{4+\delta}$.

Scanning electron microscopy using a JEOL SM 840A equipped with an energy-dispersive spectroscopy (EDS) attachment revealed that the sample was well crystallized with particle sizes of several micrometres. EDS analysis of several well crystallized, flat and oriented grains was performed. Beside Hg, Ba, Cu and O, no other element was detected in the spectra. The average metal ratio found for eight grains was Hg:Ba:Cu = 28(1):47(2):25(1), where the numbers between parentheses are the standard deviations. Determination of the oxygen content by EDS analysis was not possible, so it was estimated by structural analysis and iodometric titration. The cation stoichiometry is in qualitatively good agreement with the proposed formula of the new compound.

Alternating-current magnetic susceptibility measurements between 4.2 and 120 K, done without any additional oxygen treatment, showed that $HgBa_2CuO_{4+\delta}$ samples undergo a transition from paramagnetic to diamagnetic with an onset as high as 94 K (Fig. 1*a*, where the susceptibility is in electromagnetic units g^{-1}). The estimated magnetic susceptibility at 4.2 K corresponds to >50% of the ideal diamagnetic values.

The resistivity was measured between 4.2 and 250 K by the four-probe technique. The sample was a pressed pellet which was annealed in oxygen for 2 h. The temperature dependence of the normalized resistivity, shown in Fig. 1, exhibits a sharp drop at T_c, but the transition is broad and it reaches the value of zero resistance only at 35 K. This behaviour indicates that the sample is not homogeneous.

To determine the structure of $HgBa_2CuO_{4+\delta}$, X-ray powder data were collected by a $\theta/2\theta$ STADI P diffractometer in transmission mode. The experimental conditions were as follows: 2θ range =6–115° (0.02° steps) with fixed counting time 60 s and a rotating sample. An absorption correction was applied and the sample thickness was calculated from the primary beam absorption ($\mu R = 1.7$, where μ is absorption coefficient and R is thickness). The structural refinements were done by the Rietveld method. The initial positional parameters were deduced from a structural model containing the sequence (Hg)(BaO)-(CuO_2)(BaO)(Hg). After convergence (intensity discrepancy factor, $R_I = 0.039$), a Fourier difference map revealed that the position at $(\frac{1}{2}, \frac{1}{2}, 0)$ of the Hg layer was partially occupied. During the final cycle of refinement, the occupancy factor of a third oxygen atom placed in this position was varied together with the positional and thermal parameters for all atoms (except for the thermal parameter of O(3) which was kept fixed at 1.0 Å^2). The final intensity (R_I) and profile (R_p) discrepancy factors based on 84 reflections were $R_I = 0.0367$ and $R_p = 0.116$, with a GOF (goodness of fit) = 0.33.

The final positional and thermal parameters together with the relevant interatomic distances are given in Table 1. Observed, calculated and difference diffraction patterns are shown in Fig. 2. A schematic representation of the structure is shown in Fig. 3. Preliminary structural refinements based on powder neutron diffraction data support the presence of oxygen in the O(3) position with an occupancy factor slightly larger than that found by X-ray powder diffraction data. The neutron data also confirm the large value for the mercury thermal factors. As in the case of the X-ray data, the anisotropic model shows a very slight difference between $B_{11} = B_{22}$ and B_{33}, the thermal factors along x, y and z respectively.

TABLE 1 Crystallographic data for $HgBa_2CuO_{4+\delta}$

Positional, thermal and occupancy parameters

Atom	Position	x	y	z	B_{eq} (Å^2)	Occupancy
Hg	1a	0	0	0	2.55 (5)	1.00
Ba	2h	0.5	0.5	0.2979 (1)	1.43 (4)	1.00
Cu	1b	0	0	0.5	0.88 (9)	1.00
O(1)	2e	0.5	0	0.5	0.4 (3)	1.00
O(2)	2g	0	0	0.206 (2)	2.2 (3)	1.00
O(3)	1c	0.5	0.5	0	1.0	0.10 (3)

Selected interatomic distances (Å)

Hg–O(2) (×2)	1.85 (2)	Cu–O(1) (×4)	1.9401(1)	Ba–O(1) (×4)	2.7305(1)
Hg–O(3)*	2.742(1)	Cu–O(2) (×2)	2.79(2)	Ba–O(2) (×4)	2.889(5)
				Ba–O(3)*	2.831(1)

Data obtained using monochromatized CuKα_1 radiation ($\lambda = 1.54056$ Å) giving $a = 3.87766(4)$ Å, $c = 9.5073(1)$ Å.
* Partially occupied sites.

$HgBa_2CuO_{4+\delta}$ has a structure related to that of Hg-1212 (ref. 3). Its lattice parameters correspond to four-layered packing along the c-axis of a unit cell: $a = a_{per.}$, $c = 2a_{per.}$ (where $a_{per.}$ is the parameter of the perovskite subcell) and its structure contains the sequence $(CuO_2)(BaO)(HgO_\delta)(BaO)(CuO_2)$. The Cu cations are octahedrally coordinated, while the coordination of the other cations depends upon the value of δ. This, as obtained from powder X-ray data, is 0.10(3). An important consequence is that most of the Hg cations have two oxygen atoms near them in a 'dumb-bell' configuration, an appropriate coordination for Hg^{2+} cations. Because δ is small and different from zero (within about three standard deviations) X-ray powder data alone are insufficient to determine which sites of the rock-salt positions in the HgO layer are occupied and how they affect the Hg coordination. The extra oxygen atoms are needed in order to increase the average oxidation number of the Cu and to create the concentration of holes necessary for superconductivity. Iodometric titration performed with a large excess of KI leads to 16% of Cu^{3+}, corresponding to $\delta = 0.08$.

Similarly, the structure of $HgBa_2RCu_2O_{6+\delta}$ (the second member of the $HgBa_2R_{n-1}Cu_nO_{2n+2+\delta}$ series) can be described as six-layered blocks made of rock-salt and perovskite-type structures. In the structure of Hg-1212 the layer sequence is:

$$(BaO)(HgO_\delta)(BaO)(CuO_2)(R)(CuO_2)(BaO)(HgO_\delta)(BaO)$$

rock-salt perovskite rock-salt

The CuO_2 monolayer in Hg-1201 has been replaced by the $(CuO_2)(R)(CuO_2)$ block. As a consequence the Cu cations are

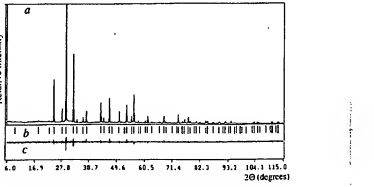

FIG. 2 Observed (*a*), calculated (*b*) and difference (*c*) powder patterns after Rietveld refinement for $HgBa_2CuO_{4+\delta}$.

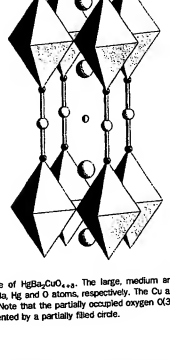

FIG. 3 Structure of $HgBa_2CuO_{4+\delta}$. The large, medium and small circles represent the Ba, Hg and O atoms, respectively. The Cu atoms are inside the octahedra. Note that the partially occupied oxygen O(3) site on the Hg layer is represented by a partially filled circle.

pyramidally coordinated. The coordination of the Ba and Hg cations in Hg-1212 is similar to that of the same cations in Hg-1201. The R cations are surrounded by 8 oxygen atoms arranged as a prism. The valence of the Cu cations depends upon the value of δ and the valence of the R cations: if the same Cu valence or hole concentration as in Hg-1201 is needed to induce the superconducting state in Hg-1212, then the R cations should be 2+ and δ_{1212} should be appreciably greater than δ_{1201}. For the previously reported Hg-1212, R was a mixture of Eu and Ca, and δ was not precisely determined[3]. It is possible that δ was not large enough to compensate for the higher valence of the R cations and to transfer the needed extra charges to CuO_2 layers.

As stated above, the structural arrangment of $HgBa_2CuO_{4+\delta}$ is similar to that of $TlBa_2CuO_{5-\delta}$, except for the oxygen stoichiometry of the HgO_δ and $TlO_{1-\delta}$ layers respectively. For the former, δ is very small and this depletion is possible because the dumb-bell coordination is appropriate for the Hg^{2+} cations. For the latter, the $TlO_{1-\delta}$ layer is only slightly oxygen depleted, creating the appropriate coordination for the thallium cations, resulting in either a distorted octahedron or a five-coordinated polyhedron. These different requirements for attaining the optimal concentration of holes are due to the different preferred coordination geometries of the Tl^{3+} and Hg^{2+} cations.

The first member of the latter series (Tl-1201) has been reported and found to become superconducting at <10 K (ref. 4). By doping the Ba sites with La this value can be increased to 52 K (ref. 7). The second member of the mono-Tl series becomes superconducting at 85 K (ref. 2). This increase is a general rule for the first few members of this series of compounds. If this behaviour holds for the Hg-series, the second member could reach values for T_c as high as those of the thallium.

The possible advantages for technical applications of $HgBa_2CuO_{4+\delta}$, in analogy with one-Tl-layer materials, would be due to the relatively short distance between CuO_2 layers. This might lead to lower anisotropy of the superconducting properties and to higher flux-melting temperatures than those of two-TlO-layer superconductors[5]. □

Received 18 December 1992; accepted 12 February 1993.

1. Bednorz, J. G. & Muller, K. A. *Z. Phys.* **B64**, 189–193 (1986).
2. Parkin, S. S. P. *et al. Phys. Rev.* **B38**, 6531–6537 (1988).
3. Putilin, S. N., Bryntse, I. & Antipov, E. V. *Mat. Res. Bull.* **26**, 1299–1307 (1991).
4. Goodenough, I. K., Yaremi, J. V. & Iyer, R. M. *Physica C* **175**, 183–186 (1991).
5. Kim, D. H. *et al. Physica C* **177**, 431–437 (1991).
6. De Leeuw, D. M., Mutsaers, C. A. H. A., Langereis, C., Smoorenburg, H. C. A. & Rommers, P. J. *Physica C* **152**, 39–49 (1988).
7. Subramanian, M. A., Kwei, G. H., Parise, J. B., Goldstone, J. A. & Von Dreele, R. B. *Physica C* **166**, 19–24 (1990).

ACKNOWLEDGEMENTS. The authors thank R. V. Shpanchenko and J. L. Tholence for their collaboration. S.N.P. thanks O. Massenet for a grant to attend the Laboratoire de Cristallographie of the CNRS, Grenoble. SNP and E.V.A are supported by grants from the Project "Polak" of the Russian Scientific Council on Superconductivity.

Dependence of aggregate morphology on structure of dimeric surfactants

R. Zana* & Y. Talmon

Department of Chemical Engineering, Technion-Israel Institute of Technology, Haifa 32000, Israel

SURFACTANT molecules in water form organized assemblies of various shapes, such as micelles and bilayer lamellae, which are of interest as analogues of biological structures, as model systems for studying complex phase behaviour and because of their technological importance, for example to the food and paint industries. The polar head groups are usually arranged randomly at the surface of these assemblies. We have studied the effect on the microstructure of these assemblies of imposing constraints on the head-group spacing. We investigate the structures formed by 'double-headed' surfactants in which two quaternary ammonium species $(C_nH_{2n+1}N^+(CH_3)_2)$ are linked at the level of the head groups by a hydrocarbon spacer (C_sH_{2s}). Here we report the microstructures formed by these dimeric surfactants with $n = 12$ and $s = 2$, 3 or 4 in aqueous solution, by rapidly cooling the micellar solutions and investigating the vitrified structures with transmission electron microscopy. The surfactants with a short spacer ($s = 2, 3$) form long, thread-like and entangled micelles even at low concentrations, whereas the corresponding monomeric ammonium surfactants can form only spherical micelles. The dimeric surfactants with $s = 4$ form spheroidal micelles. Thus short spacers (which impose reduced head-group separation) appear to promote lower spontaneous curvature in the assemblies. This approach may afford a new way to control amphiphile self-aggregation.

Conventional surfactant molecules generally comprise two distinct parts that are incompatible with each other: one polar head and either one or two alkyl chains. These molecules tend to self-associate in water, where they produce micellar solutions in the dilute range, and lyotropic mesophases at higher concentrations. Whatever the structure, the surfactant polar heads are located at the interface between the hydrocarbon and water regions. Their relative positions and distances are determined mainly by their electrostatic interactions, and also by the packing requirements of the disordered alkyl chains[1–3]. In caesium or rubidium soaps at low temperature in the presence of water, for example the head groups form well developed hexagonal or rectangular crystalline arrays[4]. Generally, however, they are arranged randomly, and little is known of their packing geometry or the width of their spacing distribution.

To investigate the effect of a perturbation of the local arrangement of polar heads on the micellar and mesomorphic properties

* To whom correspondence should be addressed in Haifa. On leave of absence from Institut Charles Sadron (CNRS), 6 rue Boussingault, 67083 Strasbourg Cedex, France.

BRIEF ATTACHMENT M

IN THE UNITED STATES PATENT AND TRADEMARK OFFICE

In re Patent Application of
Applicants: Bednorz et al.
Serial No.: 08/479,810
Filed: June 7, 1995

Date: March 1, 2005
Docket: YO987-074BZ
Group Art Unit: 1751
Examiner: M. Kopec

For: NEW SUPERCONDUCTIVE COMPOUNDS HAVING HIGH TRANSITION TEMPERATURE, METHODS FOR THEIR USE AND PREPARATION

Commissioner for Patents
P.O. Box 1450
Alexandria, VA 22313-1450

FIRST SUPPLEMENTAL AMENDMENT

Sir:

In response to the Office Action dated July 28, 2004, please consider the following:

ATTACHMENT M

Superconductivity near 70 K in a new family of layered copper oxides

R. J. Cava, B. Batlogg, J. J. Krajewski, L. W. Rupp, L. F. Schneemeyer, T. Siegrist, R. B. vanDover, P. Marsh, W. F. Peck, Jr, P. K. Gallagher, S. H. Glarum, J. H. Marshall, R. C. Farrow, J. V. Waszczak, R. Hull & P. Trevor

AT&T Bell Laboratories, Murray Hill, New Jersey 07974, USA

A new family of high-temperature superconductors is described, with the general formula $Pb_2Sr_2ACu_3O_{8+\delta}$. Although they have the planes of CuO_5 square pyramids characteristic of the other copper-oxide superconductors, the new compounds belong to a distinct structural series, with wide scope for elemental substitution. Their unusual electronic configuration also gives new insight into the role of charge distribution among the structural building blocks in controlling superconductivity.

SINCE the first observation[1] of high-transition-temperature (high-T_c) superconductivity in La–Ba–Cu–O, progress in the understanding of this remarkable phenomenon has been coupled to the discovery of new materials. Until now, three families of copper-oxide-based high-T_c superconductors have been identified, based on $(La,M)_2CuO_4$, $LnBa_2Cu_3O_7$, and $(Tl,Bi)_m(Ba,Sr)_2Ca_{n+1}Cu_nO_{m+2n+2}$ (ref. 2). (Here M represents a metal cation that may substitute on some La sites, and Ln represents a lanthanide.) Here we report the discovery of a new family of planar copper-oxide superconductors with general formula $Pb_2Sr_2ACu_3O_{8+\delta}$ (where A is a lanthanide or a mixture of Ln + Sr or Ca), and describe the synthesis, crystal structure and properties of prototype compounds. We find, for example, that one preliminary optimal composition $Pb_2Sr_2Y_{0.5}Ca_{0.5}Cu_3O_8$ has a superconducting T_c of 68 K. The new family displays the same kind of rich substitutional chemistry as is observed for $LnBa_2Cu_3O_7$, with the phase forming for Y and at least La, Pr, Nd, Sm, Eu, Gd, Dy, Ho, Tm, Yb and Lu, spanning the entire rare-earth series. Wide ranges of large-metal-atom solid solution and oxygen stoichiometry are observed, suggesting many possible avenues to be explored for the optimization of superconducting properties.

Superconductivity is induced in the host compounds $Pb_2Sr_2LnCu_3O_{8+\delta}$ ($\delta = 0$) either by partial substitution of a divalent ion (such as Sr or Ca) on the lanthanide site, or possibly by the accommodation of excess oxygen ($\delta > 0$), or a combination of both. The compounds can be synthesized only under mildly reducing conditions, which are necessary to maintain Pb in a 2+ oxidation state. Oxidation of $\delta = 0$ compounds is possible, but only at low temperatures, where decomposition to a Pb(IV)-containing perovskite is sluggish. Remarkably, the formal average oxidation state of copper in the superconductors is less than 2+, but a clear structural distinction between different types of copper layers leads us to hypothesize that holes are nonetheless present on electronically active CuO pyramidal planes.

Synthesis

The preparative conditions for the new materials are considerably more stringent than for the previously known copper-based superconductors. Direct synthesis of members of this family by reaction of the component metal oxides or carbonates in air or oxygen at temperatures below 900 °C is not possible because of the stability of the oxidized $SrPbO_3$-based perovskite. Successful synthesis is accomplished by the reaction of PbO with pre-reacted (Sr, Ca, Ln) oxide precursors. The precursors are prepared from oxides and carbonates in the appropriate metal ratios, calcined for 16 hours (in dense Al_2O_3 crucibles) at 920–980 °C in air with one intermediate grinding. Some of the $Pb_2Sr_2LnCu_3O_{8+\delta}$ compounds can be prepared in air from PbO + $LnSr_2Cu_2O_x$ precursor mixtures, which are not reacted at temperatures below ~850 °C. For example, single-phase $Pb_2Sr_2YCu_3O_{8+\delta}$ ($\delta = 0$) can be prepared by reacting PbO with $YSr_2Cu_2O_x$ at 920 °C for 1 h, followed by quenching. Slower cooling results in partial decomposition through oxidation. Short reaction times are generally sufficient to obtain single-phase products. The same air-heating/quenching process does not appear to work, however, for $Pb_2Sr_2LaCu_3O_{8+\delta}$ or $Pb_2Sr_2LuCu_3O_{8+\delta}$.

The best synthetic conditions found so far involve the reaction of PbO with the cuprate precursors in thoroughly mixed pressed pellets. Reaction temperatures are between 860 and 925 °C, for times between 1–16 h, in a flowing gas stream of 1% O_2 in N_2, a mildly reducing atmosphere. For $Pb_2Sr_2Y_{1-x}Ca_xCu_3O_{8+\delta}$, for example, single-phase materials are obtained for $0 \leq x < 0.5$ in 1% O_2 after heating overnight at 865 °C and cooling in the gas stream to room temperature in 15 minutes. Using higher temperatures, higher p_{O_2} in the gas stream or higher Ca contents of the starting mixture results in the intergrowth of 123-type $YSr_2(Pb,Cu)_3O_x$ with the new compound, or the formation of an $SrPbO_3$-based second phase. Similar procedures are successful for other Sr/rare-earth/Ca combinations. The oxygen contents of $Pb_2Sr_2Y_{1-x}Ca_xCu_3O_{8+\delta}$ for $0 \leq x \leq 0.50$, prepared under these conditions, are measured by reduction in H_2 and are uniformly $\delta = 0 \pm 0.1$. Ca is employed as a dopant on the Ln site because it has an ionic size similar to the intermediate rare-earths. We have not yet found synthetic conditions under which $Pb_2Sr_{2-x}Ln_{1-x}Cu_3O_{8+\delta}$ solid solutions can be prepared as single-phase polycrystalline samples that are good bulk superconductors, although superconducting single crystals of that stoichiometry have been prepared.

Single crystals of the superconducting compounds were grown from PbO- and CuO-rich melts using a similar precursor technique. Melt compositions were generally $Pb_{2.5}Sr_5YCu_8O_x$. Following a 30-min soak at 1,025 °C, samples were cooled at 2 °C min^{-1} in the 1% O_2 atmosphere to temperatures between 800 and 400 °C, and were then rapidly cooled to room temperature in the same gas stream. Crystals are plate-like in habit, but are generally more equiaxed than those of $LnBa_2Cu_3O_7$.

Stoichiometry and crystal structure

Compounds of stoichiometry $Pb_2Sr_2LnCu_3O_8$ ($\delta = 0$) are not bulk superconductors, although we often observe small amounts of superconductivity (1% or less) in materials of that stoichiometry prepared either by the quench or by the 1%-O_2 synthetic techniques. The non-bulk superconductivity may be due to inhomogeneities in either oxygen content or Sr/Ln distribution.

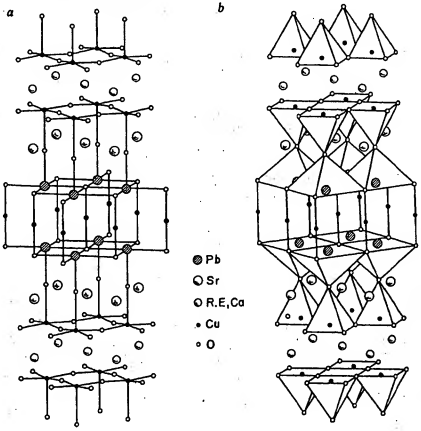

Fig. 1 Two representations of the crystal structure for the new superconducting compounds, for the case of $Pb_2Sr_{2.24}Nd_{0.76}Cu_3O_{8+\delta}$. Representation *a* emphasizes the Cu–O and Pb–O bonding scheme, and representation *b* emphasizes the manner in which Cu–O and Pb–O coordination polyhedra are arranged.

The range of oxygen contents possible for these compounds is remarkable. $Pb_2Sr_2YCu_3O_{8+\delta}$, $\delta = 0$, for example, can be oxidized by heating in O_2 to temperatures below 500 °C for short times (2–4 h) to δ values of ~1.6, retaining the same basic crystal structure. We have observed values as large as $\delta = 1.8$ for $Pb_2Sr_2Y_{0.75}Ca_{0.25}Cu_3O_{8+\delta}$. Oxidation at temperatures higher than 500 °C, or for longer reaction periods, generally results in decomposition to the $SrPbO_3$-based perovskite. Powder samples of $Pb_2Sr_2YCu_3O_{8+\delta}$ with large values of δ are not superconducting. Single crystals of the $Pb_2Sr_{2+x}La_xCu_3O_{8+\delta}$ type are superconductors with transition temperatures between 10 and 70 K. These crystals may have non-zero values of δ but have not yet been fully characterized. The range of T_cs observed suggests a complex and interesting relationship between T_c, δ and the Sr:La ratio.

Powder X-ray diffraction indicates that the new phases have an orthorhombic unit cell which is based on a many-layer perovskite structure. The characteristic X-ray pattern for the prototype compound $Pb_2Sr_2YCu_3O_8$ is presented in Table 1. The compound deviates only slightly from tetragonal symmetry. The simplest cell consistent with the X-ray pattern is *c*-centred, with lattice parameters $a \approx 5.40$, $b = 5.43$, and $c = 15.74$ Å. Systematic absences are consistent with a *c*-centred cell down to the detectability limit of 1% maximum intensity. The orthorhombic cell gives an excellent fit to the powder diffraction pattern but a hint of a shoulder on the high 2θ side of the 314 reflection indicates that the true symmetry may be weakly monoclinic. Although the lattice parameters for this family of compounds are very similar to those reported for $TlBa_2Ca_2Cu_3O_8$ (ref. 3), the crystal structures are quite different. Electron microscope investigations indicate that for some crystals, weak (but sharp) reflections are present which violate the *c*-centring. Furthermore, these studies show the presence of long-period, long-range-ordered superlattices in the *a*–*b* plane, suggesting that a variety of structural distortions and stoichiometry-driven atom-ordering schemes can occur.

The crystal structure of compounds in this family, determined for a superconducting Nd-based single crystal of approximate stoichiometry $Pb_2Sr_{2.24}Nd_{0.76}Cu_3O_{8+\delta}$ (determined by structure refinement) is shown in Fig. 1. The crystal employed in the structural determination was twinned, as expected from the pseudo-tetragonal symmetry. The atomic coordinates are reported in the *c*-centred orthorhombic cell to be consistent with the powder data, but a primitive cell with *a* and *b* rotated by 45° and reduced by $\sqrt{2}$ gives an equally good description of the single-crystal data. The very small scattering cross-section of oxygen precludes determination of δ by refinement. The data are well fitted by the structural model (refinement parameter $R = 3.7\%$), but a microscopic explanation of the orthorhombic symmetry is not apparent; if the origin is primarily in the oxygen sublattice we would not be able to detect it in the X-ray structure determination.

The basis of the structure comprises infinite planes of corner-shared CuO_5 pyramids separated by eight-coordinate rare-earth atoms, as are common to all the presently known copper-based superconductors with $T_c > 50$ K. The four in-plane copper–oxygen distances are ~1.9 Å, and the distance to the apical oxygen is ~2.3 Å, both of which are very similar to those observed in $YBa_2Cu_3O_7$. The structural components unique to the new class of materials are the $PbO–CuO_4–PbO$ planes shown in the centre of the Fig. 1. For $\delta = 0$, Pb has a distorted flattened square pyramid coordination (sharing edges with adjacent pyramids), with the lone pair pointing toward the vacant sixth site of the coordination octahedron. The PbO_5 pyramids are separated by a single copper layer, which, for $\delta = 0$, is oxygen-free, and displays an O–Cu–O coordination characteristic of Cu^{1+} (Cu–O distance ~1.8 Å), as is observed in non-superconducting $YBa_2Cu_3O_6$. During the low-temperature oxidation process, oxygen is apparently accommodated in this copper layer, resulting in a large expansion of the *c* axis. The PbO_5 and CuO_5 pyramidal planes are joined by the common oxygens at their apices. The Sr atoms are coordinated to nine oxygens, as in (La,

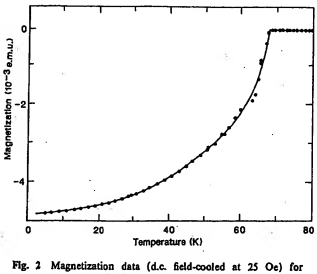

Fig. 2 Magnetization data (d.c. field-cooled at 25 Oe) for $Pb_2Sr_2Y_{0.5}Ca_{0.5}Cu_3O_8$.

Sr)CuO_4, and the Ln site is eight-coordinate, as in the $LnBa_2Cu_3O_7$ family, sandwiched between the CuO_5 pyramidal planes. In the superconducting compound $Pb_2Sr_2Y_{1-x}Ca_xCu_3O_{8+\delta}$, Ca partially substitutes for Y in the eight-coordinate site.

The crystal structures of all the known copper-oxide-based superconductors are generally described as many-layered perovskites. The similarities and differences among them are most easily illustrated in terms of the stacking sequences of rocksalt-like (AO) and perovskite-like (BO_2) layers[2]. Taking, for example, representatives from the superconductor families that have double CuO_2 pyramidal layers, the stacking sequences are:

$Pb_2Sr_2(Y, Ca)Cu_3O_{8+\delta}$
–(Y, Ca)–CuO_2–SrO–PbO–CuO_δ–PbO–SrO–CuO_2–(Y, Ca)–

$Tl_2Ba_2CaCu_2O_8$
–Ca–CuO_2–BaO–TlO–TlO–BaO–CuO_2–Ca–

$YBa_2Cu_3O_{6+\delta}$
–Y–CuO_2–BaO–CuO_δ–BaO–CuO_2–Y–

Table 1 Characteristic X-ray powder diffraction pattern for $Pb_2Sr_2YCu_3O_8$

hkl	*d*	I/I_0	*hkl*	*d*	I/I_0
001	15.74	7	116	2.164	11
002	7.87	3	025	2.057	12
003	5.25	2	205	2.050	10
004	3.94	10	008	1.967	7
110	3.831	11	220	1.915	25
111	3.722	24	118, 009	1.750	2
112	3.444	1	027, 207	1.730	1
005	3.148	11	224	1.722	2
113	3.094	11	130	1.717	2
114	2.745	100	310, 131	1.708	3
020	2.717	43	311	1.699	2
200	2.701	43	225	1.636	3
021	2.677	7	133	1.632	3
201	2.662	7	313	1.625	1
006	2.623	6	028	1.593	11
023	2.412	1	208, 119	1.591	11
203	2.401	1	134	1.574	18
024	2.236	2	314	1.568	14
204	2.227	1			

Cu Kα radiation, 0–60° 2θ *c*-centred orthorhombic cell, preliminary indexing, true symmetry may be weakly monoclinic. Lattice parameters $a = 5.4019(15)$, $b = 5.4333(15)$, $c = 15.7388(7)$ Å.

The new superconductors, then, can be seen to be intimately related in structure to those previously described. They can be considered as related to $Tl_2Ba_2CaCu_2O_8$ by insertion of a single CuO_2 layer between adjacent polarizable AO layers, or related to $YBa_2Cu_3O_{6+\delta}$ by sandwiching of the CuO_δ 'chain' layer by two PbO layers. We believe that it is the electronic screening of the CuO_2 planes from the CuO_δ layers by the PbO layers that makes the new superconductors of considerable interest. Furthermore, we expect these materials to be even more anisotropic in their physical properties than those previously known, as the double pyramidal CuO_2–A–CuO_2 layers are widely separated.

Superconducting properties

We have studied the composition dependence of the superconducting properties of compounds in the series $Pb_2Sr_2Y_{1-x}Ca_xCu_3O_8$ for $0 \le x \le 0.75$, by estimating the flux expulsion measured on cooling in a field of 25 Oe in a d.c. SQUID magnetometer (S.H.E. model 905). The greatest flux expulsion occurs for $x = 0.5$, and is ~20% of the ideal value (see Fig. 2). Because flux becomes trapped in the pores of these low-density ceramics, this is an underestimate of the true volume fraction of superconductivity. For $x \ge 0.5$, the materials were not entirely single-phase, with one or more impurity peaks having a maximum intensity of 5% of the strongest peak in the powder X-ray pattern. This, coupled with the estimate of the volume fraction of superconductivity, suggests that the optimal superconducting composition may have x somewhat greater than 0.5. This could be achieved if different synthetic methods can be found that allow a larger range of solid solution to be attained. We have measured the normal-state susceptibility (in a 20-kOe field) for temperatures below 400 K of apparently single-phase samples (no unindexed X-ray lines to 0.5% maximum intensity) of the non-superconducting endmember $Pb_2Sr_2YCu_3O_8$ and superconducting $Pb_2Sr_2Y_{0.625}Ca_{0.375}Cu_3O_8$. The susceptibility of the superconductor (χ) is essentially temperature independent ($\chi \approx 1 \times 10^{-4}$ e.m.u. per mole formula unit), with only a slight decrease at low temperatures. This temperature dependence is similar to that of high-quality $YBa_2Cu_3O_7$, and is characterized by the absence of a Curie–Weiss contribution. Furthermore, this supports our conclusion that the copper atoms between the PbO layers are Cu^{2+}. Post-oxidation at 500 °C results in oxidation of this copper to magnetic Cu^{2+}. $Pb_2Sr_2YCu_3O_8$ appears to be magnetic (~0.5 μB per Cu atom), but further studies are necessary to clarify whether this is intrinsic or is due to the presence of highly magnetic impurity phases that are undetectable by X-ray diffraction.

Figure 3 shows the temperature dependence of the resistivity for a single crystal of $Pb_2Sr_2Dy_{1-x}Ca_xCu_3O_{8+\delta}$. The midpoint of the superconducting transition is at 51.5 K (indicated by an arrow in Fig. 3), although there is a small foot which gives a zero-resistance T_c of 46 K. Above T_c the temperature

Table 2 Crystallographic data for $Pb_2Sr_{2.24}Nd_{0.76}Cu_3O_{8+\delta}$

Atom	Position	*x*	*y*	*z*	B_{iso}[Å^2]
Pb	4*i*	1/2	0	0.38858 (4)	1.09 (2)
Sr	4*k*	0	0	0.22184 (9)	0.74 (4)
Nd, Sr*	2*a*	0	0	0	0.69 (3)
Cu1	2*d*	0	0	1/2	0.86 (9)
Cu2	4*i*	1/2	0	0.11074 (13)	0.46 (5)
O1	4*i*	1/2	0	0.2546 (8)	1.5 (5)
O2	4*k*	0	0	0.384 (3)	13 (5)
O3	8*m*	1/4	1/4	0.0995 (5)	0.9 (3)

Orthorhombic cell (pseudotetragonal substructure); $a = 5.435(1)$Å, $b = 5.463(1)$Å, $c = 15.817(3)$Å; space group *Cmmm*, $z = 2$; observed reflections 707, $R_w = 0.037$.

* Mixed occupancy site: (1) Sr, 0.76(1) Nd.

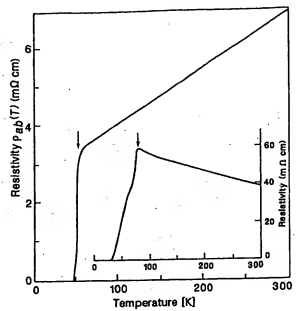

Fig. 3 Resistivity in the a–b plane as a function of temperature for a single crystal of $Pb_2Sr_2(Dy,Ca)Cu_3O_{8+\delta}$. Inset, typical temperature-dependent resistivity for a polycrystalline sample of $Pb_2Sr_2(Y,Ca)Cu_3O_8$.

dependence is fairly linear, but near T_c there is a region of positive curvature which, along with the resistivity foot, we attribute to small inhomogeneities in the metal and/or oxygen distribution. The scale of the resistivity is a factor of ten greater than for previous oxide superconductors. It is not yet clear whether this is an intrinsic property.

A typical resistivity curve for a ceramics sample is shown in the inset to Fig. 3, illustrating the typically broad transitions observed. The transition in this sample begins at 79 K (arrow) but zero resistance is achieved (within instrumental accuracy) as 32 K. Note that the resistivity scale is again quite high. We attribute the breadth of the transition and the negative normal-state temperature coefficient to inhomogeneity in the metal and/or oxygen distribution, rather than to exogenous phases at the grain boundaries. The behaviour of this system seems to be very similar to that of $(La,Sr)_2CuO_4$ (ref. 4).

Electronic aspects

Given that the average formal copper valence of previously known superconductors has always been greater than +2, the new superconductors are unique and, at first sight, anomalous. For the series $Pb_2Sr_2Y_{1-x}Ca_xCu_3O_8$, the average formal copper valence increases from 1.67 in the non-superconducting $x=0$ member to ~1.92 at the maximum Ca concentration studied. At our current estimate of the optimal superconducting composition ($x=0.5$), the average formal valence is 1.83. The linear coordination of the copper atom sandwiched between the PbO sheets, characteristic of Cu^{1+}, and the probable electronic isolation of this layer from the conducting CuO pyramidal planes, imply that the formal charge formulation becomes $Pb_2Sr_2YCu^{1+}Cu_2^{2+}O_8$ in the non-superconducting compound. When Ca is substituted for Y, we propose that holes are accommodated only in the CuO_2 planes, and at the $x=0.5$ stoichiometry the formal charge formulation becomes $Pb_2Sr_2Y_{0.5}Ca_{0.5}Cu^{1+}Cu_2^{2.25+}O_8$, which is consistent with the current assumption for previously known high-T_c materials that holes are present in the CuO_2 pyramidal planes.

For $Pb_2Sr_2ACu_3O_{8+\delta}$ compounds with $\delta>0$, excess oxygen must be accommodated near the Cu^{1+} planes, and a more complex hole-doping scheme may be operating. We expect that in that case the compound does not respond in a simple fashion to the change in charge through doping of a rigid band; the oxygen inserted in the bonding neighbourhood of the reduced Cu and Pb ions may create the electronic states in which the charge is partly or fully accommodated.

This new family of compounds has a unique crystal structure, yet it also reflects a concept common to all copper-oxide-based superconductors. By now it is well established that superconductivity is associated with layers of Cu–O octahedra, pyramids and squares. The remaining structural building blocks are seen as the electron acceptors which induce the holes necessary for superconductivity in the Cu–O layers. For $YBa_2Cu_3O_{6+\delta}$, for example, we have shown in detail how the CuO_2 chains act as charge reservoirs, and how superconductivity depends on charge transfer between chains and planes[5].

To illustrate the concept of local charge distribution, one may rewrite the formulae of the high-T_c copper-oxide superconductors as follows: $YBa_2Cu_3O_6[CuO_2]$; $Sr_2CaCu_2O_6[Bi_2O_2]$; $Ba_2CaCu_2O_6[Tl_2O_2]$; $Sr_2(Y,Ca)Cu_2O_6[Pb_2CuO_{2+\delta}]$; where the structural components in square brackets act as reservoirs which control the charge on the superconducting Cu–O planes. The PbO–CuO_δ–PbO reservoir layer is likely to be exceptionally flexible in accommodation of charge, and we therefore expect that a relationship between T_c and oxygen stoichiometry as unusual as that for $YBa_2Cu_3O_{6+\delta}$ will eventually be observed. The wide ranges of metal-atom and oxygen-atom stoichiometries in this new family of superconductors are of considerable interest, and warrant further study with the aim of understanding and optimizing the superconducting properties.

We thank D. W. Murphy and K. Rabe for helpful discussions.

Received 21 October; accepted 28 October 1988.

1. Bednorz, J. G. & Muller, K. A. *Z. Phys.* B64, 189–193 (1986).
2. Santoro, A., Beech, F., Marezio, M. & Cava, R. J. *Physica C* (in the press).
3. Parkin, S. S. P. *et al. Phys. Rev. Lett.* 61, 750–753 (1988).
4. Van Dover, R. B., Cava, R. J., Batlogg, B. & Rietman, E. A. *Phys. Rev.* B35, 5337–5339 (1987).
5. Cava, R. J. *et al. Physica C* (in the press).

BRIEF ATTACHMENT N

IN THE UNITED STATES PATENT AND TRADEMARK OFFICE

In re Patent Application of
Applicants: Bednorz et al.
Serial No.: 08/479,810
Filed: June 7, 1995

Date: March 1, 2005
Docket: YO987-074BZ
Group Art Unit: 1751
Examiner: M. Kopec

For: NEW SUPERCONDUCTIVE COMPOUNDS HAVING HIGH TRANSITION TEMPERATURE, METHODS FOR THEIR USE AND PREPARATION

Commissioner for Patents
P.O. Box 1450
Alexandria, VA 22313-1450

FIRST SUPPLEMENTAL AMENDMENT

Sir:

In response to the Office Action dated July 28, 2004, please consider the following:

ATTACHMENT N

LANDOLT-BÖRNSTEIN

Numerical Data and Functional Relationships in Science and Technology

New Series

Editor in Chief: K.-H. Hellwege

Group III: Crystal and Solid State Physics

Volume 4
Magnetic and Other Properties of Oxides and Related Compounds

Part a

J. B. Goodenough · W. Gräper · F. Holtzberg · D. L. Huber
R. A. Lefever · J. M. Longo · T. R. McGuire · S. Methfessel

Editors: K.-H. Hellwege and A. M. Hellwege

Springer-Verlag Berlin · Heidelberg · New York 1970

N

S

LANDOLT-BÖRNSTEIN

Zahlenwerte und Funktionen
aus Naturwissenschaften und Technik

Neue Serie

Gesamtherausgabe: K.-H. Hellwege

Gruppe III: Kristall- und Festkörperphysik

Band 4

Magnetische und andere Eigenschaften von Oxiden und verwandten Verbindungen

Teil a

J. B. Goodenough · W. Gräper · F. Holtzberg · D. L. Huber
R. A. Lefever · J. M. Longo · T. R. McGuire · S. Methfessel

Herausgeber: K.-H. Hellwege und A. M. Hellwege

1970 Springer-Verlag Berlin · Heidelberg · New York 1970

3 Crystallographic and magnetic properties of perovskite and perovskite-related compounds *)

3.0 Introduction — Einleitung

3.0.1 General remarks – Allgemeines

The perovskites form a family of compounds having a crystal structure similar to that of the mineral perovskite, $CaTiO_3$. There are two classes of materials crystallizing with this general structure type: primarily ionic materials having the ideal chemical formula ABX_3, (A = larger cation, B = smaller cation, X = anion), and alloys having the ideal formula $M^eXM^f_3$, (X = interstitial atom, M^e and M^f are metal atoms). Of these two classes, the former is much larger and the more important.

The stability of the ABX_3 perovskite structure is primarily derived from the electrostatic (Madelung) energy achieved if cations occupy corner-shared octahedra. Thus the first prerequisite for a stable ABX_3 perovskite is the existence of stable, polar octahedral-site building blocks. This, in turn, requires that the B cation have a preference for octahedral coordination and that there be an effective charge on the B cation. Since any A cation must occupy the relatively large anionic interstice created by corner-shared octahedra, a second prerequisite is an appropriate size for the A cation. Where it is too large, the B-X bond length cannot be optimized, and hexagonal stacking with face-shared octahedra becomes competitive. Where the A cation is too small, A-X bonding stabilizes structures having a smaller anionic coordination about the A cation. Thus ABX_3 perovskites are commonly found in fluorides and oxides having B cations with a preference energy for octahedral coordination. By contrast, the chlorides and sulfides, having larger anions, not only require the largest A cations, but also form layer structures, where the A cations are missing, because they have anionic d orbitals energetically available for orbital hybridization.

There are many perovskite-related structures, and these have been included in these tables. For example, the structure can tolerate mixed systems such as $A_{1-x}A'_xBX_3$ and $AB_{1-x}B'_xX_3$, A-cationic vacancies □ as in $□_{1-x}A_xBX_3$, and cationic ordering as in $A_2BB'X_6$. Although anion-deficient perovskites have been reported many times, the anion vacancies ⊕ are probably not distributed randomly. In compounds containing Fe^{3+} ions, for example, they appear to condense in pairs at individual B-site octahedra to convert the local anion interstice from an octahedron to a tetrahedron. In

Die Perowskite sind eine Gruppe von Verbindungen mit der gleichen Kristallstruktur wie das Mineral Perowskit, $CaTiO_3$. Man unterscheidet zwei Klassen von Substanzen, die in diesem allgemeinen Strukturtyp kristallisieren: in erster Linie Ionenverbindungen mit der idealen chemischen Formel ABX_3 (A = größeres Kation, B = kleineres Kation, X = Anion) und Legierungen mit der idealen Formel $M^eXM^f_3$ (X = Zwischengitteratom, M^e und M^f = Metallatome). Von diesen beiden Klassen ist die erstere wesentlich umfangreicher und wichtiger.

Die Stabilität der ABX_3-Perowskitstruktur beruht in erster Linie auf der elektrostatischen (Madelung-) Energie, die dann zustande kommt, wenn Kationen Oktaeder mit gemeinsamen Ecken besetzen. So ist die Existenz von stabilen, polaren Oktaeder-Bausteinen die erste Vorbedingung für ein stabiles ABX_3-Perowskit. Dies wiederum erfordert, daß das B-Kation die Oktaeder-Koordination bevorzugt und daß beim B-Kation eine effektive Ladung existiert. Da ein jedes A-Kation die relativ große Anionen-Lücke besetzen muß, die zwischen Oktaedern mit gemeinsamen Ecken entsteht, ist die passende Größe des A-Kations die zweite Vorbedingung. Wenn das A-Kation zu groß ist, läßt sich der optimale B-X-Bindungsabstand nicht erreichen, und eine hexagonale Packung von Oktaedern mit gemeinsamen Flächen kann ebenso auftreten. Wenn das A-Kation zu klein ist, ergibt die A-X-Bindung Strukturen mit einer kleineren Anionen-Koordination um das A-Kation. Daher sind ABX_3-Perowskite gewöhnlich unter den Fluoriden und Oxiden zu finden, in denen die B-Kationen Oktaeder-Koordination energetisch bevorzugen. Dagegen erfordern Chloride und Sulfide, die größere Anionen haben, nicht nur die größten A-Kationen, sondern sie bilden, weil sie anionische d-Elektronenbahnen mit der richtigen Energie für eine Bahn-Hybridisierung haben, auch Schichtstrukturen, bei denen die A-Kationen ganz fehlen.

Es gibt viele dem Perowskit verwandte Strukturen, die in diese Tabellen aufgenommen wurden. Zum Beispiel können gemischte Systeme wie $A_{1-x}A'_xBX_3$ und $AB_{1-x}B'_xX_3$ mit dieser Struktur auftreten, weiter A-Kationenlücken □ wie in $□_{1-x}A_xBX_3$ und geordnete Kationen wie in $A_2BB'X_6$. Über Perowskite mit Anionenlücken ist schon häufig berichtet worden, vermutlich sind die Anionenleerstellen ⊕ nicht willkürlich verteilt. In Verbindungen, die Fe^{3+}-Ionen enthalten, scheinen sie z. B. paarweise im Oktaeder eines einzelnen B-Platzes zusammenzutreffen und die

*) This work was sponsered by the U. S. Air Force.

compounds containing Ti^{4+} ions, on the other hand, it is more probable that local rearrangements of the anions form trigonal bipyramidal sites. Anion-deficient, ionic materials in which there are no A-cations, such as $\square WO_{3-x}$, have been shown to contain $\square BX_3$ blocks connected by "shear" planes across which the occupied octahedra share common edges (Fig. 22). On the other hand, anion deficiencies may occur randomly in the $M^cX_{1-x}M^f_x$ alloys. B-cation defects cannot occur, because the B-occupied octahedra form the basis of the ABX_3-perovskite structure. Where there are apparent B-cation vacancies, as in $A_mB_{m-1}X_{3m}$, there is either an interleaving of perovskite layers with A_xX_y layers (Fig. 23) or an interleaving of cubic (perovskite) stacking of AO_3 layers with regularly spaced hexagonal stackings at which are located the B-ion vacancies (Fig. 24). Similarly, the series of compounds $(AX)_m(ABX_3)_n$ crystallize with an interleaving of rocksalt layers (Fig. 25). Interleaving of cubic-stacked AO_3 layers and hexagonal-stacked layers also occurs in ABX_3 compounds having too large an A cation to be accommodated by the perovskite structure (Fig. 3). Finally, there are a few alloys with interesting magnetic properties that can be classified as $A_2BB'X_6$ compounds if the symbols B and B' are allowed to represent atomic clusters rather than single cations. These are illustrated, for example, by the alloy $Al_3(AlCo_{12})(Co_6)B_4$ (Fig. 18). Sections 3.1 and 3.2 are devoted to descriptions of the perovskite and perovskite-related structures.

dortige Anionenlücke von einem Oktaeder in einen Tetraeder umzuwandeln. Bei Verbindungen, die Ti^{4+}-Ionen enthalten, ist es dagegen wahrscheinlicher, daß die lokale Anordnung der Anionen trigonale Doppelpyramiden-Plätze bildet. Für Ionenverbindungen mit Anionenlücken, die keine A-Kationen haben, wie $\square WO_{3-x}$, ist gezeigt worden, daß sie $\square BX_3$-Blöcke enthalten, die durch „Gleit"-ebenen verbunden sind, in denen die besetzten Oktaeder gemeinsame Kanten innehaben (Fig. 22). In $M^cX_{1-x}M^f_x$-Legierungen können jedoch Anionenlücken auch beliebig auftreten. B-Kationenlücken können nicht vorkommen, weil die von B besetzten Oktaeder die Basis der ABX_3-Perowskitstrukturen bilden. Wo scheinbare B-Kationenleerstellen auftreten, wie in $A_mB_{m-1}X_{3m}$, sind entweder A_xX_y-Schichten zwischen Perowskitschichten eingeschoben (Fig. 23), oder kubische (Perowskit-) Anordnungen von AO_3-Schichten wechseln mit regelmäßig verteilten hexagonalen Anordnungen, in denen die B-Ionenlücken auftreten, ab (Fig. 24). Ähnlich kristallisieren die Verbindungen der Reihe $(AX)_m(ABX_3)_n$ mit einer Einschiebung von Steinsalzschichten (Fig. 25). Einschiebungen von kubisch gepackten AO_3-Schichten und hexagonal gepackten Schichten treten auch in solchen ABX_3-Verbindungen auf, deren A-Kation für die Perowskit-Struktur zu groß ist (Fig. 3). Schließlich gibt es einige wenige Legierungen mit interessanten magnetischen Eigenschaften, die als $A_2BB'X_6$-Verbindungen eingeordnet werden können, wenn man unter den Symbolen B und B' Atomgruppen statt einzelner Kationen versteht, Dies gilt z. B. für die Legierung $Al_3(AlCo_{12})(Co_6)B_4$ (Fig. 18). Die Abschnitte 3.1 und 3.2 sind der Beschreibung der Perowskit- und verwandter Strukturen gewidmet.

The ABX_3 perovskites exhibit several interesting physical properties such as ferroelectricity (as in $BaTiO_3$), ferromagnetism (as in $SrRuO_3$), weak ferromagnetism (as in $LaFeO_3$ or $HoFeO_3$), superconductivity (as in $SrTiO_{3-x}$), a large thermal conductivity due to exciton transport ($LaCoO_3$), insulator-to-metallic transitions of interest for thermistor applications (as in $LaCoO_3$), fluorescence compatible with laser action (as in $LaAlO_3$:Nd), and transport properties of interest for high-temperature thermoelectric power (as in La_2CuO_4). A few ABX_3 perovskites have been found that are simultaneously antiferromagnetic and ferroelectric [*Sm16, Mi7, Sm9*]. The simultaneous occurrence of ferroelectricity and ferromagnetism has been reported for systems like $Sr_{0.25}La_{0.75}MnO_3$-$ATiO_3$ (A = Ba, Pb, $Bi_{0.5}K_{0.5}$) [*To3, To6*]. Many of the $M^cXM^f_3$ perovskite alloys are ferromagnetic or ferrimagnetic, and a few exhibit first-order ferrimagnetic-to-ferromagnetic transitions. Nevertheless, the significance of the entire perovskite family for the field of magnetism*) lies not yet in their technological applications, but in their provision of an isostructural series of compounds having outer *d* electrons that are localized and spontaneously magnetic in

Die ABX_3-Perowskite weisen einige interessante physikalische Eigenschaften auf, wie Ferroelektrizität (in $BaTiO_3$), Ferromagnetismus (in $SrRuO_3$), schwachen Ferromagnetismus (in $LaFeO_3$ oder $HoFeO_3$), Supraleitfähigkeit (in $SrTiO_{3-x}$), große Wärmeleitfähigkeit durch Excitonentransport (in $LaCoO_3$), für Thermistoren interessante Übergänge zwischen Nichtleiter und metallischem Leiter (in $LaCoO_3$), für Laser-Anwendungen geeignete Fluoreszenz (in $LaAlO_3$:Nd), und Transporteigenschaften, die für Thermospannungen bei hohen Temperaturen von Interesse sind (in La_2CuO_4). Einige wenige ABX_3-Perowskite wurden gefunden, die sowohl ferromagnetisch als auch ferroelektrisch sind [*Sm16, Mi7, Sm9*]. Das gleichzeitige Auftreten von Ferroelektrizität und Ferromagnetismus wurde bei Systemen wie $Sr_{0.25}La_{0.75}MnO_3$-$ATiO_3$ (A = Ba, Pb, $Bi_{0.5}K_{0.5}$) [*To3, To6*] beschrieben. Viele $M^cXM^f_3$-Perowskitlegierungen sind ferromagnetisch oder ferrimagnetisch, und einige zeigen Übergänge erster Ordnung von Ferri- zu Ferromagnetismus. Trotzdem liegt die Bedeutung der gesamten Perowskit-Familie für den Magnetismus*) noch nicht in der technologischen Anwendung, sondern im Vorhandensein einer isostrukturellen Reihe von Verbin-

*) The technologically important dielectric properties are outside the scope of this summary. See Vol. 111/3 of the New Series of Landolt-Börnstein.

*) Die technologisch wichtigen dielektrischen Eigenschaften liegen nicht im Rahmen dieser Zusammenstellung. Siehe Band 111/3 der Neuen Serie des Landolt-Börnstein.

one member, collective and spontaneously magnetic in another, and collective and Pauli paramagnetic in yet another. This permits a systematic experimental investigation of the properties of the *d* electrons on passing through the transition from a localized character, where crystal-field plus superexchange and/or double-exchange theories apply, to an uncorrelated (except below a superconducting transition temperature) collective-electron character, where the conventional band theory applies. In addition, the simplicity of the perovskite ABX_3 structure minimizes competitive magnetic interactions between neighboring magnetic cations. Therefore from a study of magnetic order, as revealed by neutron diffraction, together with detailed structural information, as revealed by x-ray diffraction, it has been possible to test the semi-empirical rules for 180° cation-anion-cation isotropic superexchange interactions between localized electrons, the double-exchange hypothesis, antisymmetric exchange, and predictions of magnetic order and spontaneous atomic moments due to collective electrons.

Section 3.3 presents the general phenomenological exchange Hamiltonian for localized electrons and summarizes the microscopic models for isotropic superexchange, double exchange, and antisymmetric exchange. From these models, general rules for the interactions responsible for magnetic order are developed for comparison with the tabulated magnetic data.

Section 3.4 presents the fundamental physical concepts needed to construct a qualitative phase diagram for the outer *d* electrons as a function of the number n_l of electrons per relevant orbital, the magnitude of a nearest-neighbor transfer energy b, and the temperature T. It also summarizes the various characters of several physical properties imparted by outer electrons to show how they can be used to distinguish the electronic phases in different perovskites. Information from the tabulated data is used to show the influence of covalence and intra-atomic exchange, which help determine the parameter b, on the character of the electrons. Spontaneous collective-electron magnetism is seen to occur only in a narrow transitional interval of b between localized-electron magnetism and collective-electron Pauli paramagnetism.

Section 3.5 provides schematic energy diagrams for the alloys $M^cXM^t_3$. These are shown to be useful guides to predictions of the magnitudes of the atomic moments and the magnetic order.

dungen mit äußeren *d*-Elektronen, die lokalisiert und spontan magnetisch in der einen Verbindung, kollektiv und spontan magnetisch in einer anderen, und kollektiv und Pauli-paramagnetisch in noch einer weiteren sind. Dies erlaubt systematische experimentelle Untersuchungen der Eigenschaften der *d*-Elektronen, indem man von einem lokalisierten Zustand, in dem Kristallfeld plus Superaustausch- und/oder Doppelaustausch-Theorien gelten, zu einem Zustand unkorrelierter Kollektivelektronen (außer bei Temperaturen unterhalb des Übergangs zur Supraleitung) übergeht, in dem die konventionelle Bändertheorie anzuwenden ist. Weiterhin führt die Einfachheit der Perowskit-ABX_3-Struktur zu minimalen konkurrierenden Wechselwirkungen zwischen benachbarten magnetischen Kationen. Aufgrund der Untersuchung der magnetischen Ordnung, die man durch die Neutronenbeugung kennt, und einer genauen Kenntnis der Struktur, wie man sie durch Röntgenbeugung gewonnen hat, war es deshalb möglich, die halbempirischen Gesetze über die isotrope 180°-Kation-Anion—Kation—Superaustausch—Wechselwirkung zwischen lokalisierten Elektronen, die Doppelaustausch-Hypothese, den antisymmetrischen Austausch und Voraussagen für magnetische Ordnung und spontane Atom-Momente, die von Kollektivelektronen herrühren, zu prüfen.

' Der Abschnitt 3.3 enthält den allgemeinen phänomenologischen Hamilton–Austausch–Operator für lokalisierte Elektronen und faßt die mikroskopischen Modelle für den isotropen Superaustausch, den Doppelaustausch und den antisymmetrischen Austausch zusammen. Aus diesen Modellen werden allgemeine Regeln für die Wechselwirkungen, die für die magnetische Ordnung verantwortlich sind, zum Vergleich mit den tabellierten Daten entwickelt.

Der Abschnitt 3.4 enthält die grundlegenden physikalischen Ideen, die für die Herstellung eines qualitativen Phasendiagramms für die äußeren *d*-Elektronen als Funktion der Elektronenzahl n_l pro betreffenden Bahnzustand, der Größe einer Übertragungsenergie b zwischen nächsten Nachbarn und der Temperatur T notwendig sind. Außerdem werden hier verschiedene Charakteristika einiger durch die äußeren Elektronen gegebenen physikalischen Eigenschaften zusammengestellt, um zu zeigen, wie man mit ihrer Hilfe die elektronischen Phasen verschiedener Perowskite unterscheiden kann. Auf Grund der tabellierten Werte wird der Einfluß von Kovalenz und intra-atomarem Austausch, die den Parametor b mitbestimmen, auf den Charakter der Elektronen gezeigt. Spontane Magnetisierung der Kollektivelektronen tritt, wie man sieht, nur in einem schmalen Übergangsintervall von b zwischen dem Magnetismus lokalisierter Elektronen und dem Pauli-Paramagnetismus der Kollektivelektronen auf.

Der Abschnitt 3.5 enthält schematische Energiediagramme für die Legierungen $M^cXM^t_3$. Es wird gezeigt, daß sie zu brauchbaren Voraussagen über die Größe der Atom-Momente und die magnetische Ordnung führen können.

In the introductions to the sections 3.2···3.5 we have referenced the principle theoretical contribution discussed, but no attempt was made to do this systematically for the experimental contributions, which are thoroughly referenced in the tables. — In the crystallographic tables, the crystal parameters quoted either represent the most complete analysis, in our judgment, or belong to the most complete set of parameters for a series of similar compounds. They do not necessarily represent the historical reference that established the unit-cell dimensions.

Literature was considered up to 1969.

Finally, we would like to thank DAVID MAHONEY for his willing assistance, the library and publications personnel of Lincoln Laboratory for their efficient support, and Mrs. G. E. BOYD for her help with all the foreign references.

In den Einleitungen zu den Abschnitten 3.2···3.5 haben wir die grundlegenden theoretischen Beiträge, die diskutiert werden, mit Literaturhinweisen versehen; für die experimentellen Beiträge haben wir dies nicht systematisch durchzuführen versucht, da die entsprechenden Tabellen vollständig mit Literaturhinweisen versehen sind. — In den kristallographischen Tabellen stellen die angeführten Kristallparameter entweder die nach unserer Beurteilung vollständigste Analyse dar, oder sie gehören zum vollständigsten Satz von Parametern für eine Reihe ähnlicher Verbindungen. Sie geben nicht notwendigerweise den historischen Literaturhinweis, der die Dimensionen der Einheitszelle festlegte.

Die Literatur wurde bis 1969 berücksichtigt.

Schließlich möchten wir DAVID MAHONEY für seine bereitwillige Hilfe, den Angestellten der Bibliothek und der Veröffentlichungsabteilung des Lincoln-Laboratoriums für ihre wirksame Unterstützung und Mrs. G. E. BOYD für ihre Hilfe bei der ausländischen Literatur danken.

3.0.2 Symbols and units used in tables and figures

Crystallographic structure

symmetry	symmetry classification for perovskite structures: C = cubic, H = hexagonal, R = rhombohedral, O = orthorhombic ($a < c/\sqrt{2}$), O' = orthorhombic ($c/\sqrt{2} < a$), T = tetragonal, M = monoclinic, Tr = triclinic
a, b, c [Å]	lattice parameters
α, β, γ [deg]	angle between crystallographic axes
Θ_{kraze}, Θ_{ord} [°K]	crystallographic transition and ordering temperatures
Θ_D [°K]	Debye temperature
T_{melt} [°K]	melting temperature
c_{ij}	elastic constants
ε_i	crystalline strains
$r_{A,B,B'}$ [Å]	radius of A, B, B' cation

Magnetic properties (static measurements)

magnetic order	see magnetic structure type from Fig. 26
n_A, $n_{\downarrow}^{A}$	atomic moment and component of atomic moment parallel to net ferromagnetic moment in numbers of Bohr magnetons: $p_A = n_A \mu_B$
$\overline{n}_m$	net magnetization per molecule in numbers of Bohr magneton: $p_m = \overline{n}_m \mu_B$
n_{eff}	$n_{\text{eff}} = \sqrt{8 C_m}$ is the effective paramagnetic moment: $p_{\text{eff}} = n_{\text{eff}} \mu_B$
Θ_C [°K]	Curie temperature
Θ_N [°K]	Néel temperature; extrapolated Néel temperature
Θ_r [°K]	temperature for spin reorientation
Θ_p [°K]	paramagnetic Curie temperature ($\Theta_p < 0$ if antiferromagnetic coupling)
Θ' [°K]	temperature below which parasitic $n_{\downarrow}^{A}$ deviates appreciably from 0.05
C_m [emu °K mole^{-1}]	molar Curie constant determined from Curie-Weiss law $\chi_m = C_m/(T - \Theta_p)$
χ_g [emu/g], [cm^3/g]	specific paramagnetic susceptibility
χ_m [emu/mole]	molar paramagnetic susceptibility
p_A, $p_{\downarrow}^{A}$ [μ_B]	atomic moment, atomic moment of element A
p_m, $p^{(xy)}$	molecular moment (of molecule xy)
p^*	effective paramagnetic moment: $p^* = \sqrt{\chi_m T}$
J_{nn}/k [°K]	isotropic exchange constant of Eq. (16) for near-neighbor interactions
d	Ln-Fe interaction parameter defined by $M(t) = \sigma_s(0)\, B(t)$ [$1 + (d/t)$], where $t = T/\Theta_C$ and $B(t)$ is the Brillouin function
σ_w [erg/cm^2]	domain wall energy density
W_{nn}	net near-neighbor Weiss molecular field constant: $H_{wi} = \sum_{j=1}^{z} W_{ij} M_j$

σ [Gauss cm³/g] [emu/g]	magnetic moment per gram = specific magnetization
σ_0 [emu/g]	specific parasitic (weak) magnetization as obtained from $\sigma = \sigma_0 + \chi_g H_a$
σ_{sp}	spontaneous specific magnetization
H_a [Oe]	externally applied field
H_{crit} [Oe]	critical applied field for antiferromagnetic-ferromagnetic transition or for spin-flop transition
H_c	coercivity
α	cant angle
b_1, b_2 [dyn/cm²]	magnetoelectric coefficients
λ_{100}	magnetostriction constant for [100] direction: $\lambda_{100} = -4b_1/3(c_{11} - c_{12})$
C_{ijk}	components of the tensor describing the quadratic dependence of magnetization on applied field: Eq. (36)
μ_B	the Bohr magneton = 5585 emu/g
T [erg/g]	torque: $T = \sigma \times H_a$

Magnetic properties (resonance measurements)

H_A	effective crystalline-anisotropy field
H_{ex}	exchange field
H_D	spin-canting field (Dzialoshinskii field)
H_{int}	internal magnetic field at the nucleus
H_n	axial hyperfine field arising from nuclear polarization
H_{hyp}	hyperfine field $\boldsymbol{I} \cdot \mathbf{A} \cdot \boldsymbol{S}$, where $\boldsymbol{I}$ = nuclear spin, $\boldsymbol{S}$ = net atomic spin, and the components of the interaction tensor are A_s, A_{ns}, A_σ, A_π, A_{sp}.
f_s^A, f_n^A, f_n^A	fraction of unpaired s, p_σ or p_π electron spins involved in covalent bonding: $f_s^A = 2SA_s/A_{ns} = \frac{1}{3} N_s^2 \lambda_n^2$, $f_\sigma^A = 2SA_\sigma/A_{sp} = \frac{1}{3} N_\sigma^2 \lambda_n^2$, $f_\pi^A = 2SA_\pi/A_{sp} = \frac{1}{4} N_\pi^2 \lambda_n^2$. See Eq. (4) for N_s, N_π, λ_s, λ_σ, λ_π.
e, ΔE	nuclear quadrupole coupling constant and quadrupolc splitting
F_{ij}, G_{ij}	dipolar and quadrupolar magnetoelastic coefficients: $\delta g_i = \sum_{j=1}^{6} F_{ij} e_j$ and $d_i = \sum_{j=1}^{6} G_{ij} e_j$, where $\mathscr{H}_{spin\text{-}lattice} = \mu_B \boldsymbol{H}_a \cdot \delta\mathbf{g} \cdot \boldsymbol{S} + \boldsymbol{S} \cdot \mathbf{d} \cdot \boldsymbol{S}$
ν_R [Hz]	rcsonance frequency for NMR
$\Delta\nu$ [Hz]	half-line width
T_1 [sec]	nuclear spin-lattice relaxation timc
T_2 [sec]	nuclear spin-spin rclaxation time
T_{1e} [sec]	nuclear spin-latticc relaxation timc during a locking pulse

Optical measurements

n	indcx of refraction
ε_0	low-frequency dielectric constant
ϱ [°/cm]	Faraday rotation
ν_{TO}, ν_{LO} [Hz]	frequency of transverse and longitudinal optical modcs

Transport measurements

Θ_{cs}	superconducting critical temperature
E_F	Fermi energy
E_a	activation energy for a small-polaron hop
ϱ [Ωcm]	electrical resistivity
S [μV/°K]	Seebeck coefficient
e [esu]	magnitude of the electronic charge
c, n_i, $n_\pm$ [cm⁻³]	charge-carrier density
μ [cm²/Vsec]	charge-carrier mobility
τ [sec]	charge-carrier collision time
m^* [g]	charge-carrier effective mass
D_e [cm²/sec]	charge-carrier diffusion coefficient at $E_a = 0$
$N_\pm$	density of unoccupied states: $2(2\pi m_\pm^* \mathrm{k}T/h^2)^{3/2}$

General properties

T [°K]	temperature
p	pressure
c_p	specific heat at constant pressure

Abbreviations for text and indices

AFMR	antiferromagnetic resonance
APR	acoustic paramagnetic resonance
BPW	Bethe-Peierls-Weiss method
C, cub	cubic
DS	Danielson-Stevens method
DTA	differential thermal analysis
ESR	electron spin resonance = paramagnetic resonance
f.c.	face-centered permutation
FMR	ferromagnetic resonance
F_R	ferromagnetic with reduced n_A
H, hex, hex (nL)	hexagonal, hexagonal n-layer structure
I.R.	infrared
Ln	Lanthanon = any of the rare-earth elements
MF	molecular field approximation
M, mon	monoclinic
NAR	nuclear acoustic resonance
NMR	nuclear magnetic resonance
ncub	noncubic
O, O', orth	orthorhombic (O: $a < c/\sqrt{2}$; O': $c/\sqrt{2} < a$)
P&S	reference to preparation and structural information
Prep.	reference to material preparation
Prop.	reference to material properties
pscub	pseudocubic
psmon	pseudomonoclinic
R, rh	rhombohedral
RW	Rushbrooke-Wood method
S. G.	space group
S.S.	solid solution
T, tetr	tetragonal
Tr, tr	triclinic

3.1 Descriptions of stoichiometric ABX_3 and $M^cXM^f_3$ structures

3.1.1 The ideal perovskite structure

The ideal perovskite structure has the cubic unit cell of Fig. 1 with space group Pm3m. Fig. 1 (a) shows the corner-sharing octahedral units (BX_6 array in ABX_3 and XM^f_4 array in $M^cXM^f_3$), which form the stable skeleton of the structure. The A cation (or M^c atom) occupies the body-center position. Fig. 1 (b) shows the unit cell with the A cation (or M^c atom) at the origin, or corner position. This shows the face-centered-cubic character (with Cu_3Au-type order) of the AX_3 or $M^cM^f_3$ subarrays. Fig. 1 (c) shows the cubic perovskite on an hexagonal basis, with the c axis along the cubic [111] direction. The alternate AX_3 and B ionic layers each have cubic stacking. Also indicated is the ordering of B and B' layers in the ordered $A(B'_{2/3}B_{1/3})X_3$ structures.

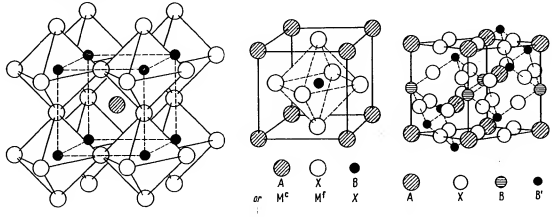

Fig. 1. ABX_3, $M^cXM^f_3$. Ideal perovskite structure: a) B cation (or X atom) at origin. b) M^c atom (or A cation) at origin. c) A cation at origin in hexagonal basis [*Ga10*].

The alloys $M^aXM^b_4$ are stabilized by covalent M-X bonding and by metallic M-M bonding, so that they are generally cubic. Only in phases exhibiting complex magnetic order are there distortions to lower symmetry. On the other hand, the ABX_3 perovskites, which are primarily stabilized by the Madelung energy, are rarely cubic at normal temperatures. Madelung energy calculations are available [*Ro15a, Sa2b, Mi1*].

Although cubic at high temperatures, most ABX_3 compounds exhibit distortions to lower symmetry below some temperature Θ_{trans} as a result of atomic displacements. Such displacive transitions can be described by a finite set of normal vibrational modes that become soft, their vibrational frequency increasing with $T > \Theta_{trans}$. From LANDAU's [*La2*] theory of phase transitions, it may be argued [*Ha1, Co2*] that at a second-order displacive transition, the frequency of one normal mode becomes zero. Thus the occurrence of ferroelectricity in perovskite-type crystals such as **$BaTiO_3$** has been correlated both theoretically and experimentally [*An2, Co1, Ba17, Co28, Ne8, Sh26*] with the existence of a transverse optic mode of lattice vibration having wave number $k \approx 0$ and a temperature-dependent frequency $\omega \sim (T - \Theta_{trans})^{1/2}$.

Similarly, in the case of **$LaAlO_3$** softening of a single normal mode can produce the R3c-to-cubic transition, and this transition is probably second-order. Investigation [*Ha1*] of the atomic displacements involved in other distortions from cubic symmetry, on the other hand, has shown that several normal modes are involved, and these displacive transitions are first-order.

$SrTiO_3$ exhibits a tetragonal (D^{18}_{4h}) with $c/a = 1.00056$) to cubic transition at $\Theta_{trans} = 110$ °K [*Ly2, Ri5*] that appears to illustrate the softening of a triply degenerate phonon at the R point of the Brillouin zone in the cubic phase. For $T < \Theta_{trans}$, it splits into two zone-center phonons having a frequency dependence $\omega \sim (\Theta_{trans} - T)^{0.31}$ [*Fi12*]. In the presence of an external electric field E_a the symmetry is further reduced to C_{4v} if $E_a \parallel c$-axis, or C_{2v} if $E_a \perp c$-axis, and the critical modes have the same symmetry as the ferroelectric TO modes. "Anticrossing" of the modes occurs for $E_a = 1.5$ kV/cm and 15 kV/cm [*Ne7, Wo1*9]. Thus the observed [*He5*] maximum in the electric susceptibility of **$SrTiO_3$** at very low temperatures does not appear to be associated with a ferroelectric transition.

Theoretical interest in the analytic description of these phase transitions continues [*Go1a, Mu4a, Ta14a, Th3*].

The physical origins of the various crystallographic distortions may be separated into three parts: relative ionic sizes, electron ordering among localized electrons, and electron ordering among collective electrons.

3.1.2 The influence of relative ionic sizes

3.1.2.1 Tolerance factor

The first prerequisite for a stable perovskite structure is the existence of a stable BX_3 skeletal subarray. If the B-cation radius is $r_B < 0.51$ Å in oxides, for example, the B cation does not achieve its optimum B-O separation in an octahedral site and therefore stabilizes a structure with a smaller anion coordination. The Al^{3+} ion is borderline, being stable in four, five or six coordination. However, Ga^{3+}, Ge^{4+} and V^{5+} ions are definitely more stable in tetrahedral sites at ambient pressures.

Given the BX_3 skeletal subarray, additional stabilization is achieved by accommodating a large A cation within this skeleton. Because there is an optimum A-X bond length, the presence of an A atom generally distorts the BX_3 array so as to optimize the A-X bonding. However, if this distortion is too large, then other space groups become competitive. GOLDSCHMIDT [*Go2*] defined the tolerable limits on the size of the A cation via a tolerance factor

$$t = (r_A + r_X)/\sqrt{2}\,(r_B + r_X) \qquad (1)$$

where r_A, r_B, r_X are empirical radii of the respective ions. By geometry, the ideal cubic structure should have $t = 1$. The perovskite structure occurs only within the range $0.75 < t < 1.00$. However, this is not a sufficient condition, since the A and B cations must, in themselves, be stable in twelvefold (12 or 8 + 4 or 6 + 6) and sixfold coordinations. This sets lower bounds for the cationic radii. In oxides these bounds are $r_A > 0.90$ Å and $r_B > 0.51$ Å. In addition, MEGAW [*Me5*] noted that, if $0.75 < t < 0.9$, a cooperative buckling of the corner-shared octahedra to optimize the A-X bond lengths enlarges the unit cell; on the other hand, if $0.9 < t < 1$, such buckling may not be found, although small distortions to rhombohedral symmetry occur. These structures are to be distinguished from perovskites that exhibit additional distortions as a result of electron ordering. The cubic phase is found at high temperatures or where the A-X bond is more ionic (especially if $t \approx 1$).

Where the A cation is too small ($r_A < 0.9$ Å) to accommodate twelve nearest neighbors, a structure in which the A and B cations are both six-coordinated becomes competitive. From the phase diagram of Fig. 2 for the oxides $A^{++}B^{3+}O_3$, which has been adapted from SCHNEIDER, ROTH, and WARING [*Sc13*], the initial competition is the C-M_2O_3 structure, which contains two unusual types of corner-shared, six-coordinated sites. The C-M_2O_3 structure consists of a face-centered-cubic array of cations with anions occupying $\frac{3}{4}$ of the tetrahedral interstices in an ordered manner. Thus each cation has six out of eight near-neighbor anions at the corners of a circumscribing cube: $\frac{1}{4}$ of the cations have two anions missing at the ends of a body diagonal and $\frac{1}{2}$ of the cations have two anions missing at the end of a face diagonal of the circumscribing cube. This arrangement minimizes the electrostatic repulsive forces between the cations.

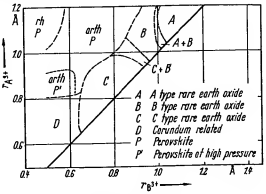

Fig. 2. General $r_A - r_B$ phase diagram for $A^{3+}B^{3+}O_3$ compounds based on ionic-size considerations. Exceptions may occur where considerations other than ionic radii r_A, r_B become important, as in the case A = Bi. A similar plot for $A^{2+}B^{4+}O_3$ perovskites is not useful because secondary considerations are amplified by ferroelectric distortions and the possibility of different layer sequences where larger A cations are present. [Adapted from *Sc13*].

Given smaller A cations, however, electrostatic screening between face-shared octahedra can be achieved by displacements of the cations away from the shared face, and the structure competitive with perovskite is generally built from an hexagonal-close-packed anion array, which has octahedral holes sharing common faces along the *c*-axis. With one octahedral hole per anion and a cation/anion ratio 2/3, the cations are ordered among these holes so as to minimize the electrostatic energy. If the A and B cations carry the same charge, as in $A^{2+}B^{4+}O_3$, only pairs of cations share common octahedral-site faces and there is no ordering of A and B within the cationic array. This allows the electrostatic force between two cations sharing a common octahedral face to be reduced by displacements of the cations away from each other, thus distorting the octahedra. The result is the corundum structure of Al_2O_3. If the cations A and B carry different charges, as in $A^{2+}B^{4+}O_3$, then the A and the B cations order into alternate puckered cationic (111) planes of the rhombohedral corundum structure to form the ilmenite structure. However, where there is a large difference in the cationic charges, as in $Li^+Sb^{5+}O_3$ and $Li^+Nb^{5+}O_3$, two other alternatives become competitive: (1) The A^+ ions order in strings of face-shared octahedra so as to permit the B^{5+}-ion octahedra to share only edges with near-neighbor occupied octahedra. This structure is illustrated by $LiSbO_3$ [*Ed1*]. (2) After ordering B^{5+} and Li^+ ions whithin each cationic (111) plane of the corundum structure in such a way that B^{5+} and Li^+ ions share common octahedral-site faces, each A^+ cation is then displaced into the far face of its octahedron, where it is equally spaced from B^{5+} cations above and below so long as the B^{5+} cations remain in the centers of their octahedra. This is the structure of paraelectric $LiNbO_3$ and $LiTaO_3$ [*Ab3*].

Where the A cation is too large ($t > 1.0$), the close-packed AX_3 layers of Fig. 1(c) tend to change their stacking sequence from cubic to hexagonal. However, the change from the all-cubic stacking of the rhombohedral perovskite structure to the all-hexagonal stacking of the hexagonal (hex. 2L) $CsNiCl_3$ structure goes via the three intermediate steps shown in Fig. 3 [*Lo1*]. The first step is the hexagonal $BaTiO_3$ structure of Fig. 3(c). It is a six-layer structure with stacking sequence *a-b-c-a-c-b-a*, corresponding to one hexagonal stacking out of three. In this structure (hex. 6L), two-out-of-three B cations form pairs sharing a common octahedral-site face, and one-out-of-three B cation shares only common octahedral-site corners as in the perovskite structure. Many ordered compounds $A_2B_2B'O_9$ are known to have this structure. The second step, illustrated by the hexagonal $BaMnO_3$ structure of Fig. 3(d), alternates hexagonal and cubic stackings with the sequence *a-b-c-b-a*. This four-layer structure (hex. 4L), contains only B-cation pairs sharing common octahedral-site faces. The electrostatic forces between paired B-cations in Figs. 3(c), (d) displace the paired cations from one another along the *c* axis, exactly as in the corundum

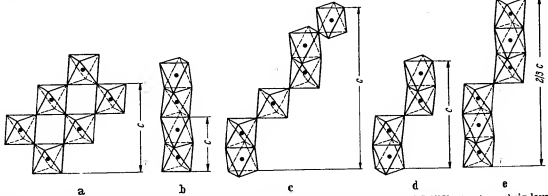

Fig. 3. Stable structures intermediate to a) cubic perovskite and b) the two-layer hexagonal $CsNiCl_3$ structure, c) six-layer hexagonal $BaTiO_3$ structure, d) four-layer hexagonal $BaMnO_3$ structure, e) nine-layer hexagonal $BaRuO_3$ structure. [Adapted from *Ca2*].

structure. The third step is the nine-layer (hex. 9L) structure of **$BaRuO_3$**, which has two hexagonal stackings out of three in the sequence *a-b-c-b-c-a-c-a-b-a*. Here the B cations form strings of three sharing common octahedral-site faces along the *c*-axis. Electrostatic forces displace the two end-member B cations away from the center B cation of each string, as shown in Fig. 3(e). Because cubic stacking is stabilized by hydrostatic pressure, it is possible to convert under pressure and high temperature the hexagonal structures to the perovskite structure through the successive sequence of steps. This is well illustrated by the $Ba_{1-x}Sr_xRuO_3$ system as shown in Fig. 4(a). These particular intermediate structures appear to be stabilized by the cation displacements, but at the cost of alternating the stacking sequence. The (hex. 4L) structure, which has the maximum alternation of stacking, is not always found, and the intermediate structures tend to be stabilized by smaller B cations, as illustrated in Fig. 4(b).

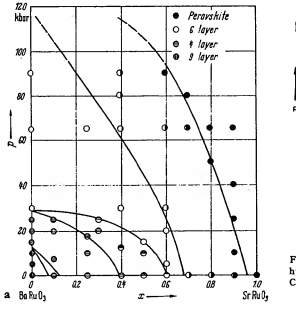

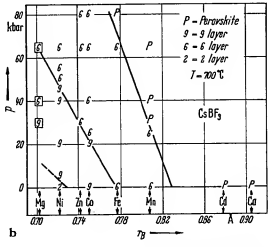

Fig. 4. a) $Ba_{1-x}Sr_xRuO_3$. $p - x$ phase diagram where p is hydrostatic pressure [*Lof*], b) structural phase diagram of $CsBF_3$ compounds [*Lot b*].

3.1.2.2 O-orthorhombic structure

Cooperative buckling of corner-shared octahedra, although indexed on a monoclinic pseudocell in earlier work, may produce the orthorhombic primitive cell of Fig. 5 containing four formula units. It was first identified in single crystals of **$GdFeO_3$** [*Ge1*] and later confirmed [*Co2f*]. Powder photographs taken with CrK_α radiation could be indexed on the monoclinic pseudocell containing a single **$GdFeO_3$** molecule, which is the origin of the earlier classification. The pseudocell dimensions of **$GdFeO_3$** are $a = c = 3.87$ Å, $b = 3.83$ Å, $\beta = 92.8°$, where $2b_{pseudocell} = c_{true\ cell}$. The true orthorhombic cell is referred to in the tables as O-orthorhombic and is distinguished from the O'-orthorhombic structure by a lattice-parameter ratio

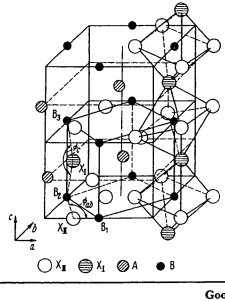

Fig. 5. $GdFeO_3$. O-orthorhombic structure.
$\phi_{ab} = \sphericalangle B_1X_1B_2$, $\phi_c = \sphericalangle B_3X_2B_2$.
Fig. from [*Ve12*], structure [*Ge1*], coordinates[*Co2f*].

ion	position	coordinates		
		x	*y*	*z*
Gd^{3+}	4(c)	−0.018	0.060	¼
Fe^{3+}	4(b)	½	0	0
O_I^{2-}	4(c)	0.05	0.470	¼
O_{II}^{2-}	8(d)	−0.29	0.275	0.05

$c/a > \sqrt{2}$, where $a < b$. The O'-orthorhombic structure, which has $c/a < \sqrt{2}$, is the result of a superposed Jahn-Teller (with or without spin-orbit coupling) distortion. It is also to be distinguished from ferroelectric O_R^R-orthorhombic and O_R^T-orthorhombic distortions in which each B cation is removed from the center of symmetry of its interstice. Other orthorhombic distortions have been reported for $NdGaO_3$ [*Br26*] and $NaCoF_3$ [*Ob5*].

The O-orthorhombic unit cell has the probable space group Pbnm with A cations in positions 4(c): $\pm(x, y, \frac{1}{4}; \frac{1}{2} - x, \frac{1}{2} + y, \frac{1}{4})$, the B cations in 4(b): $(\frac{1}{2}, 0, 0; \frac{1}{2}, 0, \frac{1}{2}; 0, \frac{1}{2}, 0; 0, \frac{1}{2}, \frac{1}{2})$, eight anions X_{II} in 8(d): $\pm(x, y, z; \frac{1}{2} - x, \frac{1}{2} + y, \frac{1}{2} - z; \bar{x}, \bar{y}, \frac{1}{2} + z; \frac{1}{2} + x, \frac{1}{2} - y, \bar{z})$, and the remaining four anions X_I in 4(c). Coordinates for the ions in $GdFeO_3$ are also given in Fig. 5.

The buckling of the corner-shared octahedra decreases the cation-anion-cation angle Φ from 180°. If the B cations and the anions are distinguished as $B_1(\frac{1}{2}, 0, 0)$, $B_2(0, \frac{1}{2}, 0)$, $B_3(\frac{1}{2}, 0, \frac{1}{2})$, $X_{II}(\frac{1}{4} + x, \frac{1}{4} - y, \bar{z})$, and $X_I(\frac{1}{4} - x, \frac{1}{4} + y, \frac{1}{4})$, then the two representative angles are $\Phi_{ab} = (B_1 - X_{II} - B_2)$ and $\Phi_c = (B_2 - X_I - B_3)$. Galileo [*Gi4*] has estimated that in $La(Co_{0.5}Mn_{0.5})O_3$ these angles are $\Phi_{ab} = 150° \pm 3°$ and $\Phi_c = 177° \pm 3°$ with $B_1 - O_{II} = 1.95$ Å, $B_2 - O_{II} = 2.10$ Å, $B_1 - O_I = B_3 - O_I = 1.96$ Å. The angles in $GdFeO_3$ are similar.

3.1.2.3 Rhombohedral structures

Where there is no buckling of the octahedra, the perovskites ABX_3 may have a small deformation from cubic to rhombohedral symmetry. Where this deformation does not enlarge the unit cell, it is possible to index it either on a unit cell containing two formula units, as shown in Fig. 6, or on a unit cell containing one formula unit. The corresponding rhombohedral angles are $\alpha \approx 60°$ or $\alpha \approx 90°$. In the early literature, detailed anion positions were not known, and it was common to use the smaller cell with $\alpha \approx 90°$. However, the anions are generally displaced so as to require the larger unit cell of Fig. 6, which has $\alpha \approx 60°$.

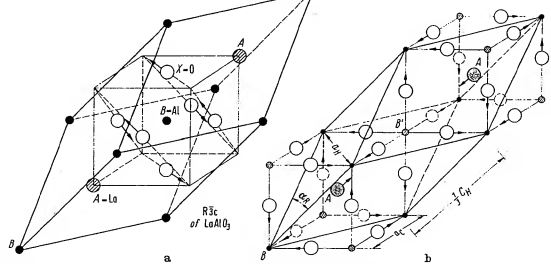

Fig. 6. Rhombohedral ABX_3 structures: a) anion shifts for symmetry R3̄c; b) the simplest ionic displacements, corresponding to symmetry R3̄m for ordered $A_2BB'X_6$ structures having $r_{B'} > r_B$ [*Ra3*].

Anion displacements from their ideal positions may be of three different types: (1) $AX_3(111)$ planes remain equidistant from neighboring B-cation (111) planes, leaving all the B-cations equivalent. Within these planes, three A—X distances are reduced and three are enlarged via cooperative rotations of the B-cation octahedra, as shown in Fig. 6(a). (2) The anions may move within pseudocubic {110} planes including the B-B axes so as to create two distinguishable B positions: B positions having a shorter B-X separation and B' positions having a larger B'-X separation. This gives the symmetry R3̄m, which allows the A cations to be displaced along the [111] axis so as to make the separations B-A ≠ B'-A. (3) In the most general case, the anion displacements may be decomposed into R3̄c and R3̄m components. The resulting symmetry R3̄ also gives distinguishable B and B' positions via its R3̄m component.

Although the distinction between these possibilities has been determined in only a few cases, it appears that R3c can be anticipated unless there is a physical reason for creating two distinguishable positions B and B'. This conclusion is based on the fact that $LaAlO_3$ has been shown to have the symmetry R3̄c by neutron diffraction, [*De14*] nuclear quadrupole resonance [*Mu5*], electron-spin resonance, [*Ki7*] and x-ray techniques [*Ge4b, De17*]. It is strongly supported by the observation [*Ra3*] that $LaCoO_3$ has the symmetry R3̄c at low temperatures, where all of the trivalent cobalt are in their low-spin state, but has the symmetry R3̄ at higher temperatures where thermal activation creates a nearly equal population of high-spin and low-spin cobalt ions. These are crystallographically distinguishable, via different ionic radii, as B and B'.

3.1.3 The influence of localized-electron ordering

3.1.3.1 Crystal-field theory

Crystal-field theory rests on the assumption that the outer electrons to be described are localized at discrete atomic positions. This assumption is valid for outer f electrons; it is valid for d electrons in fluorides and in many oxides. Given this assumption, the Schroedinger equation $\mathscr{H}\psi = E\psi$ that describes the localized orbitals and their energies contains the Hamiltonian

$$\mathscr{H} = \mathscr{H}_0 + V_{\mathrm{el}} + V_{\mathrm{ecnb}} + (V_{LS} + V_{\mathrm{ncnb}} + V_\lambda + \sum_j V_{1j}) \tag{2}$$

where $\mathscr{H}_0$ is the Hamiltonian for a hydrogen-like, spherical potential, V_{el} is the atomic correction for spherical symmetry that enters if there is more than one outer d electron, and V_{ecnb} is the energy correction due to the cubic component of the crystalline fields. For outer d electrons, V_{el} and V_{ecnb} are generally ≈ 1 eV, and the ion is in a high-spin or a low-spin state depending upon the relative magnitudes of these two terms. In the case of $3d$ electrons, the perturbations listed within the parentheses are all <0.1 eV, and they must be considered simultaneously. $V_{LS} = \lambda \boldsymbol{L}\cdot\boldsymbol{S}$ is the spin-orbit coupling energy, and covalent mixing reduces slightly the parameter λ from its free-atom value. V_{ncnb} is the noncubic component of the crystalline field, V_λ is the elastic coupling energy associated with cooperative local distortions, and V_{1j} is the magnetic exchange energy coupling localized atomic moments on neighboring cations.

Solution of the zero-order equation $\mathscr{H}_0\psi = E\psi$ gives hydrogenic wave functions $f_{l,\mathrm{m}} = R_l(r)\,Y_l^{\mathrm{m}}(\theta,\phi)$. From the spherical harmonics $Y_l^{\mathrm{m}}(\theta,\phi)$, the d electrons ($l=2$) have the following angular dependence and azimuthal-angular-momentum quantum number m derived from $L_z f = -i\hbar\,\partial f/\partial\phi = m\hbar f$:

$$\begin{aligned} f_{\mathrm{A}} &\sim (3z^2 - r^2)/r^2 && = (3\cos^2\theta - 1); && m = 0 \\ (f_{\mathrm{D}} \pm i f_{\mathrm{E}}) &\sim 2(zx \pm iyz)/r^2 && = \sin 2\theta \exp(\pm i\phi); && m = \pm 1 \\ (f_{\mathrm{B}} \pm i f_{\mathrm{C}}) &\sim (x^2 - y^2 \pm i\,2xy)/r^2 && = \sin^2\theta \exp(\pm i 2\phi); && m = \pm 2 \end{aligned} \tag{3}$$

where θ, ϕ are conventional spherical coordinates. The perturbation V_{el} reflects the fact that outer electrons of parallel spin are excluded from one another and therefore screen each other less from the positive atomic nucleus than do those of antiparallel spin. This correction is responsible for Hund's highest-multiplicity rule for the free atoms. It influences the radial part of the wave function, and hence the relative energies of states of different spin, but not the angular part.

Given the cartesian axes at a B cation formed by the principal axes of its octahedral interstice, the five d orbitals of Eq. (3) are separated into two symmetry groups; f_{A} and f_{B}, which are directed along the cartesian axes toward near-neighbor anions, have E_g symmetry and are referred to as e_g orbitals; f_{D}, f_{D}, and f_{E}, which are more stable because they are directed away from the near-neighbor anions, have T_{2g} symmetry and are referred to as t_{2g} orbitals. The principal contribution to the cubic-field splitting 10 Dq of T_{2g} and E_g energies is due to covalent mixing, not to electrostatic energies as calculated on a point-charge model. If covalent mixing with the near-neighbor anionic and A-catonic orbitals is introduced, then the crystalline localized orbitals of t_{2g} and e_g symmetry become

$$\begin{aligned} \psi_{\mathrm{t}} &= N_{\mathrm{t}}(f_{\mathrm{t}} - \lambda_\pi \phi_\pi + \lambda_{\mathrm{A}}\phi_{\mathrm{A}}) \\ \psi_{\mathrm{e}} &= N_{\mathrm{e}}(f_{\mathrm{e}} - \lambda_\delta \phi_\delta - \lambda_{\sigma'}\phi_{\sigma'}) \end{aligned} \tag{4}$$

where f_{t} and f_{e} are linear combinations of the atomic f_{C}, f_{D}, f_{B} and f_{A}, f_{B} orbitals. The symmetrized anionic p_π, s and p_σ orbitals are ϕ_π, ϕ_δ and $\phi_{\sigma'}$; the symmetrized A-catonic s, p orbitals are ϕ_{A}. The covalent-mixing parameters $\lambda_{\sigma'}$, λ_π, λ_{A}, λ_δ are roughly proportional to the overlap integral for atomic orbitals on neighboring ions and inversely proportional to their energy separation. Initially, the energy separations of cationic d and $\phi_{\sigma'}$ or ϕ_π are given by $E_{\mathrm{M}} - E_{\mathrm{I}}$, the difference between the Madelung energy and ionization potentials for the "effective" ionic charges, so that by symmetry

$$10\,\mathrm{Dq} = \Delta_{\mathrm{M}} + (\lambda_\sigma^2 - \lambda_\pi^2)\,(E_{\mathrm{M}} - E_{\mathrm{I}}),\ \lambda_\pi < \lambda_\sigma \tag{5}$$

where Δ_{M} is any electrostatic contribution to 10 Dq. The one-electron crystal-field splitting of the d-state manifold is shown in Fig. 7(a). The relationship $\lambda_\pi < \lambda_\sigma$ has been confirmed by nuclear magnetic resonance studies of $\mathbf{KMnF_3}$, $\mathbf{KNiF_3}$ and $\mathbf{K_2NiCrF_6}$ [*Sh70, Hu4*]. In these experiments the fractional occupancies by unpaired spins of the $2s$, $2p_\sigma$, and $2p_\pi$ orbitals are:

$$f x_{\mathrm{s}} = 2SA_{\mathrm{s}}/A_{2\mathrm{s}} \sim N_{\mathrm{s}}^2\lambda_{\mathrm{A}}^2, \quad f x_\sigma = 2SA_\sigma/A_{3\mathrm{p}} \sim N_\sigma^2\lambda_{\sigma'}^2, \quad f x_\pi = 2SA_\pi/A_{3\mathrm{p}} \sim N_\pi^2\lambda_\pi^2$$

where A_{s} is the isotropic component and A_σ, A_π the anisotropic components of the hyperfine interaction tensor A_{1j} entering the nuclear spin-electron spin coupling energy $\Sigma_j \boldsymbol{I}_1 \cdot \mathbf{A}_{1j} \cdot \boldsymbol{S}_j$. Interpretation of the phenomenological parameters λ_π, λ_σ and 10 Dq has been discussed extensively [*Hu4*].

With more than one outer d electron or d hole, it is necessary to introduce V_{el}, which is responsible for Hund's highest multiplicity rule (highest net S and L) for the free atoms. For four outer electrons, the atomic ground term is therefore ^{5}D. In a crystal, this rule may break down as a result of the crystalline

fields. Schematically, the Hund splitting Δ_{ex} for states of different spin and the one-electron splitting 10 Dq may be represented on the same energy diagram, as shown in Fig. 7(b). It follows from this figure that with four to eight outer d electrons, the magnitude of the net ground-state spin depends upon whether $(\Delta_{ex} - 10\,Dq)$ is positive or negative. If $\Delta_{ex} > 10$ Dq, the ion is in a high-spin state; if $\Delta_{ex} < 10$ Dq,

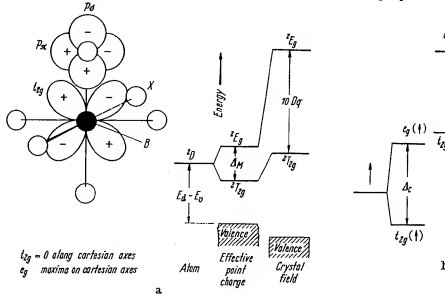

Fig. 7. One-electron crystal-field splitting of the d-state manifold of a transition-metal B cation in a cubic perovskite: a) $\Delta_{ex} = 0$ and b) schematically for $\Delta_{ex} \neq 0$, corresponding to more than one outer d electron.

Hund's rule breaks down and the ion is in a low-spin state. Since Δ_{ex} decreases with larger radial extension of the crystalline wave functions, it decreases with increasing covalent-mixing parameters λ_σ, λ_π. Simultaneously, from Eq. (5) it follows that 10 Dq increases with increasing covalency. Therefore there is a critical amount of covalent bonding beyond which Hund's rule breaks down. Covalency with a particular anionic sublattice increases with cationic charge and on going to the right through any long period of the periodic table. In oxides with the perovskite structure, only divalent and trivalent ions of the first long period are high-spin. Of these, trivalent nickel is low-spin and trivalent cobalt exhibits a variable high-spin to low-spin population as a function of temperature.

In general, it is necessary to use a multi-electron notation for the outer d electrons. Whereas atomic D states are split by the crystalline fields as shown in Fig. 7, atomic F states are split as shown in Fig. 8.

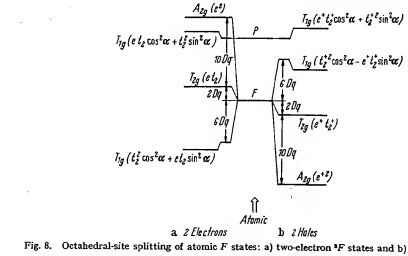

Fig. 8. Octahedral-site splitting of atomic F states: a) two-electron ^3F states and b) two-hole ^3F states.

Because the operator $L_z = -i\hbar\partial/\partial\phi$ is imaginary, the crystal-field splitting of f_B and f_O quenches the orbital angular momentum associated with these orbitals, so that the e_g orbitals have $m = 0$, 0 and the t_{2g} orbitals have $m = 0, \pm 1$. An isomorphism between f_O, f_D, f_B and atomic P orbitals simplifies calculation of V_{LS}. It is possible to treat the t_{2g} orbitals as atomic P orbitals if the sign of the spin-orbit-coupling

parameter λ is reversed [Gr9]. Therefore ground states having an orbital degeneracy and $m \neq 0$ are split by V_{LS} into $(2J + 1)$ multiplet states corresponding to states of different $J = L + S$. However, the order of the levels is inverted (largest J lowest for less than five d electrons, smallest J lowest for more than five d electrons) because of the change in sign of λ. According to the Landé interval rule, the separation between states J and $J + 1$ is $|\lambda|(J + 1)$. The first-order multiplet splittings, which do not include mixing of higher states of similar symmetry, are shown in Fig. 9 for Fe^{2+} and Co^{2+} ions. Note that the term is now identified by its symmetry character T_{2g} or T_{1g} rather than by its atomic orbital-momentum character D or F. Tab. 1 summarizes the various symmetry notations for different spin states.

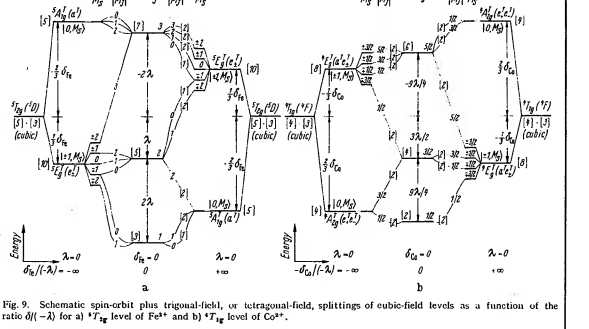

Fig. 9. Schematic spin-orbit plus trigonal-field, or tetragonal-field, splittings of cubic-field levels as a function of the ratio $\delta/(-\lambda)$ for a) $^5T_{2g}$ level of Fe^{2+} and b) $^4T_{1g}$ level of Co^{2+}.

Spin-orbit coupling introduces an axial symmetry to the charge distribution, where the spin (or atomic-moment) defines the axis. Therefore, if there is a noncubic component to the crystalline field ($V_{\text{n cub}} \neq 0$), then there is a spin-lattice interaction via the orbital-lattice interaction that introduces a magnetic anisotropy. For localized electrons, this is a local, one-ion anisotropy. Conversely, if the spins are ordered below some transition temperature, then the local interstices have time to relax about the noncubic charge distribution, thereby distorting the octahedral site. Therefore there is an intimate connection between the noncubic symmetry and the magnitude of the multiplet splitting. The noncubic component is usually parametrized as

$$V_{\text{n cub}} = \delta(L_z^2 - \tfrac{2}{3}), \tag{6}$$

and Fig. 9 includes the total perturbation $V_{LS} + V_{\text{n cub}}$ of the one-electron and two-electron ground states.

With one or two holes in a half-shell, the one-electron and two-electron energy diagrams are inverted. In these cases $M_L = \Sigma_i m_l = 0$, so that $V_{LS} = 0$, and there is no multiplet splitting.

Tab. 1 also displays the general ground-state wave functions for a magnetically ordered phase having collinear spins. The coefficients a_1, a_2, a_3 of the Kramers' doublets and b_1, b_2 of the singlets all depend upon the relative magnitudes of the five perturbation terms $V_{LS} + V_{\text{n cub}} + V_\lambda + \mathcal{H}_Z$ where $\mathcal{H}_Z$ is the Zeeman energy due to the internal molecular field resulting from magnetic order. The molecular-field approximation is used for the first-order, isotropic magnetic-coupling energy $\mathcal{H}_{ex}$, which is the dominant term in $\sum_j V_{ij}$ [see discussion of Eq. (13)]. This gives

$$\mathcal{H}_Z \approx 2J_p \langle S \rangle S_z \tag{7}$$

where J_p, the sum of all near-neighbor exchange parameters, can be determined from the temperature dependence of the magnetic susceptibility and z is along the axis of the average spin $\langle S \rangle$ on the neighboring cations. This term contributes to the spectroscopic-splitting factor g, and hence to the net atomic moment, if $V_{LS} \neq 0$. In Tab. 1, the components of the wave functions are designated by the notation $|M_L, M_S>$, where M_L, M_S are the azimuthal quantum numbers for the net orbital and spin momenta.

Tab. 1. Lowest terms and ground state wave function for octahedral-site cations having n localized outer *d* electrons

n	Ion	$t^{\zeta}e^{\eta}$	V_{el}	V_{cub}	V_{LS}	$V_{LS} + V_{n\,cub}(\delta < 0) + \mathscr{H}_Z$	$V_{LS} + V_{n\,cub}(\delta > 0) + \mathscr{H}_Z$
1	Ti^{3+}, V^{4+}, W^{5+}, Re^{6+}	t^1e^0	^2D	$^2T_{2g}$	$J = \frac{3}{2}$	$\| +1, +\frac{1}{2} >$	$a_1 \|0, +\frac{1}{2} > +a_2\| +1, -\frac{1}{2} >$
2	V^{3+}, Cr^{4+}, Mo^{4+}	t^2e^0	^3F	$^3T_{1g}$	$J = 2$	$\| +1, +1 >$	$b_1 \| +1, -1 > +b_2\| 0, 0 > +b_3 \| -1, +1 >$
3	V^{2+}, Cr^{3+}, Mn^{4+}, Mo^{3+}	t^3e^0	^4F	$^4A_{2g}$	$J = \frac{3}{2}$	$\| 0, +\frac{3}{2} >$	$\| 0, +\frac{3}{2} >$
4	Cr^{2+}, Mn^{3+}	t^3e^1	^5D	^5E_g	$J = 2$	$^5B_{1g} \| 0, +2 >$	$^5A_{1g} \| 0, +2 >$
	Fe^{IV}, Ru^{IV}, Os^{IV}	t^4e^0		$^3T_{1g}$	$J = 0$	$b_1 \| +1, -1 > +b_2 \| 0, 0 > +b_1 \| -1, +1 >$	$b_1' \| +1, -1 > +b_2' \| 0, 0 > +b_1' \| -1, +1 >$
5	Mn^{2+}, Fe^{3+}	t^3e^2	^6S	$^6A_{1g}$	$J = \frac{5}{2}$	$\| 0, +\frac{5}{2} >$	$\| 0, +\frac{5}{2} >$
	Ir^{IV}	t^5e^0		$^2T_{2g}$	$J = \frac{1}{2}$	$a_1 \| 0, +\frac{1}{2} > +a_2 \| +1, -\frac{1}{2} >$	$a_1' \| 0, +\frac{1}{2} > +a_2' \| +1, -\frac{1}{2} >$
6	Fe^{2+}, Co^{3+}	t^4e^2	^5D	$^5T_{2g}$	$J = 1$	$a_1 \| -1, +2 > +a_2 \| 0, +1 > +a_3 \| +1, 0 >$	$b_1 \| +1, -1 > +b_2 \| 0, 0 > +b_1 \| -1, +1 >$
	Co^{III}, Rh^{III}, Pt^{IV}	t^6e^0		$^1A_{1g}$	$J = 0$	$\|0, 0 >$	$\|0, 0 >$
7	Co^{2+}	t^5e^2	^4F	$^4T_{1g}$	$J = \frac{1}{2}$	$a_1 \| -1, +\frac{3}{2} > +a_2 \| 0, +\frac{1}{2} > +a_3 \| +1, -\frac{1}{2} >$	$a_1' \| -1, +\frac{3}{2} + a_2' \| 0, +\frac{1}{2} > +a_3' \| +1, -\frac{1}{2} >$
	Ni^{III}	t^6e^1		^2E_g	$J = \frac{1}{2}$	$^2B_{1g} \| 0, +\frac{1}{2} >$	$^2A_{1g} \| 0, +\frac{1}{2} >$
8	Ni^{2+}, Pd^{2+}	t^6e^2	^3F	$^3A_{2g}$	$J = 1$	$\| 0, +1 >$	$\| 0, +1 >$
9	Cu^{2+}	t^6e^3	^2D	^2E_g	$J = \frac{1}{2}$	$^2B_{1g} \| 0, +\frac{1}{2} >$	$^2A_{1g} \| 0, +\frac{1}{2} >$

3.1.3.2 Jahn-Teller distortions

If the cubic-field ground state of the B cation is an orbitally two-fold-degenerate E_g state, then the t_{2g} orbitals are either full or half-filled, so that $M_L = 0$, and there is no spin-orbit coupling ($V_{LS} = 0$). JAHN and TELLER [*Ja6*] have shown that, if there is no perturbation available to remove a ground-state orbital degeneracy, then there will be a spontaneous distortion to lower local symmetry below some transition temperature $\Theta_{trans} < T_{melt}$ where T_{melt} is the melting point. Since the energy gained by a local distortion is reduced by the work done against the elastic restoring forces of the crystal, transition temperatures Θ_{trans} are small for isolated ions. However, if all of the B cations are similar, then cooperative distortions are possible, and the net energy gained per ion is much greater because of the elastic-coupling energy V_λ of Eq. (2). Such a cooperative phenomenon is characterized by thermal hysteresis and a definite (usually first-order) transition temperature. Since they are due to electronic ordering, such transitions are martensitic.

VAN VLECK [*Va15*] pointed out that the normal vibrational modes that split an E_g electronic state are themselves twofold-degenerate with symmetry E_g. One mode gives the interstice a tetragonal distortion, the other an orthorhombic distortion. It follows that, from first-order theory, there is no static distortion of the interstice, only a dynamic coupling between the electronic charge density and the vibrational modes. Moreover, this dynamic coupling greatly enhances the two E_g vibrational modes and gives a dynamic splitting of the electronic E_g state. This mechanism has important consequences for the acoustic properties and, as discussed in 3.3, for the sign of the magnetic superexchange coupling.

Inclusion in the theory of higher-order coupling terms and anharmonic elastic terms shows that a static, tetragonal ($c/a > 1$) distortion of the interstice is stable below some Θ_{trans} [*Ka10*]. This sign for the static distortion was first established experimentally through the interpretation [*Go15*] and further study of cooperative tetragonal-to-cubic transitions in spinel systems. However, application to the perovskites requires a solution of the lowest-energy cooperative distortion via inclusion of the elastic-coupling energy V_λ. GOODENOUGH [*Go6*] proposed that individual tetragonal ($c/a > 1$) octahedra order their long axes alternately along [100] and [010] axes of the pseudocubic cell. KANAMORI [*Ka10*] generalized this solution to include an orthorhombic component to the local-octahedron distortions. This gives B-B separations within (001) planes having a long (l) and a short (s) B-X separation and along the [001] axis two intermediate (m) B-X separations where $s < m < (l + s)/2$. This prediction was later verified by HEPWORTH and JACK [*He9*] for □ MnF_3 and by OKAZAKI [*Ok1*] for $KCuF_3$ (see Fig. 10). Superposition of this distortion on an O-orthorhombic cell stabilizes the unique axis along the orthorhombic c-axis, and

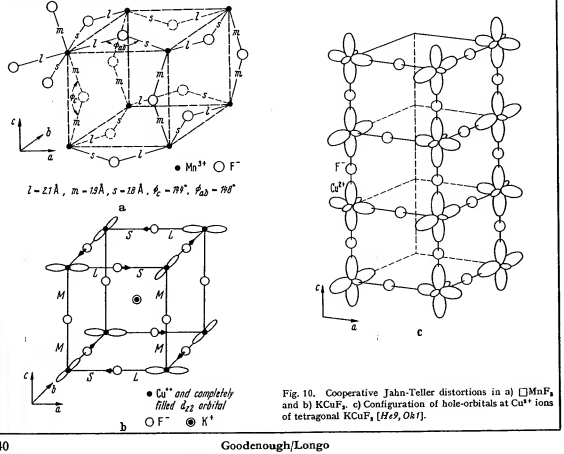

Fig. 10. Cooperative Jahn-Teller distortions in a) □MnF_3 and b) $KCuF_3$. c) Configuration of hole-orbitals at Cu^{++} ions of tetragonal $KCuF_3$ [*He9, Ok1*].

the axial ratios of the O-orthorhombic cell are transformed from $a < c/\sqrt{2}$ to $c/\sqrt{2} < a$. To signal the fact that a Jahn-Teller distortion (with or without spin-orbit coupling) has been superposed on a distortion due to relative ionic sizes, the notation O'-orthorhombic is used in Tab. 2 wherever $c/\sqrt{2} < a$.

The important B cations that exhibit dynamic and static JAHN-TELLER stabilizations in the absence of spin-orbit coupling are: Cu^{2+} $^2E_g(t_{2g}^6e_g^3)$, Cr^{2+} and Mn^{3+} $^5E_g(t_{2g}^3e_g^1)$, Ni^{III} $^1E_g(t_{2g}^6e_g^1)$, where Roman numerals are used for the valence state of a low-spin cation. Tab. 2 shows that O'-orthorhombic symmetry above a magnetic-ordering temperature is associated with these ions, provided the d electrons are localized, and only with these ions, with the exception of $LaVO_3$ and $CeVO_3$, where sharply enhanced distortions appear abruptly below Θ_N [*Ro3*; *Go10*]. The cubic $^3T_{1g}$ state of V^{3+} is orbitally threefold-degenerate, so that it may induce small distortions above Θ_N, larger distortions below Θ_N (see discussion *Go14*). $LaNiO_3$ remains $R\bar{3}c$ because the e_g electrons are collective. In $La_2Li_{0.5}Ni_{0.5}O_4$ crystals, on the other hand, the ordered Ni^{III} ions have localized e_g electrons, and there is a tetragonal ($c/a > 1$) distortion. The sign of this distortion is manifest by the large c/a ratio. Strictly speaking, this is not a Jahn-Teller distortion, since the K_2NiF_4 structure is tetragonal, but ordering of the localized electron of unpaired spin in the tetragonal field distorts the Ni^{III} octahedra to tetragonal symmetry with axes parallel to the unique axis. Pure Jahn-Teller distortions can be distinguished from distortions associated with spin-orbit coupling because they are independent of magnetic order and generally occur at a Θ_{trans} above the magnetic-ordering temperature.

3.1.3.3 Spin-orbit coupling

B cations having cubic-field ground-state terms T_{2g} or T_{1g} are orbitally threefold-degenerate with $M_L = 0, \pm 1$, so that $V_{LS} \neq 0$. The combined perturbations $V_{LS} + V_{neub}$ separate into secular equations for different M_J, as shown in Fig. 9. With a single outer electron, the $^2T_{2g}$ cubic-field term is split in two, the energies for different M_J shifting by

$$\begin{aligned} E_{3/2} &= \tfrac{1}{2}\delta - \tfrac{1}{2}\lambda \\ E_{1/2}^{\pm} &= -\tfrac{1}{4}\delta + \tfrac{1}{2}\lambda \pm \tfrac{1}{2}(\delta^2 + \lambda\delta + (\tfrac{9}{4}\lambda^2)^{1/2} \end{aligned} \tag{8}$$

where $\lambda > 0$. In a cubic field

$$E_{3/2} = E_{1/2}^{-} = E_{1/2}^{+} - \tfrac{9}{4}\lambda, \tag{9}$$

and spin-orbit coupling leaves an orbitally twofold-degenerate ground state. Therefore it is necessary to consider an additional Jahn-Teller stabilization via $V_{neub} + V_{\lambda} + \mathscr{H}_Z$. GOODENOUGH [*Go14*] has shown that it is necessary to consider two temperature regions: $T > \Theta_N$ and $T < \Theta_N$, where Θ_N is the temperature below which the spins order collinearly. In the paramagnetic domain $T > \Theta_N$, the molecular fields vanish ($\langle S \rangle = 0$) and, from Eq. (7), $\mathscr{H}_Z = 0$. In this case, the ground-state energy varies as (δ^2/λ). Since the work done against elastic restoring forces is $q_s\delta^2$, there is a spontaneous Jahn-Teller distortion, corresponding to $\delta > 0$, at a $\Theta_{trans} > \Theta_N$ only if the product λq_s is relatively small. In the magnetically ordered state ($T < \Theta_N$), on the other hand, there is an internal molecular field H_{int} at each atom, which produces a Zeeman splitting of the orbitals of different spin. The magnitude of this splitting depends upon the spectroscopic splitting factor, which has the components

$$g_{\parallel} = 2 - 2g_1(\delta/\lambda) \text{ and } g_{\perp} = 2 + g_1(\delta/\lambda) \tag{10}$$

where $g_1 > 0$. Therefore the Zeeman splitting in the molecular fields is maximized by making $\delta < 0$ and having the spins parallel to the unique axis defined by δ. Further, this energy is linear in δ, so that a spontaneous distortion should occur at some $\Theta_{trans} < \Theta_N$. A similar argument holds for the orbitally twofold-degenerate $J = 1$ and $J = \frac{1}{2}$ states of octahedral-site Fe^{2+} $^5T_{2g}$ and Co^{2+} $^4T_{1g}$.

In summary, if multiplet splitting leaves a ground state with a twofold, accidental orbital degeneracy, then there is a spontaneous Jahn-Teller distortion at some Θ_{trans} that removes this degeneracy. If $\Theta_{trans} > \Theta_N$, then $\delta > 0$. However, this alternative requires special crystallographic conditions that do not appear to be met in perovskites. On the other hand, a $\Theta_{trans} \leq \Theta_N$ and $\delta < 0$ can be generally anticipated wherever the spins order collinearly and the d electrons are localized. Further, from Eqs. (3) and (6), it follows that T_{2g} states (one outer t_{2g} electron) have $\delta < 0$ if the site symmetry is tetragonal ($c/a > 1$), whereas T_{1g} states (two outer t_{2g} electrons) have $\delta < 0$ if it is tetragonal ($c/a < 1$). Alternatively, distortions of the site symmetry may be to trigonal symmetry. A $\delta < 0$ corresponds to $\alpha < 60°$ for T_{2g} states, to $\alpha > 60°$ for T_{1g} states. These relationships are also summarized in Tab. 1. Experimentally, Fe^{2+} $^5T_{2g}$ octahedra become trigonal ($\alpha < 60°$) below Θ_N, as exhibited by $KFeF_3$, whereas Co^{2+} $^4T_{1g}$ octahedra become tetragonal ($c/a < 1$) below Θ_N, as exhibited by $KCoF_3$. Where $\Theta_{trans} = \Theta_N$, the magnetic-ordering temperature may be first-order. In addition, the spontaneous distortions introduce large magnetostriction and magnetic anisotropy.

The cubic-field ground state of V^{3+} $^3T_{1g}$ is orbitally threefold-degenerate. As a result, any spontaneous distortion must correspond to $\delta < 0$, i.e., tetragonal ($c/a < 1$) or trigonal ($\alpha > 60°$). However, as in the other cases a $\Theta_{trans} \lesssim \Theta_N$ is to be expected in the perovskite structure. The V^{3+} ion generally occurs in an O-orthorhombic perovskite, and superposition of a tegragonal ($c/a < 1$) distortion with coincident unique axes again results in O'-orthorhombic symmetry. The perovskite $LaVO_3$ exhibits an abrupt contraction of the c-axis on cooling through Θ_N.

3.1.4 The influence of collective-electron ordering

3.1.4.1 Band theory

Conventional band theory rests on three principal assumptions: (1) A description of the outer electrons may be built up from solutions of a single electron moving in a periodic potential. (2) Multiplet structure on individual atoms may be disregarded. (3) Electron-phonon interactions may be treated as a small perturbation. For an infinite crystal, the unperturbed solution of running waves in a periodic potential gives the Bloch functions and energies

$$\psi_{\boldsymbol{k}m} = \exp(i\,\boldsymbol{k}\cdot\boldsymbol{r})\; u_{\boldsymbol{k}m}(\boldsymbol{r});\; E_{\boldsymbol{k}} = E_0 + \hbar^2\boldsymbol{k}^2/2\boldsymbol{m}^* \tag{11}$$

where $\hbar\boldsymbol{k}$ is the momentum of an electron of effective mass $\boldsymbol{m}^*$ and $u_{\boldsymbol{k}}(\boldsymbol{r})$ is a periodic function. In the tight-binding approximation appropriate for narrow bands, the Bloch functions are

$$\psi_{\boldsymbol{k}}(\boldsymbol{r}) = 1/\sqrt{N}\sum_{n=1}^{N}\exp(i\,\boldsymbol{k}\cdot\boldsymbol{R}_n)\; w(\boldsymbol{r}-\boldsymbol{R}_n)$$

where $w(\boldsymbol{r}-\boldsymbol{R}_n)$ is a localized wave function for the atom at $\boldsymbol{R}_n$ defined by

$$w(\boldsymbol{r}-\boldsymbol{R}_n) = 1/\sqrt{N}\sum_{\boldsymbol{n}}\exp[i\,\boldsymbol{k}\cdot(\boldsymbol{r}-\boldsymbol{R}_n)]\,u_{\boldsymbol{k}}(\boldsymbol{r})$$

and $u_{\boldsymbol{k}}(\boldsymbol{r})$ is a localized crystalline orbital. At the Brillouin-zone boundries defined by

$$2\boldsymbol{k}\cdot\boldsymbol{K} + |\boldsymbol{K}|^2 = 0, \tag{12}$$

where $\boldsymbol{K}$ is a reciprocal lattice vector, there are energy discontinuities in energy-momentum space. In polar insulators, this introduces an energy gap E_g between occupied, primarily anionic states and empty, primarily cationic states. Cooperative displacements δ of the cationic sublattice relative to the anionic sublattice may increase this gap, thereby stabilizing the total energy of the occupied states by $\varepsilon_{\delta}\delta^2$. Since the resulting elastic-strain energy is $q_{\delta}\delta^2$, there can be a spontaneous displacement only for the exceptional case $q_{\delta} < \varepsilon_{\delta}$ and a ground state corresponding to a small distortion parameter δ. In this case vibrational entropy may stabilize the higher symmetry at the higher temperatures. This differs from the usual criterion for spontaneous distortions, where a term linear in δ is identified. There appear to be two situations occuring in perovskites where the requirement $q_{\delta} < \varepsilon_{\delta}$ is met: (1) Where B-cations have empty d orbitals, there is a critical range of covalent-mixing parameters through which the site preference changes from octahedral to tetrahedral. In this range q_{δ} is very small for B-cation displacements within an octahedron that reduce the coordination number from six towards four. The origin of the small q_{δ} is a balance of the electrostatic energy lost and covalent-bond energy gained on going to smaller anion coordination. (2) The high polarizability of the outer core electrons of Pb^{2+} and Bi^{3+} ions makes q_{δ} relatively small, so that displacements that permit a relatively large ε_{δ} can occur spontaneously.

What distinguishes these spontaneous distortions from those due to an ordering of localized electrons is the displacement of the cations from the centers of symmetry of their interstices. (The Jahn-Teller distortions, with or without spin-orbit coupling, leave the cations in the centers of symmetry of their interstices.) Unlike the structures, such as corundum, where pairs of octahedra share a common face, these cationic displacements from the centers of symmetry of their interstices do not follow from point-charge electrostatic arguments. In polar insulators, these displacements lead to ferroelectricity or antiferroelectricity, and they often induce displacements of neighboring cations. Further, where the requirement $q_{\varepsilon} \approx \varepsilon_{\varepsilon}$ occurs just above $\Theta_{trans.}$, there must be a strong interaction of the bonding (mostly anionic) electrons with those vibrational modes that anticipate the cooperative ionic displacements below $\Theta_{trans.}$ These "soft" vibrational modes impart several anomalous physical properties, including a high electric susceptibility.

3.1.4.2 Distortions due to B-X bonding

Transition-metal cations having no outer d electrons have the following site preferences:

Sc^{3+}	$\underline{Ti^{4+}}$	$\underline{V^{5+}}$	Cr^{6+}	Mn^{7+}
Y^{3+}	Zr^{4+}	$\underline{Nb^{5+}}$	$\underline{Mo^{6+}}$	Tc^{7+}
	Hf^{4+}	$\underline{Ta^{5+}}$	$\underline{W^{6+}}$	$\underline{Re^{7+}}$

where cations at the left of each row have definite octahedral-site (or larger anion coordination) preference and those to the right have definite tetrahedral-site preference. Those underlined by a solid line may be stabilized in the octahedral sites of a perovskite-type structure, but they tend to induce spontaneous ferroelectric or antiferroelectric distortions, the ions moving cooperatively out of the centers of symmetry of their interstices. The ions underlined by dashed lines only occur in ordered perovskites $A_2BB'O_6$ and $A_3BB'_2O_9$. In general, they are found in tetrahedral sites or in strongly distorted octahedral sites. However, in the ordered perosvkites they are able to strongly polarize the anion near neighbors so as to stabilize the octahedral symmetry.

It is significant that spontaneous ferroelectric distortions are only induced by B cations if these are transition-metal cations having empty d orbitals. It is also significant that the change from octahedral-site to tetrahedral-site preference is associated with a relative stabilization of the d orbitals (larger atomic number in any long period) as well as with a decrease in ionic size. (The ionic radii decrease in the order Y^{3+}, Sc^{3+}, Hf^{4+}, Zr^{4+}, Ta^{5+}, Nb^{5+}, Ti^{4+}, W^{6+}, Mo^{6+}, Re^{7+}, V^{5+}, Tc^{7+}, Cr^{6+}, Mn^{7+}). The greater the relative stability of the d orbitals, the larger are the parameters λ_σ and λ_π of Eq. (4), and these are enhanced by any displacement that decreases a B-X separation. Such an enhancement stabilizes the occupied states at the expense of the d states, and a net stabilization can occur if the d states are empty. Also the smaller the cationic size, the smaller the elastic resistance to displacements within an octahedral interstice. (Phenomenological ionic models for the ferroelectric distortions have also been given [*Me7, Ha33*].)

There are three B-cation displacements relative to their octahedral interstices that would simultaneously stabilize the occupied anionic p_π orbitals relative to the unoccupied t_{2g} orbitals: (1) *Tetragonal symmetry*. Displacements along an [001] axis that create alternate long and short B-X distances along this axis would stabilize s, p_σ and the two p_π orbitals per anion on this axis and strongly polarize the charge density toward the short B-X separation. (2) *Orthorhombic symmetry*. Displacement along a [110] axis that created two shortest and two longest B-X distances would stabilize the s, p_σ and the two p_π orbitals per anion on two out of the three cartesian axes. (3) *Rhombohedral symmetry*. Displacement along a [111] axis would stabilize the s, p_σ and the two p_π orbitals per anion on all the anions. These three possibilities are illustrated in Fig. 11.

Such distortions also induce changes in the A-X separations, and the particular cooperative distortion that is stabilized depends upon the character of the A-X bonding. The covalency contribution to the A-X bond increases with formal A cationic charge; for a fixed charge it decreases with increasing atomic number of the A cation down any column of the periodic table. If A-X covalent bonding is relatively strong and the perovskite is distorted to O-orthorhombic symmetry, all ferroelectric distortions may be quenched because the p_π orbitals are stabilized by σ-bonding with the A cations. This appears to be illustrated by $CaTiO_3$, and almost so by $SrTiO_3$. On the other hand, if the A atom is stabilized by a polarization of its outer core electrons (Pb^{2+} and Bi^{3+} as discussed in 3.1.4.3), then a tetragonal, ferroelectric distortion is stabilized so as to allow a cooperative displacement of the A and B cations, the A cation moving along the [001] axis to stabilize two p_π orbitals per anion not on [001] axes. This is illustrated by the $PbTiO_3$ structure of Fig. 12. If the covalency contribution to the A-X bonding is relatively weak, then the B-X covalency contribution should dominate. For large A cations ($t > 0.9$), this would stabilize a ferroelectric, rhombohedral distortion at lowest temperatures, as illustrated by $BaTiO_3$. As the temperature increases, successive distorted structures ($R^{\text{II}}_{\text{II}} \rightarrow O^{\text{II}}_{\text{II}} \rightarrow T^{\text{II}}_{\text{II}} \rightarrow C$) introduce incremental additions to the entropy. However, a small A cation and weak A-X covalency contribution may lead to a ferroelectric distortion superposed on the O-orthorhombic structure to give the $O^{\text{II}}_{\text{II}}$-orthorhombic structure of $CdTiO_3$ or $NaTaO_3$ shown in Fig. 13. Even more complex distortions are found in $NaNbO_3$ [*Vo6*]. The room-tem-

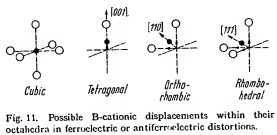

Fig. 11. Possible B-cationic displacements within their octahedra in ferroelectric or antiferroelectric distortions.

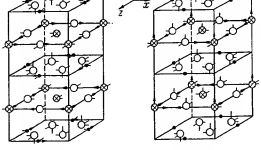

Fig. 13. Ionic displacements in a) $CdTiO_3$ and b) $NaTaO_3$ [*Ka22*].

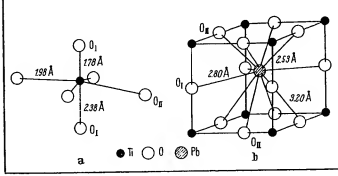

Fig. 12. Tetragonal $PbTiO_3$: a) environment of Ti and b) environment of Pb [*Sh21*].

perature form has parallel pairs of (001) NbO_2 planes coupled antiparallel to give an antiferroelectric phase, as shown in Fig. 14. The Na atoms are also displaced antiparallel to one another.

3.1.4.3 Distortions due to core polarization: Pb^{2+} and Bi^{3+}

Lead and bismuth are heavy ions, and the 6*s* orbitals are sufficiently more stable than the 6*p* orbitals that Pb^{2+} and Bi^{3+} ions are commonly stable. However, the outer $6s^2$ core electrons have a relatively large radial extension, making the ionic radius large, and this reduces the overlap of the 6*p* orbitals with the orbitals on near-neighbor anions. This reduction in overlap reduces the strength of the A-X bond. However, hybridization of 6*s* and 6*p* orbitals, which costs the energy separation of 6*s* and 6*p* orbitals, produces a polarization of the outer-core electrons, so that the effective ionic radius is much smaller on one side of the cation than on the other. This permits the formation of a much more stable bond on one side of the cation, and the energy gained in this bonding may be greater than the hybridization energy required to polarize the core. It is for this reason that Pb^{2+} and Bi^{3+} ions are stabilized in many crystals with an asymmetric anion coordination.

There are three possible displacements of the A cations that would stabilize the anion p_π orbitals (which σ-bond with the A cations): (1) *Tetragonal symmetry*. Displacement of the A cations along [001] axes to stabilize the two p_π orbitals per anion not on [001] axes, as found for $PbTiO_3$ (see Fig. 12). (2) *Orthorhombic symmetry*. Displacement of the A cations along [110] axes to stabilize strongly one p_π orbital per anion on [001] axes and less strongly one p_π orbital per anion not on [001] axes. The smallest induced distortion of the B-cation octahedra occurs for an antiferroelectric displacement of the type illustrated by $PbZrO_3$, Fig. 15. (3) *Rhombohedral symmetry*. Displacement of the A cations along [111] axes to stabilize strongly one p_π orbital per anion. To be cooperative, such a distortion must be ferroelectric, as in $BiFeO_3$, Fig. 16. Further, since the A cation is moved toward a B cation, there is an electrostatic repulsion between them that displaces the B cation from the center of symmetry of its interstice.

Given spontaneous distortions due to A-cation displacements, there remains the possibility that electron ordering among localized *d* electrons on B cations can superpose an additional distortion. Whether this is the origin of the triclinic symmetry reported for ferromagnetic $BiMnO_3$, where Mn^{3+} is a Jahn-Teller ion, is not known.

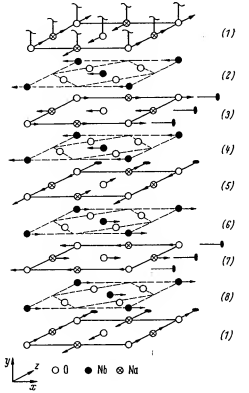

Fig. 14. Ionic displacements in orthorhombic $NaNbO_3$. The shifts of the anions in NbO_2 planes and the small *x* shifts of the Nb ions have been omitted for clarity [*Vos*].

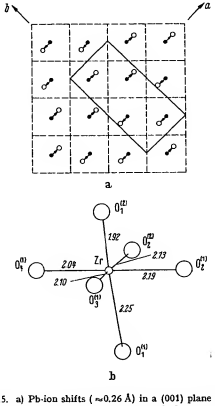

Fig. 15. a) Pb-ion shifts (≈0.26 Å) in a (001) plane of antiferroelectric $PbZrO_3$. b) Distorted Zr octahedra as a result of simultaneous anion displacements. Zr-O distances are given in [Å] [*Sas, Jos*].

3.1.4.4 Competitive phases

A few compounds have atomic radii compatible with the formation of a perovskite phase and yet are stabilized in other structures at ordinary temperature and pressure. Two important competitive structures of this type are represented by $YAlO_3$ and $PbRuO_3$. Both of these compounds convert to the perovskite structure under hydrostatic pressure.

The hexagonal $YAlO_3$ structure of Fig. 17 (a) consists of close-packed layers having the sequence *b-a-b'-a-b-c-b'-c-b*, where *b* is an A-cation layer, *b'* is a B-X layer with anions stacked beneath A cations (*b* stacking) and B cations in the trigonal bipyramids formed by face-shared tetrahedra in the hexagonal *a-b-a* or *c-b-c* anion-stacking sequence. The structure apparently forms because both the A cations and the B cations simultaneously approach the lower limit for cationic size: $r_B = 0.51$ Å, $r_A = 0.90$ Å. The small Al^{3+} ion is relatively stable in the five-fold coordination of the trigonal-bipyramid sites, and the small Y^{3+} ion is more stable in an eightfold (or 6 + 2) coordination instead of a twelvefold (or 9 + 3) coordination. These site preferences reflect an increased stabilization of the bonding, anionic orbitals as a result of closer cation-anion distances.

The antiferromagnetic, ferroelectric compound $YMnO_3$ has a similar structure, but with an *a*-axis $\sqrt{3}$ larger than that of $YAlO_3$ to give six molecules per unit cell. The Mn^{3+} ion can be stabilized in a trigonal-bipyramid site because it has four outer *d* electrons with configuration $e_g^2 e_g^2 a_1^0$, where the empty a_1 orbital is directed along the *c*-axis to bond covalently with the two collinear oxygen ions. The larger unit cell and the ferroelectricity are reflected in the complex magnetic order shown in Fig. 17 (b). Below Θ_N, exchange striction favors antiferromagnetic Mn-O-O-Mn interactions. The ferroelectric transition that occurs above 600 °C is apparently due to the relatively large size of the Mn^{3+} ion, which creates a large enough interstice for the Y^{3+} ion that it is stabilized by a displacement from the center of symmetry of its interstice so as to lower its near-neighbor anion coordination from eight toward seven.

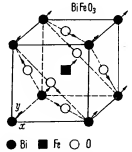

Fig. 16. Structure of $BiFeO_3$ showing displacements in perovskite subcell [*Mi0*].

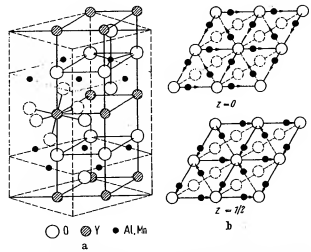

Fig. 17. a) Comparison of the unit cells of $YAlO_3$ (solid lines) and $YMnO_3$ (dashed lines). b) Magnetic structure of $YMnO_3$ [*Be36, Be39*].
$a = 3.678$ Å, $c = 10.52$ Å for $YAlO_3$.

Cubic $PbRuO_3$ gives an x-ray pattern of the pyrochlore structure, corresponding to chemical formula $A_2B_2O_7$, and therefore may be written as $Pb_2Ru_2O_6\oplus$. This structure is competitive with the perovskite structure in several $PbB^{4+}O_3$ compounds. It has been shown [*Lo4*] that the anion vacancies $\oplus$ are located at the centers of Pb^{2+}-ion tetrahedra sharing common corners and that the electrostatic repulsion between the Pb ions may be counteracted by a transfer of the two outer-core electrons per Pb ion to the $\oplus$ sites, which act as traps for four electrons per vacancy. Thus the outer core electrons at the Pb^{2+} ions induce a completely new structure rather than a ferroelectric-type displacement of the A-cations within the perovskite structure. This new structure contains B cations in corner-shared octahedra, as in perovskite, but the B-X-B angle is reduced to about 135°. This structure is also stabilized in $AgSbO_3$ [*Sc22*] presumably because there is a small effective charge on the Ag^+ ions. The pyrochlore $A_2B_2O_7$ structure itself is competitive if attempts are made to force a low valence state on one of the cations.

3.1.5 Structures encountered with ordered B, B' cations

3.1.5.1 Same B atom

There are three ways of creating two different cations from the same atom:

(1) Two A cations of different valence can create two different valence states of the same B atom, and these may order at lower temperature as a result of different cationic charge. The ordering temperature may be quite low, since only electron transfers are required for cationic ordering. This is illustrated by $(La_{0.5}^{3+}Ca_{0.5}^{2+})(Mn_{0.5}^{3+}Mn_{0.5}^{4+})O_3$, which has the Mn^{3+}, Mn^{4+} ordering in a rocksalt-type array. Because $Mn^{3+}(d_{\varepsilon_g}^3 d_{\gamma_g}^1)$ is a Jahn-Teller ion having localized outer d electrons, there is also a cooperative distortion to tetragonal ($c/a > 1$) symmetry of the Mn^{3+}-occupied octahedra, and the ordering of these distortions gives a macroscopic distortion to tetragonal ($c/a < 1$) symmetry (see Fig. 26).

(2) Where the energy difference between the high-spin and low-spin states of the B cation are nearly equal, the populations of the two energy states approach each other at higher temperatures. In $LaCoO_3$, high-spin Co^{3+} and low-spin Co^{III} are separated by only $E_{t_2} - E_{III} \approx 0.08$ eV, and the populations of the two spin states are nearly equal at 400 °K. This temperature is sufficiently low that ordering of the two different spin states occurs above this temperature, and the symmetry changes from $R\bar{3}c$ to $R\bar{3}$ [*Ra3*]. In this case, it is the difference in ionic size and covalent bonding, which results in a difference in the effective ionic charge – not the formal ionic charge – that is the driving force for the ionic ordering.

(3) Disproportionation of B^{m+} cations into $B^{(m-1)+}$ and $B^{(m+1)+}$ cations may create ions of different size and charge that become ordered. This is illustrated by $\square PdF_3$, which has been shown by magnetic susceptibility measurements to be $Pd^{2+}Pd^{IV}F_6$ [*Ba1f9*]. (The A cation is missing.) Such a disproportionation permits the formation of $(PdF_6)^{2-}$ clusters in which the anionic orbitals are stabilized by strong covalent mixing with the σ-bonding $4d$ orbitals of e_g symmetry. This is accomplished by a shifting of the F^- ions toward the Pd^{4+} ions and away from the Pd^{2+} ions. Simultaneously, the anionic shift reduces covalent mixing in the occupied, antibonding $4d$ orbitals of e_g symmetry at the Pd^{2+} ions. These orbitals are therefore localized and further stabilized by intra-atomic exchange (Hund splitting), so that each Pd^{2+} ion carries an atomic moment of $2\mu_B$. Were there no disproportionation, the single electron per low-spin Pd^{III} ion would occupy antibonding e_g orbitals that were more unstable than the occupied, localized e_g orbitals at the Pd^{4+} ions. However, the transformation $2\,Pd^{III} \rightarrow Pd^{4+} + Pd^{IV}$ costs ionization energy, and this is usually too large (as in $LaNiO_3$) for disproportionation to occur.

3.1.5.2 Different B atoms

There are many examples of ordered B, B' structures in compounds having different B atoms: $A_2^+B^+B'^{5+}F_6$; $A_2^+B^{3+}B'^{5+}O_6$, $A_2^+B^{4+}B'^{4+}O_6$, $A_2^{2+}B^{+}B'^{7+}O_6$; $A_2^{3+}B^{3+}B'^{4+}O_6$, $A_2^{3+}B^{+}B'^{5+}O_6$, and $A_2^{3+}B_2^{+}B'^{6+}O_6$. In the $A_2BB'X_6$ group, ordering is on alternate (111) planes of B cations, in the $A_3B_2'X_9$ group the B' cations occupy every third B-cation (111) layer, Fig. 1(c). The probability for an ordered arrangement of the B, B' cations is determined by the differences between their ionic charges and their ionic radii [*Fe22*, *Fe23*, *Ga1*, *Ga10*]. To first approximation, the order-disorder transition temperature Θ_{od} induced by the charge difference $\Delta q = (q' - q)$ at cations B' and B is $\Theta_{od} \sim (\Delta q)^2$. Thus superstructure has been observed in all the known compounds having $(\Delta q)^2 = 36$ and 16, whereas those having $(\Delta q)^2 = 4$ are disordered unless there is a relatively large difference in ionic sizes. The minimum difference in ionic size that results in ordered $A_2^+B^{3+}B'^{5+}O_6$ compounds is $|r_B - r_{B'}|/r_B \approx 0.09$, and this has been achieved where B' = Nb or Ta, having empty d orbitals for the formation of stable $(B'O_6)^{7-}$ clusters, while the B cation has no relatively stable, empty d orbitals.

Given the formation of $(B'X_6)$ octahedra, a confusion arises as to where the structure corresponds to an ordered $A_2BB'O_6$ perovskite built up of corner-shared octahedra plus A cations and where it corresponds to the isostructural $(NH_4)_3FeF_6$ structure, which consists of discrete $(B'X_6)$ octahedra separated by A and B cations. (The cubic K_2NaAlF_6 structure with space group T_h^1(Pa3) is similar to $(NH_4)_3FeF_6$, but has a lower symmetry because there are very small rotations of the $(B'X_6)$ octahedra.) Some authors [*Fe22*] select as a criterion for the perovskite structure the cationic radius ratio $r_B/r_A < 0.8$ where $r_B > r_{B'}$. This decision is based on the observation that a plot of the cubic lattice parameter a_0 vs. B-cation radius r_B is a straight line for $r_B/r_A < 0.8$, but bends over for $r_B/r_A > 0.8$. However, this probably reflects the ratio at which electrostatic forces inhibit (or reverse) any A-cation displacements rather than the ratio at which discrete $(B'X_6)$ octahedra are formed. For most physical properties this criterion is probably arbitrary.

Without electron-ordering distortions superposed on the size effects, ordered $A_2BB'X_6$ perovskites can be described by either the O-orthorhombic cell of Fig. 5 or by the rhombohedral $R\bar{3}$ (or $R\bar{3}m$) cell of Fig. 6. Where $\alpha = 60°$, a tetramolecular cubic cell may be chosen provided the A cations are not displaced from their ideal positions. Like cubic $(NH_4)_3FeF_6$, the cubic cell has the space group O_h^5 ($Fm3m$) with B cations in 4(b) $(\frac{1}{2}, \frac{1}{2}, \frac{1}{2})$; f.c., A cations in 8(c) $\pm$ $(\frac{1}{4}, \frac{1}{4}, \frac{1}{4})$; f.c., B' cations in 4(a) (0, 0, 0); f. c., and X-anions in 24(e) $\pm$ (u, 0, 0; 0, u, 0; 0, 0, u); f.c. with $0.2 < u < 0.25$. However, even where $\alpha = 60°$, motions of the A cations along the [111] axes may occur, thereby destroying the cubic symmetry.

If an electron-ordering transition superposes a distortion at every other octahedron of Fig. 5, either the B or the B' octahedra remaining cubic, cooperative elastic interactions between the distorted octahedra give a further reduction in symmetry. The resulting monoclinic cell [*Fi9, Bi8*], which is pseudotrichinic, is not to be confused with the pseudomonoclinic symmetry reported in early work for the O-orthorhombic structures. The origin of the superposed electron-ordering transition could be either a Jahn-Teller ordering of localized electrons or a ferroelectric-type displacement of the anions about a $(B'X_6)$ octahedron.

Several $Ca_2B^{2+}Ta^{5+}O_6$ and $Sr_2B^{3+}Nb^{5+}O_6$ perovskites having B = rare-earth atom exhibit the monoclinic symmetry of a distorted O-orthorhombic cell [*Fi8*]. Since the 4*f* electrons at the rare-earth ions are localized, it is tempting to attribute this to a Jahn-Teller distortion with spin-orbit coupling. Although Fig. 9 shows that the octahedral site splitting of one-electron 4*f* orbitals gives orbitally threefold-degenerate levels having an accidental degeneracy that is not removed by spin-orbit coupling, nevertheless there are two reasons why this explanation cannot be correct: (1) There is no magnetic ordering of the 4*f* electrons at room temperature and (2) Sr_2GdNbO_6 shows the distortion even though Gd^{3+} has a half-filled $4f^7$ shell, which has no orbital degeneracy associated with the ground state. It is therefore concluded that the additional distortions are due to the potentially ferroelectric cations Nb^{5+} and Ta^{5+}.

3.1.5.3 Complex alloys $A_2BB'X_{6}$, where $B = M_{12}$, $B' = M_8$

Several complex interstitial alloys have a formal structural relationship to the ordered perovskite $A_2BB'X_6$ as well as interesting magnetic properties. In this group, having space group Fm3m, the B position is occupied by a thirteen-atom cluster consisting of a metal atom at position 4(a) at the center of a cubo-octahedral, twelve-atom cluster of M atoms at positions 48(h); the B' position is occupied by a simple cube of eight M' atoms at 32(f). The three principal axes of each cluster are along the cubic axes of the perovskite cell, as shown schematically in Fig. 18, so that each X atom at positions 24(e) has eight near neighbors. The eight A atoms of the tetra-molecular cell are at the 8(c) positions. The 4(b) position at the center of the M_8' clusters is empty. Alloys with this structure include the ferromagnetic borides $Al_2[(AlM_{12})(M_8')]B_6$, where M = Fe, Co, Ni, as well as $Cr_{23}C_6$.

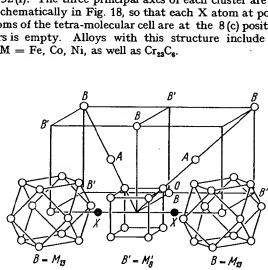

Fig. 18. One quadrant of the $A_2BB'X_6$ structure showing the atomic positions of the B = M_{12} and B' = M_8' clusters [*Wi19*].

3.1.6 First-order magnetic transition in $M^cXM_6^f$ perovskites

Many perovskites $M^cXM_6^f$ exhibit first-order phase changes at magnetic-ordering transitions. Most of these are reported to be cubic-to-cubic transitions, but in **$ZnCMn_6$** it is a tetragonal (ferrimagnetic)-to-cubic (ferromagnetic) transition. These crystallographic changes are induced by a complex interplay of collective electrons in overlapping bands. Because of the intimate connection with the magnetic properties and because of the necessarily speculative character of any model at this time, discussion of these compounds is deferred to 3.5.

3.1.7 Data: Crystallographic properties of ABX_3, $A_2BB'X_6$, $A_3B_2'BX_9$ and $A(B_2''B_2'B_2'')X_3$ compounds with perovskite or perovskite-related structure (Tab. 2)

Tab. 2.

Within any section, the compounds are in general first ordered according to the atomic number of the B cation and then by the basicity of the A cation. For the ordered perovskites of Tab. 2b, c, d, the compounds are further ordered by the atomic number of the other B cation. The order of the sections is as follows:

Tab. 2a — ABX_3

$A^{2+}LiH_3$
$A(H_2O)(Li_{1/3})_3$; $A = I^{-1}, Br^{-1}$
$A^+B^{2+}X_3$; $X = F^{-1}, Cl^{-1}, Br^{-1}$
$A^+B^{5+}O_3$; B = V, Nb, Sb, Ta, I, Pa, U
$A^{2+}B^{4+}O_3$; B = Ti, V, Cr, Mn, Fe, Co, Ni, Ge, Zr, Mo, Tc, Ru, Sn, Ce, Pr, Hf, Re, Ir, Pb, Th, U, Np, Pu
$A^{3+}B^{3+}X_3$ or $A^{2+}B^{3+}X_3$; X = S or Se, B = Ti, Zr, Ta, In, Ga
$A^{3+}B^{3+}O_3$; B = Al, Sc, Ti, V, Cr, Mn, Fe, Co, Ni, Ga, Y, Nb, Rh, In, Ho, Er, Tm, Yb, Lu

Tab. 2b — $A_2BB'X_6$

$A_2BB^{3+}X_6$; X = F^{-1}, Cl^{-1}, B^{3+} = Al, Sc, Ti, V, Cr, Mn, Fe, Co, Ni, Cu, Ga, Ag, In, Ce, Pr, Au, Tl
$A^{2+}A^{3+}B^{3+}B^{4+}O_6$; B^{4+} = Ti, Ir
$A_2BB^{4+}O_6$; B^{4+} = Ti, Mn, Ge, Zr, Ru, Ir
B^{4+} = V, Nb, Sb, Ta, Bi, Pa, Pu
B^{4+} = Mo, Te, W, $Re^{4+,5+}$, $Os^{4+,5+}$, $U^{4+,5+}$, Np^{5+}, Pu^{5+}
B^{7+} = Tc, Re, Os, I

Tab. 2c — $A_3BB_2'O_9$

$A_3BB_2^{5+}O_9$; B^{5+} = Nb, Ru, Sb, Ta
$La_3Co_2B^{5+}O_9$; B^{5+} = Nb, Sb
$A_3B_2B^{6+}O_9$; B^{6+} = Mo, W, Re, U

Tab. 2d — $A^{2+}(B_2B_2'B_2'')O_3$

Abbreviations in Tab. 2:
Symmetry: C = cubic, H = hexagonal, M = monoclinic, O = orthorhombic ($a < c/\sqrt{2}$), O' = orthorhombic ($c/\sqrt{2} < a$), R = rhombohedral, T = tetragonal, Tr = triclinic.
Remarks: for abbreviations, see p. 131.

Tab. 2a. ABX_3 compounds

Compound	Sym	a Å	b Å	c Å	angle	Ref.	Remarks	Magnetic Data
$A^+B^+Li^+H_3^{-1}$								in 3.3.4, Tab.
$BaLiH_3$	C	4.023				*Me25*	P&S [*Me26*]; Neutron diffraction shows S.G. Pm3m [*Ma11a*]	
$BaLiD_3$	C	4.02				*Ma11a*	Neutron diffraction shows S.G. Pm3m [*Ma11a*]	
$SrLiH_3$	C	3.833				*Me25*	P&S [*Me26*]	
$EuLiH_3$	C	3.796				*Me24*		
$BaLiF_3$	C	3.996				*La1*	P&S [*Ro20, Ba22a, Bu3a*]	
$A\,(H_2O)\,(Li_{1/3})_3$; A = I^{-1}, Br^{-1}								
$I(H_2O)\,(Li_{1/3})_3$	C	4.296				*Wa6*		
$Br(H_2O)\,(Li_{1/3})_3$	C	3.99				*Ke14*		
$A^+B^{2+}X_3$; X = F^{-1}, Cl^{-1}, Br^{-1}								
$CsMgF_3$	H	6.04		14.45		*Lo16*	Hex (6L), high pressure phase	
	H	6.16		22.15		*Lo16*	Hex (9L), high pressure phase	
	T	9.39		8.72		*La1*	Trans. [*Ba22a, Da4a*]	
$RbMgF_3$	M	8.19	8.19	8.19	$\beta = 98°\ 30'$	*La1*	Struct. with Co, Ttex (6L), $\Theta_D = 15$ °K (50% Co) [*Sh1a*]	
$KMgF_3$	C	3.973				*Re6*	P&S [*De22, La1, Be53*], I.R. spectra [*Pe5, Yo2*] NMR, F^{19} [*Al1a*], elastic properties [*Re7a*]	
$NaMgF_3$	O	5.363	5.503	7.676		*Ch5*	P&S [*La1, Be53, Ru8, Ba1*], NMR, F^{19} [*Al1a*]	
	T	3.942		3.933		*Ch5*	$T = 760$ °C, tetr. $760 < T < 900$ °C	
	C	3.955				*Ch5*	$T = 900$ °C, cubic $T \geq 900$ °C	
NH_4MgF_3	C	4.06				*Ch8a*	Pseudocubic	
$CsMgCl_3$	H	7.278		6.19		*Yd1*	Hex (2L)	
$KMgCl_3$	O	6.954	6.971	9.922		*Br28*	Absorption spectra: Ni [*Br28*], ESR: Mn [*Zd1*]	
$CaCaF_3$	C	4.523				*La1*		
$RbCaF_3$	C	4.457				*La1*		
$KCaF_3$	C	8.76				*Br9*	P&S [*La1*]	
$CsCaCl_3$	C	5.396				*Yd1*		
$CsTiCl_3$	H	7.297		6.048		*Yd1*	Hex (2L)	

Compound	Sym	*a* Å	*b* Å	*c* Å	angle	Ref.	Remarks	Magnetic Data
$A^+B^{2+}X_3$; X = F^{-1}, Cl^{-1}, Br^{-1} (continued)								in 3.3.4, Tab.
$CsVCl_3$	H	7.23		6.03		*Se1b*	Hex (2L), P&S [*Yd1*]	
$RbVCl_3$	H	7.04		6.0		*Gr8a*	Hex (2L), optical and magnetic properties	
$KVCl_3$	H	6.90		5.98		*Se1b*	Hex (2L), P&S [*Yd1*]	
$RbCrF_3$	T	6.149		8.088		*Vo1*	P&S [*Co27*]	
$KCrF_3$	T	6.04		8.01		*Co27*		6
	C	4.158				*Co27*	T = 500 °C, P&S [*Ed2, Vo1, Kn3, Yo1, Pe2a*]	
	T	8.544		7.968		*Sc1*	Neutron diffraction	
$NaCrF_3$	M	5.695	5.885	7.639	β = 87° 48'	*Vo1*	*a* and *b* axis said to double	
$(NH_4)CrF_3$	T	6.232		7.954		*Vo1*		
$TlCrF_3$	T	6.194		8.064		*Vo1*		
$CsCrCl_3$	H	7.249		6.228		*Yd1*	Hex (2L), P&S [*Se2*]	
$RbCrCl_3$	H	7.03		6.08		*Se2*	Hex (2L) pseudohexagonal	
$CsMnF_3$	H	6.213		15.074		*Za1*	Hex (6L), Θ_N = 54 °K, P&S [*Si14, Be19*], neutron diffraction [*Pi1*], optical properties [*St28, St30*], NMR [*Mi4, We11*], AFMR [*Wi14*], magnetic properties [*Le3, Le4, Se1*], S.S. with K and Na [*Be19a*]	
	C	4.328				*Lo1b*	High pressure phase, P&S [*Sy1*]	
$RbMnF_3$	C	4.2396				*Wa8*	P&S [*Si14, Be19, Co25, Ho17*], cubic to T = 20 °K [*Te4*], dielectric properties [*Ig1, Ch4a*], compressibility [*St29*], I.R. spectra [*Ax2, Pe5*], bibliography [*Fr10a*]	6
$KMnF_3$	C	4.186				*Be3*	P&S [*Be14, Si14, Cr4, Be2, Be4, Kn3, Ok2, Ok3, Ok4, Be53, Ok6, Ho17, Gu1a*], S.S. with Co + Ni [*Ha28*], I.R. spectra [*Ax2, Pe5, Yo2*], bibliography [*Fr10a*]	6
	O	5.885	5.885	8.376		*Be3*	T = 95 °K, $(c/a > \sqrt{2})$ 184 > T > 84 °K [*Be3, De3, Ok6*]	
	O	5.900	5.900	8.330		*Be3*	T = 65 °K, $(c/a < \sqrt{2})$ T < 84 °K [*Be3, De3, Ok6*]	
$NaMnF_3$	O	5.568	5.760	8.000		*Si14*	Prep. [*Ho17, Be19b*], *a* and *b* axis doubled [*Si14*], P&S [*Ma9*]	6
$(NH_4)MnF_3$	C	4.238				*Si14*	P&S [*Cr4, Ho17, Co25*], neutron diffraction [*Pi1*]	6
$TlMnF_3$	C	4.250				*Ki9*		6
$CsMnCl_3$	H	7.288		27.44		*Ke7*	Hex (9L), Θ_N = 69 °K, AFMR [*Ke1, Sh5*]	
$RbMnCl_3$	H	7.164		17.798		*Ke7*	Hex (6L), Θ_N = 86 °K, AFMR & ESR [*Ke1, Sh3, Sh5*]	
$KMnCl_3$	T	10.024		9.972		*Cr6*	Cubic T > 458 °C, AFMR&ESR [*Ke1, Sh5*]	6

Compound	Sym	a Å	b Å	c Å	angle	Ref.	Remarks	Magnetic Data
$A^{+}B^{2+}X_3$; X = F^{-1}, Cl^{-1}, Br^{-1} (continued)								in 3.3.4, Tab.
$CsFeF_3$	H	6.158		14.855		*Ke19*	Hex (6 L), structure [*Ba5*], $\Theta_C = 60$ °K [*Po9a, Po9b*]	
	C	4.283				*Lo1b*	High pressure phase	
$RbFeF_3$	C	4.173				*Wa12*	P&S [*Ke19*], neutron diffraction [*Wa14*], cubic $T > 97$ °K, tetr. $97 > T > 86$ °K, orth. $86 > T > 45$ °K, mon. $T < 45$ °K [*Te11*]	6
$KFeF_3$	C	4.122				*Oh6*	P&S [*Kn3, Ma29, Oh2, Oh3, Oh4*], neutron diffraction [*So7*]	
	R	4.108			$\alpha = 89°\,51'$	*Oh6*	$T = 78$ °K, rhombohedral $T < 121$ °K	6
$NaFeF_3$	O	5.495	5.672	7.890		*Tr2*	P&S [*Vo1, Ma9, Po9a*]	6
NH_4FeF_3	C	4.177				*Po9a*		6
$TlFeF_3$	C	4.188				*Vo1*	P&S [*Po9a*]	6
$CsFeCl_3$	H	7.237		6.045		*Yd1*	Hex (2L), P&S [*Se2a*]	
$RbFeCl_3$	H	7.060		6.020		*Se2a*	Hex (2L)	
$CsCoF_3$	H	6.194		22.61		*Ba5*	Hex (9L), magnetic properties [*Ru6*], P&S [*Ba4*]	
	H	6.09		14.67		*Lo1b*	Hex (6L), high pressure phase	
$RbCoF_3$	C	4.116				*Ru6*	P&S [*Ru8, Cr4*], S.S. with Mg [*Sh1a*]	6
$KCoF_3$	C	4.069				*Oh6*	P&S [*Kn3, Ma29, Oh2, Oh3, Oh4, Ru8, Cr4*] I.R. spectra [*Ax1, Ax2, Pe5, Yo2, Pe2a*]	6
	T	4.057		4.049		*Oh6*	$T = 78$ °K	
$NaCoF_3$	O	5.420	5.603	7.792		*Ru6*	P&S [*Ru8, Og2, Tu5, Ma10*]	6
NH_4CoF_3	C	4.127				*Ru6*	P&S [*Cr4, Ru8*]	6
$TlCoF_3$	C	4.138				*Ru6*	P&S [*Ru8*]	6
$CsCoCl_3$	H	7.202		6.032		*Yd1*	Hex (2L), complete structure and magnetic properties [*So1*]	
$RbCoCl_3$	H	6.996		5.996		*En1*	Hex (2L)	
$CsNiF_3$	H	6.236		5.225		*Ba2*	Hex (2L)	
	H	6.15		22.32		*Lo1b*	Hex (9L), high pressure phase	
	H	6.05		14.54		*Lo1b*	Hex (6L) high pressure form: $\Theta_C = 111$ °K	
$RbNiF_3$	H	5.843		14.31		*Ru5*	Hex (6L), P&S [*Si14*], $\Theta_C = 139$ °K, magnetic properties [*St19b, Mc1a, Sm32, Sm31, Sh1, Go3, Ku2, Go3a*], S.S. with Co [*Bo13, Su11, Pi16*], optical properties [*Sm32, Sm31, Sm21, Sm22, Sh1, Ty1, Pi8, Pi14, Pi15, Za1a, Be19c, Pi16*], Raman scattering [*Ch14a*], NMR [*Sm32a*]	
	C	4.074				*Ka4*	High pressure phase, P&S [*Sy1*]	6
$KNiF_3$	C	4.015				*Oh6*	P&S [*Oh3, Oh4, Kn3, Ma10, Ru3, Oh2*], I.R. spectra [*Pe5, Ba17a*]	6
	C	4.002				*Oh6*	$T = 78$ °K	

Compound	Sym	a Å	b Å	c Å	angle	Ref.	Remarks	Magnetic Data
$A^+B^{2+}X_3$; X = F^{-1}, Cl^{-1}, Br^{-1} (continued)								in 3.3.4, Tab.
$NaNiF_3$	O	5.360	5.524	7.688		*Ru8*	P&S [*Og2, Ru5, Oh5*]	6
NH_4NiF_3	C	8.145				*Ru5*	P&S [*Ru8*]	6
$TlNiF_3$	H	5.87		14.37		*Ko4*	Hex (6L)	
	C	4.10				*Ko4*	High pressure phase, P&S [*Sy1*]	
$CsNiCl_3$	H	7.169		5.940		*Yd1*	Hex (2L), P&S [*As4*], structure determination [*Ti4*]	
$(CH_3)_4NNiCl_3$	H	9.019		6.109		*St44*	Hex (2L)	
$CsNiBr_3$	H	7.488		12.480		*As4*	Related to Hex (2L)	
$CsCuF_3$	H	12.55		11.56		*Ba2*	Related to Hex (2L), optical properties [*Sc10a*]	
$RbCuF_3$	T	6.001		7.894		*Ru6*	Optical properties [*Sc10a*]	6
$KCuF_3$	T	5.855		7.846		*Ru6*	P&S [*Ed2, Kn3, Oh1, Oh2, Oh6,*] neutron diffraction [*Sc1*], optical properties [*Pe2a. Oe1, Sc10a*]	6
	T	4.121		3.913		*Oh6*	T = 78 °K	
$NaCuF_3$	M	11.01	11.37	7.521	β = 86° 54'	*Ru6*	P&S [*Ru3*]	6
NH_4CuF_3	T	6.09		7.78		*Cr4*		
$TlCuF_3$	T	6.083		7.866		*Ru6*	P&S [*Ru3*]	6
$CsCuCl_3$	H	7.20		18.00		*Yd1*	Related to Hex (2L), P&S [*Sc7, Ws9*] magnetic properties $\Theta_p = -3.5$ °K, μ_{eff} (300 °K) = 1.95 μ_B [*Ri8c, Fi2*]	
$KCuCl_3$	M	4.029	13.785	8.736	β = 97° 20'	*Ki10*	Not perovskite, magnetic properties Θ_N = 17.5 °K [*Ma1, Sh5*]	
NH_4CuCl_3	M	4.066	14.189	9.003	β = 97° 30'	*Ki10*	Not perovskite	
$KCuBr_3$	M	4.05	14.43	9.30	β = 96° 5'	*Ki10*	Not perovskite, magnetic properties [*In3*]	
$CsZnF_3$	T	9.90		9.05		*Lu1*		
	H	6.09		14.67		*Lo1b*	Hex (6L), high pressure phase	
$RbZnF_3$	C	4.110				*Ba1*	P&S [*Cr4, Lu1*]	
	H	5.896		14.44		*Ba1*	Hex (6L) high temperature form	
$KZnF_3$	C	4.055				*Kn3*	P&S [*Lu1, Ma29*], thermal conductivity [*Su8*], optical properties: Ni, Mn [*Fe11, Fe15*], I.R. spectra [*Yo2, Pe2a*]	
$NaZnF_3$	O	5.404	5.569	7.743		*Tu5*	P&S [*Lu1, Ru8, Ba1, Ma9, Ma10, Sc10*]	
NH_4ZnF_3	C	4.115				*Cr4*		
$AgZnF_3$	C	3.98				*De22*		
$TlZnF_3$	H	5.934		14.52		*Vo1*	Hex (6L)	
$CsGeCl_3$	R	5.444			α = 89° 38'	*Ch15*	Nuclear quadrupole resonance [*Vo0*]	
	C	5.475				*Ch15*	Cubic T > 155 °C, ferroelectric transition at 155°C	

Compound	Sym	a Å	b Å	c Å	angle	Ref.	Remarks	Magnetic Data
$A^+B^{2+}X_3$; X = F^{-1}, Cl^{-1}, Br^{-1} (continued)								in 3.3.4, Tab.
$CsSrF_3$							[*Be22a, Bu3a*] no cell dimensions	
$CsSrCl_3$	C	5.589				*Yd1*		
$CsPdF_3$							Prep. + Prop. [*Ba20, Fi3*]	
$CsCdF_3$	C	4.47				*Kl1*	P & S [*Co27a*]	
$RbCdF_3$	C	4.395				*Vo1*	Mn emission [*Kl1*], P & S [*Co27a*]	
$KCdF_3$	T	6.101		8.652		*Ba5b*	P & S [*Ma29, Br9, Kl1, Co27a, Co26, Vo1*], Mn emission [*Kl1*]	
$(NH_4)CdF_3$	T	4.368		4.447		*Co27a*		
$TlCdF_3$	C	4.400				*Co27a*	T_{melt} = 765 °C	
$CsCdCl_3$	C	5.20				*Fe20*	Slight distortion [*Na15*], P & S [*Si3*]	
	H	7.418		18.39		*Si3*	Hex (6L)	
$CsCdBr_3$	C	10.70				*Na15*	P & S [*Na19*]	
$CsSnCl_3$	C	5.58				*Do5*		
$CsSnBr_3$	C	5.94				*Do5*		
$CsEuF_3$	C	4.77				*Bo31*		6
$CsHgCl_3$	C	10.88				*Na15*	P & S [*Na19, Na18*]	
$CsHgBr_3$	C	5.77				*Na15*	P & S [*Na19*]	
$CsPbF_3$	C	4.81				*Sc9*		
$CsPbCl_3$	T	5.590		5.630		*Mo2*	Phase transition at 40 °C [*Sa2a*]	
	C	5.599				*Mo2*	Cubic T > 47 °C [*Mo3*]	
$CsPbBr_3$	C	5.874				*Mo2*		
$A^+B^{5+}O_3$								
AVO_3							Not perovskite, A = Na, K, Rb, Cs and Ag	
$RbNbO_3$						*Fe7*	Not perovskite	
$KNbO_3$	O	5.720	5.739	3.984		*Wo15*	Structure [*Ka19, Vo4, Vo5*], crystal growth [*Bu2, Sh25*], optical properties [*Ka8, Ch13*]; S.S. with: $BaTiO_3$ [*Br2*], $NaNbO_3$ [*Du3, Te8c*], Li [*Ni2a*]	
	T	4.00		4.07		*Wo15*	T = 260 °C, Tetr. 435 > T > 225 °C, S.S. with $KTaO_3$ (see $KTaO_3$)	
	C	4.024				*Wo15*	T = 500 °C, cubic T > 435 °C	
	R	4.016			α = 89° 50'	*Sh23*	T = − 140 °C, neutron diffraction	
$NaNbO_{2.8}$	C	4.2				*Ad1*	2Na + Nb_2O_5	

Compound	Sym	a Å	b Å	c Å	angle	Ref.	Remarks	Magnetic Data
$A^+B^{3+}O_3$ (continued)								in 3.3.4, Tab.
$NaNbO_3$	O	5.505	5.568	15.518		*Vo6*	Structure determined, P&S [*Vo4, Vo5, We10, Ba18, Fe7, Wo15*]; S.S. with: $KNbO_3$ [*Du3, Te8c*], $NaTaO_3$ [*Iw4, Is7, Is14*], $SrNb_2O_6$ [*Is16, Te7*], $CdTiO_3$ [*Le2*], $AgNbO_3$ [*Br24*], Cd and Sr [*Te8b*]	
$NaNbO_3$	O	5.51	5.57	7.77		*Wo17*	50 kV/cm applied to crystal; other phase transformations [*Te6, So1b, Le5, Fr1, Sh20a, Cr6a, So1a, Is5a*]; heat of transformations [*Te8a*]	
$Na_{0.975}K_{0.025}NbO_3$	O	5.528	5.582	7.782		*We10*	Structure determined	
$LiNbO_3$	H	5.1483		13.8631		*Ab4*	Not perovskite, see text	
$AgNbO_3$	M	7.888	7.888	15.660	$\beta = 90° 34'$	*Fr2*	S.S. with $KNbO_3$ [*We5*]	
	C	3.595				*Fr2*	$T = 550$ °C, cubic $T > 550$ °C	
$AgSbO_3$	C	10.32				*Sc22*	Defect pyrochlore	
$RbTaO_3$	T	3.92		4.51		*Sm11*	[*Fe7*] says not perovskite	
$KTaO_3$	C	3.9885				*Vo4*	P&S [*Vo5*], crystal growth [*Sh25, Wi4, We13*], optical properties [*Fr20, Fr2, Di7, Di8, Be27, Ax1, Fe4, Jo15, Sh20,Ra7, Sc5, St20, La7a*], Faraday rotation [*Ba7*], electrooptic properties [*Fr20,Fa7, Fa8, Fr21, Fr22, Ge13, Zo3*], S.S. with: $KNbO_3$ [*Fu3, Ha2, Ch13, Ge9, We12, We14, Di6, Hi2a, La7a*], Ca [*Se4*]; Raman spectrum [*Fl1a, Pe6, Fl1b*]; ESR: Eu, Gd [*Un1*], Fe, Ni [*Ha9a, We18b*]; ultrasonic attenuation [*Ba17b*]; Nuclear spin resonance [*Gr7a*]	
$NaTaO_3$	O	5.494	5.513	7.751		*Ka22*	Crystal structure, P&S [*Vo4, Vo5*], S.S. with: $NaNbO_3$ [*Is14, Is7*]	
$NaTaO_3$	C	3.929				*Is5*	630 °C, cubic $T \geq 630$ °C, tetr. $630 > T > 550$ °C	
$LiTaO_3$	H	5.154		13.783		*Ab2*	Not perovskite, neutron diffraction [*Ab3*] (see text)	
$CuTaO_3$						*Sh12*	Actually $Cu_{0.5}TaO_3$, see "Bronze" section	
$AgTaO_3$	M	7.862	7.862	3.914	$\beta = 90° 21'$	*Fr2*	P&S [*Br27*]	
	C	3.949				*Fr2*	485 °C; cubic $T > 485°$	
$CsIO_3$	C	4.674				*Bo30*	P&S [*Na15*]	
$RbIO_3$	R	4.541			$\alpha = 89° 44'$	*Bo30*	P&S [*Na15*]	
KIO_3	M	8.94	8.94	8.94	$\beta = 89° 12'$	*Na16*	Perovskite (?), P&S [*Na15*]	
	R	4.410			$\alpha = 89° 25'$	*Sm3*	P&S [*Ri9*]	
$TlIO_3$	R	4.510			$\alpha = 89° 20'$	*Sm3*		
NH_4IO_3	C	9.18				*Na15*		
$CsPaO_3$	C	4.368				*Ke5*		

Compound	Sym	a Å	b Å	c Å	angle	Ref.	Remarks	Magnetic Data
$A^{+}B^{5+}O_3$ (continued)								in 3.3.4, Tab.
$KPaO_3$	C	4.341				*Ke5*		
$NaPaO_3$	O	5.82	5.97	8.36		*Ke5*		
$RbUO_3$	C	4.323				*Ke12*	P&S [*Ru3a, Ip1*], Prop. [*Ke13*]	6
KUO_3	C	4.290				*Ke12*	P&S [*Ru3a, Ch1b*], Prop. [*Ke13*]	6
$NaUO_3$	O	5.775	5.905	8.25		*Ke12*	P&S [*Ru3a*], Prop. [*Ke13*]	6
$A^{3+}B^{4+}O_3$								
$BaTiO_3$	C	4.012				*Me1*	T = 200 °C, cubic 120 < T < 1372 °C [*Ed5*], cubic T > 133 °C [*We11a*], high temperature phase [*Me4, Me6, Me2, Ka23*]	
	T	3.994		4.034		*Me1*	T = 20 °C, tetragonal 5 < T < 120 °C; structure determination: by x-rays [*Ev2, Ev3, Ev4, Ch2*], by neutrons [*Sh18, Fr4*], by electron microscope [*Pl12*]; P&S [*De1, Sa5*], further remarks: *)	
	O	5.682	5.669	3.990		*Vo5*	T = −10° C, orthorhombic −90 < T < 5 ° C [*Ka24*]	
	R	3.998			α = 89° 52'	*Ka24*	T = −100 °C, rhombohedral T < −90 °C	
	H	5.735		14.05		*Bu4*	Hex (6L); structure determination [*Bu4, Ev1*]. Further remarks:**)	
$SrTiO_3$	C	3.905				*Me4*	T = 293 °K; cubic T > 110 °K, thermal expansion $\alpha = 9.4 \cdot 10^{-6}$ Å/deg., may be tetr. with c/a = 1.00008 [*Ly2*]	
	T	3.8972		3.8991		*Ly2*	T = 100 °K, Tetr. 65 < T < 110 °K, c/a = 1.00056, on single crystal [*Ly2*]. Further remarks:***) See page 156	
	O					*Ly2*	$a:b:c$ 0.9998:1:1.0002, orthorhombic 35 < T < 65 °K [*Ly2*]	
	R					*Ly2*	Possibly rhombohedral at 10°K	

*) Complete bibliography to 1961 [*Ha7*]; Raman scattering [*Di8, Du2, Pa6, Pi3, Ri8, Di9a, Ro19a*]; study of structural changes [*Ca4, Co15a, Fo6, Me6, Sc8, Ka24, We11a*]; pressure dependence of dielectric properties [*Go27, Ka1, La9, Me23, Mo7, Mo8, Po3, Po4, Po5, Po6, Sa3*]; radiation damage [*Sc6, We3*]; refractive index [*Sh31, Ho3, Ho3a*]; thermal conductivity [*Di9, Ma23, Su7, In2b*]; surface layers [*Or1, Le12, Ho10, Du1, Cr2, Ca1, Br3*]. Optical properties [*Mu11, Mu12, Mu13, Va8, Va6, Ha15, Ja1, Co10, Sh24, Re4, Po7, Na8, Kh3, Ba9, We11a*]; ultrasonic propagation [*Gr10*]; ESR: Ti [*Da4, Ta4, Ta6*], Mn [*Ih1, Ih2, Ih3, Ve10*], Pt [*Si3*], Eu [*Ta7, Ta8*], Gd [*Bu7, Ta3, Ta5, Ta8, Ri5*]; dielectric properties [*De9, Hu11, Si17, Fr17, We11a*]. Transport properties [*Uc1, Ue2, Ta9, Sc15, Ry1, Mu10, Ma32, Ma3, Ko9, Ka21, Ih5, Be28, An4*], electromicroscopic observation [*Mo12*]. Lattice vibration [*Ax1, Ha14, Ka3, Dr3*], shock-wave compression [*Do4*], elastic properties [*Fu3*], grain size influence on Θ_D [*Ri2*], relaxation time [*Wi3, Bo4*]. Properties with additives: Mg [*Is13*], Mn [*Bh1, As2*], Fe [*Sc25*], Co, Ni [*Ku1, Co23a*], Zn [*Si16*], Nb + Ta [*Gu1, Ku1*], La [*Go9, As2, Bo4, Jo1f*], Sr [*He14, Al1, He6*], Bi [*Bo3, Jo1f*], Sb [*He13, Jo1f*], Halogens [*Jo10*], $PbNb_2O_6$ [*Sr1*], Ca, Zr, Si, Fe, Mg [*Br22a*]; defect study [*Co24, Mu9, No8*], neutron scattering [*Ya2a*].

**) P&S [*Wo16, Me4, Ma36, Si19c, Ra5, Bl14a, Di4*]; effect of additives on occurrence [*Ra5, Ro20a, Di4*], hex. form due to oxygen vacancies or metal substitution for Ti [*Di4*], magnetic properties with Ti, Cr, V, Mn, Re, Fe, Co, Ru, Ir, Pt substitution [*Di4*].

Compound	Sym	a Å	b Å	c Å	angle	Ref.	Remarks	Magnetic Data
$A^{3+}B^{4+}O_3$ (continued)								in 3.3.4, Tab.
$CaTiO_3$	O	5.381	5.443	7.645		*Pe3*	P&S [*Ba18, Ze1, Ze2, Le10, Na13, Na15, Me4, Ku3*], optical properties [*St21, Pe8, Mu13*], detailed structure [*Ka21a*]	
	C					*Gr3a*	Cubic $T > 1260$ °C	
$CdTiO_3$	O	5.348	5.417	7.615		*Ka22*	Structure determined Pbn2, [*Ka22*], structure questioned [*Ge3a*], P&S [*Me4*], S.S. with $NaNbO_3$ [*Le2*], electrical properties [*Sh24a*], perovskite-ilmenite transformation [*Li0*]	
$PbTiO_3$	T	3.904		4.152		*Sh21*	Complete structure [*Sh21*], P&S [*Me4, Sh19, Co13, Sh15, Sh24b*], optical properties [*Pe8, Fu5*], piezoelectric properties [*Ue3, Fe2, Fe1, Is14a*], slow neutron scattering [*So2*], S.S. with (Ba, Sr, Ca, Pb) (Ti, Zr, Sn)O_3 [*Sh19, Ta14, Ha20, Ba12, No7, Ou1, Ou2, Th2, Oh7, Ta6, Ki17, Os4a, Pe9, Is1, Uc2, St34, Fe1, Bu10, Fe3, Fe9, Fu5, He14, Is3, St35, Di1a*], radiation damage [*Ha30*], S.S. with $PbGeO_3$ [*Di5b*]	
	C	3.960				*Sh21*	$T = 535$ °C, cubic $T > 490$ °C	
$(CuA)TiO_3$	C	≈ 7.4				*De18*	A = Ca (25%) $a = 7.393$ Å; Cd (25%) $a = 7.399$ Å; Sr (20%) $a = 7.420$ Å	
$EuTiO_3$	C	7.810				*Ho12*	P&S [*Br20, Mc1b*], Prop. [*Mc2, Mc3, Mc4, Si4*]	6
$La_{0.5}K_{0.5}TiO_3$	C	3.914				*Ro20*	Dielectric properties [*Sm8, Ag1*]	
$La_{0.5}Na_{0.5}TiO_3$	C	3.86				*Ag1*	Dielectric properties [*Sm8*]	
$Ce_{0.5}K_{0.5}TiO_3$	C	3.90				*Ro20*	S.S. with La	
$Nd_{0.5}K_{0.5}TiO_3$	C	3.874				*Ro20*		
$Y_{0.5}Na_{0.5}TiO_3$	O	5.326	5.443	7.614		*Re2*		
$Bi_{0.5}K_{0.5}TiO_3$	T	3.913		3.993		*Iv2*	Dielectric properties [*Ag1, Bu3, Sm8, Sm26*]	
$Bi_{0.5}Na_{0.5}TiO_3$	R	3.891			$\alpha = 89° 36'$	*Iv2*	Dielectric properties [*Ag1, Bu3, Sm8, Sm26*]	
$La_{2/3}TiO_3$	C	3.887				*Ke18*	S.S. with $SrTiO_3$ [*Ti1, Ve9, We16*]	
$SrVO_{2.5}$	C	3.848				*Ke18*		
$SrVO_{3.0}$	C	3.838				*Wo14*	P&S [*Re8*]	6

***) Superconductivity [*Am2, Ap2, Ea2, Fr10, Ko7, Sc19, Sc20, Sc21*]; Raman scattering [*Sc4, Sc3, Ri6, Os1, Ni1a, Fi1b*]; NMR [*We1*]; Mössbauer: Co^{57} [*Bh3*]. Optical properties [*Ba6, Ba15, Ba16, Ca6, Co9, Du1, Ea1, Gr1, Ka9, Mu11, Mu12, Mu13, Si12, Va6, Zo2, Am3, Fa4a, Fe10a*]; Hall mobility [*Fr6, Fr9, Pa5, Tu1*]; ESR: Cr^{3+} [*Ri7*], Fe^{3+} [*Ki2, Ba8, Ri7, Un2*], Ni^{3+} [*Ho1*], Gd^{3+} [*Ri7, Ri5, Sa2, Si11*]; magnetoresistance [*Fr7, Tu3, Ya3b*], piezoelectric properties [*Tu2*]; Shubnikov-deHaas effect [*Fr8*]; thermal conductivity ($33 < T < 110$ °K) [*Su7*]; diffusion and formation of oxygen defects [*Pa3, Pa4, Wa9, Wa10*]; radiation damage [*Sc5, Ro4*]; band structure [*Ka8*]; dielectric properties: doped with Fe and Cr [*Ma33*] with Nb [*Ti2*]; elastic constants from sound wave attenuation [*Be6, Jo5a*]; electromechanical behavior [*Ru12*]; pressure dependence of dielectric properties [*He6a, Sa2*]; photoconduction [*Ya4, Ya5, Ya3a, Ya3b*]; magnetic properties [*Fr5*]; vibrational modes [*Ja8, Jo14*]; thermal expansion [*De19b*], inelastic neutron scattering [*Sh16a*], electrooptic effect [*So3*].

Yaj8]; magnetic properties [Fr5]; vibrational modes [Ja8, Jo14]; thermal expansion [De19b], inelastic neutron scattering [Sh16a], electrooptic effect [So3].

Compound	Sym	a Å	b Å	c Å	angle	Ref.	Remarks	Magnetic Data
$A^{3+}B^{4+}O_3$ (continued)								in 3.3.4, Tab.
$CaVO_{3.0}$	C	3.767				*Wo14*	P&S [*Ru7, De2, Re8, Re9*]	6
	O	5.326	5.352	7.547		*Ro16*		
$CaVO_{2.85}$	C	3.780				*Wo14*		
$BaCrO_3$	H	5.62		22.95		*Ch1a*	Hex (9L), high pressure phase, semiconducting, $\Delta E = 0.09$ eV	
	H	5.659		9.359		*Ch1a*	Hex (4L), high pressure phase, semiconducting, $\Delta E = 0.11$ eV	
	H	5.627		13.690		*Ch1a*	Hex (6L), high pressure phase	
	H	5.662		27.752		*Ch1a*	Hex (12L), high pressure phase	
	H	5.652		32.515		*Ch1a*	Hex (14L), high pressure phase	
	H	5.649		62.706		*Ch1a*	Hex (27L), high pressure phase	
$SrCrO_3$	C	3.818				*Ch1*		
$CaCrO_3$	O	5.287	5.316	7.486		*Go17*		6
$PbCrO_3$	C	4.00				*Ro19*	P&S [*De2f*]	6
$BaMnO_3$	H	5.672		4.71		*Ha7*	Hex (2L), P&S [*Ha16, Sy1*]	6
	H	5.667		20.948		*Sy1*	Hex (9L), high pressure phase	
	H	5.669		9.375		*Ha7*	Hex (4L), high pressure phase, P&S [*Ha16*]	
	H	5.645		9.264		*Sy1*	Hex (4L), high temperature phase	
$SrMnO_3$	H	5.449		9.085		*Sy1*	Hex (4L), S.S. with (Bi, Ba, La)MnO_3 [*Yu1*]	
	H	5.431		13.396		*Sy1*	Hex (6L), high pressure phase	
$CaMnO_3$	O	5.270	5.275	7.464		*Ma6*	96% Mn^{4+}, P&S [*Vo12, To13, Yu1, Yu8*], S. S. with Bi [*Bo6, Bo12, St19*]	6
$Ca_{0.75}Sr_{0.25}MnO_3$	O	5.302	5.304	7.488		*Ma6*		
$BaFeO_{3-x}$	R	4.099			$\alpha = 88° 47'$	*Mo10*	$x = 0.36$ P&S [*De15, Er1, Mo11, Ma22, Va8*]	6
	C	3.997				*Mo10*	$x = 0.25$; K_β X-ray spectra [*Ko6a*]	
	T	7.956		8.006		*Mo10*	$x = 0.19$	
	H	5.672		13.90		*Mo10*	Hex (6L); $x = 0.08$	
$BaFeO_{2.5}$	O	5.83	16.98	5.54		*Ga18*	Brownmillerite structure, see Fig. 21	
	C	4.15				*Mo11*	$T = 1000$ °C, $T = 20$ °C (triclinic)	
$SrFeO_{3.0}$	C	3.850				*Ma4*	P&S [*Wa17, Ya1, Ga17, Sh17*], S.S. with La [*Ga16, Wa17, Wa20*], Bi [*Ma8*], Ti [*Cl2, Br18*]	6
$SrFeO_{2.94}$	T	3.851		3.867		*Ma4*		
$SrFeO_{2.50}$	O	5.671	15.59	5.528		*Ma4*	P&S [*Ba23*], S.S. with Al [*Ba24, Ba25*], Brownmillerite structure, see Fig. 21	
$CaFeO_{2.50}$	O	5.64	14.68	5.39		*Be40*	P&S [*Be39, Sm4*], neutron diffraction [*Ta10, Fr16, Co22*], Mössbauer [*Go4, Gr6, Ge7, Ge8, Wi15, Wi16, Ta10, Gr4*]	6
$CaFe_{0.5}Al_{0.5}O_{2.5}$	O	5.58	14.50	5.34		*Ha10*	Prop. [*Gr5, Po1, Wh4, Be40, Sm4*]	6
$PbFeO_{2.5}$	T	7.79		15.85		*Be26*	P&S [*Mo15*]	6

Compound	Sym	a Å	b Å	c Å	angle	Ref.	Remarks	Magnetic Data
$A^{3+}B^{4+}O_3$ (continued)								in 3.3.4, Tab.
$BaCoO_{2.72}$	H	5.59		4.83		*Gu7*	Hex (2L), P & S [*St41*]	
$SrCoO_{3-x}$	C	7.725				*Ya1*	1.4% Co^{4+}, S.S. with La [*Wa17*]	
$BaNiO_{2.8}$	H	5.58		4.832		*La4*	Hex (2L) [*La3, Gu7*]	
$CaGeO_3$	C	3.723				*Ri8a*	High pressure phase; doubled cell [*Sl3a*]	
$CdGeO_3$	C	3.70				*Ri8a*	High pressure phase, pseudocubic	
$BaZrO_3$	C	4.20				*Ha20*	P & S [*Ho2, Me4, Be24*]; S.S. with $BaTiO_3$ [*Va7*], $PbTiO_3$ [*Ha20*]; optical properties [*Pe7, Du5*]	
	C	4.26				*Fo4*	$T = 2000$ °C	
$SrZrO_3$	O	5.792	5.818	8.189		*Pe3*	P & S [*Ho2, Me4, Sm3, Sc18a*], D.T.A., $T < 1000$ °C [*Ca5*], optical properties [*Pe7, Du5*], S.S. with Hf [*Be24a*]	
	C	4.18				*Fo4*	$T = 2000$ °C, cubic $T > 1300$ °C	
$CaZrO_3$	O	5.587	5.758	8.008		*Ti3*	P & S [*Si15, Me4, Ru9, Ru14*], S. S. with Cr [*Ni2*]	
	C	4.10				*Fo4*	$T = 2000$ °C, cubic $T > 1600$ °C	
$PbZrO_3$	O	5.872	11.744	8.202		*Sa8*	P & S [*Is1, Me4, Sa7*], phase transitions [*Go28, Go29, Go30, Sa8, Te5, Te8, Ue1, Sh15a, Te8d*], radiation damage [*Ha30*], optical properties [*Pe7*], neutron diffraction [*Jo5*], dielectric properties [*Kh4, Kh6, Kh8, Go29*], piezo-electric effect [*Ro1, Th2, Is14a*], S.S. with Ca [*Kh4, Si15*], (BiNa) and (BiK) [*Bu3*], $Pb(Ni_{1/3}Nb_{4/3})O_3$ [*Bu10*], $BiFeO_3$ [*Ge10*], Hf [*Go31*]	
	C	4.149				*Sa8*	$T = 230$ °C, cubic $T > 230$ °C	
$EuZrO_3$	C	4.099				*Ho12*	P & S [*Me4*]	6
$Bi_{0.8}K_{0.2}ZrO_3$							Prep. + Prop. [*Sm33, Bu3*]	
$Bi_{0.8}Na_{0.2}ZrO_3$							Prep. + Prop. [*Sm33, Bu3*]	
$BaMoO_3$	C	4.04				*Sc17*	P & S [*Bo19, Sc16, Ro2a*], S.S. with Sr [*Br15*]	6
$SrMoO_3$	C	3.98				*Sc17*	P & S [*Bo19, Sc16, Ro2a*], S.S. with Ti [*Ro2a, Br17*], S.S. with Zr [*Br17*]	6
$CaMoO_3$	O	5.45	5.58	7.77		*Mc1*	P & S [*Sc16, Go17, Ro2a*]	6
$BaTcO_3$	H	5.758		14.046		*Mu7*	Hex (6L)	
	C	8.140				*Ke9*		
$SrTcO_3$	C	3.95				*Mu7*	Slight distortion, P & S [*Ke9*]	
$CaTcO_3$	O	3.87	3.96	3.76		*Ke9*		
$PbTcO_3$	C	10.360				*Mu7*	Defect pyrochlore structure	
$BaRuO_3$	H	5.75		21.60		*Ra6*	Hex (9L), structure determination [*Do2*], Prop. [*Ca2*], S.S. with Sr [*Do3, Lo1*], S.S. with Zr, Mn, Ir, Ni [*Do3a*]	
	H	5.73		9.50		*Lo1*	Hex (4L), high pressure phase	

Compound	Sym	a	b	c	angle	Ref.	Remarks	Magnetic	Ref.

Compound	Sym	a Å	b Å	c Å	angle	Ref.	Remarks	Magnetic Data
$A^{3+}B^{4+}O_3$ (continued)								in 3.3.4, Tab.
$BaRuO_3$	H	5.71		14.00		*Lo1*	Hex (6L), high pressure phase	
$SrRuO_3$	O	5.53	5.57	7.85		*Ra6*	P&S [*Kh1*], Prop. [*Ca2, Lo3*]	6
$CaRuO_3$	O	5.36	5.53	7.67		*Ra6*	Prop. [*Ca2, Lo3*]	6
$SrRu_{0.5}Ir_{0.5}O_3$	O	5.55	5.58	7.84		*Ra6*		
$PbRuO_3$	C	10.25				*Lo4*	P&S [*Ra6*], Defect pyrochlore structure	
	O	5.56	5.61	7.86		*Lo1a*	High pressure phase	
$BaSnO_3$	C	4.117				*Me4*	P&S [*Wa2, Co8, Sm3*], S.S. with Sr [*Sm3*], (Ba, Sr, Pb)TiO_3 [*Na9, Du4, My2*], optical properties [*Du5, Ya3*], Mössbauer in S.S. with Ti [*Be7, Bo9, Kr6*]; S.S. with Ti, tetragonal at 91% Ti [*Do1*]	
$SrSnO_3$	C	8.070				*Sm3*	P&S [*Ho2, Me4, Co8*], optical properties [*Du5*]	
$CaSnO_3$	O	5.519	5.668	7.885		*Sm2*	P&S [*Ro12, Co8, Me4*]; optical properties [*Du5*]; S.S. with $BaTiO_3$ cubic at 13% $CaSnO_3$ [*Do1*]	
$CdSnO_3$	O	5.457	5.577	7.867		*Sm2*	P&S [*Na13, Co8*]	
$PbSnO_3$	M	4.076	4.076	4.043	$\beta = 89°\ 45'$	*Su9*	High pressure preparation	
	C	4.07				*Su9*	$T = 125$ °C, cubic $T > 125$ °C	
$BaCeO_3$	C	4.397				*Sm3*	P&S [*Ho2*], optical properties [*Du5*], S.S. with Sr [*Sm3*], dielectric properties [*Sm7a*]	
$SrCeO_3$	O	6.011	6.156	8.588		*Sm3*	P&S [*Ho2*], optical properties [*Du5*], dielectric properties [*Sm7a*]	
$CaCeO_3$	C	7.70				*Na14*	Pseudocubic	
$CdCeO_3$	C	7.65				*Na14*	Pseudocubic	
$PbCeO_3$	C	7.62				*Na14*	Pseudocubic	
$BaPrO_3$	C	8.708				*Na15*	P&S [*Ho2*]	
$BaHfO_3$	C	4.172				*Sh16*	S.S. with $CaZrO_3$ [*Be24*], P&S [*Sc18a*]	
$SrHfO_3$	C	4.069				*Ho2*	P&S [*Na15*], S.S. with $SrZrO_3$ [*Be24a*]	
$CaHfO_3$	O	5.568	5.732	7.984		*De7*	Prep. [*Ru14*]	
$CdHfO_3$	M	3.942	3.982	3.942	$\beta = 91°\ 36'$	*Av1*		
$PbHfO_3$	T	4.136		4.099		*Sh16*	Cubic $T > 215$ °C, S.S. with $PbZrO_3$ [*Go3f*]	
	C	4.134				*Sh16*	$T = 250$ °C, cubic $T > 215$ °C	
$PbReO_3$	C	10.425				*Lo4*	Defect pyrochlore type	
$BaIrO_3$	H	5.76		44.4		*Do3*	S.S. with Sr [*Do3*], distorted Hex. (9L); structure [*Ro2b*]	
$SrIrO_3$	M	5.60	9.62	14.17	$\beta = 93°\ 16'$	*Lo1a*	Prep. [*Ro2a*], distorted Hex (6L)	
	O	5.58	5.60	7.89		*Lo1a*	High pressure phase (Perovskite)	
$PbIrO_3$	C	10.271				*Lo4*	P&S [*Ra6*], defect pyrochlore type	
$CaIrO_3$	O	3.145	9.855	7.293		*Ro2b*	Not perovskite	
$BaPbO_3$	C	4.265				*Wa2*	P&S [*We7, Ni3*], electrical properties [*Ik4*]	
$SrPbO_3$	O	5.864	5.949	8.336		*We7*		

Compound	Sym	a Å	b Å	c Å	angle	Ref.	Remarks	Magnetic Data
$A^{2+}B^{+4}O_3$ (continued)								in 3.3.4, Tab.
$BaThO_3$	C	8.985				*Sm30*	P&S [*Ho2, Na15, Me4, Ba24*]	
$SrThO_3$	C	8.84				*Na15*	Pseudocubic, S.S. with Ba [*Be24*]	
$CaThO_3$	C	8.74				*Na15*	Pseudocubic	
$CdThO_3$	C	8.74				*Na15*	Pseudocubic	
$PbThO_3$	C	8.960				*Na15*	Pseudocubic	
$BaUO_3$	C	4.387				*La5*	P&S [*Sc16, Ru4, Tr9*], S.S. with $BaTiO_3$ [*Va9*]	
$BaNpO_3$	C	4.384				*Ke4*		
$BaPuO_3$	C	4.357				*Ke3*	Pseudocubic	
$SrPuO_3$	C	4.28				*Ke3*	Pseudocubic	
$A^{2+}B^{4+}X_3$ or $A^{3+}B^{3+}X_3$; X = S, Se								
$BaTiS_3$	H	6.77		5.74		*Cl1*	Hex (2L), P&S [*No9, As3b*], orthorhombic and tetragonal modifications [*Ha6*]	
$BaTiSe_3$	H	7.054		6.033		*As3a*	Hex (2L), P&S [*No9*]	
$SrTiS_3$	H	6.730		5.829		*Ha6*	Hex (2L), P&S [*No9*], orthorhombic and tetragonal modifications [*Ha6*]	
$PbTiS_3$	T	4.16		11.752		*St27*	"Layer structure" P&S [*No9*]	
$BaZrS_3$	O	7.037	9.983	7.050		*Cl3*	Distorted perovskite, P&S [*Ha6, No9, As3b*]	
$BaZrSe_3$	H	7.188		6.025		*As3a*	Hex (2L), P&S [*No9*]	
$SrZrS_3$	O	13.49	9.79	14.23		*Cl1*	Distorted perovskite, P&S [*No9*]	
$CaZrS_3$	O	13.07	9.58	14.05		*Cl1*	Distorted perovskite	
$BaTaS_3$	H	6.847		5.742		*As3b*	Hex (2L) P&S [*No9*]	
$BaTaSe_3$	H	7.134		5.987		*As3a*	Hex (2L) P&S [*No9*]	
$ATaSe_3$	O	11.0	6.8	11.9		*No9*	A = Sr and Pb—not perovskite	
$LnInS_3$	O	≈ 3.95	≈ 11.78	20.98		*Ka13*	Ln = La, Ce, Pr, Nd and Sm; $T_{melt} \approx 1100$ °C	
$LnGaSe_3$	H	≈ 10.3		≈6.2		*Ka12a*	Ln = La, Ce, Pr, Nd, Sm; $T_{melt} = 1100$ °C	
$A^{3+}B^{3+}O_3$								
$LaAlO_3$	R	5.357			$\alpha = 60° 6'$	*Ge5*	P&S [*Be34, Da1, Re5, De14*], ESR: Gd, Cr [*Ki3, St16a*]. Luminescence: Eu [*Ya3, Bl13, Bl14*], Pr [*Ma30, De8*], Cr [*Bl15, Bo14*]; twinning + detwinning [*Fa9, Fa10*]; nuclear quadrupole resonance [*De17*]; S.S. with $BaTiO_3$ [*Sm15, Is2b*]; space group, $R\bar{3}c$ [*Ra3, Ge4b*], Review [*Ge4b*]	
	C	3.818				*Ge5*	$T = 650$ °C; cubic $T > 522$ °C [*Wo15a, Ge4b, Ax3*], inelastic neutron scattering [*Ax3*]	
$CeAlO_3$	R	5.327			$\alpha = 60° 15'$	*Ki1*	P&S [*Be34, Ro16, Sc13, Ke2*]	
$PrAlO_3$	R	5.307			$\alpha = 60° 22'$	*Ge5*	P&S [*Be34, Ma27, Yu4, Zo1, Re5, Li2, Ru10, Sc13*]	6

$PrAlO_3$	R	5.307			$\alpha = 60°\ 22'$	*Ge5*	P&S [*Be34, Ma27, Yu4, Zo1, Re5, Li2, Ru10, Sc13*]	6

Compound	Sym	a Å	b Å	c Å	angle	Ref.	Remarks	Magnetic Data
$A^{3+}B^{3+}O_3$ (continued)								in 3.3.4, Tab.
$PrAlO_3$	T	3.74		3.76		*Ma27*	Discussion of disagreement between [*Ge5*] and [*Ma27*] given in [*Ge4a*] and [*To12a*]	6
$NdAlO_3$	R	5.286			$\alpha = 60°\ 25'$	*Ge5*	P&S [*Be34, Da2, Zo1, Ke2, Ge5, Re5, Li2, Ru10, Sc13, Da1*]	6
$SmAlO_3$	O	5.285	5.290	7.473		*Ge5*	P&S [*Be34, Ke2, Re5, Li2, Sc13, Zo1*]	6
	O	7.46	7.46	7.43		*Ma27*	Discussion of disagreement between [*Ge5*] and [*Ma27*] given in [*Ge4a*] and [*To12a*]	
	R	5.316			$\alpha = 60°\ 19'$	*Ge2*	T = 850 °C, rhombohedral T > 800 °C	
$EuAlO_3$	O	5.271	5.292	7.458		*Ge5*	P&S [*Bo14, Re5, Li2*]	6
	H	3.760		10.52		*Be36*	Prep. T < 900 °C, see Fig. 17a	
$GdAlO_3$	O	5.247	5.304	7.447		*Ge5*	P&S [*Be34, Da1, Ga28, Sc13, Li2, Ma39*]; optical properties [*Bl13, Bl14, Bl16, Ca8, Oh1*]; NMR, Al^{iv} [*Bo2a*]	6
	H	3.73		10.51		*Be36*	Prep. < 900 °C, see Fig. 17a	
$TbAlO_3$	O	5.229	5.308	7.415		*Bi2*	Neutron diffraction [*Bi2*], P&S [*Ga28, Sc13*], optical properties [*Hu6, Hu6a*]	6
	H	3.730		10.51		*Be36*	Prep. < 900 °C, see Fig. 17a	
$DyAlO_3$	O	5.23	5.31	7.40		*Gi3*	P&S [*Be34,Ga28, Da1, Da2, Sc13*], neutron diffraction [*Bi1, He12*], optical properties [*Hu5, Sc24, Fa5*]	6
	H	3.700		10.50		*Be36*	Prep. < 900 °C, see Fig. 17a	
$HoAlO_3$	O	5.18	5.33	7.36		*Sc13*	P&S [*Ga28*]	6
	H	3.670		10.51		*Be36*	Prep. < 900 °C, see Fig. 17a	
$ErAlO_3$	O	5.16	5.32	7.33		*Sc13*	P&S [*Ga28*]	6
	H	3.660		10.50		*Be36*	Prep. < 900 °C, see Fig. 17a	
$TmAlO_3$	O	5.15	5.33	7.29		*Sc13*	P&S [*Ga28*]	
$YbAlO_3$	O	5.128	5.332	7.317		*Ga28*		
$LuAlO_3$							No perovskite [*Ga28, Sc13*]	
$YAlO_3$	O	5.179	5.329	7.370		*Ge6*	P&S [*Mi8, Be34*], ESR: Fe^{3+} and Gd^{3+} [*Wh3*]; decomposition of YAG [*Ma26*]	
	H	3.68		10.52		*Be36*	Prep. < 900 °C, see Fig. 17a	
$BiAlO_3$	T	7.61		7.94		*Na15*	Not able to be reproduced [*Bu3*]	
$PuAlO_3$	R	3.78			$\alpha = 90°\ 24'$	*Ru13*		
$AmAlO_3$	R	3.75			$\alpha = 90°\ 28'$	*Ke8*		
$LaScO_3$	O	5.678	5.787	8.098		*Ge2*	P&S [*Sc13, Ke2*]	
$CeScO_3$	O					*Ke2*	No dimensions	
$PrScO_3$	O	5.615	5.776	8.027		*Ge2*	P&S [*Sc13*]	
$NdScO_3$	O	5.574	5.771	7.998		*Ge2*	P&S [*Sc13, Ke2*]	
$SmScO_3$	O	5.53	5.76	7.95		*Sc13*		

Compound	Sym	a Å	b Å	c Å	angle	Ref.	Remarks	Magnetic Data
$A^{3+}B^{3+}O_3$ (continued)								in 3.3.4, Tab.
$EuScO_3$	O	5.51	5.76	7.94		*Sc13*		
$GdScO_3$	O	5.487	5.756	7.925		*Ge2*	P&S [*Sc13*], Prop. [*Bo36*]	6
$DyScO_3$	O	5.43	5.71	7.89		*Sc13*		
$HoScO_3$	O	5.42	5.71	7.87		*Sc13*		
$YScO_3$	O	5.431	5.712	7.894		*Ge2*	P&S [*Sc13, Ke2*]	
$BiScO_3$	Tr	4.042	4.127	4.042	$\alpha = \gamma = 90° 41'$ $\beta = 91° 52'$	*To11b*	High pressure preparation [*To11a*]	
$LaTiO_{3-x}$	C	3.934				*We16*	P&S [*Si4, Be33, Ho12, Ke15, Ke16, Jo4*]	6
$La_{0.97}TiO_3$	C	3.887				*Ke18*	Ti^{4+}, S.S. with $SrTiO_3$ [*Ti1, Ke18, Ve9, We16*], $BaTiO_3$ [*Jo4*]	6
$CeTiO_3$	T	5.513		7.760		*We16*	P&S [*Be33, Ho12, Si4*]	6
$PrTiO_3$	T	5.508		7.742		*We16*	P&S [*Be33, Ho12, Si4*]	6
$NdTiO_3$	O	5.482	5.521	7.728		*We16*	P&S [*Be33, Ho12, Si4*]	6
$SmTiO_3$	O	5.398	5.568	7.651		*We16*	P&S [*Be33, Si4, Mc1c*]	6
$GdTiO_3$	O	5.353	5.655	7.616		*We16*	P&S [*Bo36, Ho12, Si4, Mc1c*]	6
$EuTiO_3$	C	7.810				*Ho12*	Ti^{4+}, P&S [*Br20, Mc1b*], Prop. [*Mc3, Mc4, Si4*], neutron diffraction [*Mc2*]	6
$TbTiO_3$	O	5.388	5.648	7.676		*Mc1c*		
$DyTiO_3$	O	5.361	5.659	7.647		*Mc1c*		
$HoTiO_3$	O	5.339	5.665	7.626		*Mc1c*		
$ErTiO_3$	O	5.318	5.657	7.613		*Mc1c*		
$TmTiO_3$	O	5.306	5.647	7.607		*Mc1c*		
$YbTiO_3$	O	5.293	5.633	7.598		*Mc1c*		
$LuTiO_3$	O	5.274	5.633	7.580		*Mc1c*		
$YTiO_3$	O	5.340	5.665	7.624		*Mc1c*		
$LaVO_3$	O'	5.540	5.540	7.83		*Wo14*	P&S [*Si5, Be33, Ke16, Re8, Wo4, Ke18, Ke15, Ya1, Ro3*], S.S. with: $SrVO_{3.4}$ [*Ke18, Wo14*], S.S. with $CaVO_{2.8}$ [*Wo14*]	6
$CeVO_3$	O'	5.486	5.486	7.74		*Wo14*	P&S [*Be33, Re8, Wo4*]	6
$PrVO_3$	O'	5.487	5.562	7.751		*Wo14*	P&S [*Be33, Re8, Wo4, Vi2, Ge2*]	6
$NdVO_3$	O	5.451	5.579	7.734		*Wo14*	P&S [*Be33, Re8, Wo4, Vi2, Ge2*]	6
$SmVO_3$	O	5.393	5.588	7.672		*Wo14*	P&S [*Be33, Re8, Wo4*]	6
$GdVO_3$	O	5.343	5.614	7.637		*Wo14*	P&S [*Be33, Bo36, Re8, Ge2*]	6
$DyVO_3$	O	5.302	5.602	7.601		*Wo14*	P&S [*Re8*]	6
$ErVO_3$	O	5.262	5.604	7.578		*Wo14*	P&S [*Re8*]	6
YVO_3	O	5.284	5.605	7.587		*Wo14*	P&S [*Ro3, Re8*]	6
$PuVO_3$	O	5.45	5.58	7.76		*Ru13*		
$AmVO_3$	O	5.48	5.61	7.78		*Ke8*		

Compound	Sym	a Å	b Å	c Å	angle	Ref.	Remarks	Magnetic Data
$A^{3+}B^{3+}O_3$ (continued)								in 3.3.4, Tab.
$LaCrO_3$	O	5.479	5.515	7.753		*Qu1*	Semiconducting 0.6 eV [*Ru11*], neutron diffraction [*Ko1*], optical properties [*Ru11*], dielectric properties [*Ra8*], P&S [*Ge2, Ru11, Wo4, Ke2, Na14*], S.S. with Ni, Mn [*Be33, Be21*]; T_{melt} = 2500 °C [*Fo2*], EPR [*We4*]	6
	R	5.47			α = 60° 32'	*Ru11*	T = 280 °C, rhombohedral 280 < T < 1030 °C	
	C	3.92				*Ru11*	T = 1230 °C	
$La_{0.4}Bi_{0.1}CrO_3$	O	5.47	5.50	7.75		*Iw1*		6
$La_{0.6}Sr_{0.3}CrO_{3-x}$	C	7.754				*Ya1*		
$CeCrO_3$	O	5.475	5.475	7.740		*Qu1*	P&S [*Ru10, Be33, Wo4, Ke2*]	6
$PrCrO_3$	O	5.448	5.479	7.718		*Qu1*	P&S [*Ge2, Ru10, Be33, Wo4*], T_{melt} = 2420 °C [*Fo2*], dielectric properties [*Ra8*]	6
$NdCrO_3$	O	5.425	5.478	7.694		*Qu1*	P&S [*Ru10, Ge2, Be33, Wo4, Ke2*], T_{melt} = 2405 °C [*Fo2*]	6
$SmCrO_3$	O	5.367	5.508	7.643		*Qu1*	P&S [*Ru10, Ge2, Be33, Wo4, Ke2*], T_{melt} = 2385 °C [*Fo2*]	6
$EuCrO_3$	O	5.340	5.515	7.622		*Qu1*	P&S [*Ru10*]	6
$GdCrO_3$	O	5.312	5.525	7.606		*Qu1*	P&S [*Ru10, Ge2, Be33*], T_{melt} = 2370 °C [*Fo2*]	6
$TbCrO_3$	O	5.291	5.518	7.576		*Qu1*	Neutron diffraction [*Be42, Ma24*], specific heat [*De1a*]	6
$DyCrO_3$	O	5.265	5.520	7.552		*Qu1*	Neutron diffraction [*Be38*], T_{melt} = 2345 °C [*Fo2*]; dielectric hysteresis disappears at ≈ 540 °C indicating no center of symmetry [*Ra8*]	6
$HoCrO_3$	O	5.243	5.519	7.538		*Qu1*	Neutron diffraction [*Be32, Be47, Be50*], dielectric properties [*Co6*], T_{melt} = 2330 °C [*Fo2*], dielectric hysteresis disappears at ≈ 460 °C indicating no center of symmetry [*Ra8*], S.S. with $HoMnO_3$ [*Ap1b*]	6
$ErCrO_3$	O	5.223	5.516	7.519		*Qu1*	Dielectric properties [*Co6*], T_{melt} = 2325 °C [*Fo2*]	6
$TmCrO_3$	O	5.209	5.508	7.500		*Qu1*		6
$YbCrO_3$	O	5.195	5.510	7.490		*Qu1*	T_{melt} = 2320 °C [*Fo2*], dielectric hysteresis disappears at ≈ 520 °C indicating no center of symmetry [*Ra8*]	6
$LuCrO_3$	O	5.176	5.497	7.475		*Qu1*	Dielectric hysteresis disappears at ≈ 480 °C indicating no center of symmetry [*Ra8*]	6
$YCrO_3$	O	5.241	5.521	7.532		*Qu1*	P&S [*Ge6, Ge2, Lo5, Ka18, Pa14, Yu5*], dielectric properties [*Ra8*], T_{melt} = 2340 °C [*Fo2*]	6
$InCrO_3$	O	5.170	5.355	7.543		*Sh9*	High pressure preparation	

Compound	Sym	a Å	b Å	c Å	angle	Ref.	Remarks	Magnetic Data
$A^{3+}B^{3+}O_3$ (continued)								in 3.3.4, Tab.
$TlCrO_3$	O	5.302	5.405	7.647		*Sh9*	High pressure preparation	
$BiCrO_3$	Tr	3.90	3.87	3.90	$\alpha = \gamma = 90°35'$ $\beta = 89°10'$	*Su10*	High pressure preparation; S.S. with $BiMnO_3$ [*To11a*]	6
$PuCrO_3$	O	5.46	5.51	7.76		*Ru13*		
$LaMnO_3$	O'	5.533	5.722	7.694		*Wo2*	P&S [*Na14*], neutron diffraction [*Ko1, Wo12*], S.S. with Ba, Sr, Ca [*Wo12, Ja4, Ja5, Jo8, Jo12, Ha22, Jo7, Jo9, Ya1, Ro11*], S.S. with Cr, Fe, Co, Ni [*Be33, Be21, Gi4, Jo7, Jo8, Jo9, Wo2, Wo6, Fu2, Bi7*], S.S. with (Ba, Sr, Ca, Pb)TiO_3 [*Ha31, Ha32, To3, To6, To12*], S.S. with $GdCoO_3$ [*De23*]	6
	R	3.892			$\alpha = 90°\ 36'$	*Wo2*	24% Mn^{4+}	
$CeMnO_3$	O'	5.537	5.557	7.818		*Ve12*		
$PrMnO_3$	O'	5.445	5.787	7.575		*Ve12*	P&S [*Be33, Vi1*], complete structure [*Qu2*]	
$NdMnO_3$	O'	5.380	5.854	7.557		*Ve12*	P&S [*Be33, Vi1, Sz1*], complete structure [*Qu2*]	6
$SmMnO_3$	O'	5.359	5.843	7.482		*Ve12*	P&S [*Be33*]	6
$EuMnO_3$	O'	5.338	5.842	7.453		*Ve12*	P&S [*Sz1*]	6
$GdMnO_3$	O'	5.313	5.853	7.432		*Ve12*	P&S [*Be33, Sz1*], S.S. with $LaCoO_3$ [*De23*]	6
$TbMnO_3$	O'	5.297	5.831	7.403		*Ve12*	Complete structure determination [*Qu2*]	6
$DyMnO_3$	O'	5.275	5.828	7.375		*Ve12*	P&S [*Sz1*]	6
	H	6.177		11.43		*Sz1*	Preparation temperature 1600 °C, see Fig. 17a	
$HoMnO_3$	H	6.136		11.42		*Ya2*	Magnetic properties [*Ve12, Be32*], dielectric properties [*Be35, Co7*], P&S [*Sz1*], see Fig. 17a	
	O'	5.26	5.84	7.35		*Wa4*	High pressure phase, P&S [*Wa5, Vi1, Sz1*]	
$ErMnO_3$	H	6.115		11.41		*Ya2*	Magnetic properties [*Ve12, Be32*], dielectric properties [*Be35, Co7*], see Fig. 17a	
	O'	5.24	5.82	7.335		*Wa4*	High pressure phase	
$TmMnO_3$	H	6.062		11.40		*Ya2*	Magnetic properties [*Ve12, Be32*], dielectric properties [*Be35, Co7*], see Fig. 17a	
	O'	5.23	5.81	7.32		*Wa4*	High pressure phase	
$YbMnO_3$	H	6.062		11.40		*Ya2*	Magnetic properties [*Ve12, Be32, Ro8, Bo11*], dielectric properties [*Be35, Ro8, Bo11, Co7, Is11*], P&S [*Sz1*], see Fig. 17a	
	O'	5.22	5.80	7.30		*Wa4*	High pressure phase	
$LuMnO_3$	H	6.042		11.37		*Ya2*	Magnetic properties [*Ve12, Be32*], dielectric properties [*Be35, Co7*], see Fig. 17a	
	O'	5.205	5.79	7.31		*Wa4*	High pressure phase	
$YMnO_3$	H	6.125		11.41		*Ya2*	Dielectric or magnetic properties [*Ta13, Ro8, Be35, Co5, Co7, Co3, Bo11, Is11, Pe17, Pe16, Be32, Be39, Be43, Be44, Be49, Ko3, Ki8*], see Fig. 17a	

Ref.	Magnetic

Berichtigungen zu Band III/4a

S. 177, letzte Zeile: statt Ba_2TdPaO_6 **lies** Ba_2TbPaO_6

S. 219, Zeile 16 von unten: statt $KMg_{1-z}Ni_zFe_3$ **lies** $KMg_{1-z}Ni_zF_3$

S. 252, Zeile 26 von oben (Überschrift): statt $Sr_3Fe_3UO_9$ **lies** $Sr_3Fe_2UO_9$

Errata in Vol. III/4a

p. 177, bottom line: instead of Ba_2TdPaO_6 **read** Ba_2TbPaO_6

p. 219, line 16 from the bottom: instead of $KMg_{1-z}Ni_zFe_3$ **read** $KMg_{1-z}Ni_zF_3$

p. 252, line 26 from above (headline): instead of $Sr_3Fe_3UO_9$ **read** $Sr_3Fe_2UO_9$

Be39, Be43, Be44, Be49, Ko3, Ki8], see Fig. 17a

Compound	Sym	*a* Å	*b* Å	*c* Å	angle	Ref.	Remarks	Magnetic Data
$A^{3+}B^{3+}O_3$ (continued)								in 3.3.4, Tab.
$YMnO_3$	O'	5.26	5.84	7.35		*Wa3*	High pressure phase; S.S. with: Fe, perovskite at 15% Fe [*Ch6*]	
$BiMnO_3$	M	10.93	11.31	7.98	$\beta = 92°\ 24'$	*Bo12*	P&S [*Su10*]; S.S. with Ca [*Bo6, Bo12, St19*], $PbTiO_3$ [*Bo6, Bo7*], Sr [*Jv1*], La [*Jv1*], $BiCrO_3$ [*To11a*]; crystallographic transformation $T = 210$ °C [*To11a*]	6
$PuMnO_3$	C	3.86				*Ru13*	Pseudocubic	
$LaFeO_3$	O	5.556	5.565	7.862		*Ge6*	P&S [*Be33, Fo5, Re5, Wo3, Ke2, Da2, Na14, Ya1*], S.S. with Ni, Mn [*Be33*], S.S. with Al, Co, Cr, Sc [*Ka17, Wo3*], rhombohedral $T > 980$°C [*Da1*], S.S. with: $PbNb_2O_6$ [*Fr11*], Pb [*Re5a*], Bi [*Ri5b*]	6
$CeFeO_3$	O	5.541	5.577	7.809		*Ro1a*	P&S [*Ke2, Be33*]	6
$PrFeO_3$	O	5.495	5.578	7.810		*Ge6*	P&S [*Be33, Fo5, Re5*], S.S. with Al, Co, Cr, Sc [*Ka17*]	6
$NdFeO_3$	O	5.441	5.573	7.753		*Ge6*	P&S [*Be33, Fo5, Re5, Wo3*], S.S. with Pb [*Re5a*], Bi [*Re5b*]	6
$SmFeO_3$	O	5.394	5.592	7.711		*Ge6*	P&S [*Be33, Fo5, Re5, Wo3*], S.S. with Pb [*Re5a*], Bi [*Re5b*]	6
$EuFeO_3$	O	5.371	5.611	7.686		*Ge6*	P&S [*Re5*], S.S. with Pb [*Re5a*], Bi [*Re5b*]	6
$GdFeO_3$	O	5.346	5.616	7.668		*Ge6*	P&S [*Be33, Re5*], crystal structure [*Co21*], S.S. with Pb [*Re5a*], Bi [*Re5b*]	6
$TbFeO_3$	O	5.326	5.602	7.635		*Ei1*	P&S [*Ko6*], S.S. with: Pb [*Re5a*], Bi [*Re5b*]	6
$DyFeO_3$	O	5.302	5.598	7.623		*Ei1*	P&S [*Da2*], S.S. with: Pb [*Re5a*], Bi [*Re5b*]	6
$HoFeO_3$	O	5.278	5.591	7.602		*Ei1*	P&S [*Ko6*], S.S. with: Pb [*Re5a*], Bi [*Re5b*], $HoMnO_3$ [*Ap1a*]	6
$ErFeO_3$	O	5.263	5.582	7.591		*Ei1*	P&S [*Fo5*], crystal structure [*Wi7*], S.S. with: Pb [*Re5a*], Bi [*Re5b*]	6
$TmFeO_3$	O	5.251	5.576	7.584		*Ei1*	Crystal structure [*Wi8*], S.S. with: Pb [*Re5a*], Bi [*Re5b*]	6
$YbFeO_3$	O	5.233	5.557	7.570		*Ei1*	P&S [*Ko6, Be1, Ha21*], S.S. with: Pb [*Re5a*], Bi [*Re5b*]	6
$LuFeO_3$	O	5.213	5.547	7.565		*Ei1*	P&S [*Sa6*], S.S. with: Pb [*Re5a*], Bi [*Re5b*]	6
$YFeO_3$	O	5.283	5.592	7.603		*Ei1*	P&S [*Fo5, Ru11, Ko6, Wo3, Ge4, Ma26, Va7, Sh12a*], crystal structure [*Co21*], S.S. with: Pb [*Re5a*], Bi [*Re5b*]	6
$TlFeO_3$	O	5.319	5.448	7.796		*Sh9*		

Compound	Sym	a Å	b Å	c Å	angle	Ref.	Remarks	Magnetic Data
$A^{3+}B^{3+}O_3$ (continued)								in 3.3.4, Tab.
$BiFeO_3$	R	5.62			$\alpha = 59° 41'$	*Mi0*	P&S [*Fi12, Is10, Ko5, Kr4, To7, To9, To12, Yu3, Yu1, Za2, Sm34, To10, Ge10a, Ro22*], neutron diffraction [*Pl1, Ki4, Ki5, Ki6, Bh2*], S.S. with: $LaAlO_3$ [*Fe5*], $LnFeO_3$ [*Kr5, Kh5, Ro7, Ro9, Is10b, Ro10, Ki6*], $Pb(Ti, Zr)O_3$ [*La6, Fe8, Ge10, Fe2, Sm7*], $BaTiO_3$ [*Ve5, Ka15*], $SrTiO_3$ [*Fe6*], $LaCrO_3$ [*Ro5*], $SrSnO_3$ [*Hi1*], $Bi_4Ti_3O_{12}$ [*Is12*], $SrFeO_3$ [*Ma8*], Pb_2FeNbO_6 [*Ro10, Yu1, Yu2, Sm12, Sm13, Is10a, Zh1, Is8, Kr3, Kr5*], $Sr(Sn_{1/3}Mn_{2/3})O_3$ [*Mi6, Vi4*], $Sr_{0.7}La_{0.3}MnO_3$ [*Ro10*], $PbNb_2O_6$ [*Fr11*]; $BiMnO_3$ [*Ma31*], $Pb(Fe_{2/3}W_{1/3})O_3$ [*Sm26*], $PrFeO_3$ [*Vi4a*], complete structure S.G. R3c [*Mi0*]	6
$LaCoO_3$	R	5.436			$\alpha = 60° 48'$	*Wo9*	$R\bar{3}c$, $T < 375$ °C; $R\bar{3}$, $T > 375°$ [*Ra3*]; P&S [*As3, Wo4, He7, Sc23*], Prop. [*Me17, Ko1, Ra3, Ge12, Ra3, Jo9, Go16, Na1, Bl6, He7, Mu4, Me18*], S.S. with Sr [*Me18, Ra4, Jo13*], S.S. with Sr and Th [*Sc23*]	6
	R	5.52			$\alpha = 60° 0'$	*Ra3*	$T = 937$ °C: atomic positions demand $R\bar{3}$ symmetry	
$PrCoO_3$	O	5.331	5.373	7.587		*Be33*	P&S [*Wo4*]	
$NdCoO_3$	O	5.336	5.336	7.547		*Be33*	P&S [*Wo4*], thermal conductivity [*Ge12*]	6
$SmCoO_3$	O	5.289	5.354	7.541		*Be33*	P&S [*Wo4*]	
$GdCoO_3$	O	5.228	5.404	7.436		*Be33*	P&S [*As5*]	6
$TbCoO_3$							Studied in review of $TbBO_3$ compounds [*Ma24*]. No cell dimension	6
$BiCoO_3$	C	4.228				*To11b*	High pressure preparation [*To11a*]	6
$LaNiO_3$	R	5.461			$\alpha = 60° 49'$	*Wo8*	P&S [*Wo6*], neutron diffraction [*Ko1*]	6
$BiNiO_3$	C	4.173				*To11b*	High pressure preparation [*To11a*]	6
$LaGaO_3$	O	5.496	5.524	7.787		*Ge2*	P&S [*Ke2, Da2, Be34, Br25, Da1, Ma25a*]	
	R	5.544			$\alpha = 60° 25'$	*Ge2*	$T = 900$ °C, rhombohedral $T > 875$ °C (by DTA)	
$CeGaO_3$	C	3.87				*Ke2*	Distorted	
$PrGaO_3$	O	5.465	5.495	7.729		*Ge2*	P&S [*Be34, Br25, Ma25a*]	
$NdGaO_3$	O	5.426	5.502	7.706		*Ge2*	P&S [*Da1, Be34, Br25, Ke2, Ma25a*], complete structure [*Br26*], S.S. with $LaGaO_3$ [*Br25*]	6
$SmGaO_3$	O	5.369	5.520	7.650		*Ma25a*	High pressure preparation	
$EuGaO_3$	O	5.351	5.528	7.628		*Ma25a*	High pressure preparation	
$GdGaO_3$	O	5.322	5.537	7.606		*Ma25a*	High pressure preparation [*Ma25*]	
$TbGaO_3$	O	5.307	5.531	7.578		*Ma25a*	High pressure preparation	

Compound	Sym	a Å	b Å	c Å	angle	Ref.	Remarks	Magnetic Data
$A^{3+}B^{3+}O_3$ (continued)								in 3.3.4, Tab.
$DyGaO_3$	O	5.282	5.534	7.556		*Ma25a*	High pressure preparation	
$HoGaO_3$	O	5.251	5.531	7.536		*Ma25a*	High pressure preparation	
$ErGaO_3$	O	5.239	5.527	7.522		*Ma25a*	High pressure preparation	
$TmGaO_3$	O	5.224	5.515	7.505		*Ma25a*	High pressure preparation	
$YbGaO_3$	O	5.208	5.510	7.490		*Ma25a*	High pressure preparation [*Ma25*]	
$LuGaO_3$	O	5.188	5.505	7.484		*Ma25a*	High pressure preparation	
$YGaO_3$	O	5.257	5.536	7.533		*Ma25*	High pressure preparation [*Ma26*]	
$LaYO_3$	O	5.868	6.071	8.438		*Ge3*	P & S [*Pa2, Mo6*], optical properties (Eu^{3+}) [*Bl13*]	
$BiYO_3$	C	4.2				*To11b*	High pressure preparation [*To11a*]	
$LaNbO_3$	C	4.02				*Si5*	Pseudocubic	
$LaRhO_3$	O	5.524	5.679	7.900		*Wo5*	P & S [*Ch11, Wo9, Kh1*]	
$PrRhO_3$	O	5.4143	5.7473	7.8026		*Sh8a*	P & S [*Ch11*]	
$NdRhO_3$	O	5.3778	5.7551	7.7745		*Sh8a*	P & S [*Wo5*]	
$SmRhO_3$	O	5.3211	5.7613	7.7083		*Sh8a*	P & S [*Ch11*]	
$EuRhO_3$	O	5.2985	5.7607	7.6802		*Sh8a*		
$GdRhO_3$	O	5.2774	5.7605	7.6584		*Sh8a*	P & S [*Ch11*]	
$TbRhO_3$	O	5.2541	5.7492	7.6226		*Sh8a*		
$DyRhO_3$	O	5.2449	5.7314	7.6002		*Sh8a*		
$HoRhO_3$	O	5.2299	5.7257	7.5823		*Sh8a*	P & S [*Ch11*]	
$ErRhO_3$	O	5.2160	5.7117	7.5610		*Sh8a*	P & S [*Ch11*]	
$TmRhO_3$	O	5.2028	5.6974	7.5428		*Sh8a*		
$LuRhO_3$	O	5.1861	5.6700	7.5125		*Sh8a*		
$InRhO_3$	O	5.301	5.435	7.586		*Sh9*		
$LaInO_3$	O	5.723	5.914	8.207		*Ro16*	P & S [*Ge3, Pa2*]	
$NdInO_3$	O	5.627	5.891	8.121		*Ro16*		
$SmInO_3$	O	5.589	5.886	8.082		*Ro16*		
$EuInO_3$	O	5.567	5.835	8.078		*Sh9*	High pressure preparation	
$GdInO_3$	O	5.548	5.842	8.071		*Sh9*	High pressure preparation	
$DyInO_3$	O	5.519	5.751	8.041		*Sh9*	High pressure preparation	
$YInO_3$	O	5.500	5.787	8.053		*Sh9*	High pressure preparation	
$LaHoO_3$	O	5.888	6.092	8.480		*Mo6*		6
$LaErO_3$	O	5.85	6.07	8.43		*Sc12*	P & S [*Sc13, Mo6*]	6
$LaTmO_3$	O	5.85	6.06	8.42		*Sc12*	P & S [*Sc13, Mo6*]	6
$LaYbO_3$	O	5.85	6.02	8.41		*Sc12*	P & S [*Sc13, Mo6*], complete structure determined, S.G. $Pbn2_1$, [*Mu8*], T_{melt} = 2120 °C [*Tr0*]	6
	C	4.325				*Tr0*	T = 2080 °C	
$LaLuO_3$	O	5.82	6.02	8.37		*Sc12*	P & S [*Sc13, Mo6*]	
$PrLuO_3$	O	5.751	5.977	8.320		*Mo6*		

Tab. 2b. $A_2B'BX_6$ compounds

Compound	Sym	a Å	b Å	c Å	angle	Ref.	Remarks	Magnetic Data
$A_2^+B^{3+}X_6$; X = F^{-1}, Cl^{-1}								in 3.3.4, Tab.
Cs_2NaAlF_6	H	6.168		29.76		*Ba5a*	Hex (12 L)	
Rb_2NaAlF_6	C	8.29				*Ba5a*		
Rb_2LiAlF_6	H	5.802		28.02		*Ba5a*	Hex (12L)	
K_2LiAlF_6	H	5.574		13.648		*Wi11b*	R perovskite	
	H	5.614		13.754		*Wi11b*	Hex (6L), Prep. $T > 470$ °C	
K_2NaAlF_6	C	8.105				*Me21*		
K_3KAlF_6	C	8.65				*St33*		
Na_2NaAlF_6	M	5.46	5.61	7.80	$\beta = 90° 11'$	*Na17*	P&S [*St33, Me19, Cr5a*], S.S. with Fe [*Cr5a*]	
$(NH_4)_3(NH_4)AlF_6$	C	8.90				*Pa9*	P&S [*Pa10, Me20*]	
Cs_2CsScF_6							Prep. [*Ba0*]	
Cs_2KScF_6	C	9.32				*Ho16a*		
Rb_2RbScF_6	C						Prep. [*Ba0*]	
K_2KScF_6	C	17.46				*Bo2*	Prep. [*Ba0*]	
Na_2NaScF_6	M	5.60	5.81	8.12	$\beta = 90° 45'$	*Th1*	$T < 680$ °C	
$(NH_4)_3(NH_4)ScF_6$	T	6.49		9.45		*Bo2*		
	C	9.26				*Bo2*	High temperature form	
K_2KTiF_6	T	8.56		8.75		*Br7*	P&S [*Ba5*], magnetic properties, $n_{eff} = 1.70$, $\Theta_p = 0$ °K [*Eh1*]	
K_2NaTiF_6	C	8.367				*Br7*	Structure determined [*Bu4a*]	
Na_2NaTiF_6	M	5.53	5.83	7.99	$\beta \cong 90°$	*Br7*	P&S [*Ba5*]	
Cs_2KVF_6	C	9.04				*Ba5a*		
Cs_2NaVF_6	H	6.267		30.40		*Ba5a*	Hex (12L)	
Rb_2KVF_6	C	8.88				*Ba5a*		
Rb_2NaVF_6	C	8.47				*Ba5a*		
Rb_2LiVF_6	H	5.891		28.77		*Ba5a*	Hex (12L)	
K_2KVF_6							Magnetic properties, $80 < T < 300$ °K, $n_{eff} = 2.79$, $\Theta_p = -14$ °K [*Fi4*]	
K_2NaVF_6	C	8.315				*Ba5*		
$(NH_4)_3(NH_4)VF_6$	C	9.04				*Pa6a*		
Cs_2RbCrF_6	C	9.15				*Ba5a*		
Cs_2KCrF_6	C	8.99				*Ba5a*		
Cs_2NaCrF_6	H	6.231		30.24		*Ba5a*	Hex (12L)	
Rb_2KCrF_6	C	8.81				*Ba5a*		
Rb_2NaCrF_6	C	8.42				*Ba5a*		
Rb_2LiCrF_6	H	5.865		28.61		*Ba5a*	Hex (12L)	
K_2KCrF_6	T	8.56		8.62		*Kl6*	P&S [*Ps2*]	
K_2KCrF_6	C	8.54				*Bo2*	High temperature form	

Compound	Sym	a Å	b Å	c Å	angle	Ref.	Remarks	Magnetic Data
$A_2^+B^+B^{3+}X_6$; X = F^{-1}, Cl^{-1} (continued)								in 3.3.4, Tab.
K_2NaCrF_6	C	8.266				*Kn5*	Prop. [*Sh28*]	
Na_2NaCrF_6	M	5.468	5.679	7.878	$\beta \approx 90°$	*Vo1*		
$(NH_4)_2(NH_4)CrF_6$	C	9.01				*Pa6a*		
K_2KMnF_6	T	17.50		16.60		*Pe2*	Magnetic properties, $\mu^* = 4.95\,\mu_B$ [*Pe2*]	
K_2NaMnF_6	T	8.171		8.577		*Kn4*		
Cs_2CsFeF_6	C	10.46				*Mi2*		
Cs_2KFeF_6	C	9.05				*Ba5a*	P&S [*Ho16a*]	
Cs_2NaFeF_6	H	6.260		30.40		*Ba5a*	Hex (12L)	
Rb_2RbFeF_6	C	8.88				*Bo2*		
Rb_2KFeF_6	C	8.87				*Ba5a*		
Rb_2NaFeF_6	C	8.47				*Ba5a*		
Rb_2LiFeF_6	H	5.891		28.77		*Ba5a*	Hex (12L)	
K_2KFeF_6	C	8.58				*Bo2*		
K_2NaFeF_6	C	8.323				*Kn5*		
Na_2NaFeF_6	M	5.506	5.719	7.925	$\beta = 90° 28'$	*Cr5a*	P&S [*Mi5*], magnetic properties, $92 < T < 296$ °K, $n_{eff} = 5.85$, $\Theta_p = -2$ °K [*Fi1*]	
Li_2LiFeF_6	C	8.88				*Mi2*	Magnetic properties, $93 < T < 293$ °K, $n_{eff} = 6.00$, $\Theta_p = 0$ °K [*Fi1*]	
$(NH_4)_2(NH_4)FeF_6$	T	6.39		9.30		*Si33*	Low temperature form	
	C	9.10				*Pa9*	P&S [*Si33, Ki6*]; magnetic properties, $92 < T < 294$ °K, $n_{eff} = 5.86$, $\Theta_p = -2$ °K [*Fi1*]	
Cs_2CsCoF_6	C	9.23				*Ki6*	Magnetic properties, $90 < T < 290$ °K, $n_{eff} = 5.28$, $\Theta_p = +2$ °K [*Ki6*]	
Rb_2RbCoF_6	C	8.90				*Ki6*	P&S [*Ho13*], magnetic properties, $90 < T < 290$ °K, $n_{eff} = 5.48$, $\Theta_p = -2$° K [*Ki6*]	
K_2KCoF_6	C	8.57				*Ki6*	P&S [*Me27, Ho13*], magnetic properties, $73 < T < 300$ °K, $n_{eff} = 5.53$, $\Theta_p = -10$° K [*Co23, Ki6*]	
K_2NaCoF_6	C	8.22				*Me27*		
Na_2NaCoF_6	C	7.91				*Ki6*	Pseudocubic, P&S [*Ho13*], magnetic properties, $90 < T < 290$ °K, $n_{eff} = 5.39$, $\Theta_p = -5$ °K [*Ki6*]	
K_2KNiF_6	C	8.44				*Bo2*	P&S [*Ki6*], magnetic properties, $90 < T < 295$ °K, does not obey Curie-Weiss law [*Ki2, Ki3, We20*]	
K_2KCuF_6	C	8.50				*Ki6*	Magnetic properties, $n_{eff} = 2.8$ [*Ki2*]	
Cs_2KGaF_6	C	8.975				*Ho16a*		
K_2NaGaF_6	C	8.246				*Kn5*		
$(NH_4)_2(NH_4)GaF_6$	C	9.041				*Sc26*		
Cs_2KAgF_6	C	9.175				*Ho16*		

Compound	Sym	*a* Å	*b* Å	*c* Å	angle	Ref.	Remarks	Magnetic Data
$A_2^+B^+B^{3+}X_6$; X = F^{-1}, Cl^{-1} (continued)								in 3.3.4, Tab.
Cs_2CsInF_6	C	9.50				*Bo2*		
Cs_2KInF_6	C	9.219				*Ho16a*		
Rb_2RbInF_6	C	9.20				*Bo2*		
K_2KInF_6	C	17.71				*Bo2*		
$(NH_4)_3(NH_4)MoO_3F_3$	C	9.10				*Pa9*		
Cs_2NaCeF_6	C	9.26				*Be52a*		
Cs_2KCeF_6	C	9.61				*Be52a*		
Cs_2RbCeF_6	C	9.75				*Be52a*		
Cs_2CsCeF_6	C	9.84				*Be52a*		
$CsKKCeF_6$	C	9.36				*Be52a*		
$CsRbRbCeF_6$	C	9.60				*Be52a*		
Rb_2KCeF_6	C	9.40				*Be52a*		
Rb_2RbCeF_6	C	9.49				*Be52a*	P&S [*Bo2*]	
$RbKKCeF_6$	C	9.20				*Be52a*		
K_2KCeF_6	C	9.07				*Be52a*		
Rb_2RbPrF_6	C	9.48				*Bo2*		
Cs_2NaSmF_6	C	9.163				*Al4*		
Rb_2NaSmF_6	C	8.988				*Al4*		
Cs_2NaTbF_6	C	9.107				*Al4*		
Rb_2NaTbF_6	C	9.9208				*Al4*		
Rb_2NaHoF_6	C	8.881				*Al4*		
Cs_2NaErF_6	C	9.061				*Al4*	Structure refined	
Rb_2NaErF_6	C	8.867				*Al4*	Structure refined	
Cs_2NaYbF_6	C	9.022				*Al4*		
Rb_2NaYbF_6	C	8.824				*Al4*		
Cs_2NaYF_6	C	9.056				*Al4*		
Rb_2NaYF_6	C	8.8693				*Al4*		
$Cs_2AgAuCl_6$	T	7.38		11.01		*El3*	Magnetic properties [*El1*], P&S [*Fe19*]	
$Cs_2AgAuCl_6$	C	5.28				*El3*		
$Cs_2AuAuCl_6$	T	7.49		10.87		*El3*	Magnetic properties [*El1*]	
Cs_2KTlF_6	C	9.36				*Ho16a*		
K_2KTlF_6	C	11.86				*Bo2*		
$(A^{2+}A^{3+})$ $(B^{3+}B^{4+})O_6$								
$BaLaMnTiO_6$	C	3.960				*Ha32*	S.S. with Sr, rhombohedral > 30% Sr	
$SrLaMnTiO_6$	R	3.912			$\alpha = 90° 12'$	*Ha32*	Cubic > 700 °C	
$CaLaMnTiO_6$	R	3.872			$\alpha = 90° 6'$	*Ha32*		
$CaYMnTiO_6$	O	5.32	5.53	7.54		*Ha32*	S.S. with La	
$PbLaMnTiO_6$	R	3.933			$\alpha = 90° 12'$	*Ha32*	S.S. with $x = Pb_2NbMnO_6$; cubic ≥ 50%	

Compound	Sym	a Å	b Å	c Å	angle	Ref.	Remarks	Magnetic Data
$PbLaMnTiO_6$	R	3.933			$\alpha = 90° 12'$	*Ha32*	S.S. with $x = Pb_2NbMnO_6$; cubic $\geq 50\%$	
$(A^{3+}A^{3+})(B^{3+}B^{4+})O_6$ (continued)								in 3.3.4, Tab.
$SrLaFeTiO_6$	C	3.92				*Bl8*		
$SrLaMnIrO_6$	C	3.93				*Bl8*		
$SrLaFeIrO_6$	C	3.94				*Bl8*		
$A_2^{3+}BB'O_6$								
La_2MgTiO_6	C	3.96				*Ag1*	P&S [*Ro20*], Eu^{3+} fluorescence [*Bl14*], S.S. with: Ni and optical properties [*Re4a*]	
Nd_2MgTiO_6	C	3.90				*Ro20*	Slight distortion	
$LaCeMgTiO_6$	C	3.929				*Ro20*	Slight distortion	
Bi_2MgTiO_6	C	3.98				*Su5*	Some question on atom positions	
$Y_2Ni_{0.4}Mg_{0.6}TiO_6$	C	3.83				*Re4a*	Optical properties	
La_2MgMnO_6						*Bl7*		
La_2CoMnO_6						*Bl7*	See $LaMnO_3$ systems for magnetic properties	
La_2NiMnO_6						*Bl7*	See $LaMnO_3$ systems for magnetic properties, P&S [*Fu2*]	
La_2CuMnO_6						*Bl7*	See $LaMnO_3$ systems for magnetic properties	
La_2MgGeO_6	C	3.90				*Ro20*		
Y_2MgGeO_6	C	3.88				*Re4a*		
La_2MgZrO_6	C	4.06				*Ra1*	S.S. with Ni and optical properties [*Re4a*]	
La_2CaZrO_6	C	4.174				*Ra1*		
La_2LiNbO_6	O	5.59	5.76	7.92		*Bl1a*	Eu^{3+} fluorescence [*Bl14*]	
La_2MgRuO_6	C	7.91				*Ga5*	Semiconducting, $\Delta E = 0.046$ eV	
La_2MnRuO_6	C	7.84				*Ga5*		
La_2NiRuO_6	C	7.90				*Ga5*	Semiconducting, $\Delta E = 0.12$ eV	
La_2ZnRuO_6	C	7.97				*Ga5*		
$La_2Ni_{0.4}Mg_{0.6}SnO_6$	C	4.02				*Re4a*	Optical properties	
La_2MgReO_6	C	7.926				*Ba25a*		
La_2NiReO_6	C	7.908				*Ba25a*		
La_2CoReO_6	T	5.611		7.968		*Ba25a*		
La_2FeReO_6							Disproportionates [*Ba25a*]	
La_2MgIrO_6	C	7.92				*Ga5*	"Complex magnetic properties" [*Bl7*], P&S [*Bl8*]	
La_2MnIrO_6	C	7.86				*Ga5*		
La_2CoIrO_6	O	5.60	5.60	7.92		*Bl8*	"Complex magnetic properties" [*Bl7*]	
La_2NiIrO_6	C	7.90				*Ga5*	"Complex magnetic properties" [*Bl7*], P&S [*Bl8*]	
La_2CuIrO_6	M	5.80	5.60	7.72	$\gamma = 86° 56'$	*Bl8*	"Complex magnetic properties" [*Bl7*]	
$A_2^{3+}BV^{5+}O_6$								
Ba_2BiVO_6	O	6.123	6.180	8.622		*Ve2*	P&S [*Vi3*, *Ve3*], dielectric properties [*Vi2b*]	
	C	4.372				*Ve2*	Cubic > 320 °C	

Compound	Sym	*a* Å	*b* Å	*c* Å	angle	Ref.	Remarks	Magnetic Data
$A_2^{3+}BNb^{4+}O_6$								in 3.3.4, Tab.
Ba_2ScNbO_6	C	8.220				*Fi10*	P&S [*Ag1, Br16*]	
Ba_2VNbO_6	C	4.051				*Ch10*		
Ba_2MnNbO_6	C	4.090				*Ha32*	P&S [*Ag1*]	6
Ba_2FeNbO_6	C	4.057				*Ga1*	P&S [*Ga13, Fi10, Ag1*]	
Ba_2CoNbO_6	C	4.06				*Bl8*		
Ba_2NiNbO_6	C	4.1				*Bl8*		
$Ba_2SrNbO_{5.6}$	C	8.54				*Ga1*		
Ba_2YNbO_6	C	4.180				*Br16*	P&S [*Fi10*]	
Ba_2RhNbO_6	C	8.17				*Bl8*		
Ba_2InNbO_6	C	8.279				*Br16*	P&S [*Ga1*]	
$Ba_2BaNbO_{6.5}$	C	8.68				*Ga1*		
Ba_2LaNbO_6	T	8.607		8.690		*Ga1*	P&S [*Br16*], cubic $T > 300$ °C [*Fi10*]	
Ba_2CeNbO_6	C	4.293				*Br16*	Probably ordered	
Ba_2PrNbO_6	C	4.285				*Br16*	Probably ordered, cubic $T > 300$ °C [*Fi10*]	
Ba_2NdNbO_6	C	8.540				*Ga1*	P&S [*Br16*], cubic $T > 300$ °C [*Fi10*]	
Ba_2SmNbO_6	C	8.518				*Ga1*	P&S [*Br16*], cubic $T > 300$ °C [*Fi10*]	
Ba_2EuNbO_6	C	8.507				*Ga1*	P&S [*Br16*]	
Ba_2GdNbO_6	C	8.496				*Ga1*	P&S [*Br16*], fluorescences [*Bl11, Ni1, Bl14*]	6
Ba_2TbNbO_6	C	4.229				*Br16*	Probably ordered	
Ba_2DyNbO_6	C	8.437				*Ga1*	P&S [*Br16*]	
Ba_2HoNbO_6	C	8.434				*Ga1*	P&S [*Br16*]	
Ba_2ErNbO_6	C	8.427				*Ga1*	P&S [*Br16*]	
Ba_2TmNbO_6	C	8.408				*Ga1*	P&S [*Br16*]	
Ba_2YbNbO_6	C	8.374				*Ga1*	P&S [*Br16*], dielectric properties [*Ag1*]	
Ba_2LuNbO_6	C	8.364				*Ga1*	P&S [*Br16*]	
Ba_2TlNbO_6	C	8.42				*Sl6*		
Ba_2BiNbO_6	R	6.086			$\alpha = 60°\,21'$	*Ve2*	P&S [*Vi3, Ve3*], dielectric properties [*Vi2b*]	
Sr_2AlNbO_6	C	7.784				*Fi10*	P&S [*Sl1*]	
$Sr_2CaNbO_{5.6}$	C	8.20				*Ga13*		
Sr_2VNbO_6	C	3.965				*Ch10*		
Sr_2CrNbO_6	C	7.87				*Bl8*	P&S [*Br14*]	
Sr_2MnNbO_6	R	3.97			$\alpha \approx 90°$	*Ha32*	P&S [*Ku12*], cubic $T > 200$ °C [*Ku12*]	6
Sr_2FeNbO_6	T	3.960		3.980		*Ku6*	P&S [*Ga13, Ku12*]	
	C	3.968				*Ku6*	$T = 250$ °C, cubic $T \geq 250$ °C	
Sr_2CoNbO_6	C	3.93				*Bl8*		
Sr_2GaNbO_6	C	3.9477				*Br14*		
$Sr_2SrNbO_{5.6}$	C	8.34				*Ga13*		
Sr_2YNbO_6	R	5.184			$\alpha = 59°\,51'$	*Ku12*	Cubic $T > 630$ °C	
Sr_2InNbO_6	C	8.106				*Fi10*	P&S [*Br14*]	

Compound	Sym	a Å	b Å	c Å	angle	Ref.	Remarks	Magnetic Data
$A_2^{II}B^{V}B^{VI}O_6$ (continued)								in 3.3.4, Tab.
Sr_2PrNbO_6	T	5.822		8.431		*Ku12*		
Sr_2NdNbO_6	T	5.780		8.367		*Ku12*		
Sr_2SmNbO_6	M	5.85	5.94	8.30	$\beta = 90° 12'$	*Fi10*	P&S [*Ku12*]	
Sr_2EuNbO_6	M	5.84	5.91	8.30	$\beta = 90° 12'$	*Fi10*		
Sr_2GdNbO_6	M	5.83	5.90	8.28	$\beta = 90° 15'$	*Fi10*		
Sr_2TbNbO_6	M	5.82	5.88	8.27	$\beta = 90° 8'$	*Fi10*		
Sr_2DyNbO_6	M	5.81	5.87	8.26	$\beta = 90° 9'$	*Fi10*		
Sr_2HoNbO_6	M	5.81	5.86	8.23	$\beta = 90° 6'$	*Fi10*		
Sr_2ErNbO_6	M	5.80	5.84	8.23	$\beta = 90° 4'$	*Fi10*		
Sr_2TmNbO_6	C	8.20				*Fi10*	Slight distortion	
Sr_2YbNbO_6	C	8.196				*Ku12*	Cubic $T > 540$ °C	
Sr_2LuNbO_6	C	8.19				*Ku12*	Cubic $T > 540$ °C	
$SrLaCoNbO_6$	C	7.99				*Bl8*		6
$SrLaNiNbO_6$	C	7.95				*Bl8*		6
$SrLaCuNbO_6$	T	7.80		8.28		*Bl8*		
La_2LiNbO_6							Ordered perovskite (Eu^{3+} fluorescence) [*Bl14*]	
Ca_2AlNbO_6	O	5.382	5.408	7.614		*Fi8*		
Ca_2VNbO_6	O	5.44	5.51	7.77		*Ch9*		
Ca_2CrNbO_6	O	5.418	5.494	3.858		*Fi8*		
Ca_2MnNbO_6	O	5.44	5.55	7.74		*Ha32*		6
Ca_2FeNbO_6	O	5.451	5.551	3.881		*Fi8*		
Ca_2YNbO_6	O	5.580	5.819	8.046		*Fi8*		
Ca_2InNbO_6	O	5.532	5.715	7.913		*Fi8*		
Ca_2LaNbO_6	O	5.652	5.866	8.140		*Fi8*		
Ca_2PrNbO_6	O	5.623	5.866	8.116		*Fi8*	Possibly lower symmetry	
Ca_2NdNbO_6	O	5.612	5.858	8.104		*Fi8*	Possibly lower symmetry	
Ca_2SmNbO_6	M	5.590	5.860	8.090	$\beta = 90° 10'$	*Fi8*		
Ca_2GdNbO_6	M	5.572	5.841	8.080	$\beta = 90° 12'$	*Fi8*		
Ca_2TbNbO_6	O	5.571	5.830	8.072		*Fi8*		
Ca_2DyNbO_6	O	5.580	5.819	8.062		*Fi8*		
Ca_2HoNbO_6	O	5.580	5.812	8.050		*Fi8*		
Ca_2ErNbO_6	O	5.575	5.794	8.020		*Fi8*		
Ca_2YbNbO_6	O	5.571	5.769	8.000		*Fi8*		
Pb_2AlNbO_6	C	10.53				*Fi11*	Defect pyrochlore type P&S [*Ag1, Ve4*]	
Pb_2ScNbO_6	T	4.074		4.083		*Is2*	Dielectric properties [*Jo3, Sm18, Te8e*], S.S. with PbTi, Zr, HfO_2 [*Jo3*], crystal growth [*Ga5*]	
$Pb_2Sc_{0.4}Cr_{0.6}NbO_6$	C	4.060				*To1*	Possible rhombohedral distortion	
Pb_2CrNbO_6	C	10.54				*Fi11*	Defect pyrochlore type	
Pb_2MnNbO_6	C	4.023				*Fi11*	P&S [*Ha32*], S.S. with Fe and $PbTiO_3$ [*Ha31*]	6

Compound	Sym	a Å	b Å	c Å	angle	Ref.	Remarks	Magnetic Data
$A_2^{3+}BNb^{4+}O_6$ (continued)								in 3.3.4, Tab.
Pb_2FeNbO_6	R	4.014			$\alpha = 89° 55'$	*Ku10*	P&S [*Ro8*], S.S. with $BiFeO_3$ [*Sm12, Is8, Yu2*], complete structure [*Pl3*], crystal growth [*Ga5*], dielectric properties [*Kh8, Sm25, Sm16, Bo8, Sh32, Sh1, Sh33*], optical spectra [*Pi5*], B site ordering [*Yu9*], S.S. with Ta [*Sh33*]	6
Pb_2CoNbO_6	C	8.084				*Ro8*	Dielectric properties [*Ku10, Ag1, Va4*]	6
Pb_2NiNbO_6	C	4.030				*Ku10*	Dielectric properties [*Ku10*] with 5% Ba [*Sh32*]	6
Pb_2GaNbO_6							High pressure preparation, no dimension [*To11a*]	
Pb_2YNbO_6	C	10.65				*Fi11*	Pyrochlore type	
Pb_2InNbO_6	C	4.110				*Ku9*	Dielectric properties [*Ku10*]	
Pb_2HoNbO_6	O	5.86	5.91	8.21		*Ku9*	Dielectric properties [*Ku10*]	
Pb_2TmNbO_6	O	5.858	5.936	8.178		*Ku10*		
Pb_2YbNbO_6	O	5.848	5.918	8.186		*Fi11*	Cubic $T > 280$ °C, dielectric properties [*Sm25, Ku9, Ku10, Ag1, Is17*], S.S. with $PbFe_{2/3}W_{1/3}O_3$ [*To5, To11, Ro11*]	
Pb_2LuNbO_6	O	5.850	5.902	8.176		*Ku9*	Cubic $T > 280$ °C, dielectric properties [*Ku9, Ku10, Is17*]	
Pb_2BiNbO_6	M	10.777	10.643	10.777	$\beta = 90° 29'$	*Vi3*	Defect pyrochlore type	
$Pb_2Mg_{0.5}Mn_{0.5}NbO_6$	C	4.018				*Vi5*	Dielectric properties [*Ve4, Vi5*]	
$Pb_2Co_{0.5}Mn_{0.5}NbO_6$	C	4.020				*Vi5*	Dielectric properties [*Ve4, Vi5*]	6
$Pb_2Ni_{0.5}Mn_{0.5}NbO_6$	C	4.018				*Vi5*	Dielectric properties [*Ve4, Vi5*]	6
$Pb_2Zn_{0.5}Mn_{0.5}NbO_6$	C	4.028				*Vi5*	Dielectric properties [*Ve4, Vi5*]	
$Pb_2Cd_{0.5}Mn_{0.5}NbO_6$	C	4.060				*Ro8*	Dielectric properties [*Ve4, Vi5, Ro8, Ve3*]	6
$A_2^{3+}BSb^{5+}O_6$								
Ba_2ScSbO_6	C	8.197				*Si6*		
Ba_2CrSbO_6							Not perovskite [*Bi8*]	
Ba_2MnSbO_6							Not perovskite [*Bi8*]	
Ba_2FeSbO_6	H	5.79		14.22		*Bi8*	Hex (6L), P&S [*Si6, Bi3*]	6
Ba_2CoSbO_6	H	5.72		14.00		*Bi8*	Hex (6L)	
Ba_2NiSbO_6							Not perovskite [*Bi8*]	
Ba_2RhSbO_6	H	5.78		14.20		*Bi8*	Hex (6L)	
Ba_2InSbO_6	C	8.269				*Si6*	P&S [*Bi3, Bi8*]	
Ba_2GdSbO_6	C	8.44				*Bi8*		
Sr_2CrSbO_6	C	7.87				*Bi8*	P&S [*Si6, Bi3*]	6
Sr_2MnSbO_6	T	7.86		8.08		*Bi8*		6
Sr_2FeSbO_6	C	7.90				*Bi8*	P&S [*Si6, Bi3*]	6
Sr_2CoSbO_6	C	7.88				*Bi8*		6
Sr_2NiSbO_6	T					*Bi8*	Not single phase (no dimensions)	

Compound	Sym	a Å	b Å	c Å	angle	Ref.	Remarks	Magnetic Data
$A^{3+}_3BSb^{4+}O_9$ (continued)								in 3.3.4, Tab.
Sr_3GaSbO_9	T	7.84		7.91		*Si6*		
Sr_3RhSbO_9	O	5.55	5.77	7.99		*Bi8*		
Ca_3FeSbO_9	O	5.47	5.54	7.74		*Bi8*		6
$SrLaMgSbO_6$						*Bi14*	Eu^{3+} fluorescence, no dimensions	
$SrLaCoSbO_6$	C	7.99				*Bi8*		6
$SrLaNiSbO_6$	C	7.93				*Bi8*		6
$SrLaCuSbO_6$	T	7.80		8.35		*Bi8*		
$A^{2+}_2BTa^{4+}O_6$								
Ba_2AlTaO_6							No compound [*Ag1*, *Sm8*]	
Ba_2ScTaO_6	C	8.220				*Fi10*	Dielectric properties [*Ag1*, *Br13*, *Br14*], P&S [*Ga15*]	
Ba_2VTaO_6	C	8.104				*Si1*	P&S [*Ch10*]	
Ba_2CrTaO_6	H					*Si1*	Hex (6L) no dimensions	
Ba_2MnTaO_6	C	4.076				*Fi5*	P&S [*Si1*]	
Ba_2FeTaO_6	C	4.048				*Fi5*	P&S [*Ga13*], dielectric properties [*Ag1*], S.S. with $BaTiO_3$ [*Na9*]	
Ba_2NiTaO_6	C	8.152				*Si1*		
Ba_2YTaO_6	C	8.424				*Fi10*	P&S [*Ag1*, *Br13*, *Br14*, *Fi5*, *La9*], doped with Nd, Sm, Yb [*Ga15*]	
Ba_2InTaO_6	C	8.282				*Fi10*	P&S [*Ag1*, *Ga15*] doped with Nd, Sm, Yb [*Ga15*]	
$Ba_2BaTaO_{5.5}$	C	8.70				*Ga13*	P&S [*Br13*]	
Ba_2LaTaO_6	R	6.07			$\alpha = 60° 25'$	*Ga15*	P&S [*Br13*], doped with Nd [*Ga15*], cubic > 300 °C [*Fi5*]	
Ba_2PrTaO_6	R	6.05			$\alpha = 60° 10'$	*Fi10*	P&S [*Br13*, *Fi5*] cubic $T > 300$ °C [*Fi5*]	
Ba_2NdTaO_6	R	6.04			$\alpha = 60° 4'$	*Fi10*	P&S [*Br13*, *Fi5*] cubic $T > 300$ °C [*Fi5*]	
Ba_2SmTaO_6	R	6.01			$\alpha = 60° 4'$	*Fi10*	P&S [*Br13*, *Fi5*] cubic $T > 300$ °C [*Fi5*]	
Ba_2EuTaO_6	C	8.486				*Fi10*	P&S [*Ga15*]	
Ba_2GdTaO_6	C	8.470				*Fi10*	Doped with Nd [*Ga15*]	
Ba_2TbTaO_6	C	8.440				*Fi10*		
Ba_2DyTaO_6	C	8.420				*Fi10*	P&S [*Ga15*]	
Ba_2HoTaO_6	C	8.416				*Fi10*	P&S [*Ga15*]	
Ba_2ErTaO_6	C	8.398				*Fi10*	P&S [*Ga15*]	
Ba_2TmTaO_6	C	8.388				*Fi10*	P&S [*Ga15*]	
Ba_2YbTaO_6	C	8.378				*Fi10*	P&S [*Ga15*], dielectric properties [*Ag1*]	
Ba_2LuTaO_6	C	8.354				*Fi10*	P&S [*Ga15*], doped with Nd [*Ga15*]	
Ba_2TlTaO_6	C	8.42				*Si1*		
Ba_2BiTaO_6	R	6.047			$\alpha = 60° 15'$	*Ve2*	Dielectric properties [*Vi3*, *Ve3*]	
Sr_2AlTaO_6	C	7.786				*Fi10*	P&S [*Si1*], B-B' ordering [*Si1*]	
Sr_2NiSbO_6	T					*Bi8*	Not single phase (no dimensions)	

Compound	Sym	a Å	b Å	c Å	angle	Ref.	Remarks	Magnetic Data
$A_2^{3+}BTa^{5+}O_6$ (continued)								in 3.3.4, Tab.
Sr_2VTaO_6	C	3.967				*Ch10*		
Sr_2CrTaO_6	C	3.94				*Na7*	P&S [*Ro20*], S.S. with Fe [*Na7*]	
Sr_2MnTaO_6	C	3.994				*Ku12*		
Sr_2FeTaO_6	T	3.960		3.981		*Ku7*	P&S [*Ku12, Sl1, Na5, Na6, Na7*], B-B' ordering [*Sl1, Be5*], S.S. with $SrTiO_3$ and Ba_2FeTaO_6 [*Na5, Be5*], S.S. with $BaTiO_3$ [*Na6*]	6
	C	3.973				*Ku7*	Cubic at 250 °C [*Ku7, Na5, Na6*]	
Sr_2GaTaO_6	C	7.892				*Sl1*		
$Sr_2SrTaO_{5.5}$	C	8.34				*Ga13*	P&S [*Br13*]	
Sr_2YTaO_6	R	5.837			$\alpha = 59°\ 46'$	*Ku12*		
Sr_2RhTaO_6	C	7.936				*Sl1*		
Sr_2InTaO_6	C	8.110				*Fi10*	P&S [*Sl1*]	
Sr_2LaTaO_6	T	5.853		8.387		*Ku12*	P&S [*Br13*]	
Sr_2PrTaO_6	M	5.87	5.98	8.35	$\beta = 90°\ 9'$	*Fi10*	P&S [*Ku12*]	
Sr_2NdTaO_6	M	5.86	5.96	8.34	$\beta = 90°\ 9'$	*Fi10*	P&S [*Ku12*]	
Sr_2SmTaO_6	M	5.85	5.93	8.31	$\beta = 90°\ 11'$	*Fi10*	P&S [*Ku12*]	
Sr_2EuTaO_6	M	5.84	5.91	8.30	$\beta = 90°\ 12'$	*Fi10*		
Sr_2GdTaO_6	M	5.83	5.90	8.29	$\beta = 90°\ 13'$	*Fi10*		
Sr_2TbTaO_6	M	5.82	5.88	8.28	$\beta = 90°\ 9'$	*Fi10*		
Sr_2DyTaO_6	M	5.82	5.87	8.26	$\beta = 90°\ 8'$	*Fi10*		
Sr_2HoTaO_6	M	5.81	5.85	8.23	$\beta = 90°\ 8'$	*Fi10*		
Sr_2ErTaO_6	M	5.80	5.84	8.23	$\beta = 90°\ 4'$	*Fi10*		
Sr_2TmTaO_6	C	8.20				*Fi10*	Slight distortion	
Sr_2YbTaO_6	C	8.196				*Ku12*		
Sr_2LuTaO_6	C	8.18				*Fi10*	Slight distortion	
$SrLaCoTaO_6$	C	7.99				*Bi8*		6
$SrLaNiTaO_6$	C	7.95				*Bi8*		6
$SrLaCuTaO_6$	T	7.80		8.28		*Bi8*		
Ca_2AlTaO_6	O	5.381	5.407	7.612		*Fi8*		
Ca_2VTaO_6	O	5.45	5.49	7.76		*Ch9*		
Ca_2CrTaO_6	O	5.418	5.491	3.857		*Fi8*	P&S [*Sl1*]	
Ca_2MnTaO_6	O	5.462	5.571	3.873		*Fi8*		
Ca_2FeTaO_6	O	5.451	5.560	3.880		*Fi8*		
Ca_2YTaO_6	O	5.580	5.819	8.044		*Fi8*		
Ca_2InTaO_6	O	5.531	5.714	7.924		*Fi8*		
Ca_2LaTaO_6	O	5.654	5.890	8.146		*Fi8*		
Ca_2PrTaO_6	O	5.629	5.867	8.116		*Fi8*		
Ca_2NdTaO_6	O	5.616	5.857	8.106		*Fi8*	Possibly lower symmetry	
Ca_2SmTaO_6	O	5.606	5.853	8.096		*Fi8*	Possibly lower symmetry	

Compound	Sym	a Å	b Å	c Å	angle	Ref.	Remarks	Magnetic Data
Ca_2SmTaO_6	O	5.606	5.853	8.096		*Fi8*	Possibly lower symmetry	
$A^{3+}BTa^{3+}O_6$ (continued)								in 3.3.4, Tab.
Ca_2GdTaO_6	M	5.572	5.841	8.080	$\beta = 90° 12'$	*Fi8*		
Ca_2TbTaO_6	M	5.574	5.833	8.076	$\beta = 90° 12'$	*Fi8*		
Ca_2DyTaO_6	O	5.582	5.820	8.064		*Fi8*		
Ca_2HoTaO_6	O	5.586	5.811	8.054		*Fi8*		
Ca_2ErTaO_6	O	5.582	5.796	8.033		*Fi8*		
Ca_2YbTaO_6	O	5.570	5.772	8.002		*Fi8*		
Pb_2AlTaO_6	C	10.51				*Fi11*	Defect pyrochlore type, P&S [*Ag1*]	
Pb_2ScTaO_6	C	4.080				*Ga5*	P&S [*Ji2, Ag1*], crystal growth [*Ga5*], dielectric properties [*Sm18*]	
Pb_2MnTaO_6	C	10.73				*Fi11*	Defect pyrochlore type, 5% Sr for Pb gives perovskite [*Sh32*]	6
Pb_2FeTaO_6	C	4.011				*Ga5*	P&S [*Ag1*], crystal growth [*Ga5*], Prop. [*Sh32*]	6
Pb_2CoTaO_6 [a]	C	4.038				*Ka11*	Dielectric properties [*Ka11, Sh32*]	6
Pb_2YTaO_6	C	10.70				*Fi11*	Defect pyrochlore type	
Pb_2PrTaO_6	C	10.75				*Fi11*	Defect pyrochlore type	
Pb_2NdTaO_6	C	10.68				*Fi11*	Defect pyrochlore type	
Pb_2SmTaO_6	C	10.70				*Fi11*	Defect pyrochlore type	
Pb_2YbTaO_6	O	5.85	5.90	8.22		*Ka9*	Dielectric properties [*Ag1, Is17, Fi11*]	
Pb_2LuTaO_6	O	5.848	5.899	8.214		*Ka9*	Cubic $T > 280$ °C; dielectric properties [*Is17*]	
Pb_2BiTaO_6	F	10.686		10.816		*Vi3*	Distorted defect pyrochlore type	
$Pb_2Mg_{0.4}Mn_{0.6}TaO_6$	C	4.015				*Vi5*	Dielectric properties [*Vi5, Ve4*]	6
$Pb_2Ni_{0.4}Mn_{0.6}TaO_6$	C	4.009				*Vi5*	Dielectric properties [*Vi5, Ve4*]	6
$A^{3+}BB'O_6$; B' = Bi^{4+}, Pa^{4+}, Pu^{4+}								
Ba_2LaBiO_6	C	8.759				*Sc18b*		
Ba_2BiBiO_6	C					*Sc18b*		
Ba_2ScPaO_6	C	8.549				*Ke5*	No dimensions, Bi^{3+}-Bi^{4+}	
Ba_2SrPaO_6 [a]	C	8.860				*Sc18b*		
Ba_2YPaO_6	C	8.718				*Ke5*		
Ba_2InPaO_6 [a]	C	8.596				*Ke5*		
Ba_2BaPaO_6 [a]	C	8.932				*Ke5*		
Ba_2CePaO_6	C	8.885				*Ke5*		
Ba_2PrPaO_6	C	8.800				*Ke5*	Ce^{4+} (?)	
Ba_2NdPaO_6	C	8.762				*Ke5*		
Ba_2SmPaO_6	C	8.840				*Ke5*		
Ba_2EuPaO_6	C	8.792				*Ke5*		
Ba_2GdPaO_6	C	8.783				*Ke5*		
Ba_2TdPaO_6	C	8.770				*Ke5*		
	C	8.753				*Ke5*		

Compound	Sym	a Å	b Å	c Å	angle	Ref.	Remarks	Magnetic Data
$A_2^{II}BB'O_6$; B' = Bi^{5+}, Pa^{5+}, Pu^{5+} (continued)								in 3.3.4, Tab.
Ba_2DyPaO_6	C	8.740				*Ke5*		
Ba_2HoPaO_6	C	8.730				*Ke5*		
Ba_2ErPaO_6	C	8.716				*Ke5*		
Ba_2TmPaO_6	C	8.692				*Ke5*		
Ba_2YbPaO_6	C	8.678				*Ke5*		
Ba_2LuPaO_6	C	8.666				*Ke5*		
Ba_2PuPaO_6	C	8.748				*Ke5*		
Ba_2AmPaO_6	C	8.793				*Ke5*		
Sr_2LuPaO_6	C	8.462				*Ke5*		
$BaSrSrPaO_{5.5}$	C	8.784				*Ke5*		
Ba_2MnPuO_6	C	8.32				*Aw2*		
Ba_2InPuO_6	C	8.50				*Aw2*		
Ba_2LaPuO_6	C	8.63				*Aw2*	Pseudocubic	
Ba_2CePuO_6	C	8.72				*Aw2*		
Ba_2NdPuO_6	C	8.66				*Aw2*		
Ba_2TiPuO_6	C	8.06				*Aw2*	Pu^{4+}	
Ba_2ZnPuO_6	C	8.38				*Aw2*	Pseudocubic	
Ba_2PbPuO_6	C	8.58				*Aw2*		
$A_2^{II}BMo^{6+}O_6$								
Ba_2CaMoO_6	C	8.355				*St32*		
Ba_2CrMoO_6							No compound [*Pa7*]	
Ba_2FeMoO_6	C	8.08				*Pa7*	S.S. with Sr [*Ga12*]	6
Ba_2CoMoO_6	C	4.043				*Br14*	Probably ordered	
Ba_2NiMoO_6	C	4.022				*Br14*	Probably ordered	
Sr_2CrMoO_6	C	3.91				*Br14*		6
Sr_2MnMoO_6	C	7.98				*Br14*		6
Sr_2FeMoO_6	T	7.888		7.909		*Ga12*	P & S [*Pa7*], Prop. [*Ga12, Na4*], S.S. with Ba and Ca [*Ga12*], neutron diffraction [*Na11*]	6
Sr_2CoMoO_6	T	5.581		7.940		*Ku8*	P & S [*Br14*]	6
	C	7.918				*Ku8*	Cubic at 320 °C; no dielectric anomaly	
Sr_2NiMoO_6	T	5.560		7.886		*Ku8*	P & S [*Br14*], semiconducting, $\Delta E = 0.78$ eV $\leq$ 181 °C ≤ 1.30 eV [*No1*], S.S. with Ba, cubic at 22% Ba [*No1, No3*]	6
	C	7.878				*Ku8*	Cubic at 230 °C [*Ku8, No3*], no dielectric anomaly [*Ku8*]	
Sr_2ZnMoO_6	T	5.561		7.966		*Ku8*		
	C	7.954				*Ku8*	Cubic at 420 °C; no dielectric anomaly	

Compound	Sym	a Å	b Å	c Å	angle	Ref.	Remarks	Magnetic Data
$A_3^{II}BMo^{VI}O_6$ (continued)								in 3.3.4, Tab.
Ca_3CrMoO_6	O	5.36	5.49	7.70		*Pa7*		6
Ca_3FeMoO_6	O	5.42	5.53	7.73		*Pa7*		6
$A_3^{II}BTe^{VI}O_6$								
Ba_3MgTeO_6	C	8.13				*Sl6*	P&S [*Ba26, Re4a*]	
Ba_3CaTeO_6	C	8.393				*Sl6*	P&S [*Ba26*], S.S. with Ni [*Re4a*]	
$BaPbMgTeO_6$	C	8.08				*Ba26*		
Sr_3MgTeO_6	C	7.94				*Ba26*		
$SrPbMgTeO_6$	C	7.955				*Ba26*		
Sr_3NiTeO_6	C	3.95				*Re4a*	Optical properties and S. S. with Ba	
Sr_3CuTeO_6	T	7.680		8.465		*Re4b*	Optical properties	
Ca_3CaTeO_6	O	5.55	5.77	7.98		*Bl1a*		
Pb_3MgTeO_6	C	7.99				*Ba26*		
$A_3^{II}BW^{VI}O_6$								
Ba_3MgWO_6	C	8.099				*Si32*	P&S [*Be18*], dielectric properties [*Ag1*]	
Ba_3CaWO_6	C	8.390				*Be18*	P&S [*Si32*], S.S. with Ni [*Re4a*]	
Ba_3CrWO_6						*Pa7*	No perovskite	
Ba_3FeWO_6	C	8.133				*Fr14*		
Ba_3CoWO_6	C	8.098				*Fr14*	P&S [*Br14*], Prop., semiconducting, $\Delta E = 0.81$ eV [*Bo1*], neutron diffraction [*Co31*]	6
Ba_3NiWO_6	C	8.066				*Fr14*	P&S [*Br14, Ag1*], S.S. with Sr [*No2*], neutron diffraction [*Co31*], optical properties [*Re4a*]	6
Ba_3CuWO_6	T	7.88		8.61		*Bl8*	P&S [*Ka12, Ve2, Ve3*], complete structure [*Pl3*]	6
Ba_3ZnWO_6	C	8.116				*Fr14*	P&S [*Be18*]	
Ba_3SrWO_6	C	8.53				*Be18*	P&S [*Fi10, Si32*], S.S. with Sr_3WO_6 [*Be18*]	
Ba_3CdWO_6	C	8.383				*Be18*		
Ba_3BaWO_6	C	8.62				*Si32*	Slightly distorted; cubic $T > 805$ °C [*Ch4*]	
$Ba_3SrMgWO_6$	C	8.02				*Be18*	P&S [*Si32*]	
$Ba_{1.4}Ca_{1.6}CaWO_6$	C	8.387				*Si32*	P&S [*Be18*]	
$BaSrCaWO_6$	C	8.29				*Si32*	Distorted	
$BaCaCaWO_6$	C	8.363				*Be18*	Composition questionable	
$BaSrZnWO_6$	C	8.07				*Be18*	Distorted	
$BaCaZnWO_6$	C	8.38				*Be18*	Composition questionable	
Sr_3MgWO_6	C	7.8				*Be18*	P&S [*Si32*], distorted	
Sr_3CaWO_6	C	8.2				*Be18*	Distorted	
Sr_3CrWO_6	C	7.82				*Pa7*		6
Sr_3MnWO_6	C	8.01				*Bl8*	Prop. [*Bl4*]	6
Sr_3FeWO_6	C	7.96				*Bl8*	Prop. [*Bl4*]	6

Compound	Sym	a Å	b Å	c Å	angle	Ref.	Remarks	Magnetic Data
$A^{II}_{\frac{1}{2}}B^{W+}O_3$ (continued)								in 3.3.4, Tab.
Sr_3CoWO_6	T	7.89		7.98		*Fr14*	P&S [*Br14*], Prop. [*No1, Ku8, Bl2, Bl4*]	6
	C	7.904				*Ku8*	$T \approx 400$ °C, cubic $T > 400$ °C; no dielectric anomaly	
Sr_2NiWO_6	T	7.86		7.91		*Fr14*	P&S [*Br14*], Prop. [*No1, Bl2, Bl4, No2, Ve1, No2, Re4a*], S.S. with $LaFeO_3$ [*Sm23*], S.S. with Ba [*No2*], ESR [*No4*], S.S. with Ca [*Re4a*]	6
	C	7.908				*Ku8*	$T \approx 300$ °C, cubic $T > 300$ °C [*Ku8, No4*]	
Sr_2CuWO_6	T	7.66		8.40		*Bl8*	P&S [*Ka12*], dielectric properties [*Ve2*]	6
Sr_2ZnWO_6	T	7.92		8.01		*Fr14*	P&S [*Ku8, Be18*], S.S. with Ba, cubic > 40% Ba [*Fr14*]	
	C	7.956				*Ku8*	$T \approx 430$ °C, cubic $T > 430$ °C [*Ku8, Fr14*], no dielectric anomaly [*Ku8*]	
Sr_3SrWO_6	C	8.3				*Be18*	Distorted, P&S [*St32*]; cubic $T > 1100$ °C, S.S. with Ca [*Ch3*]	
$SrCaMgWO_6$	C	7.87				*Be18*	Distorted, P&S [*St32*]	
$SrCaCaWO_6$	C	8.1				*Be18*	Distorted, P&S [*St32*]	
Ca_2MgWO_6	C	7.75				*St32*	Distorted, P&S [*Be18*]	
Ca_3CaWO_6	C	8.02				*St32*	Distorted, P&S [*Be18*]; not cubic $T < 1500$ °K, S.S. with Sr [*Ch3, Ch4*]	
Ca_3CrWO_6	O	5.35	5.47	7.70		*Pa7*		6
Ca_3CoWO_6	O	5.43	5.60	7.73		*Bl8*	Prop. [*Bl2, Ki7*]	6
Ca_3NiWO_6	O	5.40	5.55	7.70		*Bl8*	Optical properties [*Re4a*]	
Ca_3CuWO_6							Not perovskite [*Bl8*]	
Pb_2MgWO_6	C	8.0				*Be8*	Dielectric properties [*Sm8, Ag1, Sm13, Kh5, Mi1a, Kh6, St42*], piezoelectric properties, S.S. with Ti, Zr [*St34*], S.S. with Cd [*Is15*], S.S. with $PbFe_{2/3}W_{1/3}O_3$ [*Sm10*], S.S. with $PbTiO_3$, Ca_2MgWO_6, $Pb_2MgNb_2O_6$ [*Sm20, St35*]	
Pb_2CaWO_6	C	4.2				*Be8*	Distorted, dielectric properties [*Ag1*]	
Pb_2MnWO_6	O	5.736	5.756	8.066		*Ve3*	Prop. [*Ve2, Ve4, Ro8*]	6
Pb_2FeWO_6							Prop., no cell dimensions [*Ve4*]	6
Pb_2CoWO_6	O	5.661	5.676	9.976		*Bo10*	P&S [*Fi11, Be18*], Prop. [*Te13, Bo10, Ki7, Fi6*], B site ordering [*Yu9*], S.S. with $BaTiO_3$ [*To2*]	6
	C	8.017				*Fi6*	$T \approx 20$ °C, cubic $T > 20$ °C	
Pb_2NiWO_6	C	7.997				*No6*	Dielectric properties, P&S [*To11a, To11b*]	6
Pb_2NiWO_6	T	8.006		7.920		*No6*	$T = 173$ °K → tetragonal below 290 °K	
Pb_2CdWO_6	C	4.1				*Be18*	Distorted, dielectric properties [*Ro6*], S.S. with Mg [*Is15*]	
Pb_2CdWO_6	C	4.15				*Fi7*	Cubic at 400 °C, transformations [*Po8*], S.S. with $Pb(Li_{1/3}Nb_{1/3}W_{1/3})O_3$ [*Di5*]	

Compound	Sym	a Å	b Å	c Å	angle	Ref.	Remarks	Magnetic Data
$A_2^{II}BW^{6+}O_6$ (continued)								in 3.3.4, Tab.
$Pb_2Na_{0.5}Sc_{0.5}WO_6$						*Ve4*	Dielectric properties, no cell dimensions	
$Pb_2Na_{0.5}Fe_{0.5}WO_6$						*Ve4*	Dielectric properties, no cell dimensions	
$Pb_2Na_{0.5}Yb_{0.5}WO_6$						*Ve4*	Dielectric properties, no cell dimensions	
$Pb_2Mg_{0.5}Mn_{0.5}WO_6$	T	8.202		8.104		*Vi5*	Dielectric properties [*Vi5, Ve4*]	6
$Pb_2Co_{0.5}Mn_{0.5}WO_6$	T	8.082		8.018		*Vi5*	Dielectric properties [*Vi5, Ve4*]	6
$Pb_2Ni_{0.5}Mn_{0.5}WO_6$							No cell dimensions, Prop. [*Vi5*]	6
$Pb_2Li_{0.5}Fe_{0.5}WO_6$	C	8.008				*Ve3*	Dielectric properties [*Vi5, Ve2, Ve3, Ve4*]	
$Pb_2Li_{0.5}Co_{0.5}WO_6$	C	4.013				*Ve3*	Dielectric properties [*Ve3*]	
$Pb_2Li_{0.5}La_{0.5}WO_6$	C	8.04				*Vi5*	Dielectric properties [*Vi5*]	
$Pb_2Li_{0.5}Yb_{0.5}WO_6$	C	4.100				*Ve3*	Dielectric properties [*Ve2, Ve3, Ve4*]	
$Pb_2Li_{0.85}Mn_{0.67}WO_6$						*Ve4*	Dielectric properties, no cell dimensions	
$Pb_2Li_{0.33}Zr_{0.67}WO_6$						*Ve4*	Dielectric properties, no cell dimensions	
$Pb_2Li_{0.33}Hf_{0.67}WO_6$						*Ve4*	Dielectric properties, no cell dimensions	
$Pb_2YbTi_{0.5}W_{0.5}O_6$	C	4.124				*Ve3*	Dielectric properties [*Ve2, Ve3, Ve4*]	
$Pb_2FeMn_{0.5}W_{0.5}O_6$	C	4.037				*Ro8*	Dielectric properties [*Ve4*]	6
$A_2^{II}BReO_6$, Re^{5+} and Re^{6+}								
Ba_2MgReO_6	C	8.082				*Si8*	P&S [*Lo2, Sc18*], single crystal [*Si7*]	
Ba_2CaReO_6	C	8.356				*Si8*	P&S [*Lo2, Sc18*]	
Ba_2ScReO_6	C	8.163				*Si8*	P&S [*Sc18*]	
Ba_2MnReO_6	C	8.18				*Si8*	P&S [*Lo2, Wa15*], single crystal + Prop. [*Si7*]	6
Ba_2FeReO_6	C	8.05				*Si8*	P&S [*Lo2, Wa15*], single crystal + Prop. [*Si7*], [*Ba25a*] suggests $Ba_2Fe_{1+x}Re_{1-x}O_6$	6
Ba_2CoReO_6	C	8.086				*Si8*	P&S [*Lo2, Wa15*], single crystal + Prop. [*Si7*]	6
Ba_2NiReO_6	C	8.04				*Si8*	P&S [*Lo2*], single crystal + Prop. [*Si7*]	6
Ba_2ZnReO_6	C	8.106				*Si8*	P&S [*Lo2*]	
Ba_2SrReO_6	T	8.60		8.43		*Si8*	P&S [*Sc18*]	
Ba_2YReO_6	C	8.372				*Si8*		
Ba_2CdReO_6	C	8.322				*Si8*	P&S [*Lo2*]	
Ba_2InReO_6	C	8.258				*Si8*	P&S [*Sc18*]	
Ba_2BaReO_6	T	8.65		8.33		*Si8*	P&S [*Sc18*]	
Ba_2LaReO_6	C	8.547				*Ba25a*	Prep. 900 °C, a_0 increases with prep. temperature suggesting $Ba_2Re_{1-x}^{5+}Re_x^{6+}La_{1-x}Ba_xO_6$; P&S [*Si8*]	
Ba_2NdReO_6	C	8.51				*Si8*		
Ba_2SmReO_6	C	8.458				*Ba25a*		
Ba_2EuReO_6	C	8.438				*Ba25a*		
Ba_2GdReO_6	C	8.431				*Si8*	Prop. [*Lo2*], P&S [*Sc18*]	
Ba_2TbReO_6	C	8.399				*Ba25a*		

Compound	Sym	*a* Å	*b* Å	*c* Å	angle	Ref.	Remarks	Magnetic Data
$A_2^{II}BReO_6$, Re^{6+} and Re^{5+} (continued)								in 3.3.4, Tab.
Ba_2DyReO_6	C	8.391				*Ba25a*		
Ba_2HoReO_6	C	8.375				*Ba25a*		
Ba_2ErReO_6	C	8.354				*Sl8*	Prop. [*Lo2*], P&S [*Sc18*]	
Ba_2TmReO_6	C	8.342				*Ba25a*		
Ba_2YbReO_6	C	8.329				*Ba25a*		
$Ba_{2-x}Sr_xYbReO_6$	C	8.230				*Ba25a*	$x = 1.2$, small positive deviation from Vegard's law	
$BaSrFeReO_6$							Prop. [*Sl8*, *Lo2*]	
Ba_2YReO_6							Single crystal [*Sl7*], Prep. [*Sc18*]	
Sr_2MgReO_6	T	7.88		7.94		*Sl8*	P&S [*Sc18*]	
Sr_2CaReO_6	O	5.76	5.85	8.21		*Sl8*		
Sr_2ScReO_6	C	8.02				*Sl8*	distorted	
Sr_2CrReO_6	C	7.82				*Sl8*		6
Sr_2MnReO_6	C	8.01				*Sl8*	distorted	
Sr_2FeReO_6	T	7.86		7.89		*Sl8*	P&S [*Lo2*, *Wa15*]	6
Sr_2CoReO_6	T	7.88		7.98		*Sl8*		
Sr_2NiReO_6	T	7.85		7.92		*Sl8*		
Sr_2ZnReO_6	T	7.89		8.01		*Sl8*		
Sr_2GaReO_6	C	7.843				*Sl8*		
Sr_2SrReO_6	T	8.41		8.13		*Sl8*	P&S [*Sc18*]	
Sr_2YReO_6	C	8.197				*Ba25b*		
Sr_2CdReO_6	O	5.73	5.81	8.16		*Sl8*		
Sr_2InReO_6	C	8.071				*Sl8*		
Sr_2GdReO_6	C	8.239				*Ba25b*		
Sr_2TbReO_6	C	8.223				*Ba25b*		6
Sr_2DyReO_6	C	8.210				*Ba25b*		6
Sr_2HoReO_6	C	8.200				*Ba25b*		
Sr_2ErReO_6	C	8.181				*Ba25b*		6
Sr_2TmReO_6	C	8.167				*Ba25b*		
Sr_2YbReO_6	C	8.155				*Ba25b*		6
Ca_2MgReO_6	O	5.48	5.56	7.77		*Sl8*	P&S [*Sc18*]	
Ca_2CaReO_6	O	5.67	5.78	8.05		*Sl8*	P&S [*Sc18*]	
Ca_2ScReO_6	O	5.49	5.63	7.86		*Sl8*		
Ca_2CrReO_6	O	5.38	5.47	7.67		*Sl8*		6
Ca_2MnReO_6	O	5.52	5.55	7.82		*Sl8*		
Ca_2FeReO_6	O	5.41	5.53	7.69		*Sl8*	P&S [*Lo2*]	6
Ca_2CoReO_6	O	5.46	5.58	7.71		*Sl8*		

Compound	Sym	*a* Å	*b* Å	*c* Å	angle	Ref.	Remarks	Magnetic Data
$A_2^{II}BReO_6$, Re^{3+} and Re^{4+} (continued)								in 3.3.4, Tab.
Ca_2NiReO_6	O	5.45	5.55	7.67		*Sl8*		
Ca_2CdReO_6	O	5.64	5.77	7.99		*Sl8*		
Pb_2MnReO_6	O	5.69	5.74	8.024		*Ro8*	Claim Mn^{3+}—Re^{5+}, Prop. [*Ro8, Ro11*]	6
Pb_2MnReO_6	O	5.67	5.75	8.008		*Ro8*	Claim Mn^{3+}—Re^{5+}, Prop. [*Ro8, Ve4*]	6
$A_2^{II}BOsO_6$								
Ba_2MgOsO_6	C	8.08				*Sl8*		
Ba_2CaOsO_6	C	8.362				*Sl8*		6
Ba_2ScOsO_6	C	8.152				*Sl8*		
Ba_2MnOsO_6	H	5.82		14.2		*Sl8*	Hex (6L)	
Ba_2FeOsO_6	H	5.76		14.1		*Sl8*	Hex (6L)	
Ba_2ZnOsO_6	C	8.095				*Sl8*		
Ba_2SrOsO_6	T	8.43		8.72		*Sl8*		
Ba_2CdOsO_6	C	8.325				*Sl8*		
Ba_2InOsO_6	C	8.224				*Sl8*		
Ba_2BaOsO_6	T	8.66		8.34		*Sl8*		
Sr_2MgOsO_6	T	7.86		7.92		*Sl8*		
Sr_2CaOsO_6	C	8.21				*Sl8*	Distorted	
Sr_2ScOsO_6	C	8.02				*Sl8*	Distorted	
Sr_2CrOsO_6	C	7.84				*Sl8*		
Sr_2FeOsO_6	C	7.85				*Sl8*	Distorted	
Sr_2CoOsO_6	T	7.86		7.92		*Sl8*		
Sr_2GaOsO_6	C	7.82				*Sl8*		
Sr_2SrOsO_6	T	8.32		8.12		*Sl8*		
Sr_2InOsO_6	C	8.06				*Sl8*		
Ca_2CaOsO_6	O	5.73	5.80	7.87		*Sl8*		
Ca_2CrOsO_6	O	5.38	5.47	7.66		*Sl8*		
Ca_2CoOsO_6	O	5.47	5.59	7.70		*Sl8*		
$A_2^{II}BUO_6$								
Ba_2BeUO_6	C	8.82				*Aw1*	Doubtful	
Ba_2MgUO_6	C	8.381				*Sl5*		
Ba_2CaUO_6	C	8.67				*Sl5*	Distorted, P&S [*Ru4*]	
Ba_2ScUO_6	C	8.49				*Sl5*		
Ba_2TiUO_6	C	8.05				*Aw1*	Ti^{4+}	
Ba_2CrUO_6	C	8.297				*Sl5*	Also prepared as Hex (6L)	
Ba_2MnUO_6	C	8.52				*Sl5*	P&S [*Aw1*]	
Ba_2FeUO_6	C	8.312				*Sl5*	Prop. [*Di5*]	6
Ba_2CoUO_6	C	8.372				*Sl5*		

Compound	Sym	a Å	b Å	c Å	angle	Ref.	Remarks	Magnetic Data
$A_2^{2+}BUO_6$ (continued)								in 3.3.4, Tab.
Ba_2NiUO_6	C	8.336				*SI5*	Optical properties [*Re4a*]	
Ba_2CuUO_6	T	8.18		8.84		*SI5*		
Ba_2ZnUO_6	C	8.397				*SI5*		
Ba_2GeUO_6	C	8.56				*Aw1*	Doubtful	
Ba_2SrUO_6	C	8.84				*SI5*	Distorted, P & S [*Ru4*]	
Ba_2YUO_6	C	8.69				*SI5*	Distorted	
Ba_2ZrUO_6	C	8.35				*Aw1*		
Ba_2RhUO_6	H	5.84		14.9		*SI5*	Hex (6 L)	
Ba_2CdUO_6	O	6.07	6.13	8.64		*SI5*		
Ba_2InUO_6	C	8.521				*SI5*		
$Ba_2InUO_{5.5}$	C	8.551				*SI5*		
Ba_2BaUO_6	T	6.285		8.943		*Ri4*	Complete structure determined, P & S [*SI3*, *Ru4*]	
Ba_2LaUO_6	C	8.73				*Aw1*	Distorted	
Ba_2CeUO_6	C	8.87				*Aw1*	Ce^{4+}	
Ba_2NdUO_6	C	8.76				*Aw1*		
Ba_2SmUO_6	C	8.76				*Aw1*		
Ba_2EuUO_6	C	8.68				*Aw1*		
Ba_2GdUO_6	C	8.66				*Aw1*		
Ba_2DyUO_6	C	8.65				*Aw1*		
Ba_2HoUO_6	C	8.65				*Aw1*		
Ba_2ErUO_6	C	8.67				*Aw1*	Distorted	
Ba_2YbUO_6	C	8.60				*Aw1*		
Ba_2LuUO_6	C	8.57				*Aw1*		
Ba_2HfUO_6	C	8.31				*Aw1*		
Ba_2HgUO_6	C	8.83				*Aw1*	Doubtful	
Ba_2PbUO_6	C	8.85				*Aw1*	Doubtful	
$BaSrSrUO_6$	C	8.66				*Ru4*		
Sr_2MgUO_6	C	8.19				*SI5*	Distorted	
Sr_2CaUO_6	O	5.93	6.06	8.46		*SI5*		
Sr_2CrUO_6	C	8.09				*SI5*	Distorted	
Sr_2MnUO_6	C	8.28				*SI5*	Distorted	
Sr_2FeUO_6	C	8.11				*SI5*	Distorted	
Sr_2CoUO_6	C	8.19				*SI5*	Distorted	6
Sr_2NiUO_6	C	8.15				*SI5*	Distorted, optical properties [*Re4a*]	
Sr_2SrUO_6	M	5.959	6.179	8.553	$\beta = 90° 11'$	*Ri4*	Complete structure; P & S [*SI5*, *Ru4*, *Be25*, *Ip1*]	
Sr_2CdUO_6	O	5.91	6.03	8.42		*SI5*		
Sr_2InUO_6	C	8.33				*SI5*	Distorted; Prop. [*Ke13*]	6
$SrCaCaUO_6$	O	5.83	6.01	8.36		*SI5*		

Ref. Remarks Magnetic Data

Compound	Sym	a Å	b Å	c Å	angle	Ref.	Remarks	Magnetic Data
$A_4^{2+}BUO_6$ (continued)								in 3.3.4, Tab.
Ca_2CaUO_6	M	5.728	5.958	8.301	$\beta = 90° 33'$	*Ri4*	Complete structure determined, P&S [*Si5, Ru4, Be25, Ip1*]	
Pb_2PbUO_6	O	13.71	12.36	8.21		*St26*	Not perovskite	
$A_4^{2+}BB'O_6$; B' = Np^{5+}, Pu^{6+}								
Ba_2SrNpO_6	C	8.799				*Ke4*		
Ba_2BaNpO_6	C	8.860				*Ke4*		
$BaSrSrNpO_6$	C	8.735				*Ke4*		
Ba_2SrPuO_6	C	8.780				*Ke3*		
Ba_2BaPuO_6	C	8.840				*Ke3*		
$BaSrSrPuO_6$	C	8.717				*Ke3*		
Sr_3SrPuO_6						*Ke3*	Not perovskite	
$A_4^{2+}B^+B'O_6$; B' = Tc^{7+}, Re^{7+}, Os^{7+}, I^{7+}								
Ba_2LiTcO_6	C	8.092				*Wa16*	P&S [*Ke9*]	
Ba_2NaTcO_6	C	8.292				*Wa16*	P&S [*Ke9*]	
Sr_2LiTcO_6	C	7.84				*Wa16*	Distorted, P&S [*Ke9*]	
Sr_2NaTcO_6	T	8.09		8.14		*Wa16*	P&S [*Ke9*]	
Ca_2LiTcO_6							Not able to be made [*Wa16*]	
Ba_2LiReO_6	C	8.118				*Si4*	S.S. with Na [*Si4*]	
Ba_2NaReO_6	C	8.296				*Si4*		
Sr_2LiReO_6	C	7.87				*Si8*		
Sr_2NaReO_6	C	8.13				*Si8*		
Ca_2LiReO_6	C	7.83				*Si8*	Distorted	
Ba_2LiOsO_6	C	8.100				*Si8*	S.S. with Re [*Si8*]	6
Ba_2NaOsO_6		8.282				*Si8*		
Sr_2LiOsO_6	C	7.86				*Si8*		
Sr_2NaOsO_6	C	8.13				*Si8*		
Ca_2LiOsO_6	C	7.83				*Si8*	Distorted	
Ba_2NaIO_6	C	8.33				*Si6*		
Ba_2AgIO_6	C	8.46				*Si6*		

Tab. 2c. $A_3BB'_3O_9$ (for H symmetry see Fig. 1c)

Compound	Sym	a Å	b Å	c Å	angle	Ref.	Remarks	Magnetic Data
$A_3BB'_3O_9$								in 3.3.4, Tab.
$Ba_3MgNb_3O_9$	H	5.77		7.08		*Ga9*	P&S [*Ga13*, *Bl8*], see Fig. 1 (c)	
$Ba_3CaNb_3O_9$	H	5.92		7.25		*Ga9*	See Fig. 1 (c)	
$Ba_3FeNb_3O_9$	C	4.085				*Ga9*		
$Ba_3CoNb_3O_9$	C	4.09				*Ga13*		
$Ba_3NiNb_3O_9$	C	4.074				*Ga9*	P&S [*Ro20*, *Ag1*], dielectric properties [*Sm8*], optical properties [*Re4a*]	
$Ba_3CuNb_3O_9$	T	8.04		8.40		*Bl8*	Dielectric properties [*Ka12*, *Ve3*]	
	C	8.166				*Ve2*	Cubic > 653 °K	
$Ba_3ZnNb_3O_9$	C	4.094				*Ga9*	P&S [*Ga13*, *Ag1*]	
$Ba_3CdNb_3O_9$	C	4.168				*Ga9*		
$Ba_3BaNb_3O_9$	H	6.01		8.0		*Ga9*	P&S [*Bl8*], see Fig. 1 (c)	
$Ba_3PbNb_3O_9$	C	4.26				*Ga9*		
$Sr_3MgNb_3O_9$	H	5.66		6.98		*Ga9*	See Fig. 1 (c)	
$Sr_3CaNb_3O_9$	H	5.76		7.16		*Ga9*	See Fig. 1 (c)	
$Sr_3FeNb_3O_9$	T	3.997		4.018		*Ga9*		
$Sr_3CoNb_3O_9$	C	8.01				*Bl8*		
$Sr_3NiNb_3O_9$	H	5.64		6.90		*Ga9*	P&S [*Ag1*], optical properties of S.S. with Ba and Ca [*Re4a*], see Fig. 1 (c)	
$Sr_3CuNb_3O_9$	T	7.888		8.148		*Ka12*	Prop. [*Ve2*]	
$Sr_3ZnNb_3O_9$	H	5.66		6.95		*Ga9*	P&S [*Ga13*], see Fig. 1 (c)	
$Sr_3CdNb_3O_9$	C	4.089				*Ga9*		
$Ca_3CaNb_3O_9$						*Bl8*	Distorted perovskite	
$Ca_3NiNb_3O_9$	C	3.88				*Ag1*		
$Pb_3MgNb_3O_9$	C	4.04				*Ag1*	Dielectric properties [*Sm27*, *Ag1*, *Ou1*, *Ou1a*, *Ou2*, *Bo5*, *Is4*, *Bo16*, *Be23*, *Kh5*, *Kh4*, *Kh8*, *Sm14*, *Sm20*, *Sm29*, *Sm8*, *Cr6b*], crystal growth [*Ba5*, *My3*], electrooptic effect [*Sm29*]	
$Pb_3MnNb_3O_9$						*Ag1*	No cell dimensions	
$Pb_3CoNb_3O_9$	C	4.05				*Bo5*	Dielectric properties [*Bo5*, *Ag1*]	
$Pb_3NiNb_3O_9$	C	4.02				*Ag1*	Dielectric properties [*Ag1*, *Sm8*, *Bo5*, *Is4*], crystal growth [*Bo5*, *My3*], S.S. with Mg [*Sm20*, *Sm27*, *Sm14*, *Is4*, *Cr6b*], S.S. with $Pb(Ti, Zr)O_3$ [*Bu10*], electrooptic effect [*Sm29a*]	
$Pb_3ZnNb_3O_9$	C	4.05				*Bo5*	Dielectric properties [*Bo5*, *Kh7*, *Be23a*]	
$Pb_3Sc_{3/8}W_{1/8}NbO_9$	C	4.074				*To1*	Dielectric properties [*Ve4*]	
$Pb_3CdNb_3O_9$	C	8.246				*To1*	Dielectric properties [*Ve2*, *Ve3*, *Ve4*]	

Compound	Sym	a Å	b Å	c Å	angle	Ref.	Remarks	Magnetic Data
$A_3BB'^{+}O_9$ (continued)								in 3.3.4, Tab.
$Ba_3MgRu_2O_9$	H					*Ca2*	Hex (6L), magnetic properties $84 < T < 948$ °K, $\Theta_N = 390$ °K [*Ca2*]	
$Ba_3MgSb_2O_9$	H	5.83		14.26		*Bl8*	Hex (6L)	
$Ba_3CaSb_2O_9$	H	5.99		14.84		*Bl8*	Hex (6L)	
$Ba_3CoSb_2O_9$	H	5.84		14.35		*Bl8*	Hex (6L)	
$Ba_3NiSb_2O_9$	H	5.82		14.25		*Bl8*	Hex (6L), optical properties of S.S. with Sr and Nb [*Re4a*]	
$Ba_3CuSb_2O_9$	H	5.82		14.22		*Bl8*	Hex (6L)	
$Ba_2SrSb_2O_9$	H	6.15		15.6		*Bl8*	Hex (6L)	
$Ba_2BaSb_2O_9$	H	6.09		15.9		*Bl8*	Hex (6L)	
$Sr_3MgSb_2O_9$	C	7.96				*Bl8*		
$Sr_3CaSb_2O_9$	C	8.17				*Bl8*		
$Sr_3CoSb_2O_9$	C	7.99				*Bl8*		
$Sr_3NiSb_2O_9$	C	3.98				*Re4a*	Cell probably doubled, optical properties [*Re4a*]	
$Sr_3CuSb_2O_9$	T	7.84		8.19		*Bl8*	Optical properties [*Re4b*]	
$Sr_2SrSb_2O_9$	O	5.78	5.80	8.34		*Bl8*		
$Sr_2La_{0.8}Li_{0.8}Sb_2O_9$	O	5.62	5.68	8.00		*Bl8*		
$Ba_3MgTa_2O_9$	H	5.782		7.067		*Ga10*	Crystal growth [*Ga7*], see Fig. 1 (c)	
$Ba_3CaTa_2O_9$	H	5.895		7.284		*Ga10*	P & S [*Ga8*], crystal growth [*Ga7*], see Fig. 1 (c)	
$Ba_3MnTa_2O_9$	H	5.819		7.127		*Ga10*	See Fig. 1 (c)	
$Ba_3FeTa_2O_9$	C	4.10				*Ga13*		
$Ba_3CoTa_2O_9$	H	5.776		7.082		*Ga10*	P & S [*Ro20*], see Fig. 1 (c)	
$Ba_3NiTa_2O_9$	H	5.758		7.052		*Ga10*	P & S [*Ro20*], crystal growth [*Ga7*], optical properties [*Re4a*], see Fig. 1 (c)	
$Ba_3CuTa_2O_9$	T	8.132		8.432		*Ka12*	P, S + Prop. [*Ve2, Ve3*]	
$Ba_3ZnTa_2O_9$	H	5.782		7.097		*Ga10*	P & S [*Ga13*], crystal growth [*Ga7*], see Fig. 1 (c)	
$Ba_3SrTa_2O_9$	H	5.95		7.47		*Ga11*	P & S [*Ga13*], see Fig. 1 (c)	
$Ba_3CdTa_2O_9$	C	4.167				*Ga10*		
$Ba_3BaTa_2O_9$	H	6.10		8.05		*Bl8*	See Fig. 1 (c)	
$Ba_3PbTa_2O_9$	C	4.250				*Ga10*		
$Ba_3Zn_{0.9}Ni_{0.8}Ta_2O_9$	C	4.08				*Ga13*		
$Sr_3MgTa_2O_9$	H	5.652		6.951		*Ga10*	P & S [*Ro20*], see Fig. 1 (c)	
$Sr_3CaTa_2O_9$	H	5.764		7.096		*Ga10*	See Fig. 1 (c)	
$Sr_3CoTa_2O_9$	H	5.630		6.937		*Ga10*	P & S [*Ga13*], see Fig. 1 (c)	
$Sr_3NiTa_2O_9$	H	5.607		6.923		*Ga10*	P & S [*Ga13*], see Fig. 1 (c)	
$Sr_3CuTa_2O_9$	T	7.860		8.248		*Ka12*	P, S + Prop. [*Ve2, Ve3*]	
$Sr_3ZnTa_2O_9$	H	5.664		6.951		*Ga10*	P & S [*Ga13*], see Fig. 1 (c)	
$Pb_3MgTa_2O_9$	C	4.03				*Bo5*	Prop. [*Ag1*], electrooptic effect [*Sm29a*]	
$Pb_3CoTa_2O_9$	C	4.02				*Bo5*		
$Pb_3NiTa_2O_9$	C	4.02				*Bo5*	Prop. [*Ag1*]	

Compound	Sym	a Å	b Å	c Å	angle	Ref.	Remarks	Magnetic Data
$La_3Co_2B^{5+}O_9$								in 3.3.4, Tab.
$La_3Co_2NbO_9$	O	5.58	5.58	7.89		*Bi8*		
$La_3Co_2SbO_9$	O	5.57	5.57	7.87		*Bi8*		
$A_3B_2B^{4+}O_9$								
$Ba_3Cr_2MoO_9$	H	5.72		14.02		*Pa7*	Hex (6L)	
$Ba_3Fe_2MoO_9$	H	5.74		14.08		*Bi8*	Hex (6L)	
$Ba_3In_2MoO_9$	C	4.168				*Ka12*		
$Ba_3Bi_2MoO_9$	O	6.148	6.184	8.642		*Ve2*	P&S [*Vi3, Ve3*], dielectric properties [*Vi2b*]	
	C	4.37				*Vi2b*	$T > 500$ °C	
$Ba_3LiNbMoO_9$	R	4.091			$\alpha = 89° 50'$	*Ka12*		
$Ba_3LiTaMoO_9$	C	4.090				*Ka12*		
$Pb_3Bi_2MoO_9$	T	11.262		11.452		*Vi3*	Defect pyrochlore type	
$Ba_3Sc_2WO_9$	C	8.24				*Fr14*	P&S [*Ga15*], dielectric properties [*Ka12*]	
$Ba_3Cr_2WO_9$	H	5.75		14.35		*Pa7*	Hex (6L)	
$Ba_3Fe_2WO_9$	H	5.74		14.08		*Bi8*	Hex (6L)	
$Ba_3Co_2WO_9$	H	5.74		14.10		*Bi8*	Hex (6L)	
$Ba_3Y_2WO_9$	C	8.374				*Ga15*		
$Ba_3Rh_2WO_9$	H	5.74		14.15		*Bi8*	Hex (6L)	
$Ba_3In_2WO_9$	C	8.321				*Ga15*	Structure + Prop. [*Ka12*]	
$Ba_3La_2WO_9$	C	8.58				*Bi8*		
$Ba_3Nd_2WO_9$	C	8.513				*Ga15*		
$Ba_3Eu_2WO_9$	C	8.605				*Ga15*		
$Ba_3Gd_2WO_9$	C	8.411				*Ga15*	P&S [*Bi8*]	
$Ba_3Dy_2WO_9$	C	8.386				*Ga15*	Structure + Prop. [*Ka12*]	
$Ba_3Ho_2WO_9$	C	4.252				*Ka12*	Probably ordered	
$Ba_3Er_2WO_9$	C	8.386				*Ga15*		
$Ba_3Yb_2WO_9$						*Ga15*	No cell dimensions	
$Ba_3Lu_2WO_9$						*Ga15*	No cell dimensions	
$Ba_3Bi_2WO_9$	R	6.131			$\alpha = 60° 23'$	*Ve2*	Dielectric properties [*Vi3, Ve3, Vi2b*]	
$Ba_3LiNbWO_9$	R	4.098			$\alpha = 89° 52'$	*Ka12*		
$Ba_3LiTaWO_9$	R	4.095			$\alpha = 89° 53'$	*Ka12*		
$Sr_3Fe_2WO_9$	T	3.945		3.951		*Ga15*	P&S [*Bi8*], S.S. with $Sr_3Fe_2UO_9$ [*Se6a*]	
$SrLa_2Mg_2WO_9$	C	7.91				*Bi8*		
$SrLa_2Co_2WO_9$	C	7.90				*Bi8*		
$Pb_3Sc_2WO_9$	C	8.134				*Ve3*	Dielectric properties [*Ve4, Ve2, Ve3, To1*]	
$Pb_3Mn_2WO_9$						*Ro8*	No cell dimensions, Prop. [*Ve4, Ro8*], S.S. with $PbTiO_3$ [*Di5a*]	6
$Pb_3Fe_2WO_9$	C	4.02				*Ro8*	Prop. [*Ag1, Ro8, Sm10, Sm16, Sm28, To5, To11, Te13, Pi1, Ki6*], *B* site ordering [*Yu9*]	6
$Pb_3Bi_2WO_9$	T	10.637		10.799		*Vi3*	Defect pyrochlore type	

Compound	Sym	a Å	b Å	c Å	angle	Ref.	Remarks	Magnetic Data
$A_3B_3B^{2+}O_9$ (continued)								in 3.3.4, Tab.
$Pb_3ScMnWO_9$						*Ve4*	No cell dimensions	
$Pb_3CrMnWO_9$						*Ve4*	No cell dimensions	6
$Pb_3FeMnWO_9$						*Ve4*	No cell dimensions	6
$Pb_3CdMnWO_9$	O	5.80	5.90	8.138		*Ro8*	Prop. [*Ve4*, *Ro8*]	6
$Pb_3CoFeWO_9$						*Ve4*	No cell dimensions	6
$Pb_3LiNbWO_9$	C	8.090				*Vi5*	Dielectric properties [*Ve2*, *Ve4*, *Vi5*]	
$Pb_3Cd_{4/9}Nb_{5/9}WO_9$	O	5.813	5.877	8.178		*To1*	Dielectric properties [*Ve2*, *Ve4*]	
$Ba_3Cr_2ReO_9$	H	5.70		13.8		*Sl8*	Hex (6L)	
$Ba_3Fe_2ReO_9$	H	5.81		14.10		*Sl8*	Hex (6L)	
$Sr_3Cr_2ReO_9$	C	8.015				*Sl8*		
$Sr_3Fe_2ReO_9$	C	7.890				*Sl8*		
$Sr_3In_2ReO_9$	C	8.297				*Sl8*		
$Ba_3Sc_2UO_9$	C	8.49				*Sl5*		
$Ba_3Cr_2UO_9$	H	5.82		14.6		*Sl5*	Hex (6L)	
$Ba_3Fe_2UO_9$	C	8.232				*Sl5*	P&S [*Ro14*]	
$Ba_3Y_2UO_9$	C	8.70				*Sl5*	Slight distortion	
$Ba_3In_2UO_9$	C	8.512				*Sl5*		
$Sr_3Cr_2UO_9$	C	8.00				*Sl5*		
$Sr_3Fe_2UO_9$	C	8.066				*Ro14*	Prop. [*Be51*], S.S. with $Sr_3Fe_2WO_9$ [*Se6a*]	6

Tab. 2d. $A^{2+}(B_2'B_1''')O_3$

Compound	Sym	a Å	b Å	c Å	angle	Ref.	Remarks	Magnetic Data
$Ba[Zn_{0.2}Fe_{0.2}Nb_{0.6}]O_3$	C	4.08				*Ga13*		
$Ba[Zn_{0.2}Fe_{0.2}Ta_{0.6}]O_3$	C	4.08				*Ga13*		
$Sr[Zn_{0.2}Fe_{0.2}Ta_{0.6}]O_3$	C	4.01				*Ga13*		
$Ba[Li_{0.25}Nb_{0.75}]O_3$	C	4.095				*Ka12*		
$Ba[Na_{0.25}Nb_{0.75}]O_3$	C	4.107				*Ka12*		
$Ba[Na_{0.25}Ta_{0.75}]O_3$	C	4.137				*Ga6*		
$Sr[Na_{0.25}Ta_{0.75}]O_3$	C	4.055				*Ga6*		
$Ba[Fe_{0.75}Nb_{0.25}]O_{2.75}$	C	4.07				*Ga13*		
$Ba[Fe_{0.75}Ta_{0.25}]O_{2.75}$	C	4.07				*Ga13*		
$Sr[Fe_{0.7}Nb_{0.3}]O_{2.8}$	C	3.96				*Ga13*		
$Ba[Fe_{1/7}Fe_{3/7}Ta_{3/7}]O_3$	C	4.08				*Ga13*		
$Ba[Co_{1/7}Co_{3/7}Ta_{3/7}]O_3$	C	4.09				*Ga13*		
$Sr[Co_{1/7}Co_{3/7}Ta_{3/7}]O_3$	C	4.00				*Ga13*		
$Ba[Na_{0.4}W_{0.6}]O_3$	C	4.158				*Ka12*		

3.2 Descriptions of perovskite-related structures

3.2.1 A-cation vacancies

3.2.1.1 No A cations

Because a skeleton of shared-corner octahedra is stable, it is possible to remove all the A cations from the perovskite structure without collapsing the BX_3 subarray. In the case of □ ReO_3 for example, the structure remains cubic. However, a partial or a complete collapse of the skeleton is found in many □ BX_3 compounds. The completely collapsed structure has hexagonal-close-packed X layers with one-third of the octahedral sites occupied by B atoms, as indicated in Fig. 19. This results in a simple-cubic array of B cations with corner-shared octahedra having a B-X-B angle of 132°. For comparison, Fig. 19 also shows the corner-shared octahedra across a close-packed □ X_3 plane of the cubic □ ReO_3 structure, where the B-X-B angle is 180°. It is possible to go from one structure to the other by a simple increase of the B-X-B angle, the B cations forming a simple-cubic array in all structures. In the partially collapsed structure, represented by CrF_3, and B-X-B angle is intermediate, $\approx$ 150°. Trifluorides of the first-row transition metals have the partially collapsed structure, those of the second- and third-row transition metals have the ReO_3 structure where the number of outer d electrons per cation is $\leqq 3$, but the completely collapsed structure where it is $\geqq 6$. The B cations of the latter group either have no atomic moment (Rh^{III} and Ir^{III} have $t_{2g}^6e_g^0$) or disproportionate into magnetic and nonmagnetic ions (Pd^{2+}, $t_{2g}^6e_g^2$ and Pd^{IV}, $t_{2g}^6e_g^0$), so that there are no magnetic interactions between neighboring cations. The other trifluorides, on the other hand, are all antiferromagnetic, and coupling between like atoms of the second and third long periods is stronger than that between like atoms of the first long period. Since the B-X-B superexchange interaction is enhanced by a larger B-X-B angle, it is reasonable to assume that the interactions between neighboring B cations stabilizes the ReO_3 structure. These interactions may be either weaker interactions between localized electrons, as in the magnetic fluorides, or stronger interactions, as in metallic ReO_3. In this connection, stabilization of the cubic structure in the tungsten bronzes $A_x^{m}WO_3$ for $mx > 0.3$ is significant. The conduction electrons introduce cation-anion-cation interactions while simultaneously reducing the energy gained by a ferroelectric distortion.

Electron-ordering distortions may be superposed on the array of corner-shared octahedra. MnF_3, for example, exhibits the Jahn-Teller distortions shown in Fig. 10(a) superposed on the partially collapsed structure. WO_3, on the other hand, exhibits several low-temperature phases characteristic of an interplay of antiferroelectric distortions and different degrees of the collapse of the B-X-B angle.

3.2.1.2 The bronze structures

Although □ BX_3 compounds with the ReO_3 structure and cubic ABX_3 compounds have the same BX_3 array, complete solid solutions $□_xA_{1-x}BX_3$, $0 \leqq x \leqq 1$, are not possible. Although there is no ordering of the vacancies for larger x, except for $Na_{0.75}WO_3$ [*Alt*], for smaller x there is ordering accompanied by a collapse of the BX_3 array within basal planes perpendicular to a unique axis. Such a collapse creates the tetragonal and hexagonal tunnel structures of Fig. 20. The tetragonal structure contains three types of tunnels, one containing cubic, twelve-coordinated A' sites, one containing pentagonal-prism, fifteen-coordinated A'' sites, and one small tunnel containing nine-coordinated A''' sites, which are only occupied by Li^+ ions. Without Li^+ ions, all these sites are filled at $A'_{0.4}A''_{0.4}BX_3$. This phase, which may occur for a

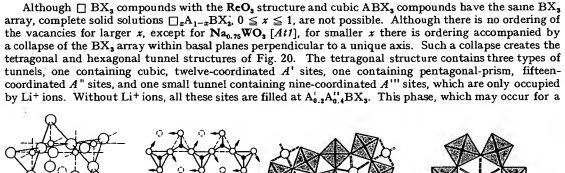

Fig. 19. Projections on B-cation planes of two $□BX_3$ structures. Triangles in full and dotted lines represent faces of octahedra below or above the B-cation plane. a) Cubic $□ReO_3$ structure DO_1. Arrows indicate cooperative atomic motions that collapse the structure. b) Completely collapsed $□RhF_3$ structure.

Fig. 20. Bronze structures found in $A_x□_{1-x}BX_3$ systems. a) Tetragonal (II) structure occurring for $x \leqq 0.6$. b) Hexagonal structure occurring for $x \leqq 0.33$ [*Wad*].

range of $x \leqq 0.6$, is labelled tetragonal (II) in Tab. 3 to distinguish it from the antiferroelectric tetragonal (I) phase of WO_3. The hexagonal structure contains hexagonal-prism, eighteen-coordinated A sites and is restricted to the range of composition $x \leqq 0.33$. An orthorhombic tunnel structure has also been identified for AB_2O_6 compounds [*Ga15a*].

Tab. 3. Color vs. x for Na_xWO_3 and compositional ranges for the bronze structures in the $A_x^{1+}WO_3$ perovskites. Adapted from [*Di3*]

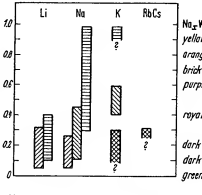

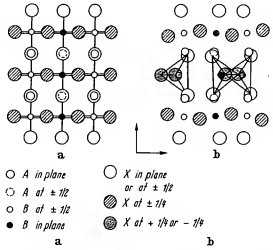

Fig. 21. Projections onto (110) planes of a) cubic perovskite and b) brownmillerite structures. Brownmillerite structure is formed by removing alternate [110] strings of oxygen from central row of a) and regrouping remaining oxygen into the tetrahedra shown in b) [*Wa1*].

3.2.2 Anion-deficient compounds

3.2.2.1 Compounds ABX_{3-x}

Several systems ABX_{3-x}, where $0 \leq x \leq 0.5$, have been reported as anion-deficient perovskites. $SrTiO_{2.5}$ and $SrVO_{2.5}$, for example, both give simple x-ray powder patterns in qualitative agreement with the assumption of a perovskite structure having one-sixth of the anions missing at random. Further, the homogeneity range of $SrTiO_{3-x}$ is reported [*Wa1*] to extend over $0 \leq x \leq 0.5$ without any change of lattice parameter. However, if an anion is removed from a close packed structure, the metal atoms to which it was formerly bonded will have highly unsymmetrical coordination, and some local rearrangement of the anion can be expected. The nature of this local rearrangement depends upon the character of the B cation. In order to learn what rearrangements may occur locally, it is necessary to examine those special cases where long-range order occurs, since local changes of cation coordination are difficult to detect by x-ray diffraction and have not been investigated by other methods.

In the system $SrFe^{3+}_{\frac{2}{3}+x}Fe^{4+}_{\frac{1}{3}-x}O_{3-x}$, $0 \leq x \leq 0.5$, it is known that the Fe^{3+} ions are stable in either tetrahedral or octahedral coordination. Therefore, it is reasonable to anticipate the creation of fourfould coordination about half of the Fe^{3+} ions in the system. This is possible because the d electrons of Fe^{3+} ions are localized, so that Fe^{3+} and Fe^{4+} ions are distinguishable, even though the d electrons of the end member $SrFe^{4+}O_3$ appear to be collective. Support for the creation of tetrahedral sites, as well as a suggestion of how the tetrahedra might be arranged, is given by $Ca_2Fe_2O_5$, which has the brownmillerite structure [*Be4f*] of Fig. 21. Within every other (001) BX_2 plane of the cubic perovskite, alternate [110] rows of anions are removed. The remaining anions in these planes are displaced alternately along [1$\bar{1}$0] and [$\bar{1}$10] directions toward the anion vacancies, the B cations shifting slightly also to maintain equal B-X distances with all four near-neighbor anions. The result is fourfold coordination for all B cations in these (001) BX planes, sixfold coordination for all B cations in the alternate (001) BX_3 planes.

The x-ray pattern of $K_2Ti_2O_5$ has a strong resemblance to that of perovskite. However, $KTiO_{2.5}$ is not an anion-deficient perovskite, but is completely ordered, each Ti^{4+} ion having five oxygen near neighbors forming a trigonal bipyramid [*An3*]. It has little similarity to perovskite.

The oxygen-deficient, tetragonal compounds $(Ba_{1+x}Bi_{1-x})BiO_{3-x}$, $0.22 < x < 0.5$, retain an octahedral grouping for Bi in the B sites, but the A positions have only six oxygen near neighbors, two each at 2.7, 3.1 and 3.6 Å [*Au1*].

These examples indicate that a variety of orderings must occur in anion-deficient perovskites. Further structural work needs to be done.

3.2.2.2 Alloys $M^cX_{1-z}M^f_z$

Since the alloys $M^cXM^f_2$ are generally considered to represent interstitial X atoms in an ordered, face-centered-cubic $M^cM^f_2$ alloy, it is not surprising that the phase is stable over a considerable range of anion deficiency. Since these alloys are metallic, it is probable that the X-atom vacancies are randomly distributed.

3.2.2.3 Shear structures $\square BO_{3-z}$

Ranges of composition have been reported for BO_{3-z}, where B = Mo or W. MAGNÉLI [*Ma14*] has shown that these compositional ranges consist of a series of discrete phases having an x-ray diffraction pattern dominated by a cubic $\square$ **ReO_3**-type (DO_9) subcell, but exhibiting superlattice lines. The superlattice of any discrete phase is not due to an ordering of anion vacancies within this basic structure, but to a regular interruption of the DO_9 structure by planes of discontinuity across which octahedra share edges rather than corners. In these structures the oxygen vacancies condense into regularly spaced planes and are then eliminated by a shear displacement of the type shown schematically in Fig. 22. These "shear" planes may be constituted in different ways: For the series of phases B_nO_{3n-z}, six octahedra in a group share edges, and for the phases B_nO_{3n-1} groups of four octahedra share edges. In both cases the discontinuities continue in two dimensions throughout the structure where they separate DO_9 blocks n octahedra thick. The β-**WO_{3-z}** phases, $0.10 \leq x \leq 0.17$, belong to the series B_nO_{3n-z} with $12 < n \leq 20$. The observed compositional range **(W, Mo)O_{3-x}**, $0.07 \leq x \leq 0.12$, contains six discrete B_nO_{3n-1} phases corresponding to $n = 8, 9, 10, 11, 12$, and 14 [*Ma17a*]. The origin of the shear planes appears to be an interplay between electrostatic and elastic forces: Electrostatic repulsive energies between B cations sharing common octahedral-site edges is minimized by cationic displacements (of ferroelectric type) away from the center of symmetry of the interstice and the shared octahedral edge. These displacements can be cooperative, costing a minimum of elastic energy, if the shared edges are coplanar. The origin of the regular spacing between planes is not established. Presumably it is primarily due to elastic energy, although collective-electron effects [*Go11*] probably play a contributing role.

3.2.3 Structures deficient in B cations

3.2.3.1 Bismuth compounds

Bismuth compounds with chemical formula $(Bi_2A_{m-3})B_{m-1}O_{3m}$ have the structural formula $(Bi_2O_2)^{2+}(A_{n-1}B_nO_{3n+1})^{2-}$, $n = m - 1$. These compounds consist of a regular intergrowth of the perovskite structure with **Bi_4O_5** sheets consisting of **BiO_4** square pyramids sharing edges [*Au2*], as indicated in Fig. 23. Between the **Bi_4O_5** sheets are n layers of corner-shared octahedra and $(n - 1)$ layers of perovskite-type A cations in the twelve-coordinated interstices. Where $n = 1$, the pyramidal sheets alternate with

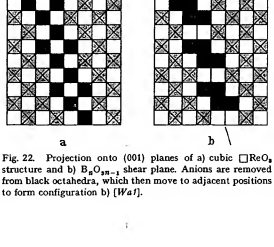

Fig. 22. Projection onto (001) planes of a) cubic $\square ReO_3$ structure and b) B_nO_{3n-1} shear plane. Anions are removed from black octahedra, which then move to adjacent positions to form configuration b) [*Wa1*].

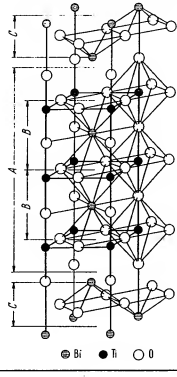

Fig. 23. One half of the pseudo-tetragonal unit cell of $Bi_4Ti_3O_{12}$ (from $z \approx 0.25$ to $z \approx 0.75$). A denotes the perovskite layer $(Bi_4Ti_4O_{13})^{2-}$, C the $(Bi_2O_2)^{2+}$ layers, and B the unit cells of the hypothetical perovskite structure $BiTiO_3$ [*Au5*].

single octahedral layers, and no sites are available for A cations. This particular phase has been prepared in a large number of oxides and oxyfluorides, where B = Ti, Nb, Ta and the O/F ratio depends upon the valencies of the A and B cations (see Tab. 4).

Many of these compounds are reported to exhibit ferroelectric distortions within the perovskite layers, and they will certainly be important for technical applications in the future.

3.2.3.2 Hexagonal $A_nB_{n-1}X_{3n}$ structures

As shown in Fig. 1(c), the cubic perovskite may be indexed on an hexagonal basis. It consists of cubic stacking of close-packed AX_3 layers with B cations in the all-anion octahedral interstices. Within a (110) plane, B-cation octahedra share common corners as shown schematically in Fig. 3(a). In the $Ba_6Ta_4O_{15}$ structure [*Ga5a*], the stacking sequence of the AX_3 layers is *a-b-c-b-c-a*, as shown in Fig. 24, and the B-cation vacancies are where the stacking is hexagonal. Thus the structure consists of perovskite blocks n AX_3 layers and $(n - 1)$ B layers thick, separated by a stacking fault at a layer of B-cation vacancies. These hexagonal structures appear to be stabilized where the tolerance factor is $t > 1$.

3.2.3.3 $AX \cdot (ABX_3)_n$ structures

Materials having compositions intermediate between ABX_3 and A_2BX_4 may have similar diffraction patterns. However, this compositional region contains several phases having the structural formula $AX \cdot (ABX_3)_n$. Each phase contains perovskite sheets n units thick separated by AX (NaCl-type) sheets. The limiting composition A_2BX_4, corresponding to $n = 1$, is shown in Fig. 25. It is important for the theory of magnetism because, if A is nonmagnetic, then by symmetry there is no net molecular field within an antiferromagnetic layer from cations in adjacent antiferromagnetic layers. This permits the study of two-dimensional antiferromagnetism. The A_2BX_4 structure also permits the study of B^{2+} cations in oxides with a smaller B-X-B separation (hence stronger interaction) than is found in the BO compounds with rocksalt structure. The possible significance of this is illustrated by La_2NiO_4. The Ni^{i+} electrons of e_g symmetry appear to be collective in La_2NiO_4, localized in NiO.

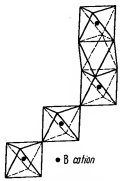

Fig. 24. Schematic (110) projection of the $Ba_6Ta_4O_{15}$ structure. Horizontal lines refer to BaO_3 close-packed layers with stacking *a*, *b*, or *c*.

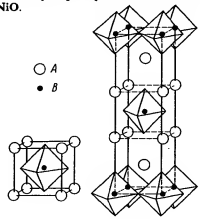

Fig. 25. Comparison of ABX_3 and A_2BX_4 structures [*Trf*].

3.2.4 Data: Crystallographic properties of non-ABX_3 compounds of composition A_nBX_3, $\square BX_3$, $(AX)_n(ABX_3)_m$ and $Bi_2O_3(A_{n-1}B_nO_{3n+1})$ with perovskite-related structure (Tab. 4)

Tab. 4.

See Fig. 20(a) for the tetragonal II bronze structure with $a \approx 12.5$ Å, $c \approx 4$ Å
and Fig. 20(b) for the hexagonal bronze structure with $a \approx 7.4$ Å, $c \approx 7.5$ Å.

Within any section, the compounds are ordered by B-cation atomic number, and the order of the sections is as follows:

Tab. 4a — A_xBX_3
A_xBO_3: B = Nb, Mo, Ta, W, Re
A_xFeF_3
Tab. 4b — $\square$ BX_3
Tab. 4c — $\square$ $BB'X_6$
Tab. 4d — $(AX)_n(ABX_3)_m$
X = F^{-1}, Cl^{-1}; B^{2+} = Mg, Cr, Mn, Fe, Co, Ni, Cu, Zn, Cd
X = O^{-2}; B = Al, Ti, Cr, Mn, Fe, Co, Ni, Cu, Ga, Ge, Zr, Nb, Mo, Tc, Ru, Rh, Sn, Hf, Ir, Pb, U
Tab. 4e — $Bi_2O_3(A_{n-1}B_nO_{3n+1})$
$n = 1$; B = Mo, W $n = 2$; B = Nb, Ta $n = 3$; B = Nb, Ti $n = 4$, 5 and 8; B = Ti

For abbreviations, see p. 131.

Tab. 4a. A_xBX_3 compounds

Compound	Sym	a Å	b Å	c Å	angle	Ref.	Remarks	Magnetic Data
A_xNbO_3								in 3.3.4, Tab.
$Ba_{0.8}NbO_3$	O	12.17	20.5	7.87		*Fr1b*	Structure and review [*Ga15a*], S. S. with (Pb, Ca, Sr)$_{0.8}$NbO$_3$ [*Su4c, Fr1b, Is3a*], dielectric properties [*Gi0*]	
$Ba_{0.5}NbO_{2.5}$	T	12.60		3.95		*Ga14*		
$Sr_{0.86}NbO_3$	C	4.016				*Ri3*	Studied $x = 0.5 \cdots 1.0$	
$Sr_{0.7}NbO_3$	C	3.981				*Ri3*		
$Sr_{0.7}NbO_3$	O	11.021	7.33	5.604		*He12a*		
$Ca_{0.4}NbO_3$	O	5.764	15.09	5.232		*He12a*		
$Pb_{0.8}NbO_3$	O	17.51	17.81	7.72		*Fr2a*	Dielectric properties [*Go20, Su4b*], S. S. with (Ba, Sr)Nb$_2$O$_6$ [*Ba25c, Fr1b, Is2a, Kv7, Sm16a, Su4c*], P & S [*Ro16a*], S. S. with Ti, Zr, Sn [*Su1a, Su4b, Su4c*], S. S. with Li, Na, K, Rb, Cs, Y, La, Sm [*Su4b, Su4c*]	
	R	8.664			$\alpha = 88° 30'$	*Fr1a*	Prep. $T < 1250$ °C	
	T	12.46		3.907		*Fr2a*	$T = 570$ °C	
$La_{0.33}NbO_3$	O	3.911	3.917	7.908		*Iy1*	P & S [*Ke8, Ro13, Sa6a*]; dielectric properties, S.S. with $KSr_2Nb_5O_{15}$ [*Bu5*]	
$Ce_{0.33}NbO_3$	O	3.901	3.917	7.886		*Iy1*	P & S [*Ke8, Ro13*]	
$Ce_{0.33}NbO_3$	O	3.881	3.897	7.843		*Ko10*		
$Pr_{0.33}NbO_3$	O	3.891	3.915	7.862		*Iy1*	P & S [*Ke8, Ro13*]	
$Nd_{0.33}NbO_3$	O	3.878	3.907	7.840		*Iy1*	P & S [*Ke8, Ro13*]	
$Ln_{0.33}NbO_3$						*Ro13*	(Ln = Sm $\cdots$ Lu) not able to be prepared	
$Th_{0.33}NbO_3$	T	7.783		7.837		*Ke6*	P & S [*Ko10*], detailed structure [*Tr7*]	
$Pa_{0.25}NbO_3$	T	7.75		7.81		*Ke6*		
$U_{0.33}NbO_3$	T	7.727		7.792		*Ke6*	P & S [*Ko10*]	
$Np_{0.25}NbO_3$	T	7.69		7.76		*Ke6*		
$Pu_{0.25}NbO_3$	T	7.67		7.74		*Ke6*		
$Am_{0.33}NbO_3$	T	3.819		7.835		*Ke8*		
$Ba_2KNb_5O_{15}$	T	12.55		4.019		*Bu5a*	$T_{melt} = 1395$ °C	
$Ba_2NaNb_5O_{15}$	O	17.626	17.592	3.995		*Va13*	Dielectric and optical properties [*Va13, Ge14, Sm6a, Bu5a, Va11a*], Raman effect [*Bu4b*]; S. S. with K [*Bu5a*], Sr [*Va11a*]; elastic properties [*Sp0*], piezoelectric properties [*Wa15a*]	
$Sr_2KNb_5O_{15}$	T	13.47		3.942		*Gi1a*	Dielectric + optical properties [*Gi1a, Bu5*]	

Compound	Sym	a Å	b Å	c Å	angle	Ref.	Remarks	Magnetic Data
A_2NbO_3 (continued)								in 3.3.4, Tab.
$Sr_2NaNb_5O_{15}$	O	17.4	17.4	3.90		*Va13*	Dielectric + optical properties [*Va11a, Va13*]	
$Na_3LaNb_5O_{15}$	C	3.918				*Is5b*		
$Na_3BiNb_5O_{15}$	C	3.925				*Is5b*		
$K_3Li_2Nb_5O_{15}$	T	12.47		4.01		*Fu2a*	Tetr. W bronze type—dielectric + optical properties [*Va12, Va13, Va11a*]	
$K_2LaNb_5O_{15}$	T	12.580		3.930		*Sc27*	P & S [*Is5b*]	
$K_2CeNb_5O_{15}$	T	12.545		3.913		*Sc27*		
$K_2PrNb_5O_{15}$	T	12.530		3.918		*Sc27*		
$K_2NdNb_5O_{15}$	T	12.497		3.924		*Sc27*		
$K_2SmNb_5O_{15}$	T	12.474		3.917		*Sc27*		
$K_2EuNb_5O_{15}$	T	12.457		3.914		*Sc27*		
$K_2GdNb_5O_{15}$	T	12.450		3.912		*Sc27*		
$K_2TbNb_5O_{15}$	T	12.440		3.910		*Sc27*		
$K_2DyNb_5O_{15}$	T	12.431		3.903		*Sc27*		
$K_2HoNb_5O_{15}$	T	12.426		3.899		*Sc27*		
$K_2YNb_5O_{15}$	T	12.424		3.901		*Sc27*		
$K_3BiNb_5O_{15}$	O	17.75	17.90	7.84		*Is5b*	P & S [*Kr2, Kr8*]	
$Rb_2LaNb_5O_{15}$	T	12.633		3.945		*Sc27*		
$Ba_6(Ti_2Nb_8)O_{30}$	T	12.54		4.01		*St23*	Tetr. W bronze type, structure determined [*Ja9*]	
$Ba_6(Zr_2Nb_8)O_{30}$	T					*Fa1*	Tetr. W bronze	
$Ba_6(FeNb_8)O_{30}$	O	17.95	17.95	7.98		*Is5b*	Prop. [*Fa2, Fa1*] S. S. with Nd, Sm, Eu, Gd [*Fa1, Fa2*]	
$Sr_6(FeNb_8)O_{30}$	O	17.50	17.50	7.72		*Is5b*		
$A_6(B_2Nb_{10-2})O_{30}$	T	≈ 12.5		≈ 3.9		*Kr2*	Tetr. W bronze type, A = Ba, Sr, Pb, Bi, La, Ce, Nd, Sm, Gd, K; B = Fe, Ni, Mg; dielectric properties [*Kr2*] gives review of the tetr. W bronze structure type	
$Ba_3MgNb_{14}O_{45}$	O	18.00	18.00	8.02		*Is5b*		
$Sr_3MgNb_{14}O_{45}$	O	17.55	17.55	7.82		*Is5b*		
$Ba_{0.27}Sr_{0.73}Nb_2O_{5.73}$	T	12.4032		3.9134		*Ja8a*	T = 25 °C, complete structure determination	
$K_{0.6}NbO_{3.8}F_{0.5}$	T	12.632		3.950		*Ma19a*	Tetragonal tungsten bronze	
A_xMoO_3								
$Rb_{0.27}MoO_3$	H	7.321		7.683		*Bi6*	High pressure preparation, metallic conductivity, P & S [*Ch1b*]	
$K_{0.93}MoO_3$	C	3.917				*Bi6*	High pressure preparation, metallic conductivity, P & S [*Ch1b*]	
$K_{0.59}MoO_3$	C	3.920				*Bi6*	High pressure preparation, metallic conductivity	
$K_{0.3}MoO_3$	T	12.32		3.859		*Bi6*	High pressure preparation, metallic conductivity, Θ_{∞} = 4.2 °K [*Si7a*]	

Compound	Sym	a Å	b Å	c Å	angle	Ref.	Remarks	Magnetic Data
A_xMoO_3 (continued)								in 3.3.4, Tab.
$K_{0.28}MoO_3$	M	18.249	7.560	9.855	$\beta = 117° 32'$	*Gr2*	"Blue Mo bronze"; Prep. [*Wo10*], metallic conductivity [*Bo20*], structural discussion [*St22*], optical properties [*Di2a*]	
$K_{0.33}MoO_3$	M	14.278	7.723	6.387	$\beta = 92° 34'$	*St24*	"Red Mo bronze"; Prep. [*Wo10*]. Semiconducting [*Bo20*], structural discussion [*St22*]	
$Na_{0.97}MoO_3$	C	3.853				*Bi6*	High pressure preparation, $\Theta_{cs} < 1.3$ °K [*Sl7a*]	
$Na_{0.90}MoO_3$	C	3.847				*Bi6*	High pressure preparation	
$Na_{0.15}MoO_{2.88}$	M	9.57	5.50	12.95		*St25*	Complete structure, random vacancies [*St25*]; optical properties [*Di2a*]	
A_xTaO_3								
$Ba_{0.7}TaO_{3-x}$	T	12.60		3.95		*Ga14*	($x = 0 \cdots 0.5$), P&S [*Is2a*]	
$Ba_{0.5}TaO_3$	H	21.14		3.917		*La8*	Dielectric properties, P&S [*Is2a, Ga14*], review [*Ga15a*]	
$Sr_{0.5}TaO_{3-x}$	T	12.41		3.90		*Ga14*	($x = 0 \cdots 0.5$), review [*Ga15a*]	
$Ca_{0.5}TaO_3$	C	3.886				*Ja7*	Review [*Ga15a*]	
$Pb_{0.5}TaO_3$	O	17.635	17.695	7.757		*Is9*	Review of literature, P&S [*Is2a*]	
$Pb_{0.5}TaO_3$	T	17.71		7.788		*Is9*	$T = 300$ °C, tetr. $T > 270$ °C	
$Cu_{0.5}TaO_3$	C	7.522				*Ka16*	P&S [*Sh12*], optical properties [*Ka16*]	
$La_{0.33}TaO_3$	T	3.918		7.913		*Iy1*	P&S [*Ke8, Ro13, Tr8*], Prep. [*Sa6a*]	
$Ce_{0.33}TaO_3$	T	3.915		7.878		*Iy1*	P&S [*Ke8, Ro13*], Prep. [*Sa6a*]	
$Pr_{0.33}TaO_3$	O	3.895	3.910	7.836		*Iy1*	P&S [*Ke8, Ro13*], Prep. [*Sa6a*]	
$Nd_{0.33}TaO_3$	O	3.876	3.916	7.829		*Iy1*	P&S [*Ke8, Ro13*], Prep. [*Sa6a*]	
$Sm_{0.33}TaO_3$	O	3.882	3.896	7.785		*Iy1*	P&S [*Ke8, Ro13*]	
$Eu_{0.33}TaO_3$	O	3.871	3.885	7.792		*Ke8*		
$Gd_{0.33}TaO_3$	T	3.874		7.795		*Iy1*	P&S [*Ke8, Ro13*]	
$Tb_{0.33}TaO_3$	T	3.851		7.780		*Ke8*		
$Dy_{0.33}TaO_3$	T	3.847		7.769		*Iy1*	P&S [*Ke8, Ro13*]	
$Ho_{0.33}TaO_3$	T	3.841		7.756		*Iy1*	P&S [*Ke8*]	
$Er_{0.33}TaO_3$	T	3.825		7.754		*Iy1*	P&S [*Ke8*]	
$Yb_{0.33}TaO_3$	M	3.828	7.749	3.839	$\beta = 90° 54'$	*Ro13*		
$Y_{0.33}TaO_3$	T	3.824		7.758		*Iy1*	P&S [*Ke8, Tr8, Ro13, Ly1*]	
$Th_{0.25}TaO_3$	C	7.810				*Ke6*	P&S [*Ko10*]	
$Pa_{0.25}TaO_3$	T	7.77		7.78		*Ke6*		
$U_{0.25}TaO_3$	T	7.739		7.773		*Ke6*	P&S [*Ko10*]	
$Np_{0.25}TaO_3$	T	7.70		7.75		*Ke6*		
$Pu_{0.25}TaO_3$	T	7.654		7.731		*Ke6*		
$Am_{0.25}TaO_3$	T	3.889		7.820		*Ke8*		
$K_{0.5}TaO_{2.5}F_{0.5}$	T	12.569		3.961		*Ma19a*	Tetragonal tungsten bronze	

Compound	Sym	a Å	b Å	c Å	angle	Ref.	Remarks	Magnetic Data
A_xWO_3								in 3.3.4, Tab.
$Cs_{0.32}WO_3$	H	7.42		7.63		*Ma17*	Superconducting, $\Theta_{cs} = 1.12$ °K [*Sw3*]	
$Cs_{0.30}WO_3$	H	7.38		7.59		*Ma17*	Thermal expansion to 720 °C [*We15*]	
$Rb_{0.32}WO_3$	H	7.386		7.54		*Si7*	P&S [*Ma17*], metallic conduction and magnetic susceptibility [*Si7, Si9*], optical properties [*Do6*]	
$Rb_{0.27}WO_3$	H	7.394		7.516		*We15*	Superconductivity, $\Theta_{cs} = 1.98$ °K [*Sw3*], thermal expansion to 970 °C [*We15*]	
$(NH_4)_{0.33}WO_3$	H	7.395		7.525		*Gi1*	Superconductivity 2.2 °K $\geq \Theta_{cs}$ [*Gi1*]	
$(NH_4)_{0.05}WO_3$	T	7.60		6.36		*Ne8a*		
$K_{0.9}WO_3$	C	3.926				*Bi6*	High pressure preparation (metallic conductivity), P&S [*Ch1b*]	
$K_{0.82}WO_3$	T	12.326		3.845		*We15*	Magnetic susceptibility ($x = 0.53$) [*Ku5*], electric properties ($x = 0.57$ and 0.63) [*St43*], thermal expansion to 750 °C ($x = 0.3 \cdots 0.55$) [*We15*]	
$K_{0.3}WO_3$	H	7.385		7.513		*We15*	Electric + magnetic properties [*Sh8, Si9, Si7*], S.S. with Li [*Ba11*], S.S. with Na [*Br8*], P&S [*Ma12, Ma17, De19*], review [*Di3, Ma15, Ma18, Si9*]	
$K_{0.13}WO_3$	H	7.370		7.515		*Ba11*	Superconductivity, Θ_{cs} (Hex) = 0.5 °K, Θ_{cs} (Tetr.) = 1.5 °K [*Sw3*], magnetic properties [*Ku5, Fu1, Gr8, St43*]	
Na_xWO_3	C	3.8				*Br22*	$a = (0.0819\ x + 3.7846)$ Å [*Br22, We2*]; cubic, $0.26 < x < 1.0$; early preparation [*Bo17, Wr1, Ph1, Wo1, Sp1, Sp2, Ka5*], P&S [*St37, St38, St39, Va5, De6, Ha5, Br8, Ha4, Bi6, Ch1b*]; neutron diffraction ($0.56 < x < 0.86$) [*Al1*]; electrical properties [*Hu8, Hu9, Hu10, Mu3, Mu4, Br21, Fu1, Ga2f*], reviews [*Di3, Ma15, Ma18, Ri1, Si7*], optical properties [*Di3a*]	
	T	12.094		3.748		*Ma13*	$x = 0.28$, tetragonal II [*Ri1*]. Superconductivity, $\Theta_{cs} < 1$ °K [*Sw3, Ra12*], optical properties [*Br22, Da3*], NMR [*Fr18, Fr19, Na12*]	
	T	5.248		3.895		*Ma16*	$x = 0.10$, tetragonal I [*Ri1*]; thermal properties [*Sh7, Fu1, Ge11, Ta2, Ve11*], Na diffusion [*Sm6*], electrostatic energy calculated [*Sm5*]	
$Li_{0.36}WO_3$	H	7.405		7.554		*Gi1*	Metallic conductivity, superconducting $\Theta_{cs} <$ 1.3 °K [*Gi1*]	
$Li_{0.394}WO_3$	C	3.715				*Si10*	Magnetic properties, Pauli paramagnetic or diamagnetic [*Si10, Co17*], metallic conductivity [*Co17, Si10, Si7, Sh8*], P&S [*Ma19, Ma16, Si40*]	
$Li_{0.86}WO_3$	C	3.718				*Co17*	Review [*Di3*]	

Compound	Sym	a Å	b Å	c Å	angle	Ref.	Remarks	Magnetic Data
A_xWO_3 (continued)								in 3.3.4, Tab.
$Li_{0.05}WO_3$	C	3.723				*Co17*		
$H_{0.3}WO_3$	C	3.755				*Gl1*	I. R. spectra [*Si7a*]	
$H_{0.28}WO_3$	T	5.22		3.88		*Di2*	Structure determination by x-ray and neutron diffraction, I. R. spectra [*Si7a*]	
$H_{0.1}WO_3$	O	7.247	7.502	3.84		*Gl1*	I. R. spectra [*Si7a*]	
$Ba_{0.12}WO_3$	T	12.16		3.843		*Co19*	$x = 0 \cdots 0.13$; $\chi_{dia} = 20 \cdot 10^{-6}$ emu/mole, Novel preparation [*Co16*]; superconductivity, $x = 0.13$, $\Theta_{cs} = 1.9$ °K [*Sw4*]	
$Ba_{0.10}Na_{0.32}WO_3$	T	12.12		3.834		*Co19*	Metallic conductivity	
Ca_xWO_3	O	7.340	7.420	3.840		*Va2*	$x = 0.02$, $0 < x < 0.01$ (monoclinic); $0.01 < x < 0.03$ (orthorhombic), studied as function of T [*Va2, Va4*]	
	T	5.240		3.854		*Va2*	$x = 0.035$, $0.03 \leq x < 0.40$ (tetragonal); $0.04 < x < 0.095$ (two phase)	
	T	5.292		3.832		*Va2*	$x = 0.10$, $0.095 \leq x < 0.105$ (tetragonal); $0.105 \leq x < 0.125$ (cubic $a = 3.790$ Å); $x > 0.125$ (two phase)	
$Sn_{0.24}WO_3$	H	7.430		7.581		*Gi1*	Metallic conductivity, superconducting $\Theta_{cs} < 1.3$ °K [*Gi1*]	
$Sn_{0.19}WO_3$	T	12.241		3.774		*Gi1*	Superconducting $\Theta_{cs} < 1.3$ °K [*Gi1*]	
$Pb_{0.17}WO_3$	T	12.163		3.767		*Be30*	$x = 0.057 \cdots 0.16$ monoclinic, $x = 0.16 \cdots 0.35$ tetr.	
$Pb_{0.35}WO_3$	T	12.207		3.782		*Be30*	Novel preparation [*Co16*]	
$La_{0.08}WO_3$	C	3.829				*Br23*	Cubic, ($x = 0.08 \cdots 0.19$), metallic conductivity [*Sh6*]	
$La_{0.19}WO_3$	T	7.52		3.89		*Br23*		
$Ce_{0.1}WO_3$	C	3.828				*Os2*	$n_{eff} = 2.5$, all rare-earth bronzes blue-violet	
$Pr_{0.1}WO_3$	C	3.827				*Os2*	$n_{eff} = 3.6$	
$Nd_{0.1}WO_3$	C	3.822				*Os2*	$n_{eff} = 3.8$	
$Sm_{0.1}WO_3$	C	3.817				*Os2*	$n_{eff} = 1.6$ (temperature dependent), crystal growth [*Co14*]	
$Eu_{0.15}WO_3$	C	3.828				*Os2*		
$Eu_{0.10}WO_3$	C	3.815				*Os2*	$n_{eff} = 3.4$ (temperature dependent), P&S [*Sh6*]	
$Eu_{0.085}WO_3$	C	3.808				*Os2*		
$Gd_{0.1}WO_3$	C	3.810				*Os2*	$n_{eff} = 7.9$, crystal growth [*Co14*], P&S [*Sh6*], relation of a vs. x [*We2*]	
$Tb_{0.1}WO_3$	C	3.808				*Os2*	$n_{eff} = 9.6$	
$Dy_{0.1}WO_3$	C	3.805				*Os2*	$n_{eff} = 10.6$	
$Ho_{0.1}WO_3$	C	3.801				*Os2*	$n_{eff} = 10.6$, P&S [*Sh6*]	
$Er_{0.1}WO_3$	C	3.797				*Os2*	$n_{eff} = 9.5$	
$Tm_{0.1}WO_3$	C	3.794				*Os2*	$n_{eff} = 7.5$, crystal growth [*Co14*]	

Compound | a Å | b Å | c Å | Ref. | Remarks | Magnetic | Ref.

						0S2	n_{eff} = 7.5, crystal growth [*Co14*]	

Compound	Sym	a Å	b Å	c Å	angle	Ref.	Remarks	Magnetic Data
A_xWO_3 (continued)								in 3.3.4, Tab.
$Yb_{0.1}WO_3$	C	3.791				*Os2*	n_{eff} = 4.5	
$Lu_{0.1}WO_3$	C	3.788				*Os2*	n_{eff} = 0	
$Y_{0.09}WO_3$	C	3.800				*Br23*	Tetr. $x < 0.09$, metallic conductivity [*Sh6*]	
Al_xWO_3	O	7.368	7.476	3.850		*Po10*	$x = 0.015$, $0.010 < x < 0.030$ orthorhombic; $0.030 < x < 0.105$, two phase; studied as function of T [*Va4*]	
	O	5.387	5.440	3.784		*Po10*	$0.105 < x \leq 0.135$; $x > 0.135$, two phase	
$Cu_{0.77}WO_3$	O	3.73	3.88	7.74		*Co18*	Semiconducting $\approx$ 0.15 eV	
$Cu_{0.26}WO_3$	Tr	5.85	6.65	4.88	α = 134° 45′ β = 91° 40′ γ = 93° 37′	*Co18*	Magnetic susceptibility $\chi_m = 34 \cdot 10^{-6}$ emu/mole	
$Ag_{0.01}WO_3$	O	3.73	3.85	7.35		*Si8*	Metallic conductivity, P&S [*Po2*]	
Cd_xWO_3	O	7.316	7.532	3.848		*Va3*	$x = 0.005$, $0.005 \leq x < 0.02$ orthorhombic	
	T	5.244		3.867		*Va3*	$x = 0.020$, $0.02 \leq x < 0.04$ tetragonal	
$In_{0.01}WO_3$	T	5.233		3.863		*Bo21*	$x = 0.01 \cdots 0.05$, P&S ($x = 0.11$) [*Bi3*]	
$In_{0.20}WO_3$	H	7.384		7.508		*Bo21*	$x = 0.2 \cdots 0.3$, metallic conductivity, weak diamagnetism	
$In_{0.33}WO_3$	H	7.50		7.56		*Sw1*	$x = 0.26 \cdots 0.33$; metallic conductivity	
$Tl_{0.26}WO_3$	T	7.31		12.80		*Si6*	Metallic conductivity, $x = 0.19 \cdots 0.36$; novel preparation [*Co16*]	
$U_{0.083}WO_3$	C	3.812				*Ko10*	relationship of a vs. x [*We2*]	
$U_{0.125}WO_3$	C	3.821				*Ko10*	P&S [*Sh9*]	
$Cs_{0.3}(Ta_{0.3}W_{0.7})O_3$	H	7.450		7.821		*Ga4*	Thermal expansion and resistivity (10^8 Ωcm)	
$Rb_{0.3}(Ta_{0.3}W_{0.7})O_3$	H	7.342		7.715		*Ga4*	Thermal expansion and resistivity (10^8 Ωcm)	
$K_{0.3}(Ta_{0.3}W_{0.7})O_3$	H	7.333		7.685		*Ga4*	Thermal expansion and resistivity (10^8 Ωcm)	
$K_{0.5}(Ta_{0.5}W_{0.5})O_3$	T	12.36		3.90		*Ga14*	Entire range of S.S. with Ta and Nb [*De19a*]	
A_xReO_3								
$K_{\approx 0.5}ReO_3$	C	3.895				*Si2*	Metallic conductivity	
$K_{\approx 0.3}ReO_3$	H	7.318		7.485		*Ch1b*	High pressure preparation, Θ_m = 3.6 °K [*Si7a*]	
$Na_{\approx 0.6}ReO_3$	T	3.825		3.841		*Si7a*	Metallic, Θ_m < 1.3 °K, P&S [*Si2*]	
A_xFeF_3								
$Rb_{0.32}FeF_3$	H	7.36		7.53		*Tr1*	Hex ($x = 0.18 \cdots 0.30$); P&S [*De13a*]	
$K_{0.36}FeF_3$	C	4.113				*De11*	($x = 0.95 \cdots 1.0$) cubic	
$K_{0.36}FeF_3$	T	12.60		3.936		*De11*	($x = 0.40 \cdots 0.60$) tetr	
$K_{0.40}FeF_3$	H	7.385		7.510		*De11*	($x = 0.18 \cdots 0.25$) hex	
$Na_{0.11}FeF_3$	R	5.37			α = 59°	*Tr1*	$x = 0.0 \cdots 0.16$; P&S [*De13a*]	
$Tl_{0.36}FeF_3$	H	7.35		7.52		*Tr1*	Hex ($x = 0.20 \cdots 0.31$); P&S [*De13a*]	

Tab. 4b. □ BX_3 compounds

Compound	Sym	a Å	b Å	c Å	angle	Ref.	Remarks	Magnetic Data
								in 3.3.4, Tab.
AlF_3	R	5.029			$\alpha = 58° 31'$	*Ke20*		
ScF_3	R	5.708			$\alpha = 59° 32'$	*No10*		
TiF_3	R	5.519			$\alpha = 58° 53'$	*Si2*	P&S [*Eh2*]	6
$TiOF_2$	C	3.798				*Vo3*		
VF_3	R	5.373			$\alpha = 57° 31'$	*Ja2a*	Neutron diffraction [*Wo13*]	6
CrF_3	R	5.2643			$\alpha = 56° 37'$	*Kn2*	Prop. [*Bi7, Ha11, Ha12, Bo33, Ra9*], structure [*Ja3*], neutron diffraction [*Wo13*]	6
	R	5.332			$\alpha = 56° 37'$	*Kn2*	300 °C	
MnF_3	M	8.904	5.037	13.448	$\beta = 92° 44'$	*He9*	Neutron diffraction [*Wo13*], Prop. [*Bo33, Bo34, Ny1, Ki5, He10, Sm1*]	6
FeF_3	R	5.362			$\alpha = 58° 0'$	*He11*	Neutron diffraction [*Wo13*], Prop. [*Bi7, Sh5, We17, Bu1*], crystal transformation [*Cr5*]	6
CoF_3	R	5.279			$\alpha = 57° 0'$	*He11*	Neutron diffraction [*Wo13*], Prop. [*He8, Ny1*]	6
GaF_3	R	5.20			$\alpha = 57° 30'$	*Br6*	P&S [*Mu1*]	
ZrF_3	C	3.96				*Eh3*		
NbF_3	C	3.903				*Eh4*	P&S [*Sc2*], "doubtful"	6
NbO_2F	C	3.902				*Fr15*		
MoF_3	C	3.8985				*Gu8*	Neutron diffraction [*Wi6*], P&S [*La7*]	6
RuF_3	R	5.408			$\alpha = 54° 90'$	*He11*	Neutron diffraction [*Wi6*]	6
RhF_3	R	5.330			$\alpha = 54° 25'$	*He11*		
PdF_3	R	5.5234			$\alpha = 53° 55'$	*He11*	Neutron diffraction [*Wi6*], Prop. [*Ba19, Ba20, Ny1, Fi3*]	6
InF_3	R	5.722			$\alpha = 56° 15'$	*Mu1*		
TeO_3	R	5.180			$\alpha = 56° 25'$	*Du2*	Prop. [*Lo8*]	
TaF_3	C	3.9012				*Gu8*	Prop. [*Ny1*], "doubtful"	6
TaO_2F	C	3.896				*Fr15*		
WO_3	M	7.297	7.539	7.688	$\beta = 90° 55'$	*Lo6*	Structure [*Br1, Ta15*], neutron diffraction [*Lo6*], Prop. [*Cr7, Cr8, Ta15, Co16, Be22, Iw2, De16, Ke10*], optical properties [*Di3a*], phase transformations [*Fe3a*]	
$Re_{0.33}W_{0.67}O_3$	C	3.7574				*Si2*		
ReO_3	C	3.7477				*Si2*	P&S, [*Me11, Bi4, Bi5*], crystal growth [*Fe21*], Prop. [*Si2, Fe21, Fe10, Gu6a*], structure vs. oxygen content [*Si2*], DeHaas-Van Alphen effect [*Ma27a*], NMR [*Na11a*]	
IrF_3	R	5.418			$\alpha = 54° 8'$	*He11*	P&S [*Ro2*]	
UO_3	C	4.156				*Wa6*	P&S [*En2*]	

UF_6	R	5.416			$\alpha = 54° 8'$	*He11*	P & S [*Ko04*]		
UO_3	C	4.156				*Wa6*	P & S [*Em2*]		

Tab. 4c. □ $BB'X_6$ compounds

Compound	Sym	*a* Å	*b* Å	*c* Å	angle	Ref.	Remarks	Magnetic Data
$BB'X_6$							Structural review [*Gi2, Ke11, Co29*]	in 3.3.4, Tab.
$NaVF_6$	R	5.63			$\alpha = 56° 30'$	*Ke11*		
$LiVF_6$	R	5.30			$\alpha = 56° 18'$	*Ke11*		
$CaMnF_6$	R	5.59			$\alpha = 55° 36'$	*Ho14*		
$MgMnF_6$	R	5.26			$\alpha = 56° 54'$	*Ho14*		
$NaNbF_6$	C	8.26				*Ke11*	P & S [*Co29*]	
$LiNbF_6$	R	5.47			$\alpha = 58° 6'$	*Ke11*		
$NaMoF_6$	C	8.194				*Ed3*	Magnetic properties $80 < T < 300$ °K, $n_{eff} = 1.66$, $\Theta_p = -218$ °K [*Ha18*]	
$LiMoF_6$	R	5.43			$\alpha = 57° 6'$	*Bo18*		
$NaTcF_6$	R	5.77			$\alpha = 55° 48'$	*Ed4*	P & S [*Hu7*]	
$NaRuF_6$	R	5.80			$\alpha = 54° 30'$	*Bo18*		
$LiRuF_6$	R	5.39			$\alpha = 56° 0'$	*Bo18*		
$GePdF_6$	R	5.53			$\alpha = 54° 0'$	*Ba21*	Magnetic properties, $n_{eff} = 2.82$, $\Theta_p = 31$ °K [*Ba21*]	
$PdPdF_6$	R	5.52			$\alpha = 53° 54'$	*Ba21*	P & S [*He11*], see PdF_3	
$SnPdF_6$	R	5.70			$\alpha = 53° 6'$	*Ba21*	Magnetic properties, $n_{eff} = 2.98$, $\Theta_p = 28$ °K [*Ba21*]	
$PtPdF_6$	R	5.55			$\alpha = 54° 0'$	*Ba21*	Magnetic properties, $n_{eff} = 2.72$, $\Theta_p = 1.2$ °K [*Ba21*]	
$NaSbF_6$	C	8.184				*Te12*	P & S [*Sc22*]	
$LiSbF_6$	R	5.44			$\alpha = 57° 0'$	*Bu6*	Complete structure; P & S [*Ke11*]	
$CaHfF_6$	C	8.462				*Ke7*		
$NaTaF_6$	C	8.28				*Ke11*	P & S [*Co29*]	
$LiTaF_6$	R	5.48			$\alpha = 58° 0'$	*Ke11*		
$NaWF_6$	C	8.18				*Ke11*	Magnetic properties $80 < T < 300$ °K, $n_{eff} = 0.5$, $\Theta_p = -125$ [*Ha18*]	
$LiWF_6$	R	5.45			$\alpha = 57° 24'$	*Ke11*		
$NaReF_6$	C	8.18				*Ke11*	P & S [*Pe1*]; magnetic properties $80 < T < 300$ °K, $n_{eff} = 1.57$, $\Theta_p = -100$ °K [*Ha19*]	
$NaOsF_6$	R	5.80			$\alpha = 55° 12'$	*Bo18*		
$LiOsF_6$	R	5.43			$\alpha = 55° 30'$	*Bo18*		
$NaIrF_6$	R	5.80			$\alpha = 55° 12'$	*Bo18*		
$LiIrF_6$	R	5.41			$\alpha = 56° 0'$	*Bo18*		
$PdPtF_6$	R	5.55			$\alpha = 54° 0'$	*Ba21*		
$CaPbF_6$	C	8.476				*Ho15*		

Tab. 4d. $(AX)_n(ABX_3)_m$ compounds

Compound	Sym	a Å	b Å	c Å	angle	Ref.	Remarks	Magnetic Data
Halides								in 3.3.4, Tab.
Cs_3MgF_4							No cell dimensions [*Be22a*]	
Rb_3MgF_4	T	4.055		13.79		*Ba1*		
K_3MgF_4	T	3.955		13.706		*Re6*	P & S [*Wi12*], S.S. with K_2NiF_4 [*We20*]	
$(NH_4)_3MgF_4$	T	4.07		13.88		*Ch8a*		
Tl_3MgF_4	T	4.007		14.43		*Vo1*		
Na_3CrF_4	M	3.344	9.533	5.657	$\beta = 87^c\ 12'$	*Vo1*	Not K_2NiF_4 type	
Cs_3CrCl_4	T	5.215		16.46		*Se2*		
Rb_3CrCl_4	T	5.143		15.73		*Se2*		
K_3CrCl_4							Possibly distored K_2NiF_4 [*Se2*]	
Cs_3MnF_4	T	4.31		14.63		*Co25*		
Cs_3MnCl_4	T					*Le7*	K_2NiF_4 type	6
Rb_3MnF_4	T	4.228		13.89		*Co25*	P & S [*Vo1*], Prop. [*De20, Br5*]	6
K_3MnF_4	T	4.20		13.14		*Br5*	P & S [*Vo1, Co25*], Prop. [*De20, Co15*]	6
Rb_3FeF_4	T	4.20		13.38		*Tr1*		6
K_2FeF_4	T	4.140		12.98		*De12*		
$K_3Fe_2F_7$	T	4.130		21.15		*De12*		
Tl_3FeF_4	T	4.194		13.91		*Vo1*		
Rb_3CoF_4	T	4.135		13.67		*Ru6*	P & S [*Ru3, Ru8*]	6
K_3CoF_4	T	4.07		13.08		*Ru6*	Prop. [*Ru8, Sr3, Sr2, Va1, Le8*], dielectric properties [*La1a*]	6
Tl_3CoF_4	T	4.11		14.05		*Ru6*	P & S [*Ru3, Ru8*]	6
Rb_3NiF_4	T	4.087		13.71		*Ru8*	Prop. [*Ru5*]	6
K_2NiF_4	T	4.006		13.076		*Ba10*	Prop. [*Sr2, Go26, De20, Ru5, Ti5, We20*], dielectric properties [*La1b*], neutron diffraction [*Pl4, Pl5, Pl6, Pl7, Le6, Le7*]	6
$(NH_4)_2NiF_4$	T	4.08		13.78		*Ru8*		6
Tl_2NiF_4	T	4.051		14.22		*Ru8*		6
Rb_2CuF_4	T	4.238		13.28		*Ru6*	P & S [*Ru3*], optical properties [*Sc10a*]	6
K_2CuF_4	T	4.145		12.72		*Ru6*	Prop. [*Ru6, Va1*], P & S [*Kn1, Gu1a*]	6
Na_2CuF_4	M	3.261	9.354	5.601	$\beta = 87^c\ 30'$	*Ba3*	P & S [*Ru3*]—not K_2NiF_4 type	
Tl_2CuF_4	T	4.199		13.66		*Ru6*	P & S [*Ru3*]	6
$(NH_4)_2CuCl_4$	O	7.20	7.20	15.46		*Wi9*		
$(CH_3NH_3)_2CuCl_4$	O	7.30	7.54	18.55		*Gr7*	Prop. [*De20, Bo15, Ko8*], Prep. [*Re7*]	6
$(C_2H_5NH_3)_2CuCl_4$	O	7.35	7.47	21.18		*Wi9*	Prop. [*De20, Bo15, Ko8*], Prep. [*Re7*]	6
Rb_2ZnF_4	T	4.125		13.67		*Ba1*	P & S [*Sc10*]	
K_2ZnF_4	T	4.02		13.05		*Sc10*		
$K_2Zn_2F_7$	T	4.063		21.22		*Br12*		

Compound	Sym	a Å	b Å	c Å	angle	Ref	Remarks	Magnetic Data
$K_2Zn_2F_7$	T	4.063		21.22		*Br12*		
Halides (continued)								in 3.3.4, Tab.
$(NH_4)_2ZnF_4$	T	4.14		13.97		*Cr3*		
Tl_2ZnF_4	T	4.105		14.10		*Vo1*		
Rb_2CdF_4	T	4.414		13.98		*Co27a*		
$Rb_3Cd_2F_7$	T	4.403		22.71		*Co27a*		
K_2CdF_4							Prep. [*Co26, Co27a*]	
$K_3Cd_2F_7$							Prep. [*Co26, Co27a*]	
Cs_2CdCl_4	T	5.26		16.88		*Si3*		
Oxides								
$SrLaAlO_4$	T	3.75		12.5		*Ru1*	Eu^{3+} fluorescence [*Ni1*]	
Sr_2TiO_4	T	3.88		12.58		*Ba10*	P&S [*Ru1, Br11, Lu2, Po9, Ha19a*], Eu^{3+} fluorescence [*Ni1*]	
$Sr_3Ti_2O_7$	T	3.90		20.38		*Ru2*	P&S [*Lu2*]	
$Sr_3Ti_2O_{10}$	T	3.90		28.1		*Ru2*		
$Ca_3Ti_2O_7$	O	5.412	5.426	19.50		*Pe3*	P&S [*Ro17*]	
$Ca_4Ti_4O_{10}$	O	5.404	5.435	27.14		*Pe3*	P&S [*Ro17*]	
$NaLaTiO_4$	T	3.76		12.95		*Bl12*	(Na and Ln ordered). Fluorescence: Eu [*Bl12a*]	
$NaNdTiO_4$	T	3.76		12.79		*Bl12*		
$NaSmTiO_4$	T	3.77		12.59		*Bl12*		
$NaGdTiO_4$	T	3.77		12.46		*Bl12*	Fluorescence: Eu [*Bl12a*]	
$NaDyTiO_4$	T	3.77		12.22		*Bl12*		
$NaTmTiO_4$	T	3.78		12.05		*Bl12*		
$NaLuTiO_4$	T	3.78		11.92		*Bl12*	Fluorescence: Eu [*Bl12a*]	
$NaYTiO_4$	T	3.786		12.209		*Re2*	P&S [*Bl12*], fluorescence: Eu [*Bl12a*]	
$Na_2Y_2Ti_4O_{14}$	T	3.79		20.2		*Re2*		
$Na_2Y_4Ti_6O_{10}$	T	3.79		28.2		*Re2*		
Eu_2TiO_5	T	3.89		12.53		*Ro21*	P&S [*Mc1b*]	
$Eu_4Ti_2O_7$	T	3.899		20.295		*Ro21*	P&S [*Mc1b*]	
Sr_2CrO_4	T	3.82		12.4		*Lo1a*	Cr^{4+}, high pressure preparation	
$Sr_3Cr_2O_7$	T	3.82		20.1		*Lo1a*	Cr^{4+}, high pressure preparation	
$SrLaCrO_4$	T	3.84		12.52		*Bl9*		
Sr_2MnO_4	T	3.79		12.43		*Ba10*	Substitution of La [*Sr2*]	
Ca_2MnO_4	T	3.667		12.063		*Ma6*	P&S [*Ru1, Br11*]	6
$Ca_3Mn_2O_7$	T	3.709		19.44		*Ma6*	97% Mn^{4+}; P&S [*Ru1, Br11*]	6
$Ca_4Mn_3O_{10}$	T	3.724		26.90		*Ma6*	97% Mn^{4+}; P&S [*Ru1, Br11*]	6
$Sr_{1-x}La_xMnO_4$	T					*Le7*		6
$SrLaMnO_4$	T	3.88		12.5		*Bl9*		
Sr_2FeO_{4-x}	T	3.864		12.390		*Ga19*	$x = 0.3$	
$Sr_3Fe_2O_{7-x}$	T	3.853		20.149		*Ga19*	$x = 0.1$, P&S [*Br10*], Prop. [*Ma7*]	6

Compound	Sym	a Å	b Å	c Å	angle	Ref.	Remarks	Magnetic Data
Oxides (continued)								in 3.3.4, Tab.
$Sr_3Fe_2O_{7-z}$ cont.	T	3.892		20.054		*Ga19*	$x = 1$, Prop. [*Ma7*]	
Sr_3FeO_3F	T	3.84		12.98		*Ga3*		
$SrLaFeO_4$	T	3.86		12.69		*Bl9*	Prop. [*As6*]	6
$SrLaCoO_4$	T	3.80		12.50		*Bl9*		
La_2CoO_4	O	5.482	5.539	12.66		*Ra2*	Prep. [*Fo1, Fo3*] substitution of Sr [*Sr2, Go6*]	
$La_2Co_{0.5}Li_{0.5}O_4$	T	3.77		12.58		*Bl9*		6
$La_{1.5}Sr_{0.5}CoO_4$	T						Prop. [*Sr2, Go26*]	6
$La_{1.5}Sr_{0.5}Co_{0.5}Mg_{0.5}O_4$	T	3.82		12.58		*Bl9*		6
$Sr_{1.5}La_{0.5}Co_{0.5}Ti_{0.5}O_4$	T	3.85		12.62		*Bl9*		6
La_2NiO_4	T	3.855		12.652		*Ra2*	P&S [*Fo1, Fo3*], Prop. [*Sm34, Sm24*]	6
Pr_2NiO_4							Prop. [*Sm34*]	6
Nd_2NiO_4	T	3.81		12.31		*Fo1*	Prop. [*Sm34, Sm24*]	6
$SrLaNiO_4$	T	3.80		12.51		*Bl9*		
$La_2Ni_{0.5}Li_{0.5}O_4$	T	3.75		12.89		*Bl9*		6
La_2CuO_4	O	5.36	5.41	13.17		*Lo1c*	Prep. [*Fr25, Fo1, Fo3*]	
	T	3.81		13.24		*Lo1c*	at 420 °C, tetr. $T > 250$ °C	
Pr_2CuO_4	T	3.96		12.23		*Fr25*		
Nd_2CuO_4	T	3.94		12.15		*Fo1*	P&S [*Fr25*]	
Sm_2CuO_4	T	3.91		11.93		*Fo1*	P&S [*Fr25*]	
Eu_2CuO_4	T	3.91		11.92		*Fr25*		
Gd_2CuO_4	T	3.89		11.85		*Fo1*	P&S [*Fr25*]	
$SrLaGaO_4$	T	3.84		12.71		*Bl9*		
Ca_2GeO_4	T	3.70		11.88		*Re2*	100 kbars, 900 °C required, P&S [*Ri8b*]	
Ba_2ZrO_4	T	4.187		13.48		*Sc18a*		
Sr_2ZrO_4	T	5.801		12.445		*Pe3*	P&S [*Sc18a*]	
$Sr_3Zr_2O_7$	O	5.798	5.808	20.94		*Pe3*		
$Sr_4Zr_3O_{10}$	O	5.795	5.814	29.34		*Pe3*		
K_2NbO_3F	T	3.96		12.67		*Ga2*		
Sr_2MoO_4	T	3.92		12.84		*Ba10*	P&S [*Sc16*], Prop. [*Ro2a*]	6
Ba_2TcO_4	T	4.011		13.40		*Ke9*		
Sr_2TcO_4	T	3.902		12.72		*Ke9*		
Sr_2RuO_4	T	3.870		12.74		*Ra6*	Prop. [*Ca2*]	6
Sr_2RhO_4	T	3.85		12.90		*Ra6*		
$SrLaRhO_4$	T	3.92		12.78		*Bl9*		
Ba_2SnO_4	T	4.130		13.27		*We8*	P&S [*Wa2*]	
Sr_2SnO_4	T	4.037		12.53		*We8*	P&S [*Wa2*]	
Ca_2SnO_4							Not K_2NiF_4 type, [*We8*]	
Ba_2HfO_4	T	4.161		13.45		*Sc18a*		
Sr_2HfO_4	T	4.089		12.52		*Sc18a*		

Sr_2HIO_6	T	4.069		12.52		56764		

Compound	Sym	a Å	b Å	c Å	angle	Ref.	Remarks	Magnetic Data
Oxides (continued)								in 3.3.4, Tab. 6
Sr_2IrO_4	T	3.89		12.92		*Ra7*	Prop. [*Ro2a*]	
Ca_2IrO_4	H	9.423		3.195		*Ba5a*	Not K_2NiF_4 type	
Ba_2PbO_4	T	4.296		13.30		*We8*	P&S [*Wa2*]	
A_2PbO_4						*We8*	A = Sr + Ca, not K_2NiF_4 type	
Cs_2UO_4	T	4.38		14.79		*Ko11*		
Rb_2UO_4	T	4.345		13.83		*Ko11*		
K_2UO_4	T	4.335		13.10		*Ko11*		
β-Na_2UO_4	O	5.795	5.97	11.68		*Ko11*		

Tab. 4e: see next page

Tab. 4e. $Bi_2O_3(A_{n-1}B_nO_{3n+1})$ compounds

Compound	Sym	a Å	b Å	c Å	angle	Ref.	Remarks	Magnetic Data
								in 3.3.4, Tab.
Bi_2MoO_6	O	5.49	5.50	16.24		*Bl10*	P&S [*Ze3*]	
Bi_2WO_6	O	5.49	5.50	16.24		*Bl10*		
$BaBi_2Nb_2O_9$	O	5.533	5.533	25.55		*Au2*	P&S [*Su3*], S.S. with Sr and Ca [*Sm19*]	
$SrBi_2Nb_2O_9$	O	5.504	5.504	25.05		*Au2*	P&S [*Sm19; Su3*]	
$CaBi_2Nb_2O_9$	O	5.435	5.485	24.87		*Au2*	P&S [*Sm19; Su3*], dielectric properties [*Is3*]	
$PbBi_2Nb_2O_9$	O	5.492	5.503	25.53		*Au2*	P&S [*Su2; Su3*], S.S. with Ba and Sr [*Sm19*], dielectric properties [*Sm19, Is3*]	
	T	5.535		25.72		*Is3*	T = 520 °C	
$K_{0.5}Bi_{2.5}Nb_2O_9$	O	5.506	5.506	25.26		*Au2*		
$Na_{0.5}Bi_{2.5}Nb_2O_9$	O	5.47	5.47	26.94		*Au2*		
$BaBi_2Ta_2O_9$	O	5.556	5.556	25.60		*Su4*	P&S [*Sm19; Su3*]	
$SrBi_2Ta_2O_9$	O	5.509	5.509	25.06		*Au2*	P&S [*Sm19; Su3*]	
$CaBi_2Ta_2O_9$	O	5.435	5.468	24.97		*Is3*	Dielectric properties	
	T	5.479		25.085		*Is3*	T = 600 °C	
$PbBi_2Ta_2O_9$	O	5.496	5.496	25.40		*Su4*	P&S [*Sm19, Su2, Su3*]	
Bi_2NbTiO_9	O	5.405	5.442	25.11		*Au2*	P&S [*Su3, Sm19*], dielectric properties [*Is11b, Is3*]	
Bi_2TaTiO_9	O	5.402	5.436	25.15		*Au2*	P&S [*Su3*], dielectric properties [*Is11b*]	
$BaBi_4Ti_3NbO_{12}$	T	3.874		33.70		*Su2*		
$PbBi_4Ti_3NbO_{12}$	T	3.867		33.55		*Su2*		
$Bi_4Ti_3O_{12}$	O	5.410	5.448	32.84		*Au3*	Dielectric properties [*Kr1, Su4, Sm19, Va11*], S.S. with $BaTiO_3$ [*Is6*], S.S. with $Pb_2Nb_2O_7$ [*Su1*], tetragonal at 675 °C [*Su1*], Electrooptic properties [*Cu2*], switching behavior [*Cu1*], monoclinic symmetry [*Cu2*]	
$BaBi_4Ti_4O_{15}$	T	5.461		41.85		*Su4*	P&S [*Su3, Sm19, Au4, Is6, Su2*]	
$SrBi_4Ti_4O_{15}$	T	5.428		40.95		*Su4*	P&S [*Su3, Sm19*]	
$CaBi_4Ti_4O_{15}$	T	5.418		40.75		*Su4*	P&S [*Su3, Sm19*]	
$PbBi_4Ti_4O_{15}$	T	5.437		41.35		*Su4*	P&S [*Su2, Sm19, Su3*]	
$Bi_4Ti_3GaO_{15}$	T	5.408		41.05		*Su4*	P&S [*Su3*]	
$Bi_4Ti_3FeO_{15}$	O	5.445	5.455	41.31		*Is12*	Tetr. T > 740 °C, Prop. [*Is11a*]	
$K_{0.5}Bi_{4.5}Ti_4O_{15}$	T	5.440		41.15		*Su4*	P&S [*Su3*]	
$Na_{0.5}Bi_{4.5}Ti_4O_{15}$	T	5.427		40.65		*Su4*	P&S [*Su3, Ha9*], structure determination [*Ne9*]	
$Ba_2Bi_4Ti_5O_{18}$	O	5.514	5.526	50.37		*Is6*	P&S [*Su3*], tetr. at 310 °C [*Is6*]	
$Ba_2Bi_4Ti_4Fe_2O_{18}$	O	5.490	5.500	50.185		*Is12*		
$Sr_2Bi_4Ti_5O_{18}$	T	5.461		48.80		*Su4*	Probably orthorhombic	
$Pb_2Bi_4Ti_5O_{18}$	T	5.461		49.70		*Su4*	P&S [*Su3*]	
$Ba_2Bi_4Ti_3Fe_6O_{27}$	O	5.491	5.502	76.20		*Is12*		

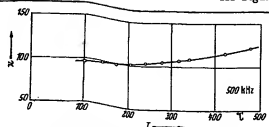

Fig. 871. $CaBi_4Nb_2O_9$ (ceramics). $\varkappa$ vs. T [61S11].

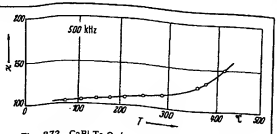

Fig. 872. $CaBi_2Ta_2O_9$ (ceramics). $\varkappa$ vs. T [61S11].

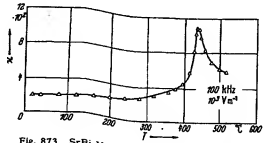

Fig. 873. $SrBi_4Nb_2O_9$ (ceramics). $\varkappa$ vs. T [62S17].

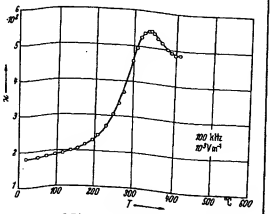

Fig. 874. $SrBi_2Ta_2O_9$ (ceramics). $\varkappa$ vs. T [62S17].

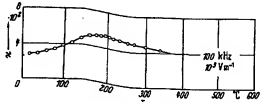

Fig. 875. $BaBi_4Nb_2O_9$ (ceramics). $\varkappa$ vs. T [62S17].

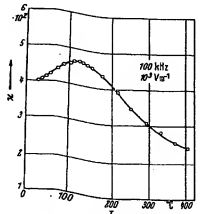

Fig. 876. $BaBi_2Ta_2O_9$ (ceramics). $\varkappa$ vs. T [62S17].

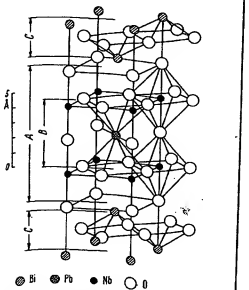

Fig. 877. $PbBi_4Nb_2O_9$. Schematic drawing of crystal structure. One half of the pseudotetragonal unit cell from $z \approx 0.25$ to $z \approx 0.75$ is given. A denotes the perovskite layer $PbNb_2O_7^{2-}$, B denotes a unit of hypothetical perovskite structure $PbNbO_3$ and C denotes $(Bi_2O_2)^{2+}$ layers [62S15].

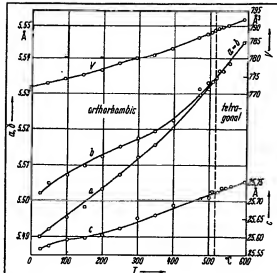

Fig. 878. $PbBi_4Nb_2O_{15}$ (ceramics). Lattice parameters vs. T [601].

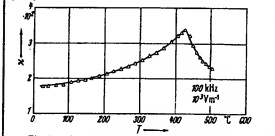

Fig. 880. $PbBi_4Ta_2O_{15}$ (ceramics). $\varkappa$ vs. T [625 I7].

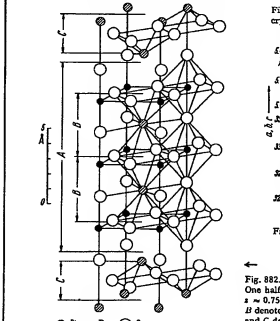

Fig. 882. $Bi_4Ti_3O_{12}$. Schematic drawing of crystal structure. One half of the pseudotetragonal unit cell from $z \approx 0.25$ to $z \approx 0.75$ is given. A denotes the perovskite layer $Bi_4Ti_3O_{12}^{2-}$, B denotes a unit of hypothetical perovskite structure $BiTiO_3$ and C denotes $(Bi_2O_2)^{2+}$ layers [625 I5].

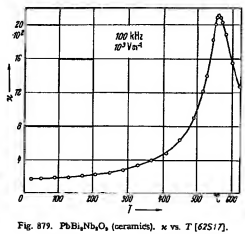

Fig. 879. $PbBi_2Nb_2O_9$ (ceramics). $\varkappa$ vs. T [625 I7].

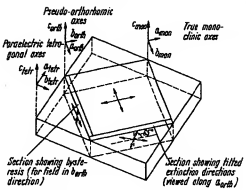

Fig. 881. $Bi_4Ti_3O_{12}$. Relationship between the three sets of crystallographic axes [67C6].

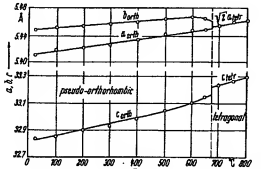

Fig. 883. $Bi_4Ti_3O_{12}$. Lattice parameters vs. T [615 I6].

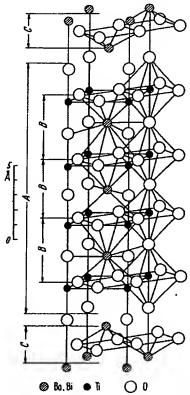

Fig. 890. $BaBi_4Ti_4O_{15}$. Schematic drawing of crystal structure. One half of the pseudotetragonal unit cell from $z \approx 0.25$ to $z \approx 0.75$ is given. *A* denotes the perovskite layer $BaBi_4Ti_4O_{15}^{2-}$, *B* denotes a unit of hypothetical perovskite structure $(Ba, Bi)TiO_3$, *C* denotes $(Bi_2O_2)^{2+}$ layers [*62S15*].

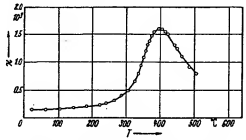

Fig. 891. $BaBi_4Ti_4O_{15}$ (ceramics). $\varkappa$ vs. T [*61S15*].

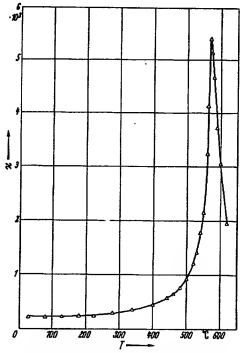

Fig. 893. $PbBi_4Ti_4O_{15}$ (ceramics). $\varkappa$ vs. T [*61S15*].

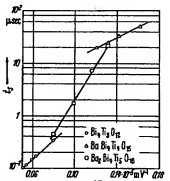

Fig. 892. $BaBi_4Ti_4O_{15}$, $Ba_2Bi_4Ti_5O_{18}$, $Bi_4Ti_3O_{12}$. t_s vs. $1/E$. [*62F1*]. t_s: switching time.

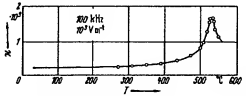

Fig. 894. $SrBi_4Ti_4O_{15}$ (ceramics). $\varkappa$ vs. T [*62S1*].

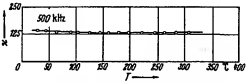

Fig. 895. $CaBi_4Ti_4O_{15}$ (ceramics). $\varkappa$ vs. T [*61S1*].

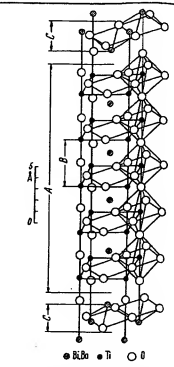

Fig. 896. $Ba_2Bi_4Ti_5O_{18}$. Schematic drawing of the crystal structure. One half of the tetragonal unit cell from $z = 0.25$ to $z = 0.75$ is given. *A* denotes the perovskitic layer of $Ba_2Bi_4Ti_5O_{17}$; *B* denotes a unit cell of the hypothetical perovskite structure $(Ba, Bi)TiO_x$, and *C* denotes the layers of $(Bi_2O_2)^{++}$ [*62A5*].

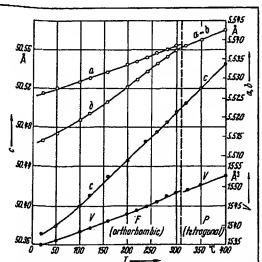

Fig. 897. $Ba_2Bi_4Ti_5O_{18}$. Lattice parameters vs. *T* [*63I5*].

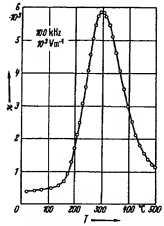

Fig. 899. $Pb_2Bi_4Ti_5O_{18}$ (ceramics). $\varkappa$ vs. *T* [*62S17*].

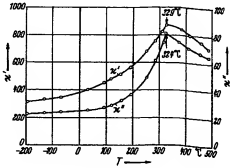

Fig. 898. $Ba_2Bi_4Ti_5O_{18}$. $\varkappa'$ and $\varkappa''$ vs. *T* [*62A5*].

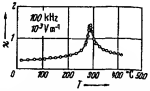

Fig. 900. $Sr_2Bi_4Ti_5O_{18}$ (ceramics). $\varkappa$ vs. *T* [*62S17*].

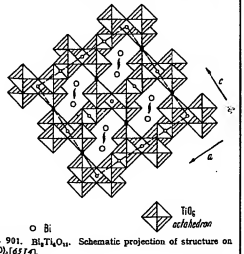

Fig. 901. $Bi_4Ti_4O_{11}$. Schematic projection of structure on $(010)_t$ [*65J4*].

BRIEF ATTACHMENT O

IN THE UNITED STATES PATENT AND TRADEMARK OFFICE

In re Patent Application of
Applicants: Bednorz et al.
Serial No.: 08/479,810
Filed: June 7, 1995

Date: March 1, 2005
Docket: YO987-074BZ
Group Art Unit: 1751
Examiner: M. Kopec

For: NEW SUPERCONDUCTIVE COMPOUNDS HAVING HIGH TRANSITION TEMPERATURE, METHODS FOR THEIR USE AND PREPARATION

Commissioner for Patents
P.O. Box 1450
Alexandria, VA 22313-1450

FIRST SUPPLEMENTAL AMENDMENT

Sir:

In response to the Office Action dated July 28, 2004, please consider the following:

ATTACHMENT O

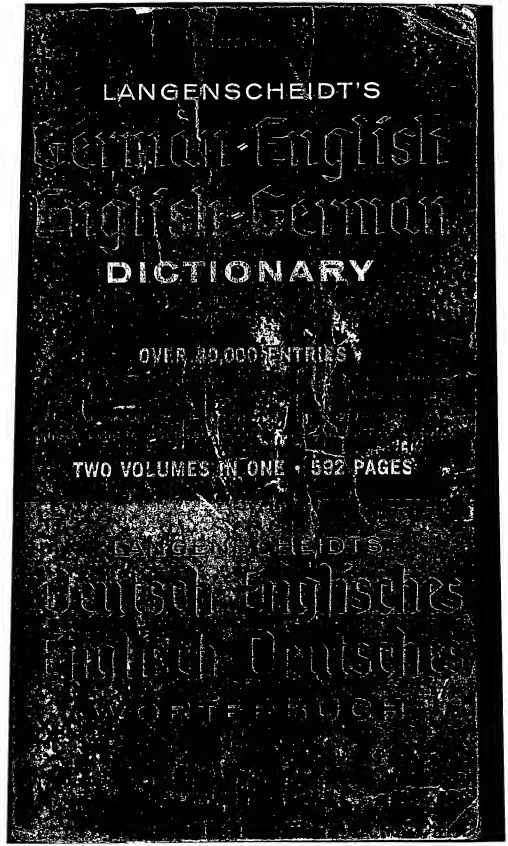
LANGENSCHEIDT'S
German-English
English-German
DICTIONARY
OVER 80,000 ENTRIES
TWO VOLUMES IN ONE • 592 PAGES
LANGENSCHEIDTS
Deutsch-englisches
English-Deutsches

LANGENSCHEIDT'S GERMAN-ENGLISH
ENGLISH-GERMAN DICTIONARY

A *Washington Square Press* edition

1st printing.....January, 1953
37th printing.....August, 1969

New Revised and Enlarged Edition

1st printing.....January, 1970

This WASHINGTON SQUARE PRESS edition is published by arrangement with Langenscheidt KG, Publishers, Berlin and Munich, Germany, and is printed from brand-new plates made from newly set, clear, easy-to-read type.

WSP

Published by Washington Square Press,
a division of Simon & Schuster, Inc., 630 Fifth Avenue, New York, N.Y.

WASHINGTON SQUARE PRESS editions are distributed in the U.S. by Simon & Schuster, Inc., 630 Fifth Avenue, New York, N.Y. 10020 and in Canada by Simon & Schuster of Canada, Ltd., Richmond Hill, Ontario, Canada.

Standard Book Number: 671-47825-7.

ne Fläche; (gleiche) Höhe, Niveau *n*, Stand *m*; *fig.* Maßstab *m*; Wasserwage *f*; *sea* ~ Meeresspiegel *m*; *on the* ~ F offen, aufrichtig; **3.** *v/t.* gleichmachen, ebnen; *fig.* anpassen; richten, zielen mit; ~ *up* erhöhen; *v/i.* ~ *at, against* zielen auf (*acc.*); **~-headed** vernünftig, nüchtern.

lever ['li:və] Hebel *m*; Hebestange *f*; **~age** [~əridʒ] Hebelkraft *f*.

levity ['leviti] Leichtfertigkeit *f*.

levy ['levi] **1.** Erhebung *f von Steuern*; ✕ Aushebung *f*; Aufgebot *n*; **2.** *Steuern* erheben; ✕ ausheben.

lewd □ [lu:d] liederlich, unzüchtig.

liability [laiə'biliti] Verantwortlichkeit *f*; ⚖ Haftpflicht *f*; Verpflichtung *f*; *fig.* Hang *m*; *liabilities pl.* Verbindlichkeiten *f/pl.*, † Passiva *pl.*

liable □ ['laiəbl] verantwortlich; haftpflichtig; verpflichtet; ausgesetzt (*to dat.*); *be* ~ *to* neigen zu.

liar ['laiə] Lügner(in).

libel ['laibəl] **1.** Schmähschrift *f*; Verleumdung *f*; **2.** schmähen; verunglimpfen.

liberal ['libərəl] **1.** □ liberal (*a. pol.*); freigebig; reichlich; freisinnig; **2.** Liberale(r) *m*; **~ity** [libə'ræliti] Freigebigkeit *f*; Freisinnigkeit *f*.

liberat|e ['libəreit] befreien; freilassen; **~ion** [libə'reiʃən] Befreiung *f*; **~or** ['libəreitə] Befreier *m*.

libertine ['libə(:)tain] Wüstling *m*.

liberty ['libəti] Freiheit *f*; *take liberties* sich Freiheiten erlauben; *be at* ~ frei sein.

librar|ian [lai'brɛəriən] Bibliothekar(in); **~y** ['laibrəri] Bibliothek *f*.

lice [lais] *pl. von louse.*

licen|ce, *Am.* **~se** ['laisəns] **1.** Lizenz *f*; Erlaubnis *f*; Konzession *f*; Freiheit *f*; Zügellosigkeit *f*; *driving* ~ Führerschein *m*; **2.** lizenzieren, bescheinigen; *et.* genehmigen; **~see** [laisən'si:] Lizenznehmer *m*.

licentious □ [lai'senʃəs] unzüchtig; ausschweifend.

lichen ♀, ✠ ['laikən] Flechte *f*.

lick [lik] **1.** Lecken *n*; Salzlecke *f*; F Schlag *m*; **2.** (be)lecken; F verdreschen; übertreffen; ~ *the dust* im Staub kriechen; fallen; geschlagen werden; ~ *into shape* zurechtstutzen.

licorice ['likəris] Lakritze *f*.

lid [lid] Deckel *m*; (Augen)Lid *n*.

lie[1] [lai] **1.** Lüge *f*; *give s.o. the* ~ j-n Lügen strafen; **2.** lügen.

lie[2] [~] **1.** Lage *f*; **2.** [irr.] liegen; ~ *by* still-, brachliegen; ~ *down* sich niederlegen; ~ *in wait for j-m* auflauern; *let sleeping dogs* ~ *fig.* daran rühren wir lieber nicht; **~-down** ['lai'daun] Nickerchen *n*; **~-in**: *have o* ~ sich gründlich ausschlafen.

lien ⚖ ['li:ən] Pfandrecht *n*.

lieu [lju:]: *in* ~ *of* (an)statt.

lieutenant [lef'tenənt; ✠ le'tenənt; *Am.* lu:'tenənt] Leutnant *m*; Statthalter *m*; **~-commander** ✠ Korvettenkapitän *m*.

life [laif], *pl.* **lives** [laivz] Leben *n*; Menschenleben *n*; Lebensbeschreibung *f*; *for* ~ auf Lebenszeit; *for one's* ~, *for dear* ~ ums (liebe) Leben; *to the* ~ naturgetreu; ~ *sentence* lebenslängliche Zuchthausstrafe; ~ **assurance** Lebensversicherung *f*; **~-belt** ['laifbelt] Rettungsgürtel *m*; **~-boat** Rettungsboot *n*; **~-guard** Leibwache *f*; Badewärter *m* *on Strand*; **~-insurance** Lebensversicherung *f*; **~-jacket** ✠ Schwimmweste *f*; **~less** □ ['laiflis] leblos; matt (*a. fig.*); **~-like** lebenswahr; **~-long** lebenslänglich; **~-preserver** *Am.* ['laifprizə:və] Schwimmgürtel *m*; Totschläger *m* (*Stock mit Bleikopf*); **~time** Lebenszeit *f*.

lift [lift] **1.** Heben *n*; *phys.*, ✈ Auftrieb *m*; *fig.* Erhebung *f*; Fahrstuhl *m*; *give s.o. a* ~ j-m helfen; j-n (im Auto) mitnehmen; **2.** *v/t.* (auf)heben; erheben; beseitigen; *sl.* klauen, stehlen; *v/i.* sich heben.

ligature ['ligətʃuə] Binde *f*; ♯ Verband *m*.

light[1] [lait] **1.** Licht *n* (*a. fig.*); Fenster *n*; Aspekt *m*, Gesichtspunkt *m*; Feuer *n*; Glanz *m*; *fig.* Leuchte *f*; ~*s pl.* Fähigkeiten *f/pl.*; *will you give me a* ~ darf ich Sie um Feuer bitten; *put to* ~ *s.o.* anzünden; **2.** licht, hell; blond; **3.** [irr.] *v/t. oft* ~ *up* be-, erleuchten; anzünden; *v/i. mst* ~ *up* aufleuchten; ~ *out Am. sl.* schnell losziehen, abhauen.

light[2] [~] **1.** *adj.* □ *u. adv.* leicht (*a. fig.*); ~ *current* ⚡ Schwachstrom *m*; *make* ~ *of et.* leicht nehmen; **2.** ~ (*up*)*on* stoßen *od.* fallen auf (*acc.*), geraten an (*acc.*); sich niederlassen auf (*dat.*).

lighten ['laitn] blitzen; (sich) erhellen; leichter machen; (sich) erleichtern.

lighter ['laitə] Anzünder *m*; (Taschen)Feuerzeug *n*; ✠ L(e)ichter *m*.

light|-headed ['lait'hedid] wirr im Kopf, irr; **~-hearted** □ [~'ha:tid] leichtherzig; fröhlich; **~house** ['laithaus] Leuchtturm *m*.

lighting ['laitiŋ] Beleuchtung *f*; Anzünden *n*.

light|-minded ['lait'maindid] leichtsinnig; **~ness** ['laitnis] Leichtigkeit *f*; Leichtsinn *m*.

lightning ['laitniŋ] Blitz *m*; ~ *bug Am. zo.* Leuchtkäfer *m*; **~-conductor**, **~-rod** ⚡ Blitzableiter *m*.

light-weight ['laitweit] *Sport:* Leichtgewicht *n*.

like [laik] **1.** gleich; ähnlich; wie; *such* ~ dergleichen; *feel* ~ F sich